UNIVERSIDAD COMPLUTENSE DE MADRID
FACULTAD DE CIENCIAS QUÍMICAS
Departamento de Química Orgánica I

TESIS DOCTORAL

Non-covalent functionalization of graphene by mono-and tripodal electroactive systems

(Funcionalización no-covalente de grafeno con sistemas electroactivos mono- y tripodales)

MEMORIA PARA OPTAR AL GRADO DE DOCTOR

PRESENTADA POR

Marina Garrido Serrano

Directores

Mª Ángeles Herranz Astudillo
Nazario Martín León

Madrid, 2018

UNIVERSIDAD COMPLUTENSE DE MADRID
FACULTAD DE CIENCIAS QUÍMICAS

Departamento de Química Orgánica I

Non-covalent functionalization of graphene by mono- and tripodal electroactive systems

---

(Funcionalización no-covalente de grafeno con sistemas electroactivos mono- y tripodales)

TESIS DOCTORAL

Marina Garrido Serrano

Madrid, 2017

Non-covalent functionalization of graphene by mono- and tripodal electroactive systems

---

(Funcionalización no-covalente de grafeno con sistemas electroactivos mono- y tripodales)

Directores:

Dra. Mª Ángeles Herranz Astudillo

Dr. Nazario Martín León

Memoria que para optar al grado de

DOCTOR EN CIENCIAS QUÍMICAS

presenta

Marina Garrido Serrano

Madrid, 2017

Dª. Mª Ángeles Herranz Astudillo, Profesora Titular del Departamento de Química Orgánica de la Universidad Complutense de Madrid y **D. Nazario Martín León**, Catedrático de Universidad del Departamento de Química Orgánica de la Universidad Complutense de Madrid,

CERTIFICAN:

Que la presente Memoria titulada: *Non-covalent functionalization of graphene by mono- and tripodal electroactive systems (Funcionalización no-covalente de grafeno con sistemas electroactivos mono- y tripodales)* se ha realizado bajo su dirección en el Departamento de Química Orgánica de la Facultad de Ciencias Químicas de la Universidad Complutense de Madrid por la Graduada en Ciencias Químicas Dª. Marina Garrido Serrano y autorizan su presentación para ser calificada como Tesis Doctoral.

Y para que conste firman el presente certificado en Madrid, a 24 de abril de 2017

Fdo. Dra. Mª Ángeles Herranz Astudillo Fdo. Dr. Nazario Martín León

Esta Tesis se ha realizado en el Departamento de Química Orgánica de la Universidad Complutense de Madrid bajo la dirección de los Profesores Mª Ángeles Herranz y Nazario Martín.

Primero quiero dar las gracias a mis directores de Tesis, Nazario y Mª Ángeles, por haber confiado en mí para realizar este trabajo, por su ayuda y por haberme permitido formar parte del grupo de investigación durante todos estos años.

A la Dra. Laura Rodríguez, gracias por haber hecho posible gran parte de esta Tesis. Sin ti, muchos de los resultados no estarían incluidos en esta memoria. Gracias por haberme enseñado a lo largo de todos estos años y por tu ayuda.

En la realización de este trabajo han participado otros grupos de investigación, a los que agradezco su contribución:

Al grupo de la Prof. Encarnación Lorenzo de la Universidad Autónoma de Madrid, en especial al Dr. Emiliano Martínez por el estudio electroquímico de los derivados de π-exTTF.

Al Prof. Enrique Ortí y al Dr. Joaquín Calbo de la Universidad de Valencia, por los cálculos teóricos realizados de la interacción de los distintos sistemas con la superficie del grafeno.

Al grupo del Prof. Dirk M. Guldi de la Universidad Friedrich-Alexander de Erlangen/Nürnberg (Alemania) por los estudios fotofísicos de los derivados de porfirina.

También quiero agradecer al personal de los diferentes CAI de la Facultad de Ciencias Químicas y del SIdI de la Universidad Autónoma de Madrid su apoyo para la caracterización incluida en este trabajo: a Ana Soubrié por la realización de las imágenes de microscopía de AFM y SEM. A Ángel Sánchez y a las Dras. Dolores Molero y Elena Sáez del CAI de RMN por su ayuda y disponibilidad a la hora de realizar los distintos experimentos de RMN.

A Francisco Javier García por los espectros de FTIR incluidos en esta Tesis.

A los técnicos de laboratorio Laura García, Francisco Javier García y Javier Cornejo por su ayuda y disposición en todo momento.

A continuación quiero dar las gracias a todos los compañeros y amigos del departamento y en especial del laboratorio.

A los "mayores", Salvo, Carmen, David, Beti, Luis…gracias por estar siempre dispuestos a ayudar.

A todos los compañeros del laboratorio, espero no dejarme a nadie: Javi, Juan, Antonio, Jaime, María, "Muchachito" que ya no están. Sarita, Andrés, Paul, Chus, Marta, Valentina, Alicia, Antonio José, Alfonso, Inés, Rafa, Javi, Agus, Jose. Gracias por todos los buenos momentos tanto dentro como fuera del laboratorio y por vuestra ayuda.

A Virginia, Ana y Helena, gracias por ocuparos de que todo funcione, de que haya caramelos y por estar dispuestas a echar una mano siempre.

A Paula, Alberto y Dani.

Al grupo de comida, que con el paso de los años ha ido cambiando y disminuyendo: Jorge, Yeray, Laura, Julia y Miki. Gracias por las risas, sobremesas y conversaciones, en definitiva por poder desconectar.

A Sonia, Miki, Rosa, Silvia, Julia, Carmen y Laura. Gracias por vuestra amistad, por los buenos momentos, los consejos, los viajes y sobre todo por estar ahí y por vuestra ayuda.

A Irene, Clara y Rebeca. Gracias por seguir a mi lado después de todos estos años, a pesar de la distancia. Gracias por confiar en mí y por vuestra amistad. Clara, gracias por todo. Rebeca, tú más que nadie entiende y sabe lo difícil que ha sido llegar hasta aquí y el esfuerzo que ha supuesto (autobuses, carreras, madrugones), en unos meses las dos seremos Doctoras. Gracias.

A Luna, gracias por haber sido mi compañera de series y cenas estos dos años.

Finalmente quiero darle las gracias a mi familia, por su apoyo y cariño. A mis padres por haber apoyado cada una de las decisiones que he tomado, por confiar en mí y por el esfuerzo que habéis realizado a lo largo de todos estos años para que yo pudiera elegir. A mis hermanos, gracias por vuestro cariño, amistad y confianza. Esta memoria va dedicada a vosotros. GRACIAS.

ABBREVIATIONS AND ACRONYMS

In addition to the standard abbreviations and acronyms in organic chemistry (as defined in the *Journal of Organic Chemistry* author guidelines, http://pubs.acs.org/paragonplus/submission/joceah/joceah_authguide.pdf) the following terms have been used in this manuscript:

AFM	Atomic force microscopy
BTP	Bis(terpyridine)
ca.	Circa (“around”, “about”)
CTAB	Cetyltrimethylammonium bromide
CNT	Carbon nanotube
CVD	Chemical vapor deposition
DCTB	*trans*-2-[3-(4-*tert*-Butylphenyl)-2-methyl-2-propenylidene] malononitrile
DOSY	Diffusion-ordered NMR spectroscopy
EC	Ethyl cellulose
FLG	Few layer graphene
FWHM	Full-width half-maximum
GC	Glassy carbon
GO	Graphene oxide
GO-ER	Graphene oxide electrochemically reduced
HBPE	Hyperbranched polyethylene
HMTA	Hexamethylenetetramine
HRP	Horseradish peroxidase
HRTEM	High-resolution transmission electron microscopy
IL	Ionic liquid
MWCNT	Multi-walled carbon nanotube
o-DCB	*ortho*-dichlorobenzene
π-exTTF	π-extended tetrathiafulvalene

P	Porphyrin
PAH	Polycyclic aromatic hydrocarbon
PBI	Perylene bisimide
PBS	Phosphate buffer solution
Pc	Phthalocyanine
PCTE	Polycarbonate track etched
PPV	Poly(*p*-phenylene vinylene)
PTCDA	Perylene-3,4,9,10-tetracarboxylic dianhydride
PTFE	Polytetrafluoroethylene
PVP	Polyvinylpyrrolidone
Py	Pyrene
QD	Quantum dot
QT	3,3’’’-dioctyl-2,2’:5’,5’’:2’’,2’’’-quaterthiophene
QTDA	3,3’’’-dioctyl-2,2’:5’,5’’:2’’,2’’’-quaterthiophene-5,5’’’-dicarboxylic acid
SC	Sodium cholate
SDBS	Sodium dodecylbenzene sulfonate
SWCNT	Single-walled carbon nanotube
TBAP	Tetrabutylammonium perchlorate
$TBAPF_6$	Tetrabutylammonium hexafluorophosphate
TCNQ	7,7’,8,8’-tetracyano-*p*-quinodimethane
Tpy	Terpyridine
TEM	Transmission electron microscopy
TGA	Thermogravimetric analysis
vs.	*Versus* (“against”)
XPS	X-ray photoelectron spectroscopy

Table of contents

SUMMARY

Graphene is nowadays the most popular nanomaterial due to its excellent mechanical, electronic, and thermal properties. However, two major drawbacks hamper its implementation in practical applications: its lack of solubility in common solvents and its relative inert surface. To overcome such setbacks, both covalent and non-covalent chemical methods have been investigated in recent years. The covalent functionalization results in stable products, but implies the saturation of some of the double bonds affecting the electronic properties of graphene, whereas the non-covalent functionalization allows its solubilization while preserving the structural and electronic features.

Within this general perspective, the main aim of this PhD work was to explore the chemical modification of graphene with different electroactive molecules through non-covalent interactions, specifically π-π stacking, which preserves the π-conjugated system of graphene. We have prepared different molecular receptors endowed with one (monopodal derivatives) or three pyrene units (tripodal derivatives), which favor the interactions between these systems and the basal plane of graphene through π-π stacking interactions. In addition, these receptors have been decorated with different electroactive moieties (π-exTTF, porphyrins and C_{60}), in order to modulate the electronic properties of graphene.

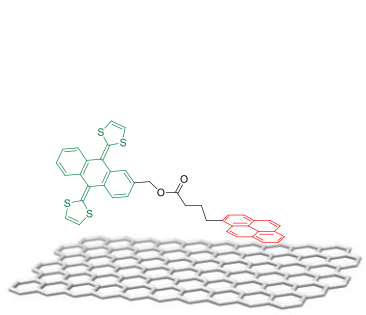

PyexTTF/FLG

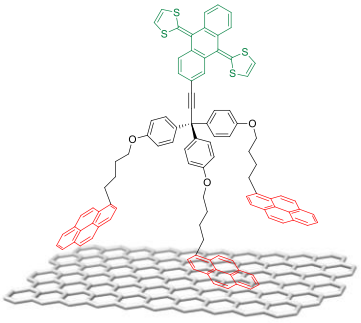

3PyexTTF/FLG

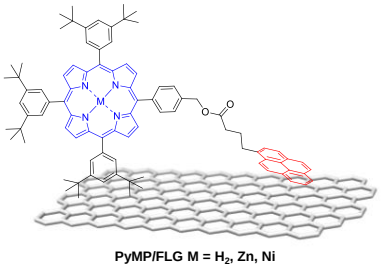

PyMP/FLG M = H_2, Zn, Ni

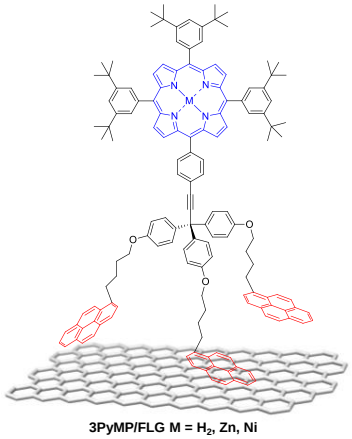

3PyMP/FLG M = H_2, Zn, Ni

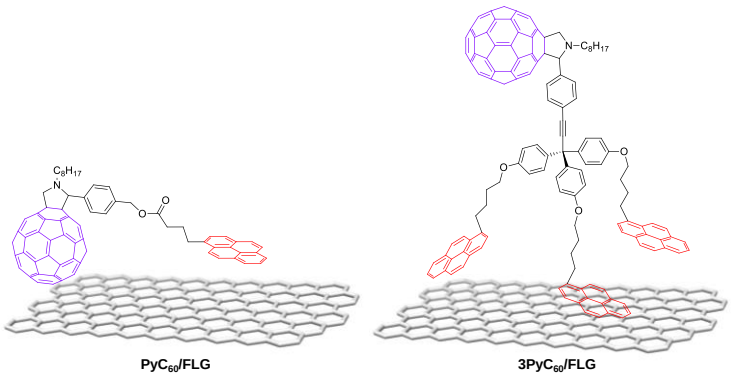

As starting point of this work, we tested the exfoliation of graphite to obtain graphene in different solvents (NMP, *o*-DCB and DMF) with the objective to determine the optimum solvent for the exfoliation. The study of the obtained material by transmission electron microscopy (TEM) and Raman spectroscopy allowed to conclude that NMP is the best solvent to exfoliate graphite and to obtain a few layer graphene material (FLG). Afterwards, the influence of the sonication time in the exfoliation was investigated. It was observed that an increase in the sonication time produces more concentrated graphene dispersions, although the dimensions of the flakes decrease and they tend to agglomerate. For this reason, we decided to work with dispersions of moderate concentration in graphene, but with higher sheet dimensions, in order to facilitate the non-covalent functionalization of graphene.

Subsequently, the series of receptors, containing one or three pyrene anchoring groups, covalently linked to π-exTTF, porphyrin (free base, Zn, or Ni) and C_{60} electroactive units, were prepared and completely characterized. To complement the characterization of these molecules, we performed ^{1}H-NMR titrations to investigate the supramolecular interactions between different pyrene-based systems in solution. In the case of the monopodal derivatives which are electronically complementary, for example the porphyrins and C_{60}, it was concluded that the interaction depends on the central atom present in the porphyrin unit. While in the case of PyexTTF, this interaction is much weaker. With the aim to determine if the self-assembly of $3PyC_{60}$ was possible, concentration and temperature dependent ^{1}H-NMR studies were carried out, observing the formation of small aggregates

Before accomplishing the non-covalent functionalization of FLG with the different molecular systems, studies in solution were performed by UV-Vis and, in some cases, fluorescence titrations in NMP, in order to determine the possible interactions between the receptors and FLG. In all the experiments

carried out with the different systems, changes in the spectra were observed due to the presence of FLG in the medium, confirming the interaction between the receptors and the material.

The synthesis of the supramolecular complexes of FLG and the molecular receptors was carried out following a procedure that combines sonication, filtration and washings steps. All the non-covalent hybrids were characterized by several analytical, spectroscopic, electrochemical and microscopic techniques (TGA, FTIR, Raman, UV-Vis, cyclic voltammetry, TEM and XPS) and the experimental results corroborate the non-covalent functionalization of FLG with the different molecular receptors. Furthermore, additional studies were performed for each family of compounds, due to their different electronic properties.

The electrochemical behavior of PyexTTF and 3PyexTTF was studied onto different graphene surfaces, allowing to determine the differences between both systems and their affinity for the distinct surfaces. In addition, the non-covalent hybrid formed by PyexTTF has been used for the development of an enzymatic biosensor able to operate at very low potentials.

In the case of the porphyrin derivatives, preliminary photophysical measurements were performed with the aim to study the electronic communication between the molecular receptors and FLG in the non-covalent hybrids. By transient absorption spectroscopy, the spectral features of the porphyrin cation were observed in the case of PyZnP, due to the photoinduced electron transfer from the porphyrin unit to FLG.

In order to shed light into the interaction between the different supramolecular receptors and FLG, theoretical investigations were carried out using molecular mechanics calculations. These studies have allowed to determine the more probable conformations for each system and the contribution of each interaction to the binding process.

RESUMEN

El grafeno es en la actualidad el nanomaterial más popular debido a sus excelentes propiedades mecánicas, electrónicas y térmicas. Sin embargo, presenta dos limitaciones fundamentales de cara a su implementación práctica: su escasa solubilidad en los disolventes de uso habitual y que es una superficie muy inerte. Con objeto de superar estos obstáculos, en los últimos años se han investigado tanto métodos de funcionalización química covalente como no-covalente. La funcionalización covalente proporciona productos estables, pero supone la saturación de algunos de los dobles enlaces del grafeno modificando sus propiedades electrónicas, mientras que la funcionalización no-covalente permite mejorar la solubilidad manteniendo las características estructurales y electrónicas del grafeno.

Dentro de esta perspectiva general, el objetivo principal que nos planteamos en este trabajo de tesis, fue el llevar a cabo la modificación química de grafeno con diferentes moléculas electroactivas mediante el empleo de interacciones no-covalentes, en concreto de tipo π-π, que preservan el esqueleto π-conjugado del grafeno. Para ello se han preparado diferentes receptores moleculares que poseen en su estructura una (derivados monopodales) o tres unidades de pireno (tripodales), favoreciendo la interacción entre dichos sistemas y el plano basal del grafeno mediante interacciones π-π. Además, estos receptores moleculares presentan diferentes unidades electroactivas (π-exTTF, porfirinas o C_{60}), con el fin de modular las propiedades electrónicas del grafeno.

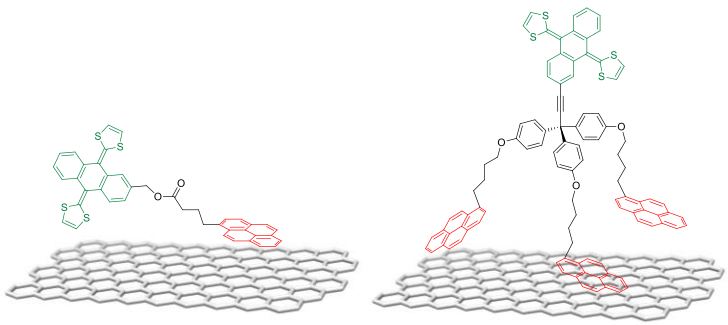

PyexTTF/FLG 3PyexTTF/FLG

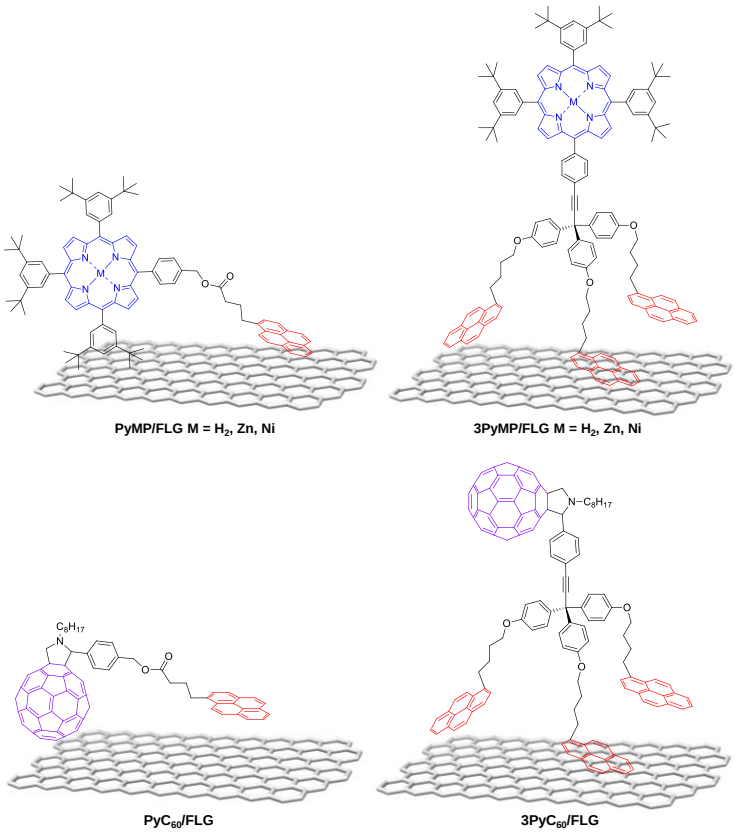

Para ello, en primer lugar se estudió la exfoliación de grafito para la obtención de grafeno en diferentes disolventes (NMP, *o*-DCB y DMF), con objeto de comprobar cuál de ellos era el más adecuado. El estudio del material obtenido mediante microscopía de transmisión electrónica (TEM) y espectroscopía Raman, permitió determinar que el disolvente óptimo para la exfoliación del grafito es la NMP, que proporciona un material de pocas láminas de grafeno (*few layer graphene*, FLG, en sus siglas inglesas). Posteriormente, también se estudió la influencia del tiempo de sonicación en dicho proceso, observándose cómo el aumento del tiempo permite obtener dispersiones más concentradas de grafeno, pero disminuyendo las dimensiones de las láminas obtenidas y aumentando la aglomeración de las mismas. Por estas razones, se decidió continuar el trabajo de investigación con dispersiones de concentraciones moderadas, pero que proporcionan láminas de grafeno de mayores dimensiones, con la idea de facilitar la funcionalización no covalente del grafeno con los diferentes receptores moleculares.

A continuación, la serie de receptores moleculares, con una o tres unidades de pireno como grupos de anclaje, y conectados covalentemente a unidades

electroactivas de π-exTTF, porfirina (base libre, Zn o Ni) y C_{60}, fue sintetizada y todas las moléculas caracterizadas. Para completar la caracterización de las mismas, se realizaron estudios de complejación en disolución entre los diferentes sistemas derivados de pireno, mediante valoraciones de ^{1}H-RMN. En el caso de los derivados monopodales, que presentan complementariedad electrónica, por ejemplo los derivados de porfirina y el derivado de C_{60}, se observa que la interacción depende del átomo central de la unidad de porfirina. Mientras que en el caso del derivado de PyexTTF esta interacción es mucho más débil. Para el sistema tripodal 3PyC_{60}, los estudios de ^{1}H-RMN se llevaron a cabo a concentración y temperatura variable, con el fin de determinar su autoasociación, observándose la formación de pequeños agregados.

Antes de sintetizar los complejos supramoleculares entre los diferentes receptores y FLG, se realizaron estudios en disolución para determinar la posible interacción entre ambos sistemas, consistentes en valoraciones de UV-Vis y, en algunos casos, también fluorescencia en NMP. En todos los experimentos llevados a cabo con los diferentes compuestos, tanto con los derivados monopodales como con los tripodales, se observaron cambios en los espectros debidos a la presencia de FLG en el medio, confirmando la interacción entre los receptores y el material.

La síntesis de los complejos supramoleculares de FLG y los receptores moleculares ha sido llevada a cabo por un procedimiento que combina etapas de sonicación, filtración y lavado. Todos los complejos supramoleculares han sido caracterizados mediante diversas técnicas analíticas, espectroscópicas, electroquímicas y microscópicas (ATG, IRTF, Raman, UV-Vis, voltamperometría cíclica, TEM y XPS). Los resultados experimentales corroboraron la funcionalización no-covalente del grafeno con los diferentes receptores moleculares. Debido a las diferentes propiedades electrónicas que poseen las unidades electroactivas presentes tanto en los derivados monopodales como en los tripodales, se han realizado estudios adicionales para cada una de las familias de receptores.

Para los derivados de PyexTTF y 3PyexTTF, se realizó su estudio electroquímico sobre diferentes superficies derivadas de grafeno, pudiéndose determinar las diferencias entre ambos sistemas y su afinidad por las distintas superficies. Además, el complejo supramolecular formado a partir de PyexTTF se ha usado para el desarrollo de un biosensor enzimático capaz de trabajar a potenciales muy bajos.

En el caso de los derivados de porfirina, se han llevado a cabo estudios fotofísicos preliminares con el objetivo de determinar la comunicación electrónica entre estos sistemas y el grafeno en los complejos supramoleculares. Mediante medidas de absorción transitoria, se ha podido observar la formación del catión radical de la porfirina de Zn en el complejo PyZnP, como consecuencia de la transferencia electrónica fotoinducida desde la unidad de porfirina al grafeno.

Con el fin de entender la interacción de los diferentes receptores moleculares con el grafeno, se han realizado cálculos teóricos mediante mecánica molecular. Estos análisis han permitido determinar las conformaciones más probables para cada uno de los sistemas estudiados, así como la contribución de cada una de las interacciones al proceso global de enlace.

1. INTRODUCTION

1. INTRODUCTION

Carbon, which is not the most abundant element in nature, has however a remarkable ability to form different structures with a high degree of versatility, giving rise to the possibility of near-infinite combinations. The position of carbon, midway in the periodic table, makes it equally prone to interact with electropositive or electronegative elements to form different carbon compounds such as polymers, hydrocarbons, carbonates…Besides, carbon can also bond to itself and, depending on its hybridization, it forms different allotropes.[1]

Diamond (sp^3 hybridization) and graphite (sp^2 hybridization) were considered the only known natural allotropes of carbon until 1985. In that year, [60]fullerene was discovered during the simulation of the conditions under which carbon nucleates in the atmosphere of red giant stars.[2] This astonishing molecule is considered since then the third allotropic form of carbon. Because of the importance of the discovery of [60]fullerene, Robert F. Curl Jr, Sir Harold W. Kroto and Richard E. Smalley were awarded with the Nobel Prize in Chemistry in 1996.

Few years later, in 1991, carbon nanotubes (CNTs) were discovered by Sumio Iijima, who reported the production of a new carbon structure with needle form. With the development of electronic microscopy in the early 30's, it was found that each needle was constituted by several concentric tubes of graphitic sheets.[3] These structures are known as multi-walled carbon nanotubes (MWCNTs). In 1993, Iijima also reported the synthesis of single-walled carbon nanotubes (SWCNTs), formed only by one tube.[4] Although the attribution of this discovery has aroused some controversy and discussion due to the considerable amount of work between the 1950-1970 decades on these filamentous carbon structures.

Eleven years later from the discovery of SWCNTs, in 2004, Alexander Geim and Konstantin Novoselov reported the isolation of a single layer of graphite,

1. a) E. H. L. Falcao, F. Wudl, *J. Chem. Technol. Biotechnol.* **2007**, *82*, 524-531. b) J. L. Delgado, M. A. Herranz, N. Martín, *J. Mater. Chem.* **2008**, *18*, 1417-1426.
2. a) H. W. Kroto, J. R. Heath, S. C. O'Brien, R. F. Curl, R. E. Smalley, *Nature* **1985**, *318*, 162-163. b) J. R. Heath, R. F. Curl, R. E. Smalley, *J. Chem. Phys.* **1987**, *87*, 4236-4238.
3. S. Iijima, *Nature* **1991**, *354*, 56-58.
4. a) S. Iijima, T. Ichihashi, *Nature* **1993**, *363*, 603-605. b) D. S. Bethune, C. H. Klang, M. S. de Vries, G. Gorman, R. Savoy, J. Vazquez, R. Beyers, *Nature* **1993**, *363*, 605-607.

known as graphene.[5] Graphene films were initially obtained by mechanical exfoliation using sticky tape to peel atomically thin layers of graphite. In 2010, these two researchers were laureated with the Nobel Prize in Physics.

The capability of carbon to exist in different allotropic forms, has resulted in a wide variety of other carbon nanostructures (intermediate or mixed states between a curved sheet and a fullerene): nanohorns, nanoonions, fullerene peapods or nanotori have been described during the last decades,[6] but their development cannot be compared with the huge importance that fullerenes, CNTs and graphene present. Interestingly, these three nanomaterials are formed by hexagonal rings constructed from sp^2 hybridized carbon atoms. In fullerenes the curvature is introduced by pentagonal rings and CNTs can be considered rolled graphene sheets (Figure 1).

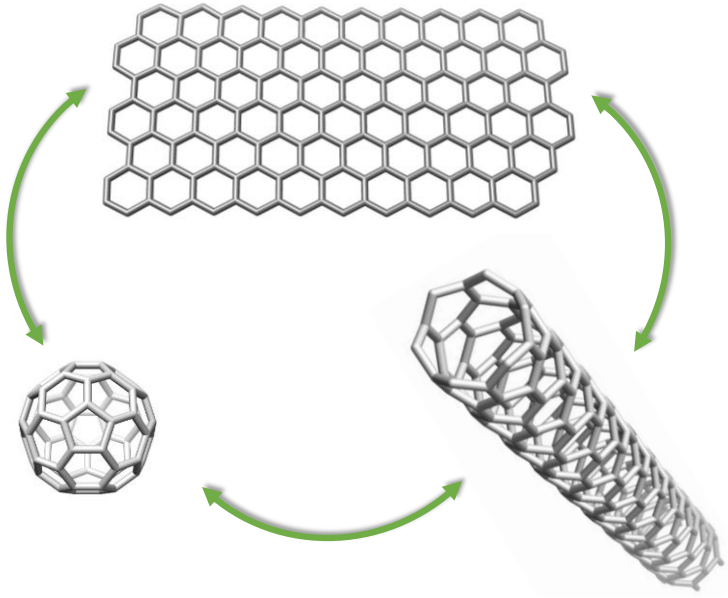

Figure 1. Schematic representation of different carbon nanostructures: [60]fullerene, single-walled carbon nanotube and graphene.

The great attention in these carbon nanostructures is related to their attractive properties. The presence of conjugated π-electronic systems provide unprecedented electronic features. [60]Fullerene presents interesting photo- and electrochemical characteristics that have allowed the application of

5. K. S. Novoselov, A. K. Geim, S. V. Morozov, D. Jiang, Y. Zhang, S. V. Dubonos, I. V. Grigorieva, A. A. Firsov, *Science* **2004**, *306*, 666-669.
6. T. Akasaka, F. Wudl, S. Nagase, *Chemistry of Nanocarbons*, John Wiley&Sons, Chichester, **2010**.

modified fullerenes in organic electronics or photovoltaic devices.[7] In addition to these properties, the unique spherical shape of [60]fullerene makes it useful for different biological applications.[8] As a remarkable example, a [60]fullerene derivative decorated with 120 carbohydrates, which maintains a globular shape, has been able of inhibit the virus infection of an artificial Ebola model by blocking the receptor implied in its expansion.[9]

While [60]fullerene is a molecular structure, both CNTs and graphene are nanostructured materials with improved mechanical and thermal properties to those of fullerenes.[10] Just to name a few: high current density, ballistic transport, ultrahigh thermal conductivity and extremely high mechanical strength,[11] which make them interesting for different applications.[12] Considering their mechanical properties, CNTs have been used extensively for the mechanical reinforcement of polymers.[13] Their electronic properties allow to build different devices such as supercapacitors, flat panel displays, nanotube-based lamps, organic photovoltaic devices (OPVs) and organic light-emitting diodes (OLEDs). Graphene presents similar features to that of CNTs but with a better performance (Table 1).

Table 1. Comparative table for graphene and CNTs main properties.[14]

Properties	Graphene	CNTs
Fracture strength (GPa)	≈ 124 (Modulus: ≈ 1100 GPa)	45
Density (g/cm^3)	>1	1.33
Thermal conductivity (W/m·K)	≈ 5000	3000
Electrical conductivity (S/cm)	10^6	5000
Charge mobility (cm^2/V·s)	200000	100000
Specific surface area (m^2/g)	2630	400 (for nanotube "paper")

7. a) D. M. Guldi, B. M. Illescas, C. M. Atienza, M. Wielopolski, N. Martín, *Chem. Soc. Rev.* **2009**, *38*, 1587-1597. b) K. A. Mazzio, C. K. Luscombe, *Chem. Soc. Rev.* **2015**, *44*, 78-90.
8. A. Montellano, T. Da Ros, A. Bianco, M. Prato, *Nanoscale* **2011**, *3*, 4035-4041.
9. A. Muñoz, D. Sigwalt, B. M. Illescas, J. Luczkowiak, L. Rodríguez-Pérez, I. Nierengarten, M. Holler, J.-S. Remy, K. Buffet, S. P. Vincent, J. Rojo, R. Delgado, J.-F. Nierengarten, N. Martín, *Nat. Chem.* **2016**, *8*, 50-57.
10. D. M. Guldi, N. Martín, *Carbon Nanotubes and Related Structures*, Wiley-VCH, Weinheim, **2010**.
11. R. H. Baughman, A. A. Zakhidov, W. A. d. Heer, *Science* **2002**, *297*, 787-792.
12. M. F. L. De Volder, S. H. Tawfick, R. H. Baughman, A. J. Hart, *Science* **2013**, *339*, 535-539.
13. J. N. Coleman, U. Khan, Y. K. Gun'ko, *Adv. Mater.* **2006**, *18*, 689-706.
14. L. Dai, D. W. Chang, J.-B. Baek, W. Lu, *Small* **2012**, *8*, 1130-1166.

Graphene is the thinnest and the strongest material ever known, also presents flexibility and brittleness at the same time, and is impermeable to gases, even though what makes graphene unique are its electronic properties. Electrons move through graphene sheets as if they have no mass and they can cover submicrometer distances thanks to ballistic transport, because of that, quantum effects can survive even at room temperature.[15]

The first reported application of graphene was a device, a graphene-based field effect transistor, developed by Alexander Geim and Konstantin Novoselov when they reported its isolation.[5] From that initial investigation, graphene has been incorporated in many electronic devices such as transparent electrodes, touch screens[16] and lamps[17] (Figure 2).

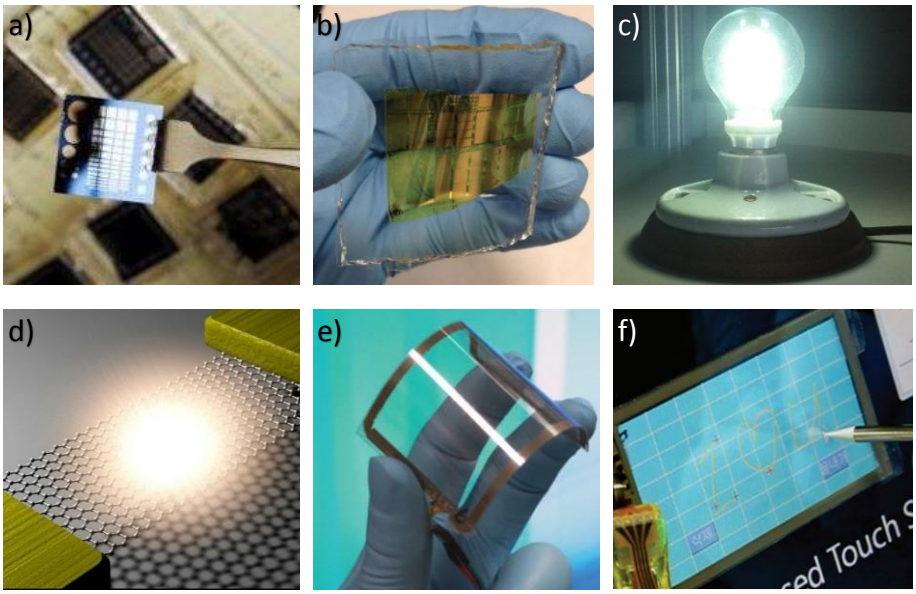

Figure 2. Different devices built with carbon nanostructures. a) field effect transistor fabricated with [60]fullerene developed in the Georgia Institute of Technology. b) thin-film transistor built with CNTs created by Chongwu Zhou group. c) and d) light bulb made with graphene, a collaboration between mechanical engineers from the USA and Korea. e) and f) graphene touch panel developed by Sumio Iijima group.

15. A. K. Geim, *Science* **2009**, *324*, 1530-1534.
16. S. Bae, H. Kim, Y. Lee, X. Xu, J.-S. Park, Y. Zheng, J. Balakrishnan, T. Lei, H. Ri Kim, Y. I. Song, Y.-J. Kim, K. S. Kim, B. Ozyilmaz, J.-H. Ahn, B. H. Hong, S. Iijima, *Nat. Nanotechnol.* **2010**, *5*, 574-578.
17. Y. D. Kim, H. Kim, Y. Cho, J. H. Ryoo, C.-H. Park, P. Kim, Y. S. Kim, S. Lee, Y. Li, S.-N. Park, Y. Shim Yoo, D. Yoon, V. E. Dorgan, E. Pop, T. F. Heinz, J. Hone, S.-H. Chun, H. Cheong, S. W. Lee, M.-H. Bae, Y. D. Park, *Nat. Nanotechnol.*, **2015**, *10*, 676-681.

Furthermore, graphene is a zero band-gap semiconductor, the conduction band touches the valence band at the Brillouin zone corners (Figure 3a).[18] For many electronic applications it is necessary to open this band gap. To carry out this opening there are four kinds of methods: heteroatom doping,[19] electrostatic field tuning,[20] cutting graphene into nanoribbons[21] and chemical modification[22] (Figure 3b). Considering the strong tendency that graphene presents to aggregate due to the electrostatic force and the strong π-π interactions between individual sheets, the chemical approach is particularly useful, since allows the further manipulation and solubilization of graphene.

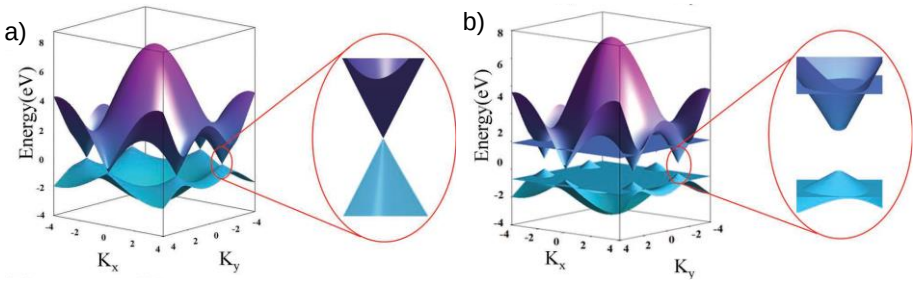

Figure 3. a) Zero band-gap of graphene, b) Band-gap opening by chemical modification.[23]

In addition, the chemical modification of graphene is critical to improve its processability for any practical applications. Functionalization schemes that confer an additional element of control over the nanomaterial properties are particularly attractive. In this regard, the combination of carbon nanostructures with electroactive molecules attracts considerable attention for their potential

18. a) K. S. Kim, Y. Zhao, H. Jang, S. Y. Lee, J. M. Kim, K. S. Kim, J.-H. Ahn, P. Kim, J.-Y. Choi, B. H. Hong, *Nature* **2009**, *457*, 706-710. b) A. H. Castro Neto, F. Guinea, N. M. R. Peres, K. S. Novoselov, A. K. Geim, *Rev. Mod. Phys.* **2009**, *81*, 109-162.
19. M. L. Mueller, X. Yan, B. Dragnea, L.-s. Li, *Nano Lett.* **2011**, *11*, 56-60.
20. T. Ohta, A. Bostwick, T. Seyller, K. Horn, E. Rotenberg, *Science* **2006**, *313*, 951-954.
21. L. Jiao, L. Zhang, X. Wang, G. Diankov, H. Dai, *Nature* **2009**, *458*, 877-880.
22. H. Liu, Y. Liu, D. Zhu, *J. Mater. Chem.* **2011**, *21*, 3335-3345.
23. H.-X. Wang, Q. Wang, K.-G. Zhou, H.-L. Zhang, *Small* **2013**, *9*, 1266-1283.

as electron donor-acceptor systems for artificial photosynthesis[24] and photovoltaics.[25]

Within this context, we have explored the chemical modification of graphene with different electroactive molecules through non-covalent interactions, specifically π-π stacking, which preserves the π-conjugated system of graphene. We have built functional supramolecular structures which, at a final stage, could have a potential impact in the development of nanomaterials for opto-electronics and sensing.

24. a) X. Huang, Z. Yin, S. Wu, X. Qi, Q. He, Q. Zhang, Q. Yan, F. Boey, H. Zhang, *Small* **2011**, *7*, 1876-1902. b) X. Wan, Y. Huang, Y. Chen, *Acc. Chem. Res.* **2012**, *45*, 598-607.
25. a) L. Dai, *Acc. Chem. Res.* **2013**, *46*, 31-42. b) N. Martín, *Adv. Energy Mater.* **2017**, *7*, 1601102.

2. BACKGROUND

2. BACKGROUND

2.1. GRAPHENE STRUCTURE DEFINITIONS

Graphite is the most abundant natural carbon allotrope due to its thermodynamic stability at ambient temperatures and pressures. Graphite is constituted by carbon atoms layers with sp^2 hybridization, in each single layer (graphene) each atom is bonded to other three, forming hexagons that are fused throughout the layer. Layers are separated by a distance of 3.35 Å and linked by van der Waals interactions generated by the delocalization of π-orbitals (Figure 4). This delocalization generates conjugated π-electrons that are responsible of the electronic properties of graphite. Graphite is anisotropic because of the nature of this binding forces, it presents good electrical and thermal conductivity through the layers and it is a poor electrical and thermal conductor in the perpendicular direction.[26]

Graphene is a monolayer of sp^2 hybridized carbon atoms arranged into a two dimensional honeycomb structure, therefore is a single atomic layer of graphite. Because of its atomic thickness, graphene is the thinnest known material which, in addition, presents outstanding mechanical, thermal and electronic properties.[15]

Until graphene was isolated,[5] it was supposed that two dimensional materials could not exist because they were thermodynamically unstable.[27,28] Nevertheless, these materials are stabilized by deformations in the third dimension. Although it was expected that graphene was perfectly flat, A. Geim and K. Novoselov reported that graphene layers present intrinsic corrugations and can exist without a substrate.[29] Real graphene exhibits edges that have either a zig-zag or an armchair arrangement. The high-resolution transmission electron microscopy (HRTEM) image of graphene in Figure 4d shows a graphene layer with a typical edge.[30] Ideally, a two dimensional material is considered a single atomic layer, but graphene can be considered a two dimensional material until a 10 layers thickness. Depending on its electronic

26. D. D. L. Chung, *J. Mater. Sci.* **2002**, *37*, 1475-1489.
27. R. E. Peierls, *Ann. Inst. Henri Poincare* **1935**, *5*, 177-222.
28. L. D. Landau, *Phys. Z. Sowjetunion* **1937**, *11*, 26.
29. J. C. Meyer, A. K. Geim, M. I. Katsnelson, K. S. Novoselov, T. J. Booth, S. Roth, *Nature* **2007**, *446*, 60-63.
30. S. Eigler, A. Hirsch, *Angew. Chem. Int. Ed.* **2014**, *53*, 7720-7738.

structure, graphene could be classified in three different types: single layer, bilayer and few-layer graphene.[31]

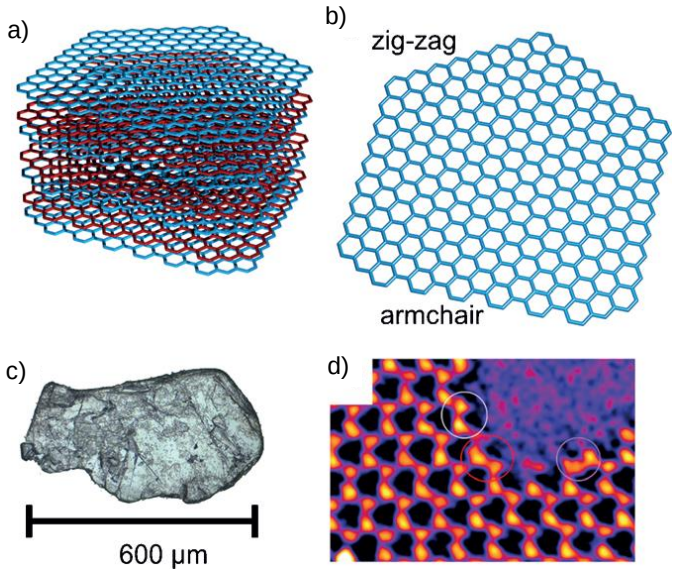

Figure 4. Schematic representation of a) the ideal structure of AB-stacked graphite and b) the structure of a sheet of graphene with zig-zag and armchair edges. c) Photograph of natural graphite with visible macroscopic cracks and holes. d) HRTEM image of graphene with one edge.

Other form to classify graphene relates with the modification of its structure: pristine graphene (without defects or functional groups) and chemically modified graphene (graphene oxide and reduced graphene oxide). Graphene oxide (GO) is a chemically modified graphene layer. The modification consists in the presence of epoxide, hydroxyl, carbonyl and carboxyl groups that make GO hydrophilic and allow the stabilization of layers in water (Figure 5). This material is obtained by the oxidative treatment of graphite, where the graphene layers in graphite become intercalated by the acid to form, in a first instance, an intercalation compound. Subsequent oxygenation of such intercalation material occurs on both sides of the basal plane and, in this way, graphite oxide is formed. Delamination of single layers of graphite oxide provides GO.

31. A. K. Geim, K. S. Novoselov, *Nat. Mater.* **2007**, *6*, 183-191.

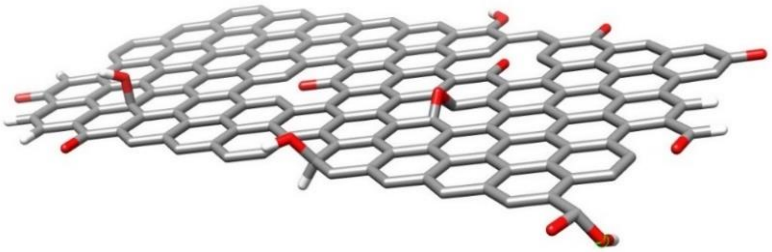

Figure 5. Structural model of GO with oxygenated functional groups in the basal plane and at the edges.

The major drawback of this method is that both, graphite oxide and therefore GO are insulators due to the disruption of the π-conjugated graphene layer by the oxygenated functions that severely modify the structure and, hence, the properties. Although these functional groups can be removed by reduction (chemical,[32] thermal and electrochemical[33]) obtaining reduced graphene oxide, the structural defects introduced by the oxidative treatment continue modifying the unique properties of graphene, in particular its high electrical and thermal conductivity.[34] Nevertheless, in some applications related with catalysis or the biomedical area GO and reduced GO have been extensively used, since they are large surfaces that feature great chemical complexity.

In the following, we will discuss the production of "pristine graphene" and its chemical functionalization, where the term "pristine" refers to graphene produced without inducing any chemical functionalization.

32. S. Stankovich, D. A. Dikin, R. D. Piner, K. A. Kohlhaas, A. Kleinhammes, Y. Jia, Y. Wu, S. T. Nguyen, R. S. Ruoff, *Carbon* **2007**, *45*, 1558-1565.
33. D. R. Dreyer, S. Park, C. W. Bielawski, R. S. Ruoff, *Chem. Soc. Rev.* **2010**, *39*, 228-240.
34. C. Gómez-Navarro, R. T. Weitz, A. M. Bittner, M. Scolari, A. Mews, M. Burghard, K. Kern, *Nano Lett.* **2007**, *7*, 3499-3503.

2.2. GRAPHENE PRODUCTION METHODS

The methods for graphene production can be divided in: bottom-up and top-down. The former consider the preparation of graphene from the covalent assembly of polycyclic aromatic hydrocarbons (PAHs),[35] by growth in different supports by silicon evaporation from SiC,[36] or by chemical vapor deposition (CVD) of small molecular precursors.[18a] These methods produce high quality graphene sheets with large areas but in limited quantities, which is a drawback for industry.

On the other hand, top-down methods consist in the exfoliation of graphite in graphene layers. This exfoliation can be accomplished by mechanical cleavage (the scotch-tape technique)[5] that allows obtaining high quality sheets, if carefully carried out, but cannot be up-scaled considering its time-consuming manual nature. Other method to exfoliate graphene is ball-milling[37], where large quantities of inexpensive materials like graphite and melamine can be used for massive and fast production of few layer graphene (Figure 6). However, additional treatments are necessary to remove the impurities that might be introduced and to process the product in liquid phase to isolate the graphene material.

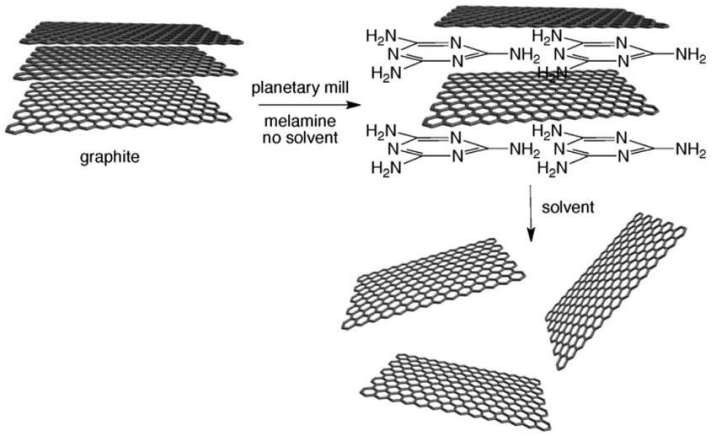

Figure 6. Schematic illustration for the exfoliation of graphite through the ball-milling approach.

35. X. Yang, X. Dou, A. Rouhanipour, L. Zhi, H. J. Räder, K. Müllen, *J. Am. Chem. Soc.* **2008**, *130*, 4216-4217.
36. C. Berger, Z. Song, X. Li, X. Wu, N. Brown, C. Naud, D. Mayou, T. Li, J. Hass, A. N. Marchenkov, E. H. Conrad, P. N. First, W. A. de Heer, *Science* **2006**, *312*, 1191-1196.
37. a) V. Leon, M. Quintana, M. A. Herrero, J. L. G. Fierro, A. d. l. Hoz, M. Prato, E. Vazquez, *Chem. Commun.* **2011**, *47*, 10936-10938. b) E. Vazquez, F. Giacalone, M. Prato, *Chem. Soc. Rev.* **2014**, *43*, 58-69.

A third method stands out within the previously mentioned top-down approaches, the liquid phase dispersion and exfoliation of graphite. In particular, the ultrasound-induced liquid-phase exfoliation[38] presents some advantages such as its potential scalability, the good quality of the obtained sheets (free of structural defects) and the straightforward transfer to different substrates for many applications.[39]

The liquid phase exfoliation process usually involves three steps: i) dispersion of graphite in a solvent, ii) exfoliation and iii) separation from the bulk graphitic starting material (usually by centrifugation). Graphene can be produced by ultrasonication in organic solvents or with the assistance of surfactants and dispersion stabilizing agents in a wider selection of solvents (Figure 7).

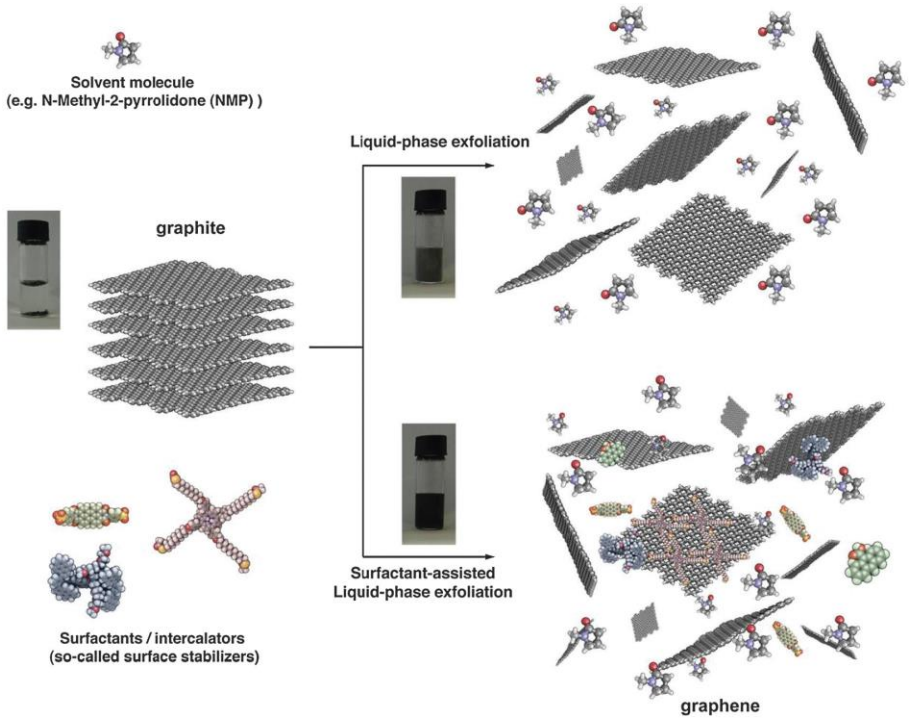

Figure 7. Schematic representation of the liquid-phase exfoliation of graphite in the absence (top) and presence (bottom) of dispersion stabilizing agents.

38. Y. Hernandez, V. Nicolosi, M. Lotya, F. M. Blighe, Z. Sun, S. De, I. T. McGovern, B. Holland, M. Byrne, Y. K. Gun'Ko, J. J. Boland, P. Niraj, G. Duesberg, S. Krishnamurthy, R. Goodhue, J. Hutchison, V. Scardaci, A. C. Ferrari, J. N. Coleman, *Nat. Nanotechnol.* **2008**, *3*, 563-568.
39. F. Torrisi, T. Hasan, W. Wu, Z. Sun, A. Lombardo, T. S. Kulmala, G.-W. Hsieh, S. Jung, F. Bonaccorso, P. J. Paul, D. Chu, A. C. Ferrari, *ACS Nano* **2012**, *6*, 2992-3006.

In the next sections we will focus on these two approaches of sonication assisted liquid-phase exfoliation.

2.2.1. Ultrasound-induced liquid-phase exfoliation without dispersion stabilizing agents

To exfoliate graphite into graphene is necessary to overcome the van der Waals interactions between layers, which can be achieved by external forces such as ultrasonication in liquid phase. The exfoliation takes place due to the cavitation and the shear forces that act on the bulk material.[40] Besides, once that the exfoliation occurs, it is required to stabilize graphene layers to avoid its re-aggregation. When the exfoliation is carried out only in the presence of solvents, the stabilization of graphene layers is due to the strong interaction between the solvent and the graphene sheets, which minimizes the enthalpy of mixing. This enthalpy depends on the balance of the solvent and the graphene surface energies. Coleman and co-workers[38] found that solvents with a surface energy close to the surface energy of graphene are the best solvents for its dispersion. These solvents possess surface energies of ~ 70 mJ/m^2, which are equivalent to surface tensions of ~ 40 mJ/m^2, *N*-methyl-2-pyrrolidone (NMP = 40 mJ/m^2) or *N*,*N*-dimethylformamide (DMF = 37 mJ/m^2) are some of the solvents in this range. These initial observations were complemented with investigations that demonstrated that the surface energy can be divided in dispersive, polar and H-bonding components (Hansen solubility parameters).[41] With the Hansen parameters values for graphene, a larger number of solvents compatible with this material were discovered: cyclopentanone, benzonitrile or *N*-ethyl pyrrolidone (Figure 8). Considering all these solvent parameters, NMP was found to be the best solvent for the exfoliation of graphene, being the one with the best number fraction of few-layer graphene and the highest number fraction of monolayer graphene.

Other solvent that allows an efficient exfoliation of graphene is *ortho*-dichlorobenzene (*o*-DCB),[42] which is a nonpolar solvent with an appropriate surface tension (*o*-DCB ~ 37 mJ/m^2). The dispersions obtained in *o*-DCB are homogeneous and the layers do not present defects.

40. T. J. Mason, J. P. Lorimer, *Applied Sonochemistry*, Wiley-VCH, Weinheim, **2002**.
41. Y. Hernandez, M. Lotya, D. Rickard, S. D. Bergin, J. N. Coleman, *Langmuir* **2010**, *26*, 3208-3213.
42. C. E. Hamilton, J. R. Lomeda, Z. Sun, J. M. Tour, A. R. Barron, *Nano Lett.* **2009**, *9*, 3460-3462.

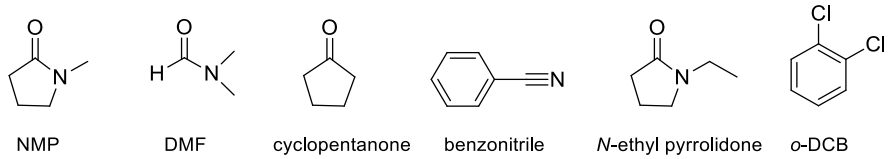

Figure 8. Common solvents used in the exfoliation of graphite.

The major drawback of these solvents is that most of them have high boiling points, which is an inconvenient for many applications. In the search for graphene's exfoliation solvents, Bourlinos and co-workers showed an enhancement on graphene dispersions concentration while exfoliating graphite with aromatic electron-accepting solvents, such as hexafluorobenzene, octafluorotoluene, pentafluorobenzonitrile and pentafluoropyridine.[43] The electron-withdrawing solvents stabilize the electron-rich graphene in a charge transfer phenomena through π-π stacking. Furthermore, the exfoliation capability of each solvent is related with its electronic nature. Blank experiments with the non-fluorinated analogues benzene, toluene and nitrobenzene, reveal little effectiveness in terms of stabilization of the graphene dispersions.

The situation was markedly different when using pyridine as exfoliating solvent, where stable dispersions were obtained. The pyridine case suggests that aromatic donors may also exfoliate graphite in the reverse way, that is, charge transfer through π-π stacking from the solvent molecules to graphene, forcing the latter to act as a withdrawing host. In this sense, other organic amine-based solvents also provided colloidal dispersions of graphene. Significant examples are the direct exfoliation of graphite with 3,3'-iminobis(*N*,*N*-dimethylpropylamine) (DMPA), *N*-[3-(dimethylamino)propyl]methacrylamide (DMAPMA), 2-(*tert*-butylamino)ethyl methacrylate (BAEMA) and 2-(dimethylamino)ethyl methacrylate (MAEMA). An extremely high concentration (~15 mg/mL) was achieved and approximately 98% of the obtained graphene remained stably dispersed, without sedimentation, over long periods of time.[44]

43. A. B. Bourlinos, V. Georgakilas, R. Zboril, T. A. Steriotis, A. K. Stubos, *Small* **2009**, *5*, 1841-1845.
44. Z. Sun, X. Huang, F. Liu, X. Yang, C. Rosler, R. A. Fischer, M. Muhler, W. Schuhmann, *Chem. Commun.* **2014**, *50*, 10382-10385.

In order to obtain more tractable graphene dispersions, Feringa and co-workers[45] reported the formation of graphene stable dispersions in ethanol after its previous exfoliation in NMP, by a simple solvent exchange the obtained graphene sheets present a low degree of defects. Recent work on the exfoliation of 2D materials, not only graphene but also MoS_2, WS_2, h-BN, Bi_2Se_3, $MoSe_2$, SnS_2 and TaS_2, has as key point the use of a mixed solvent strategy, which combines two mediocre solvents that form strong co-solvents.[46] This approach incorporates interesting advantages: i) avoids the health damage that the high toxicity of the typically used NMP, *o*-DCB and DMF can produce, by using green and healthy friendly solvents (alcohols, acetone and water) that attain similar surface tension properties; ii) reduces the costs by using common co-solvents instead of expensive single ones and; iii) provides a large library of co-solvents by multiple combinations. In particular, water/acetone mixtures achieved graphene dispersions, composed of around a 50% of thin nanosheets, and of concentrations up to 0.21 mg/mL, with free basal plane defects or oxygenated groups.

In order to optimize the graphene production, Coleman and co-workers have studied the influence of the different process parameters.[47] Firstly, they studied the sonication time and observed that the concentration increased with this parameter, while the dimensions of the sheets decreased, meaning that longer sonication times result in smaller flakes which can be dispersed at higher concentration (for NMP, 0.06 mg/mL after 30 minutes sonication *vs.* 1.20 mg/mL after 270 hours sonication). Another key parameter evaluated was the centrifugation rate, in this case the concentration decreased for a fixed sonication time with rotation rate (for NMP, 0.5 mg/mL at 500 rpm *vs.* 0.13 mg/mL at 4000 rpm), since only the smaller flakes remained dispersed due to their weight and they were in lower quantity. This last observation allows to separate the flakes by size in different fractions.

Because of the long sonication times required for obtaining higher concentrations of graphene, Coleman and co-workers modified the exfoliation

45. X. Zhang, A. C. Coleman, N. Katsonis, W. R. Browne, B. J. van Wees, B. L. Feringa, *Chem. Commun.* **2010**, *46*, 7539-7541.
46. a) J. Shen, J. Wu, M. Wang, P. Dong, J. Xu, X. Li, X. Zhang, J. Yuan, X. Wang, M. Ye, R. Vajtai, J. Lou, P. M. Ajayan, *Small* **2016**, *12*, 2741-2749. b) U. Halim, C. R. Zheng, Y. Chen, Z. Lin, S. Jiang, R. Cheng, Y. Huang, X. Duan, *Nat. Commun.* **2013**, *4*, 2213. c) Y. Min, S. Zhigang, Z. Xiaojing, M. Shulin, *J. Phys. D: Appl. Phys.* **2013**, *46*, 025301.
47. U. Khan, A. O'Neill, M. Lotya, S. De, J. N. Coleman, *Small* **2010**, *6*, 864-871.

method with a single solvent.[48] This modification involves an initial sonication step as pretreatment that facilities the dispersion of the graphene layers, after this pretreatment the dispersion is filtered without centrifugation to obtain a filter cake which is the starting material. To this solid is added NMP and is sonicated. It was found that with the pretreatment, the concentration of graphene is higher than the values obtained before, reaching dispersions with a concentration of 17 mg/mL. With another subtle modification in the pretreatment (centrifugation of the pretreated dispersion to remove unexfoliated graphite), the centrifuged dispersions can be filtered to give a powder of exfoliated few-layer graphene. This powder can be redispersed at concentrations of around 65 mg/mL. The dispersed flakes are ~ 1 μm long and ~ 3-4 layers thick on average (Figure 9). Although some sedimentation occurs, ~ 28 mg/mL of the dispersed graphene appear to be indefinitely stable.

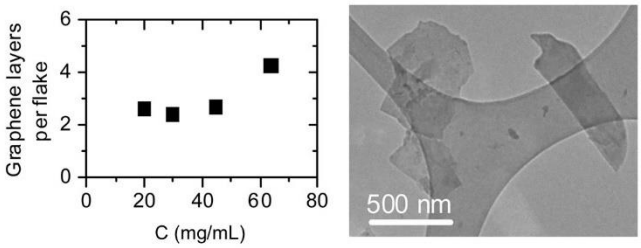

Figure 9. Left: graphene layers as a function of dispersed concentration. Right: TEM image of graphene flakes deposited from the dispersions described above.[48]

To test the efficiency of the sonication process (concentration) and the quality of the graphene obtained (number of layers, lateral size, surface area, impurities, defects…) different characterization techniques provide very useful information (Figure 10).[49]

UV-Vis spectroscopy allows to estimate the concentration of dispersed material using the Lambert-Beer Law. The number of layers can be determined by transmission electron microscopy (TEM), atomic force microscopy (AFM) and/or Raman spectroscopy. *TEM* is useful for the morphological study of the material, besides the number of graphene layers can be estimated by the

48. U. Khan, H. Porwal, A. O'Neill, K. Nawaz, P. May, J. N. Coleman, *Langmuir* **2011**, *27*, 9077-9082.
49. D. Parviz, F. Irin, S. A. Shah, S. Das, C. B. Sweeney, M. J. Green, *Adv. Mater.* **2016**, *28*, 8796-8818.

analysis at the edges[50] and by the study of the electron diffraction patterns.[51] *AFM* makes possible the estimation of layers by measuring the height of the graphene flakes. This height depends on the substrate and on the environmental conditions.[52,53]

Raman spectroscopy is a routinary tool to characterize graphene samples. It allows to obtain information about the thickness of the material and the structural defects. Raman spectra of graphene are characterized by three bands: D band (~1350 cm^{-1}, associated to carbon atoms with sp^3 hybridization, meaning defects), G band (~1580 cm^{-1}, associated to carbon atoms with sp^2 hybridization) and 2D band (~2700 cm^{-1}, indicating the number of layers). Raman spectra of graphene when increasing their number of layers, from single layer, bilayer to few-layer graphene, present very different features, which permit their differentiation.[50]

Complementary techniques can be used to determine the surface area (BET analysis)[54], the colloidal stability of the dispersions (zeta-potential),[49] the presence of impurities or different components (thermogravimetric analysis, TGA)[55] and the elements present in a graphene layer (X-ray photoelectron spectroscopy, XPS).[33]

50. A. C. Ferrari, J. C. Meyer, V. Scardaci, C. Casiraghi, M. Lazzeri, F. Mauri, S. Piscanec, D. Jiang, K. S. Novoselov, S. Roth, A. K. Geim, *Phys. Rev. Lett.* **2006**, *97*, 187401.
51. J. C. Meyer, A. K. Geim, M. I. Katsnelson, K. S. Novoselov, D. Obergfell, S. Roth, C. Girit, A. Zettl, *Solid State Commun.* **2007**, *143*, 101-109.
52. C. Vallés, C. Drummond, H. Saadaoui, C. A. Furtado, M. He, O. Roubeau, L. Ortolani, M. Monthioux, A. Pénicaud, *J. Am. Chem. Soc.* **2008**, *130*, 15802-15804.
53. K. S. Novoselov, D. Jiang, F. Schedin, T. J. Booth, V. V. Khotkevich, S. V. Morozov, A. K. Geim, *Proc. Natl. Acad. Sci. U. S. A.* **2005**, *102*, 10451-10453.
54. K. S. Subrahmanyam, S. R. C. Vivekchand, A. Govindaraj, C. N. R. Rao, *J. Mater. Chem.* **2008**, *18*, 1517-1523.
55. M. Shtein, I. Pri-Bar, M. Varenik, O. Regev, *Anal. Chem.* **2015**, *87*, 4076-4080.

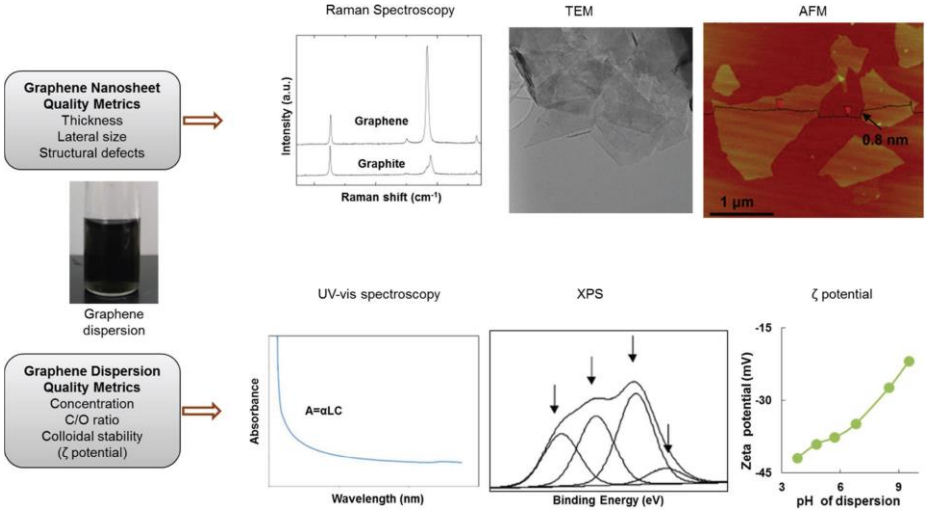

Figure 10. Measurement techniques used to determine the quality of graphene flakes and their dispersions.

2.2.2. Ultrasound-induced liquid-phase exfoliation with dispersion stabilizing agents

Due to the limited number of solvents in which graphene can be exfoliated, an alternative is the use of more common solvents (water, alcohol, THF, $CHCl_3$…) and a dispersion-stabilizing agent that hampers the re-aggregation of the graphene layers. These dispersion-stabilizing agents can be surfactants, polymers and organic molecules. Ionic liquids are a special case because they are at the same time the solvent and the dispersion-stabilizing agent.

Ionic Liquids (IL) are semiorganic (organic and inorganic ions) salts whose melting point is below 100 °C and present hydrophobic and hydrophilic components. Due to its ionic form the stabilization of graphene layers by Coulombic interactions may be possible, besides, they present surface tensions near that of graphite. Dai and co-workers reported the first exfoliation of graphene with an IL.[56] They obtained stable dispersions of few-layer graphene in 1-butyl-3-methylimidazolium bis(trifluoromethanesulfonyl)imide ([BMIM][Tf_2N]) with concentrations of 0.95 mg/mL (Figure 11). Other group that achieved the exfoliation of graphite in an IL was the one of Mariani and co-workers,[57] in this case the IL was 1-hexyl-3-methylimidazolium hexafluorophosphate ([HMIM][PF_6]).

56. X. Wang, P. F. Fulvio, G. A. Baker, G. M. Veith, R. R. Unocic, S. M. Mahurin, M. Chi, S. Dai, *Chem. Commun.* **2010**, *46*, 4487-4489.
57. D. Nuvoli, L. Valentini, V. Alzari, S. Scognamillo, S. B. Bon, M. Piccinini, J. Illescas, A. Mariani, *J. Mater. Chem.* **2011**, *21*, 3428-3431.

In a recent work, Quitevis and co-workers, tested four different ILs for the dispersion of graphene.[58] They found that depending on the substituents of the IL, the capacity of exfoliation varies, being better for the ILs with aromatic groups, $[(Bnz)_2IM][Tf_2N]$. In all these examples, the presence of the IL was confirmed by XPS, even after several washings, due to the strong adsorption of the IL on the graphene surface.

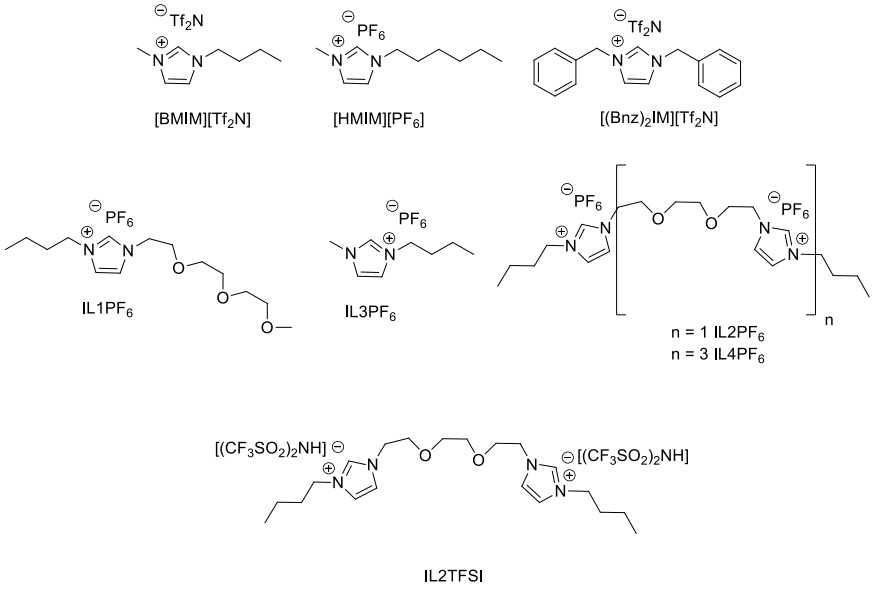

Figure 11. Ionic liquids (ILs) used in the exfoliation of graphene.

One of the most striking investigations carried out with ILs is the work published by Aida and co-workers,[59] based on a microwave assisted exfoliation of graphite with molecularly engineered oligomeric ionic liquids (IL(1-4)PF_6 and IL2TFSI). Almost quantitative yields (93%) were obtained, with a high selectivity (95%) towards single layer graphene. The authors claim that this technique is able to exfoliate graphite in 30 minutes with an awesome structural integrity of the graphene flakes obtained.

Surfactants have been utilized for the dispersion of graphene mainly in water, acting as stabilizers (Figure 12). Coleman and co-workers were the first that

58. R. Bari, G. Tamas, F. Irin, A. J. A. Aquino, M. J. Green, E. L. Quitevis, *Colloids Surf. A* **2014**, *463*, 63-69.
59. M. Matsumoto, Y. Saito, C. Park, T. Fukushima, T. Aida, *Nat. Chem.* **2015**, *7*, 730-736.

exfoliated graphene in water/surfactant solutions,[60] using sodium dodecylbenzene sulfonate (SDBS). By means of TEM demonstrated that the dispersed phase consists of small graphitic flakes, where more than a 40% of these flakes had < 5 layers with ~ 3% of flakes consisting of monolayers. In addition, atomic resolution TEM showed the monolayers to be generally free of defects. Sodium cholate (SC)[61] has also been investigated in the exfoliation of graphene in water, where graphene dispersions of up to 0.3 mg/mL were obtained. Detailed TEM analysis showed the flakes consisting of 1-10 stacked monolayers with up to 20% of flakes containing just one layer. The average flake contains ~ 4 stacked graphene layers and has a length and width of 1 μm and 400 nm, respectively. However, the mean flake length decreases with increasing centrifugation rates. The ultrasound-induced liquid-phase exfoliation was employed to directly exfoliate graphene in DMF from graphite and using cetyltrimethylammonium bromide (CTAB)[62] as surfactant. Characterization of the flakes by UV-visible spectroscopy, SEM. TEM, AFM and Raman spectroscopy showed the successful exfoliation into graphene flakes of average thickness ~ 1.2 nm. In all cases, the dispersed flakes are stabilized against re-aggregation by Coulomb repulsion due to the adsorbed surfactant.

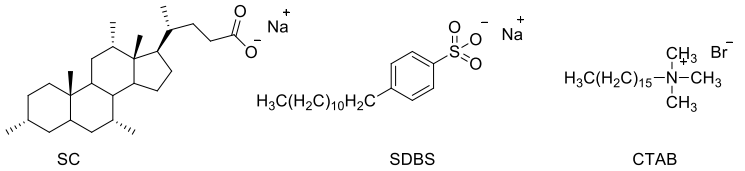

Figure 12. Surfactants used in the stabilization of graphene dispersions.

Polymers act as stabilizing agents in aqueous and organic dispersions of graphene. One of the first examples was reported by Bourlinos and co-workers,[63] who demonstrated that polyvinylpyrrolidone (PVP) forms stable colloidal aqueous dispersions of graphene (Figure 13). Soon after, Hersam and co-workers reported an efficient exfoliation of graphene in ethanol (poor

60. M. Lotya, Y. Hernandez, P. J. King, R. J. Smith, V. Nicolosi, L. S. Karlsson, F. M. Blighe, S. De, Z. Wang, I. T. McGovern, G. S. Duesberg, J. N. Coleman, *J. Am. Chem. Soc.* **2009**, *131*, 3611-3620.
61. M. Lotya, P. J. King, U. Khan, S. De, J. N. Coleman, *ACS Nano* **2010**, *4*, 3155-3162.
62. S. Vadukumpully, J. Paul, S. Valiyaveettil, *Carbon* **2009**, *47*, 3288-3294.
63. A. B. Bourlinos, V. Georgakilas, R. Zboril, T. A. Steriotis, A. K. Stubos, C. Trapalis, *Solid State Commun.* **2009**, *149*, 2172-2176.

solvent) stabilized by ethyl cellulose (EC).[64] They were able to enhance the concentration of graphene tenfold in the obtained dispersion with a simple iterative solvent exchange using terpineol. Shepherd and co-workers have demonstrated that graphene can be dispersed in THF and chloroform in the presence of hyperbranched polyethylene (HBPE).[65] The graphene obtained is a dispersion of few-layer graphene. Initial insights, when comparing the ability of different non-ionic and ionic polymers in graphene dispersion and stabilization, indicate that the non-ionic polymers significantly outperform their ionic counterparts. However, more recent investigations considering three polysaccharides with different electrostatic nature: non-ionic pullulan, cationic chitosan and anionic alginate, demonstrated that the different surface free energy and thermodynamic affinity also play a major role in the stabilization of the graphene sheets.[66] Graphene aqueous dispersions, with concentrations of up to 2.3 mg/mL in pullulan solutions and 5.5 mg/mL in chitosan solutions, were achieved, whereas alginate barely interacts with graphene. As in the case of stabilization with ILs, the adsorbed polymers are difficult to remove even after several washings, due to the strong interactions with graphene's surface.

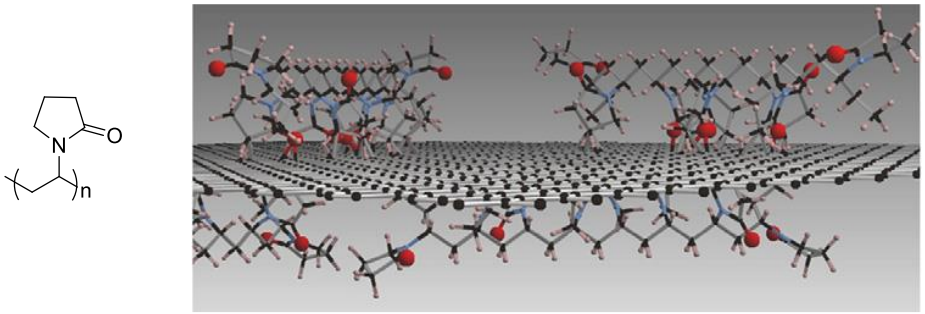

Figure 13. PVP structure and schematic model of PVP-coated graphene.

Polycyclic aromatic hydrocarbons (PAHs) can be used as stabilizers in graphene dispersions. They are adsorbed onto its surface through π-π interactions and are able to stabilize these layers in different solvents. In these non-covalent interactions, both PAHs and graphene aromatic planar surfaces share the electrons of π-orbitals, resulting in the reduction of the surface free energy of the dispersions. The π-π stacking modification with pyrene

64. Y. T. Liang, M. C. Hersam, *J. Am. Chem. Soc.* **2010**, *132*, 17661-17663.
65. L. Xu, J.-W. McGraw, F. Gao, M. Grundy, Z. Ye, Z. Gu, J. L. Shepherd, *J. Phys. Chem. C* **2013**, *117*, 10730-10742.
66. I. Uysal Unalan, C. Wan, S. Trabattoni, L. Piergiovanni, S. Farris, *RSC Adv.* **2015**, *5*, 26482-26490.

derivatives (i.e. pyrene butanoic acid succinimidyl ester) helped to stabilize graphene in aqueous solutions,[67] and has been extensively investigated. The exfoliation of graphene with pyrene-based molecules that also incorporate a hydrophilic dendron was reported by Lee and co-workers.[68] In this case the conformationally flexible aromatic segment includes four pyrene units that maximize the π-π interactions with graphene. Stable aqueous dispersions with a concentration of 1.5 mg/mL were obtained (Figure 14). In fact, various pyrene derivatives have been employed to stabilize graphene dispersions. For example, Green and co-workers studied a whole family of pyrene derivatives to investigate the mechanism of stabilization of dispersions by these molecules.[69] They found that the effectiveness of pyrene derivatives for graphene stabilization in water depends on the electron density. Considering this aspect, pyrenes with sulfonyl groups (highest electronegativity) have greater affinity for accepting electrons from graphene than pyrenes with carboxyl groups (lower electronegativity). Both of them present better affinity for graphene than pyrenes with amino functional groups, which are less electronegative. In all cases, stable aqueous dispersions have been obtained. The 1-pyrenesulfonic acid salt was found to be the most effective one, yielding graphene concentrations of 0.8-1.0 mg/mL. Other aromatic molecules that permit the stabilization of graphene in water are based on triphenylene,[70] diazaperopyrenium dications[71] or naphthalenediimide derivatives.[72] Again, in all these examples the dispersions are stable and the obtained material is formed by few layers, which indicates that graphene is efficiently exfoliated.

67. Y. Xu, H. Bai, G. Lu, C. Li, G. Shi, *J. Am. Chem. Soc.* **2008**, *130*, 5856-5857.
68. D.-W. Lee, T. Kim, M. Lee, *Chem. Commun.* **2011**, *47*, 8259-8261.
69. D. Parviz, S. Das, H. S. T. Ahmed, F. Irin, S. Bhattacharia, M. J. Green, *ACS Nano* **2012**, *6*, 8857-8867.
70. S. Das, F. Irin, H. S. Tanvir Ahmed, A. B. Cortinas, A. S. Wajid, D. Parviz, A. F. Jankowski, M. Kato, M. J. Green, *Polymer* **2012**, *53*, 2485-2494.
71. S. Sampath, A. N. Basuray, K. J. Hartlieb, T. Aytun, S. I. Stupp, J. F. Stoddart, *Adv. Mater.* **2013**, *25*, 2740-2745.
72. L. Zhang, Z. Zhang, C. He, L. Dai, J. Liu, L. Wang, *ACS Nano* **2014**, *8*, 6663-6670.

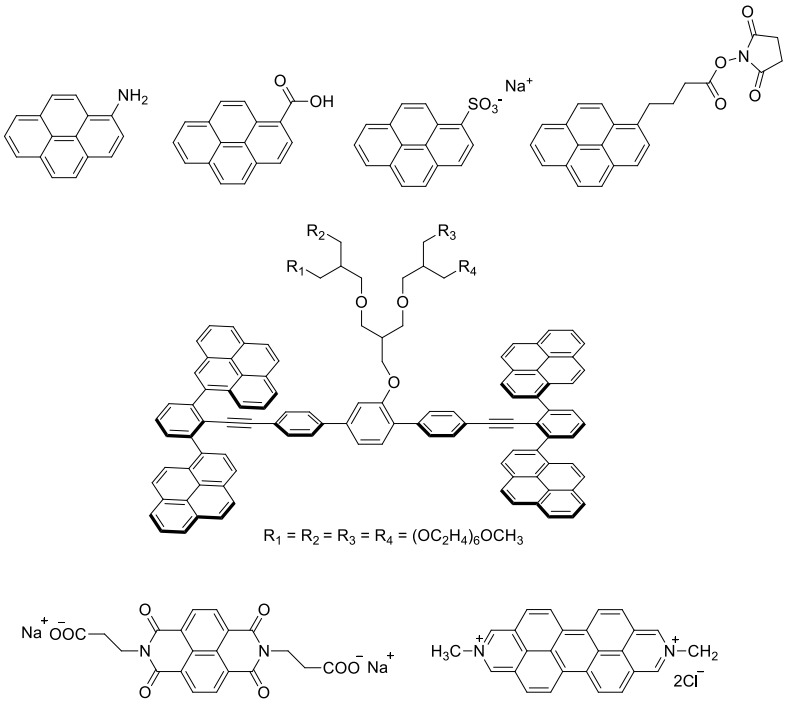

Figure 14. Some PAHs used in the stabilization of graphene dispersions.

2.3. NON-COVALENT FUNCTIONALIZATION OF GRAPHENE

As mentioned above, graphene presents a great tendency to aggregate as a consequence of the strong π-π interactions between layers. Moreover, graphene sheets are hydrophobic, which makes difficult its solubilization in polar solvents. In fact, the obtained dispersions present low concentrations and are instable resulting in the re-aggregation and sedimentation of the material.[41]

It has been demonstrated that the exfoliation of graphene in the presence of molecules that act as dispersion stabilizing agents permits the exfoliation of graphene in common solvents and avoids the re-aggregation of the layers, meaning that chemical functionalization is essential to make graphene tractable for different applications. These molecules are, however, difficult to remove due to the strong interactions between them and graphene. In addition, when these molecules present photo- and/or electroactive moieties, besides modulating the zero bandgap of the material, they might induce new properties, that could allow its application in photovoltaic and optoelectronic devices.

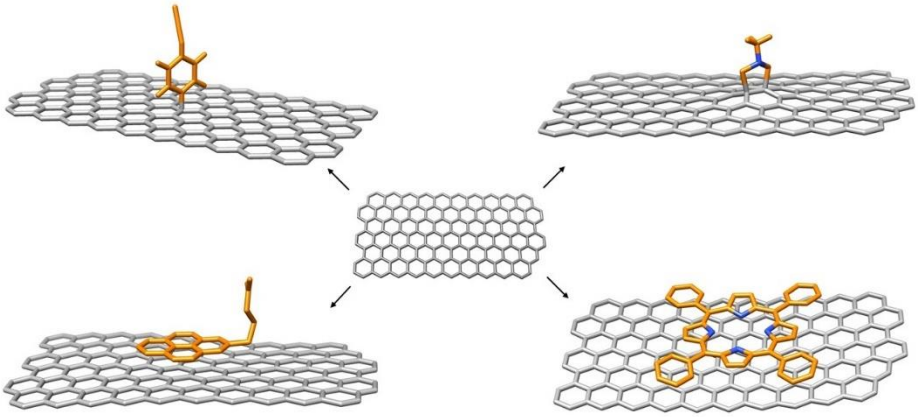

Figure 15. Schematic representation of the covalent (up) and non-covalent (down) functionalization of graphene.

In this sense, any disruption of the π structure of the basal plane of graphene implies the modification of the properties that make it an outstanding material. That includes the covalent functionalization, because the creation of new bonds changes the hybridization of carbon atoms from sp^2 to sp^3. Non-covalent functionalization is a physical process that takes advantage of the adsorption of the molecules onto the graphene surface and allows the preservation of its π-skeleton and the properties related to it (Figure 15).

In the next paragraphs we will comment some selected examples related with the non-covalent functionalization of graphene with electroactive molecules considering two general avenues, i) non-covalent functionalization in solution and ii) non-covalent functionalization on solid surfaces.

2.3.1. Non-covalent functionalization in solution

π-π Interactions are the dominating non-covalent forces in π-systems. For that reason, it is not strange that a vast majority of the examples related with the non-covalent functionalization of graphene employ planar aromatic molecules and their derivatives. In the next pages, only some examples will be discussed due to the several recent reviews published on this topic.[73,74,75]

Pyrene derivatives are known to feature strong affinities towards the graphene basal plane via π-π stacking. As such, graphene electron donor-acceptor hybrids have been created using this anchoring motif. Kar and co-workers reported the non-covalent functionalization of graphene with 1-pyrenecarboxylic acid in aqueous media.[76] They found that the pyrene derivative allows the exfoliation of graphite and characterized the obtained material by AFM, Raman and UV-Vis spectroscopy. The modified graphene layers can be transferred to a polymer film, which permits the use of this new material in different applications such as a UV filter or an air pressure sensor.[77]

Guldi and co-workers described an example in which trimethyl-(2-oxo-2-pyren-1-yl-ethyl)ammonium bromide acts as dispersion stabilizing agent of graphene in water and as anchoring group for the next functionalization.[78,79] Graphene was successfully exfoliated in the presence of the pyrene derivative, as determined by AFM and Raman analysis. Afterwards, the exfoliated material was used to construct donor-acceptor nanohybrids by electrostatic interactions

73. V. Georgakilas, M. Otyepka, A. B. Bourlinos, V. Chandra, N. Kim, K. C. Kemp, P. Hobza, R. Zboril, K. S. Kim, *Chem. Rev.* **2012**, *112*, 6156-6214.
74. L. Rodriguez-Perez, M. A. Herranz, N. Martín, *Chem. Commun.* **2013**, *49*, 3721-3735.
75. a) A. Ciesielski, P. Samorì, *Adv. Mater.* **2016**, *28*, 6030-6051. b) A. Ciesielski, P. Samori, *Chem. Soc. Rev.* **2014**, *43*, 381-398.
76. X. An, T. Simmons, R. Shah, C. Wolfe, K. M. Lewis, M. Washington, S. K. Nayak, S. Talapatra, S. Kar, *Nano Lett.* **2010**, *10*, 4295-4301.
77. X. An, T. W. Butler, M. Washington, S. K. Nayak, S. Kar, *ACS Nano* **2011**, *5*, 1003-1011.
78. J. Malig, C. Romero-Nieto, N. Jux, D. M. Guldi, *Adv. Mater.* **2012**, *24*, 800-805.
79. G. Katsukis, J. Malig, C. Schulz-Drost, S. Leubner, N. Jux, D. M. Guldi, *ACS Nano* **2012**, *6*, 1915-1924.

with porphyrins and CdTe quantum dots (QD) (Figure 16). In both cases, it was found that photoexcitation promotes the formation of charge transfer states.

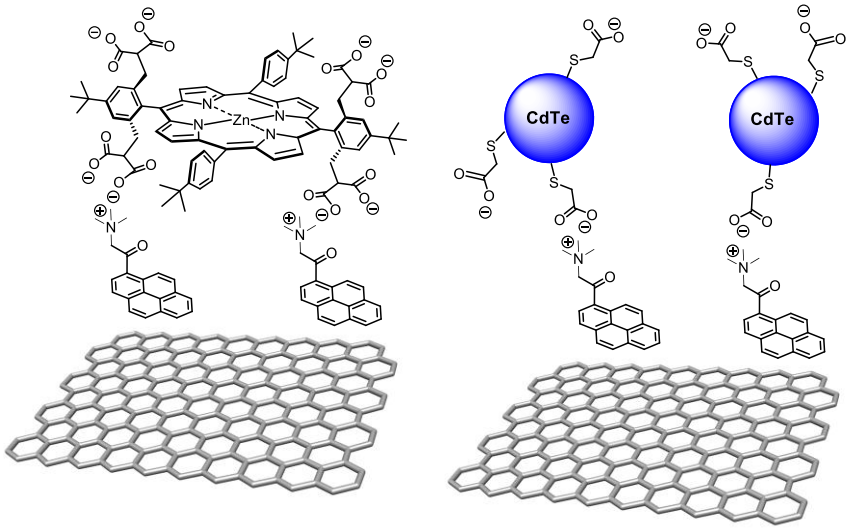

Figure 16. Examples of non-covalently functionalized pyrene^{+}/porphyrin^{-}/graphene (left) and pyrene^{+}/QD^{-}/graphene (right) nanohybrids.

Pyrene covalent dyads, where this anchoring motif was attached to different electroactive units (porphyrins, cyanine derivatives…), have also been reported. For example, a phthalocyanine-pyrene conjugated was able to exfoliate graphite in DMF forming a complex with the graphene layers.[80] The interaction between graphene and the phthalocyanine was monitored by UV-Vis and fluorescence spectroscopy. In addition, transient absorption studies revealed a photoinduced electron transfer from graphene to phthalocyanine (Figure 17).

80. A. Roth, M.-E. Ragoussi, L. Wibmer, G. Katsukis, G. d. l. Torre, T. Torres, D. M. Guldi, *Chem. Sci.* **2014**, *5*, 3432-3438.

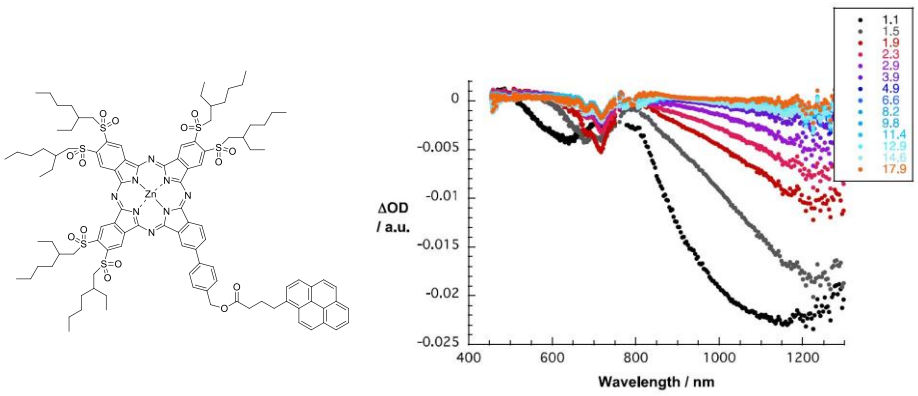

Figure 17. Phthalocyanine-pyrene dyad used in the non-covalent functionalization of graphene (left). Differential absorption spectra of phthalocyanine-pyrene/graphene nanohybrids (right). Time delays between 1.1 and 17.9 ps at room temperature.

Recently, Wood and co-workers reported a photo-switchable Zn^{2+} sensitive material prepared by non-covalent functionalization of graphene with a pyrene-spiropyran derivative.[81] Spiropyran is a photochromic molecule that switches to merocyanine, its structural isomer, by UV light exposition (Figure 18). This structural isomer interacts with the metal, forming a chelate complex characterized by its absorption spectrum. The change in the spectrum is only observed in presence of the metal.

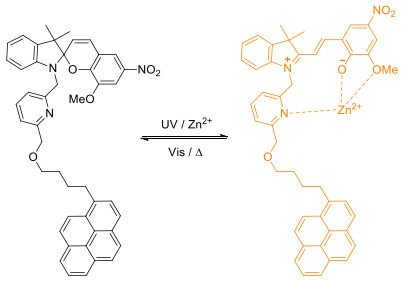

Figure 18. Spiropyran-merocyanine equilibrium.

In spite of the numerous examples that employ pyrene for the non-covalent functionalization of graphene, the strength of this interaction has not been determined in a quantitative analyses. Dichtel and co-workers were able to determine the thermodynamic binding parameters and the kinetic stability of

81. A. Perry, S. J. Green, D. W. Horsell, S. M. Hornett, M. E. Wood, *Tetrahedron* **2015**, *71*, 6776-6783.

graphene/pyrene films.[82] They used for the first time electrochemistry to characterize the self-assembly on the graphene surface. By cyclic voltammetry, it was compared the behavior of a tripodal pyrene derivative and a monovalent pyrene derivative (Figure 19) and was found that ΔG_{ads} was similar for both structures (≈ -38 kJ/mol). The authors suggest that the disruption of the interactions among the pyrene rings in the tripodal molecule has an energetic cost reflected in the binding energy. However, the kinetic stability differs in each case. A desorption rate constant value of $k = 1.4 \cdot 10^{-3}$ s^{-1} was obtained for the monovalent derivative and a $k = 3.5 \cdot 10^{-6}$ s^{-1} for the tripodal structure, which implies that the tripodal motif forms monolayers more stable under similar conditions. Soon after, this study was complemented considering the size influence of the anchoring groups. The number of rings in the PAHs, namely pyrene, phenanthrene and naphthalene, did not modify the binding energy of the tripodal motif, but the desorption rate increased with the decrease in rings number.[83]

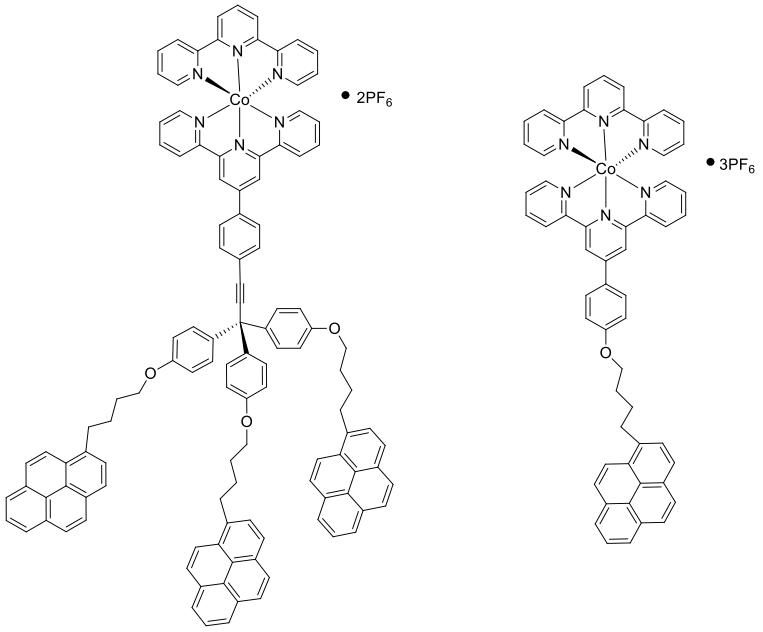

Figure 19. Tripodal and monovalent pyrene derivatives developed by Dichtel and co-workers.

82. J. A. Mann, J. Rodríguez-López, H. D. Abruña, W. R. Dichtel, *J. Am. Chem. Soc.* **2011**, *133*, 17614-17617.
83. J. A. Mann, W. R. Dichtel, *ACS Nano* **2013**, *7*, 7193-7199.

D'Souza and co-workers described the non-covalent modification of graphene with a multimodular donor-acceptor conjugated system bearing a very similar tripodal motif for the anchoring to graphene (Figure 20).[84] A subphthalocyanine acts as the electron-donor moiety, C_{60} is the electron-acceptor unit and the three pyrene units complete the system. The measured redox potentials revealed the influence of graphene on the pyrene and subphthalocyanine units, leaving C_{60} unperturbed because of its distant position from the graphene surface. Furthermore, femtosecond transient absorption spectroscopy demonstrates charge separation and recombination processes, which are faster in the graphene complex than in the organic molecule. These experimental findings reveal that graphene accelerates the charge-transfer processes.

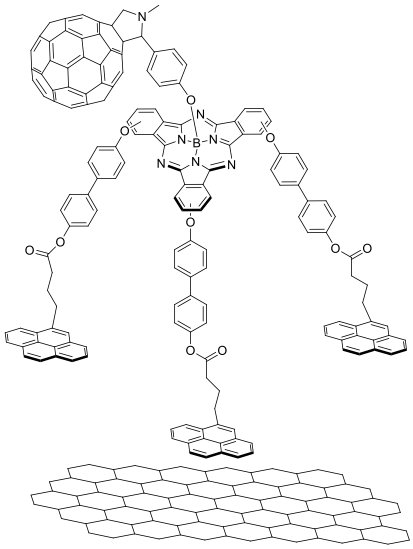

Figure 20. Multimodular donor-acceptor/graphene nanohybrid.

Other PAHs that can interact with the basal plane of graphene are perylene bisimides (PBIs). Hirsch and co-workers described for the first time the electronic communication between graphene and a PBI, which besides being well-suited for π-π stacking interactions are powerful dye-type chromophores.[85] PBI-based bolaamphiphiles (Figure 21) exhibit a remarkable stability in their interaction with graphene. Raman studies showed signals corresponding to the PBI in combination with the signals characteristics of graphene when the sample was irradiated at 532 nm, but no emission background was present in

84. C. B. Kc, G. N. Lim, F. D'Souza, *Angew. Chem. Int. Ed.* **2015**, *54*, 5088-5092.
85. N. V. Kozhemyakina, J. M. Englert, G. Yang, E. Spiecker, C. D. Schmidt, F. Hauke, A. Hirsch, *Adv. Mater.* **2010**, *22*, 5483-5487.

the spectrum. This absence of emission indicates a quenching of the fluorescence of the PBI due to the electronic communication with graphene.

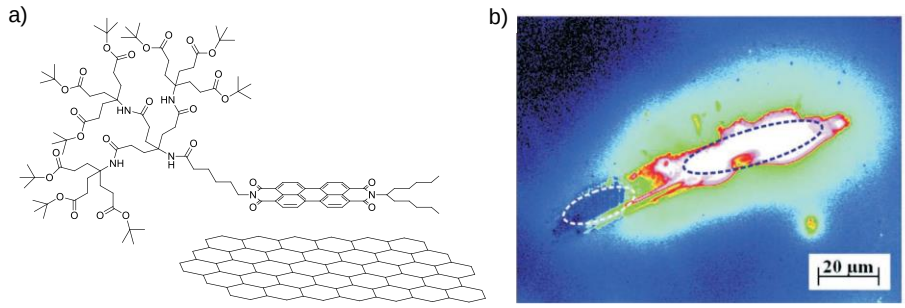

Figure 21. a) Bolaamphiphile dendronized perylene bisimide/graphene complex. b) Micrograph of perylene bisimide/graphene dispersion, fluorescence is observed for unbound perylene (blue oval) and is quenched for the complex (white oval).

The interaction of graphene with electron-donor or acceptor molecules causes a remarkable shift of the G-band in the Raman spectra of graphene due to the changes in its electronic structure.[86] Rao and co-workers reported the non-covalent functionalization of graphene with the tetrapotassium salt of coronene tetracarboxylic acid, an electron deficient molecule.[87] The functionalized material was characterized by several spectroscopic techniques. In the UV-Vis spectrum it can be observed a significant redshift of the coronene bands, whereas in fluorescence studies the quenching of the emission was accompanied by a new emission band at 600 nm attributed to the complex. However, the evident proof for charge-transfer interaction was the shift of the G-band of graphene to higher frequencies due to the interaction with the electron-acceptor molecules (Figure 22).

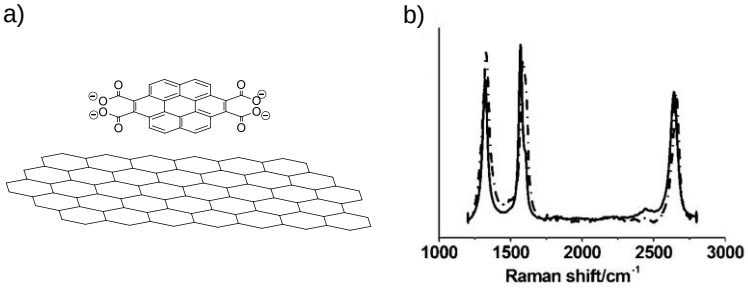

Figure 22. a) Coronene/graphene complex. b) Raman spectra of graphene (solid line) and non-covalent complex (dashed line).

86. R. Voggu, B. Das, C. S. Rout, C. N. R. Rao, *J. Phys. Condens. Matter.* **2008**, *20*, 472204.
87. A. Ghosh, K. V. Rao, S. J. George, C. N. R. Rao, *Chem. Eur. J.* **2010**, *16*, 2700-2704.

Other groups have employed the direct interaction with electron-donor molecules (phthalocyanines or porphyrins) in the non-covalent functionalization of graphene.[80,88,89] Jung and co-workers detailed the modification of graphene with a symmetric porphyrin functionalized with alkyl groups.[90] The interaction with graphene was described by UV-Vis and Raman spectroscopy. The porphyrin showed the redshift of its Q bands and the decrease of the Soret band, in the graphene was observed the shift to lower frequencies of the G-band due to the interaction with electron-donor molecules.

All the aforementioned examples have in common that in all of them the interactions with the graphene basal plane are through the π-π stacking of planar systems. In a different approach, Martín and co-workers reported the supramolecular functionalization of graphene with the curved molecule 9,10-di(1,3-dithiole-2-ylidene)-9,10-dihydroanthracene (π-ex-TTF).[91] In particular, gold nanoparticles decorated with multiple units of π-exTTF (Figure 23) proved that a multivalent approach can be used to produce graphene supramolecular composites even with non-planar binding motifs. Several approaches between π-exTTF and graphene were found to be energetically favorable through DFT calculations. The energetic stabilization arises from a combination of CH-π and π-π interactions. Scrutiny under TEM of a mixture of previously exfoliated graphene and the π-exTTF gold nanoparticles showed that the basal planes of graphene were heavily functionalized with nanoparticles. A closer examination of the micrographs suggested that the nanoparticles maximize their non-covalent interactions by localizing preferentially between layers of graphene.

88. J. Malig, A. W. I. Stephenson, P. Wagner, G. G. Wallace, D. L. Officer, D. M. Guldi, *Chem. Commun.* **2012**, *48*, 8745-8747.
89. C. B. K. C, S. K. Das, K. Ohkubo, S. Fukuzumi, F. D'Souza, *Chem. Commun.* **2012**, *48*, 11859-11861.
90. J. Geng, B.-S. Kong, S. B. Yang, H.-T. Jung, *Chem. Commun.* **2010**, *46*, 5091-5093.
91. F. G. Brunetti, H. Isla, J. Aragó, E. Ortí, E. M. Pérez, N. Martín, *Chem. Eur. J.* **2013**, *19*, 9843-9848.

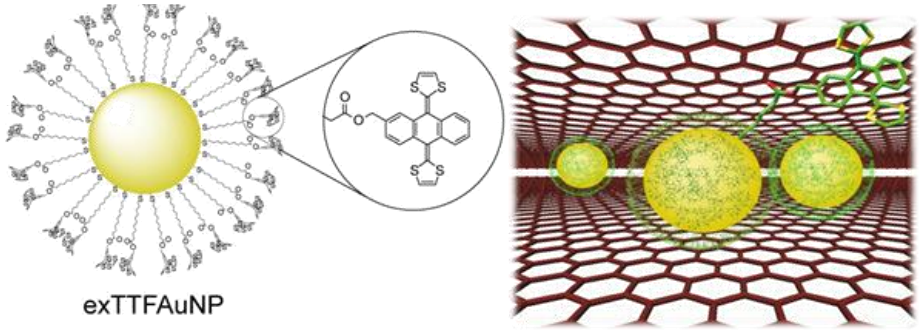

Figure 23. Cartoon depicting the non-covalent interaction of graphene with gold nanoparticles, scaffolds endowed with multiple π-exTTF units.

Other kind of multivalent approach is the non-covalent modification of graphene with polymers. For example, Guldi and co-workers described the use of a zinc phthalocyanine (ZnPc) based poly(*p*-phenylene vinylene) (PPV) oligomer to exfoliate and functionalize graphene in one-pot.[92] The oligomeric backbone acts as scaffold for several units of ZnPc and increases the overall π-π interactions (Figure 24). The obtained material was tested as active layer and transparent electrode material for solar-cell applications due to the photoinduced electron transfer that takes place from the electron-donor ZnPc to the electron-acceptor graphene. When investigating the influence of the length of the oligomeric backbone, it was found that longer backbones increase the exfoliation yield and the charge transfer efficiency.[93]

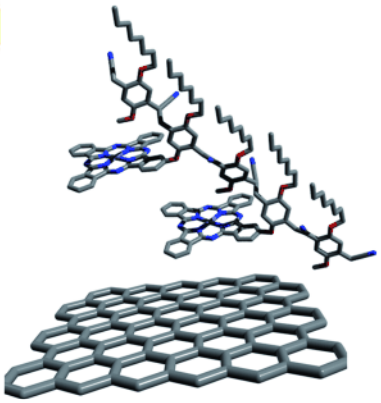

Figure 24. ZnPc-PPV oligomer/graphene nanohybrid.

92. J. Malig, N. Jux, D. Kiessling, J.-J. Cid, P. Vázquez, T. Torres, D. M. Guldi, *Angew. Chem. Int. Ed.* **2011**, *50*, 3561-3565.
93. L. Brinkhaus, G. Katsukis, J. Malig, R. D. Costa, M. Garcia-Iglesias, P. Vázquez, T. Torres, D. M. Guldi, *Small* **2013**, *9*, 2348-2357.

Salavagione and co-workers[94] similarly developed the non-covalent functionalization of graphene with poly(fluorene-*alt*-phenylene) endowed with anthracene units. Recently, Schuhmann and co-workers were able to exfoliate and functionalize graphene with a redox polymer modified with an osmium complex.[95] The new hybrid material can be used as redox mediator in enzymatic reactions since it increases the current density even with small graphene loadings, being able to have application in enzymatic biofuel cells.

In a remarkable example about the features that can be implemented in graphene upon non-covalent functionalization, Green and co-workers developed a graphene magnetic hybrid by using polyvinylpyrrolidone-grafted Fe_3O_4 nanoparticles.[96] This material possesses superparamagnetic properties and could be used for biomedical applications and environmental remediation.

2.3.2. Non-covalent functionalization on surfaces

Other kind of non-covalent functionalization is the surface supported graphene functionalization. This approach allows the formation of 2D supramolecular structures onto graphene surfaces and pursues two objectives: the study of the interactions that generate the molecular self-assembly and the modulation of graphene properties for technological applications.

It is important to take into account that the surface which supports graphene interacts with it.[97] This interaction can be strong or weak depending on the substrate, SiC(0001), Ir (111) and Pt (111) have weak interactions, whereas Ru(0001) and Ni (111) strongly interact with graphene. One of the consequences of this interaction is the influence on the molecular self-assembly, since the surface can act as a template,[98] where molecule-substrate and molecule-molecule interactions determine the final organization.[99]

94. M. Castelain, H. J. Salavagione, R. Gomez, J. L. Segura, *Chem. Commun.* **2011**, *47*, 7677-7679.
95. Z. Sun, J. Vivekananthan, D. A. Guschin, X. Huang, V. Kuznetsov, P. Ebbinghaus, A. Sarfraz, M. Muhler, W. Schuhmann, *Chem. Eur. J.* **2014**, *20*, 5752-5761.
96. R. J. Fullerton, D. P. Cole, K. D. Behler, S. Das, F. Irin, D. Parviz, M. N. F. Hoque, Z. Fan, M. J. Green, *Carbon* **2014**, *72*, 192-199.
97. R. Otero, J. M. Gallego, A. L. Vázquez de Parga, N. Martín, R. Miranda, *Adv. Mater.* **2011**, *23*, 5148-5176.
98. K. S. Mali, J. Greenwood, J. Adisoejoso, R. Phillipson, S. De Feyter, *Nanoscale* **2015**, *7*, 1566-1585.
99. T.-C. Tseng, C. Urban, Y. Wang, R. Otero, S. L. Tait, M. Alcamí, D. Écija, M. Trelka, J. M. Gallego, N. Lin, M. Konuma, U. Starke, A. Nefedov, A. Langner,

Although several studies considering the deposition of molecules onto graphene grown on metallic surfaces have been reported, we will discuss just a few examples to illustrate the interaction between electroactive molecules and the epitaxially grown graphene on different metal surfaces.

Phthalocyanines (PCs) are the clear case in which the self-assembly can be influenced by the balance of substrate-graphene, molecule-molecule and graphene-molecule interactions. Gao and co-workers studied the self-assembly of several phthalocyanines on graphene in two different substrates, Ru(0001) and Pt(111).[100] They found that depending on the metal ion (Fe^{2+}, Mn^{2+}, Ni^{2+} or H_2) the molecules presented different behavior onto the graphene surface. FePc showed a preferential adsorption (Figure 25), NiPc had not anyone and MnPc presented an intermediate behavior. These observations evidenced the different molecule-substrate interactions. The behavior of FePc was further investigated in Pt(111). In this case, close-packed islands without a preferential adsorption are observed. This indicates a weaker interaction with the substrate and no influence in the self-assembly.

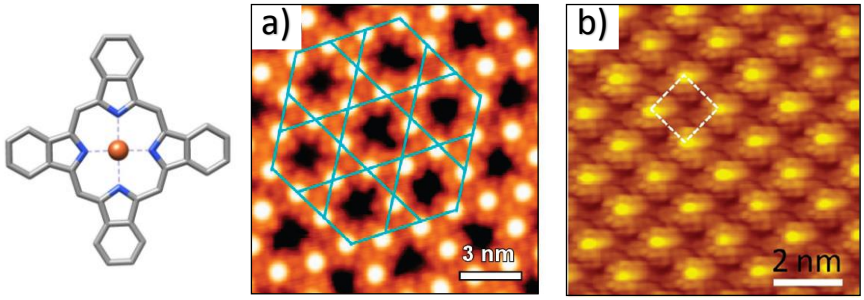

Figure 25. FePc structure. a) Kagome lattice on graphene/Ru(0001).[101] b) Square lattice on graphene/Pt(111).

Other example that shows the influence of the different interactions to consider in molecular assembly on surfaces, was reported by Miranda and co-workers.[102] The different self-assembly of 7,7',8,8'-tetracyano-*p*-quinodimethane (TCNQ) and 2,3,5,6-tetrafluoro-7,7',8,8'-tetracyano-*p*-quinodimethane (F_4-TCNQ) on

C. Wöll, M. Á. Herranz, F. Martín, N. Martín, K. Kern, R. Miranda, *Nat. Chem.* **2010**, *2*, 374-379.

100. K. Yang, W. D. Xiao, Y. H. Jiang, H. G. Zhang, L. W. Liu, J. H. Mao, H. T. Zhou, S. X. Du, H. J. Gao, *J. Phys. Chem. C* **2012**, *116*, 14052-14056.
101. J. Mao, H. Zhang, Y. Jiang, Y. Pan, M. Gao, W. Xiao, H. J. Gao, *J. Am. Chem. Soc.* **2009**, *131*, 14136-14137.
102. S. Barja, M. Garnica, J. J. Hinarejos, A. L. Vazquez de Parga, N. Martín, R. Miranda, *Chem. Commun.* **2010**, *46*, 8198-8200.

graphene grown on Ir(111) was investigated. TCNQ molecules formed a well-ordered, compact monolayer in which the intermolecular interactions directed the self-assembly. However, in the case of F_4-TCNQ molecules, the intermolecular interactions were repulsive and the self-assembly was conducted by the substrate, forming a regular hexagonal array.

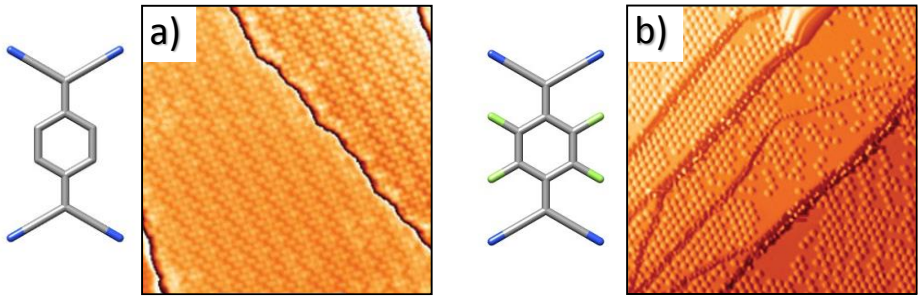

Figure 26. a) TCNQ self-assembly and b) F_4-TCNQ self-assembly on graphene/Ir(111).

In contrast to the aforementioned study involving Ir(111), deposition on an epitaxial buffer layer of graphene grown on Ru(0001) affords TCNQ molecules exhibiting a magnetic moment which induces the formation of ferromagnetic order in the 2D molecular arrangement.[103] This magnetic moment stems from the charge transferred from the graphene/Ru(0001) to the electron accepting TCNQ molecule.

On the other hand, in some cases the formed structure is independent of the substrate, for example the self-assembly of C_{60} molecules is quite similar on graphene grown in Ru(0001)[104] or in SiC(0001).[105]

Recently, more complex self-assemblies have been constructed. 2,4'-bis(terpyridine) (2,4'-BTP, Figure 27) forms 2D supramolecular arrays due to the formation of C-H···N H-bonding (Figure 27a). Interestingly, all the molecules were located in the lower part of the corrugated surface (valleys) remaining the upper parts (hills) mostly free (Figure 27b). Again, the strong influence of the underlying metal surface is responsible for the observed

103. M. Garnica, D. Stradi, S. Barja, F. Calleja, C. Diaz, M. Alcami, N. Martín, A. L. Vazquez de Parga, F. Martin, R. Miranda, *Nat. Phys.* **2013**, *9*, 368-374.
104. J. Lu, P. S. E. Yeo, Y. Zheng, Z. Yang, Q. Bao, C. K. Gan, K. P. Loh, *ACS Nano* **2012**, *6*, 944-950.
105. J. Cho, J. Smerdon, L. Gao, Ö. Süzer, J. R. Guest, N. P. Guisinger, *Nano Lett.* **2012**, *12*, 3018-3024.

findings since when using Ag as a base substrate, densely packed 2D structures were formed.[106]

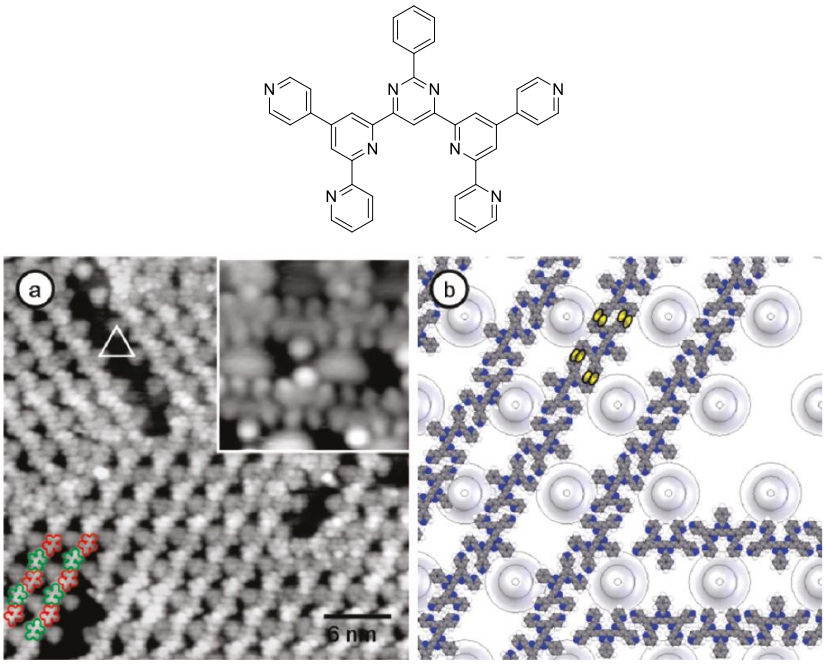

Figure 27. 2,4'-BTP chemical structure and, a) STM image of 2,4'-BTP molecules on graphene/Ru(0001). b) True to scale model of 2,4'-BTP molecules on graphene with hydrogen bonding configuration (double hydrogen bonds, yellow ellipses).

Oligothiophenes, namely QT and QTDA (Figure 28) have been deposited on CVD-grown graphene on copper foil by using scanning tunneling microscopy (STM) under ambient conditions. Remarkably, QT molecules form large domains, in the range of hundreds of nanometers, showing lamellae features mostly covering the underlying mono- and multi-atomic steps. Similarly, QTDA molecules form smaller domains in a preferentially lamellar array. However, in contrast to the QT, these domains span over the step edges as well as terraces of the underlying copper surface (Figure 28). It is interesting to note that although Cu(111) and Cu(100) facets dominate the surface of polycrystalline copper after annealing, the authors reported to get identical supramolecular assemblies regardless of the facets nature.[107]

106. M. Roos, D. Künzel, B. Uhl, H.-H. Huang, O. Brandao Alves, H. E. Hoster, A. Gross, R. J. Behm, *J. Am. Chem. Soc.* **2011**, *133*, 9208-9211.
107. X. Sun, J. Zhang, X. Wang, C. Zhang, P. Hu, Y. Mu, X. Wan, Z. Guo, S. Lei, *Chem. Commun.* **2013**, *49*, 10317-10319.

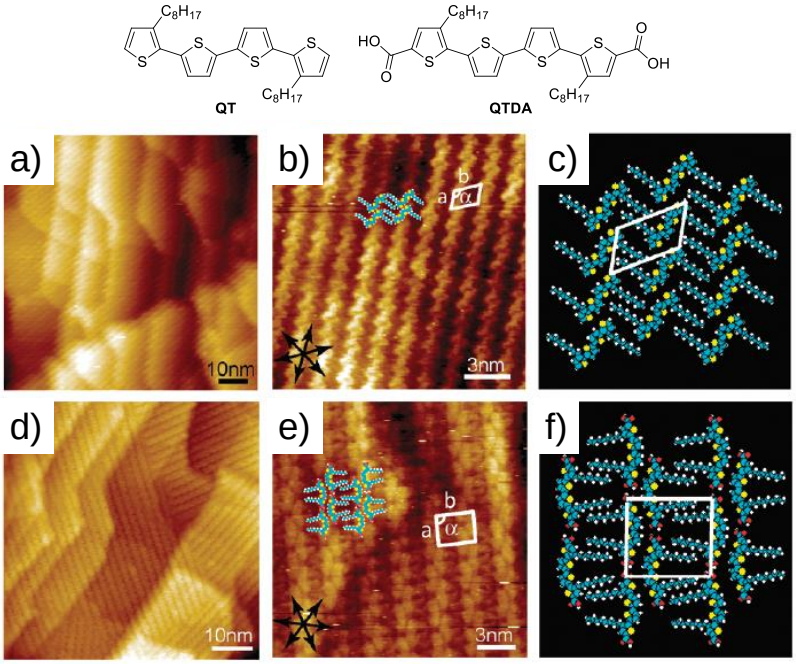

Figure 28. Oligothiophenes (QT and QTDA) chemical structures, and large scale and high resolution STM images of the a), b) QT and d), e) QTDA molecules on graphene/copper. c) and f) are the tentative models of the QT and QTDA assembly structures, respectively. The black stars in the lower left corner of the STM images indicate the orientation of the graphene lattices. The orientation of the step edges in a) and d) indicates that graphene is grown on the Cu(111) facet.

Molecular self-assemblies allow to modulate the reactivity and the properties of graphene for future applications. Wee and co-workers demonstrated the p-type doping of graphene on SiC(0001) with the electron-acceptor F_4-TCNQ.[108] Synchrotron-based high-resolution photoemission spectroscopy was used to study the charge transfer between graphene and the molecular overlayer. The work function increased with the deposition of F_4-TCNQ, behavior observed when the electrons transfer from the substrate (graphene) to the adsorbate (F_4-TCNQ) (Figure 29). Other example of doping was reported by Ma and co-workers. In this case they employed a CuPc derivative for the functionalization of graphene, and were able to modulate the electronic interaction by varying

108. W. Chen, S. Chen, D. C. Qi, X. Y. Gao, A. T. S. Wee, *J. Am. Chem. Soc.* **2007**, *129*, 10418-10422.

the applied voltage on graphene, which allows to control the molecule-graphene charge transfer.[109]

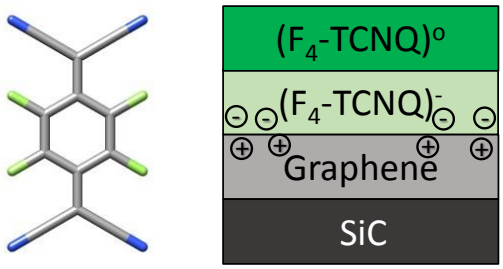

Figure 29. F_4-TCNQ molecular model and device configuration to measure the charge transfer from graphene to F_4-TCNQ.

De Feyter and co-workers reported the functionalization of graphene with a self-assembled monolayer of oleylamine.[110] After the functionalization, they monitored the electronic properties of the new hybrid by fabricating a field effect transistor based on graphene. They observed that after the functionalization, the voltage of its neutrality point (V_{NP}) was shifted to negative values respect to the pristine graphene, which implies n-type doping.

In addition to doping graphene, the non-covalent functionalization of supported graphene allows its band gap opening. Li and co-workers demonstrated to open the band gap of bilayer graphene in field effect transistors.[111] In the device configuration the graphene layer was in contact with a SiO_2 substrate and the organic layer was functionalized with triazine. The bottom layer is positively charged due to the p-doping of graphene in contact with SiO_2 and the top layer is negatively charged due to the n-doping nature of triazine. The Raman G band for the bilayer graphene has to be fitted with two Lorentzian peaks after triazine decoration, which likely confirms that the top and bottom graphene layers are different (Figure 30). These differences between layers allow to break the symmetry and open the band gap up to an estimated value of ≈ 111 meV at room temperature.

109. Y.-L. Wang, J. Ren, C.-L. Song, Y.-P. Jiang, L.-L. Wang, K. He, X. Chen, J.-F. Jia, S. Meng, E. Kaxiras, Q.-K. Xue, X.-C. Ma, *Phys. Rev. B* **2010**, *82*, 245420.
110. B. Li, A. V. Klekachev, M. Cantoro, C. Huyghebaert, A. Stesmans, I. Asselberghs, S. De Gendt, S. De Feyter, *Nanoscale* **2013**, *5*, 9640-9644.
111. W. Zhang, C.-T. Lin, K.-K. Liu, T. Tite, C.-Y. Su, C.-H. Chang, Y.-H. Lee, C.-W. Chu, K.-H. Wei, J.-L. Kuo, L.-J. Li, *ACS Nano* **2011**, *5*, 7517-7524.

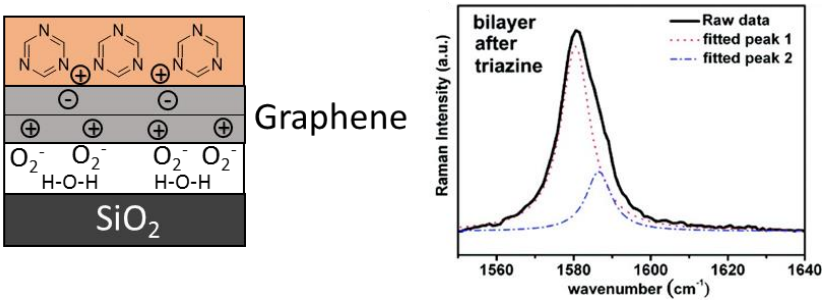

Figure 30. Schematic illustration for the charge distribution on the device (left). Raman G-band of graphene after triazine functionalization (right).

Finally, the supramolecular functionalization of graphene by means of molecular self-assembly lets graphene suitable for a second functionalization, without modifying its properties, because the new reaction takes place onto the molecular layer. Hersam and co-workers reported the atomic layer deposition of metal oxides onto functionalized graphene.[112] Firstly, they formed an ordered self-assembled monolayer of perylene-3,4,9,10-tetracarboxylic dianhydride (PTCDA) on graphene/SiC(0001), then the oxygenated groups can react with the metallic precursors to obtain the atomic layer of Al_2O_3 and HfO_2 (Figure 31). This method can be used for depositing and combining high-κ dielectrics with graphene for electronic applications.

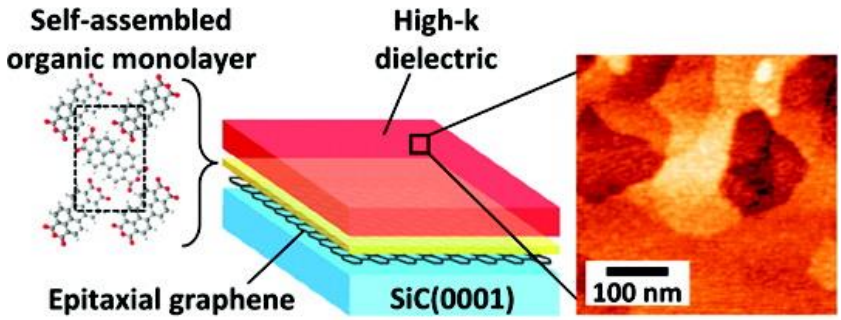

Figure 31. Structure of high-κ dielectric on epitaxial graphene with organic self-assembled monolayers.

112. J. M. P. Alaboson, Q. H. Wang, J. D. Emery, A. L. Lipson, M. J. Bedzyk, J. W. Elam, M. J. Pellin, M. C. Hersam, *ACS Nano*, **2011**, *5*, 5223-5232.

3. OBJECTIVES

3. OBJECTIVES

The ultimate goal of this thesis is the preparation of graphene-based supramolecular assemblies that could eventually have an impact on the photovoltaic and optoelectronic properties of this nanomaterial.

The exceptional features of graphene depend on the quality of the obtained layers, with a low concentration of defects to preserve its intact properties. In this sense, we have developed a general method to anchor active functionalities onto graphene's pristine basal plane. Our approach is based on the strong π-π stacking interactions of pyrene units with the graphene surface and/or the multivalent binding of tripodal receptors with three pyrene "feet". Furthermore, our supramolecular receptors for graphene have been decorated with three different electroactive units (π-extended tetrathiafulvalene (π-exTTF), porphyrins or C_{60}) with the aim to modulate graphene's electronic properties and to establish structure-property relationships in the obtained hybrids (Figure 32).

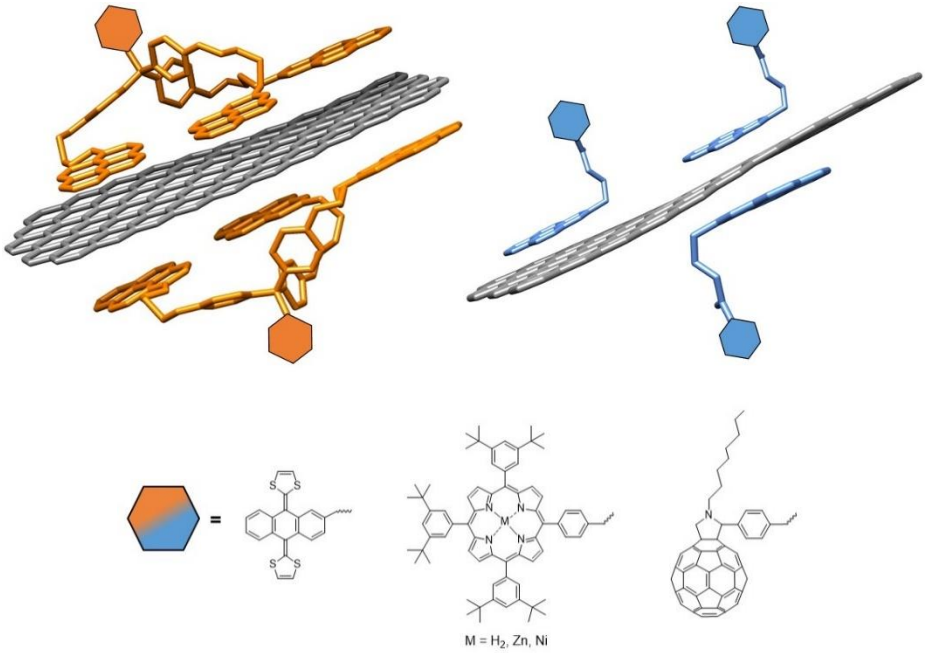

Figure 32. General description of the pyrene monopodal and tripodal electroactive molecules used for the recognition of graphene.

Within this general context, the specific objectives that we have pursued in this thesis are the following:

- Development of a practical procedure for the exfoliation of graphite sheets by ultrasound-induced liquid-phase exfoliation.
- Design and synthesis of monopodal and tripodal molecular receptors for graphene endowed with π-exTTF, porphyrin and C_{60} electroactive units.
- Study of the solution interactions of the different systems with graphene by UV-Vis and fluorescence titrations.
- Study of the electronic communication between graphene and the molecular systems by preliminary steady-state and time resolved spectroscopy experiments.
- Formation of the supramolecular hybrids with graphene and investigation of properties by a thorough set of analytical, spectroscopic, electrochemical and microscopic techniques (TGA, FTIR, Raman, UV-Vis, fluorescence, cyclic voltammetry, TEM and XPS).
- Electrochemical investigation of the thermodynamic and kinetic binding parameters of model monopodal and tripodal systems adsorbed on modified graphene electrodes.
- Theoretical investigations on the non-covalent binding of the molecular receptors to graphene, to evaluate the different contributions to the supramolecular interaction.

The next section is divided in five consecutive parts. In the first part, the general methodology to obtain the pristine graphene material is presented. Following, in three separate sections, each family of electroactive molecules is presented and their interaction with graphene discussed. To conclude the results and discussion, a final section details the comprehensive theoretical analysis carried out on the non-covalent functionalization of graphene with the monopodal and tripodal families of receptors.

4. RESULTS AND DISCUSSION

4. RESULTS AND DISCUSSION

4.1. ULTRASOUND-INDUCED LIQUID-PHASE EXFOLIATION OF GRAPHENE

The graphene used as starting material has been exfoliated by the method developed by Coleman and co-workers,[38] which implies the dispersion of graphite in a solvent with a surface energy nearest to that of graphite. This solvent, besides, has to be able to stabilize the graphene flakes in the obtained dispersion. The graphene dispersion is isolated after a sonication and centrifugation sequence.

In order to produce an optimum starting graphene and with a suitable concentration, the exfoliation has been carried out in different solvents and considering several sonication times.

In a first instance, we investigated the suitability of various solvents in the exfoliation of graphene. For this reason, NMP, *o*-DCB and DMF were tested. The sonication time (150 minutes) and the conditions of centrifugation (45 minutes, 500 r.p.m) were the same in the three cases, after this sequence the supernatant was isolated. In Figure 33 it is shown the aspect of the three dispersions obtained after the centrifugation process.

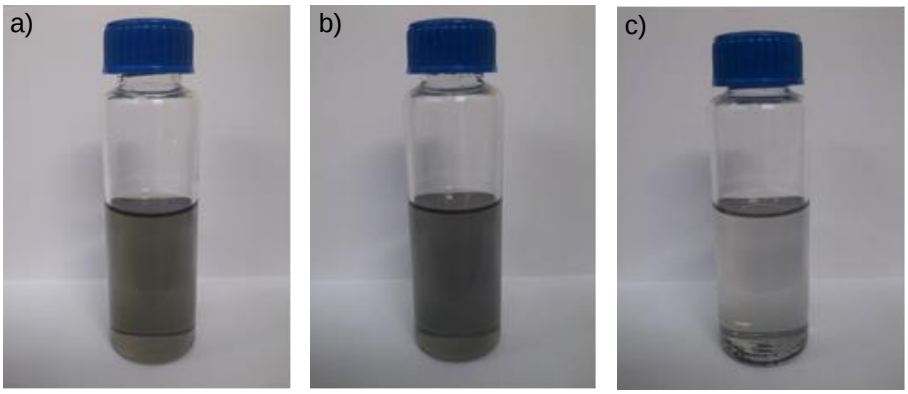

Figure 33. Dispersions of graphite in a) NMP, b) *o*-DCB and c) DMF.

As it can be noticed in the images, the dispersions obtained in NMP and *o*-DCB are homogeneous without sedimentation in the bottom of the vials. However, when using DMF as solvent, it can be perceived the sedimentation of graphite and a clearest aspect of the dispersion. These observations evidence a poor capability of DMF to stabilize graphene layers and, for that reason, this solvent was not used in further experiments.

To determine if graphene is exfoliated in both NMP and *o*-DCB dispersions, TEM studies were performed. TEM images showed few layer graphene (FLG) nanosheets of several layers stacked with smaller flakes on their surface (Figure 34). Lateral dimensions of the nanosheets range from 100 to 500 nm. However, when using NMP, the dispersions are formed by more homogenous aggregates and these aggregates present a lower number of layers, as it can be observed in the images taken at 10 nm. In the sample obtained in NMP, aggregates of about five layers can be visualized, meanwhile in the sample in *o*-DCB, larger aggregates, of about twenty graphene layers are obtained. With this analysis, it can be concluded that the dispersions obtained in *o*-DCB present a lower degree of exfoliation.

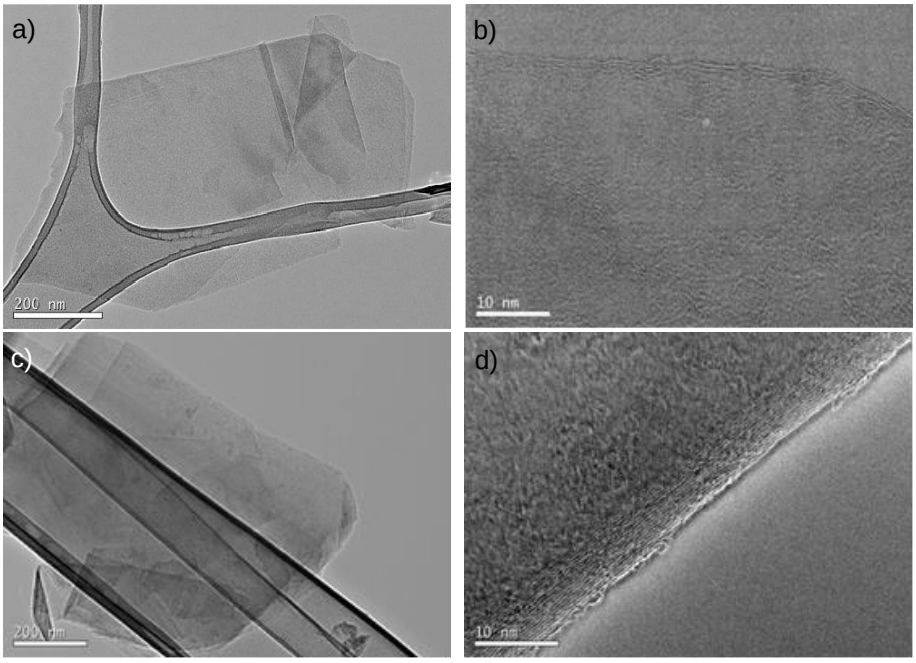

Figure 34. Graphene exfoliated in NMP a) and b), or in *o*-DCB c) and d), with a sonication time of 150 min.

Since TEM analysis does not allow to precisely determine the number of graphene layers, we further investigate the FLG dispersions obtained in *o*-DCB and NMP by Raman spectroscopy.

As discussed above, Raman spectroscopy is a powerful non-destructive tool to characterize graphene samples and to obtain straightforward information about

the number of layers present in a sample,[50] the edges,[113] the doping effects, or the functionalization efficiency of a given reaction.[114]

Graphene's Raman spectrum, as already mentioned, is characterized by three main bands: the D band (~ 1350 cm^{-1}) related with defects, in fact, requires a defect for its activation; the G band (~ 1580 cm^{-1}) due to the in-plane vibration of carbon atoms with sp^2 hybridization and; the 2D band (~ 2700 cm^{-1}) whose evolution with the number of layers allows to obtain information about how many flakes form the material (Figure 35). In addition, in the case of non-covalent immobilization of molecules onto the basal plane of graphene, G and 2D bands are very sensitive to doping. Besides an overall broadening of the two modes, p-doping (n-doping) results in an upshift (downshift) of the G band.[115,116]

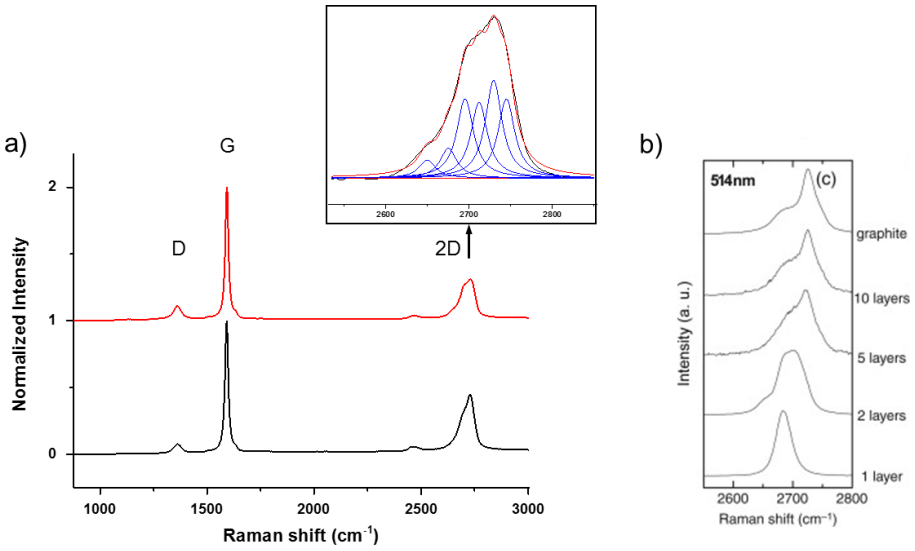

Figure 35. a) Raman spectra of graphite (black) and graphene exfoliated in NMP (red) recorded at 532 nm. The upper image shows the deconvolution of the 2D band. b) Evolution of the 2D band recorded at 514 nm.[50]

113. C. Casiraghi, A. Hartschuh, H. Qian, S. Piscanec, C. Georgi, A. Fasoli, K. S. Novoselov, D. M. Basko, A. C. Ferrari, *Nano Lett.* **2009**, *9*, 1433-1441.
114. J. M. Englert, P. Vecera, K. C. Knirsch, R. A. Schäfer, F. Hauke, A. Hirsch, *ACS Nano* **2013**, *7*, 5472-5482.
115. X. Dong, D. Fu, W. Fang, Y. Shi, P. Chen, L.-J. Li, *Small* **2009**, *5*, 1422-1426.
116. Q. Su, S. Pang, V. Alijani, C. Li, X. Feng, K. Müllen, *Adv. Mater.* **2009**, *21*, 3191-3195.

In Figure 35a, it is shown the Raman spectrum of a sample of graphene exfoliated in NMP. The deconvolution of the 2D band allows to determine the number of layers present in this sample. For a single layer of graphene, the 2D band displays a single Lorentzian fit with a full-width half-maximum (FWHM) value of ~ 24 cm^{-1} and a very high intensity originating from a triple resonance process only present in the perfect monolayer. Already in the bilayer, due to π-π* interactions between the two layers, more electron-phonon scattering processes are possible, which leads to a broadening of the 2D band. In this case, the 2D band is fitted to six components and it can be established that it is a three layer graphene.[50,117] From now on, we will refer to this material as FLG. In Figure 35b it is shown that for more than five layers the Raman spectra of graphite and FLG are indistinguishable, for this reason with the samples exfoliated in *o*-DCB we have not tried to fit the 2D band.

Once that we established that NMP is the optimum solvent to obtain FLG, we tried to determine the influence of the sonication time in the exfoliation efficiency.

The study was carried out increasing the sonication time (2.5, 18 and 24 hours) for several graphite dispersions with the same initial concentration and keeping constant the centrifugation conditions (45 minutes, 500 r.p.m). For longer sonication times, the obtained dispersions after centrifugation showed a darker color, which implies an increase in graphene's concentration (Figure 36).[47]

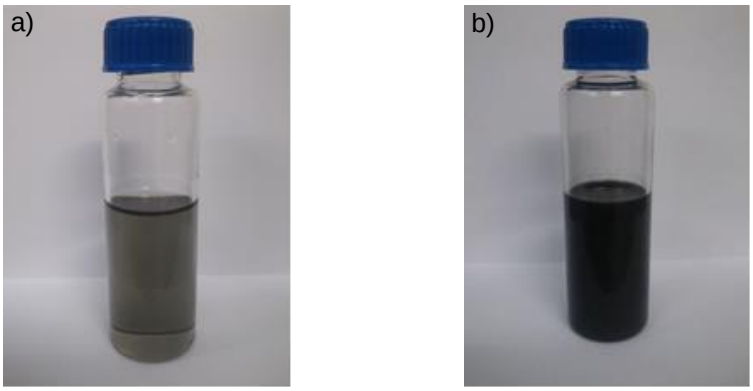

Figure 36. Graphite dispersions in NMP with different sonication times: a) 2.5 hours and b) 24 hours.

117. a) Z. Ni, Y. Wang, T. Yu, Z. Shen, *Nano Res.* **2008**, *1*, 273-291. b) L. M. Malard, M. A. Pimenta, G. Dresselhaus, M. S. Dresselhaus, *Phys. Rep.* **2009**, *473*, 51-87.

TEM analysis reveals that an increase in the sonication time results in flakes with smaller dimensions that tend to agglomerate (Figure 37). An observation that can be rationalized in part considering the relationship between the layers dimensions and the concentration of the dispersions. Solvent volume for each flake has to be proportional to the sphere volume defined by the length of each flake. It means that for smaller layers, the solvent volume is lesser and the concentration is greater.[118]

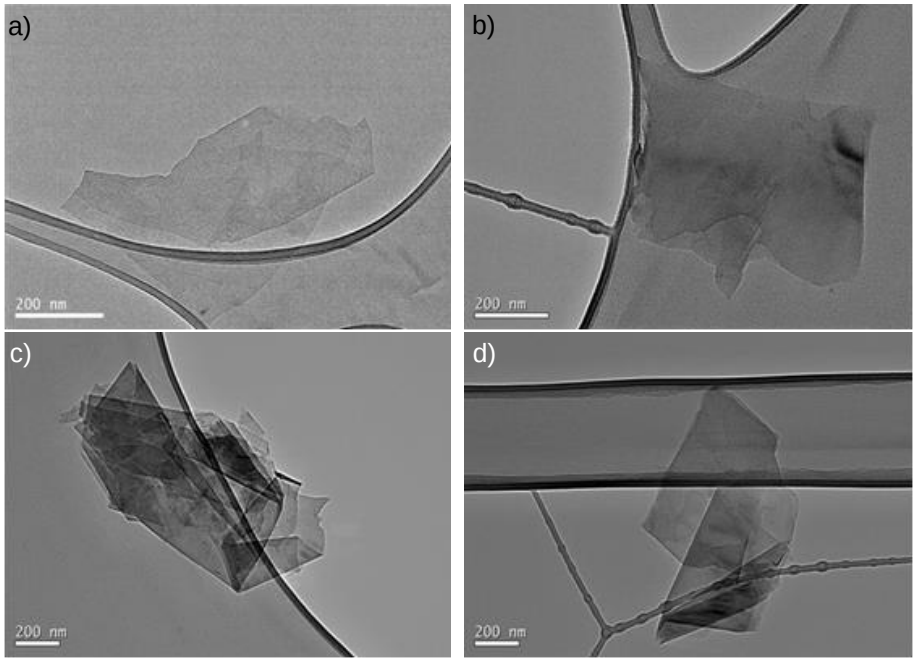

Figure 37. FLG exfoliated in NMP at different sonication times: a) 2.5 hours, b) and d) 24 hours and c) 18 hours.

The stability of the FLG obtained after different sonication times was further investigated by TGA. The starting graphite does not present a significant weight loss, so the weight loss observed in FLG samples is due to the solvent that interacts with layers and allows its exfoliation. Assuming that the concentration grows with the sonication time because the exfoliation process is more efficient, it can be predicted that the solvent which interacts with FLG is greater. This reasoning could explain the increase of weight loss observed in the TGA for the samples sonicated during 24 hours (Figure 38).

118. J. N. Coleman, *Acc. Chem. Res.* **2013**, *46*, 14-22.

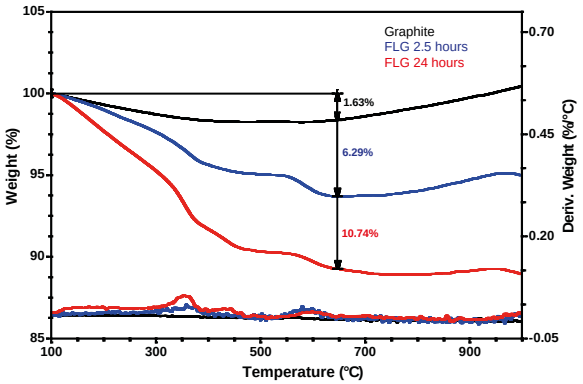

Figure 38. TGA analysis for the starting graphite and FLG obtained in NMP at different sonication times.

In order to facilitate the non-covalent immobilization of different receptors onto the basal plane of FLG, we decided to work with the FLG obtained after 2.5 hours sonication, which features a larger effective surface.

The FLG dispersions obtained in NMP were additionally characterized by UV-Vis-NIR absorption spectroscopy. The concentration of a FLG dispersion can be estimated by using the Lambert-Beer Law ($A = \alpha cl$), where A is the absorbance at 660 nm, α is the absorption coefficient (L/g·m), c is the concentration and l is the length of the optical path.[38]

Concentrations of FLG in NMP of 0.061 mg/mL (measured by filtration and weighing) were obtained by initial dispersion of 0.2 g of graphite in 100 mL of NMP (see Experimental Section for full details of the exfoliation process). This dispersion of a known concentration was diluted several times and the spectra of each dilution recorded. The representation of the absorbance at 660 nm divided by the length of the optical path *versus* concentration, showed a Lambert-Beer behavior, and allowed to determine the value of the absorption coefficient (Figure 39), which can be used subsequently to estimate the concentration of FLG in any other dispersion.

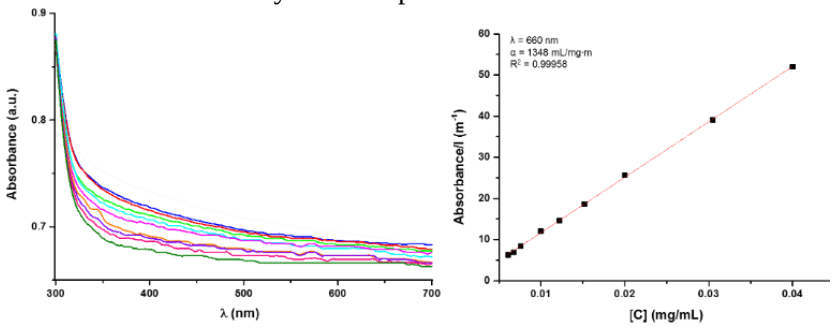

Figure 39. UV-Vis spectra of FLG in NMP (left). Optical absorbance divided by cell length *vs*. concentration (right).

4.2. NON-COVALENT FUNCTIONALIZATION OF GRAPHENE WITH π-EXTTF-BASED RECEPTORS

4.2.1. π-Extended tetrathiafulvalene (π-exTTF)

9,10-Bis(1,3-dithiol-2-ylidene)-9,10-dihydroanthracene (π-exTTF) is a derivative of tetrathiafulvalene (TTF) in which the 1,3-ditihiole rings are separated by an anthraquinone spacer (Figure 40).[119]

π-exTTF has widely been used as a donor moiety and is characterized by a butterfly shape in the neutral state, in contrast to the planar TTF. During the oxidation, in which π-exTTF exhibits a two-electron process to form a dication species (E_{ox}^1 = 0.44 V *vs.* SCE, in DCM), its geometry changes to a planar structure, where aromatic dithiolium rings are perpendicular to the aromatic anthracene skeleton. The remarkable gain of aromaticity and planarity upon oxidation stabilizes the π-exTTF dication species.

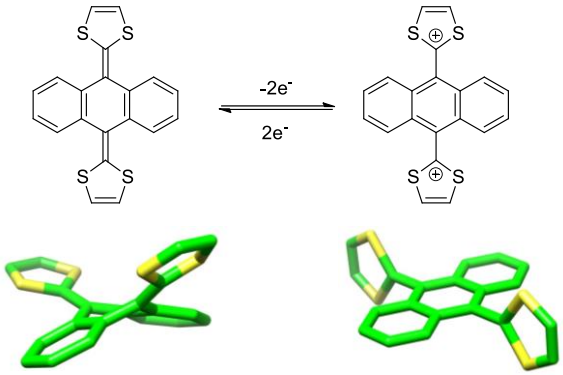

Figure 40. Geometrical change of π-exTTF upon oxidation.

Due to this electronic and structural features, several systems based on π-exTTF have been reported with applications in different fields (Figure 41), in particular in organic electronics. In the next paragraphs some examples will be discussed.[120]

119. Y. Yamashita, Y. Kobayashi, T. Miyashi, *Angew. Chem. Int. Ed.* **1989**, *28*, 1052-1053.
120. F. G. Brunetti, J. L. Lopez, C. Atienza, N. Martín, *J. Mater. Chem.* **2012**, *22*, 4188-4205.

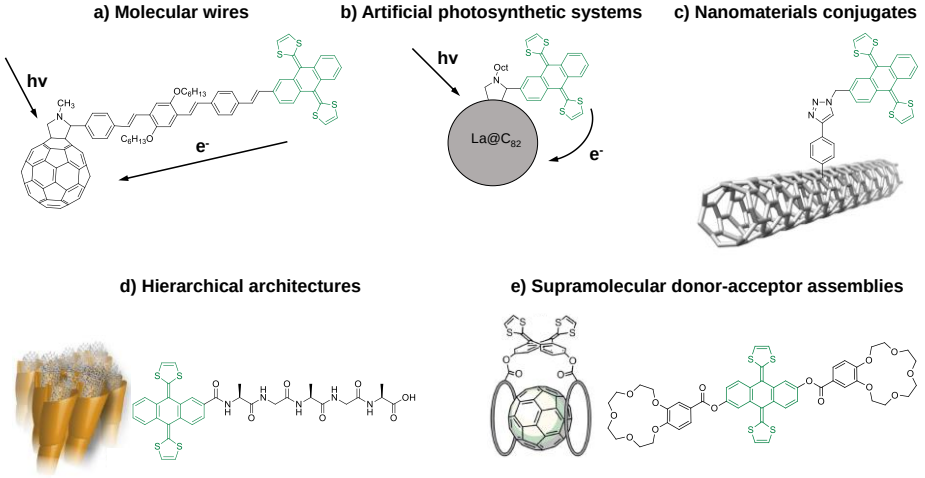

Figure 41. Some of the applications of π-exTTF in organic electronics and supramolecular chemistry.

The π-exTTF ability to get oxidized, makes it a suitable candidate for the preparation of donor-acceptor assemblies, which behave as molecular wires when endowed with different π-conjugated systems as bridges (Figure 41a).[7a] In order to mimic the photosynthetic process, several dyads and triads were investigated upon photoinduced electron-transfer conditions. For example, taking advantage of the remarkable properties of endohedral metallofullerenes such as La@C_{82} or La_2@C_{80}, stable radical ion pair species were obtained upon photoinduced electron transfer of covalent π-exTTF-based dyads (Figure 41b).[121]

The difference between SWCNTs, MWCNTs and graphene chemical reactivity has also been investigated through the covalent modification with π-exTTF units. Important differences in the grafting density were noticed by TGA measurements, with a significantly higher degree of functionalization for SWCNTs. For these nanoconjugates, a series of steady-state and time resolved spectroscopy revealed a photoinduced electron transfer from the π-exTTF units to the electron-accepting SWCNTs (Figure 41c).[122]

121. Y. Takano, S. Obuchi, N. Mizorogi, R. García, M. Á. Herranz, M. Rudolf, S. Wolfrum, D. M. Guldi, N. Martín, S. Nagase, T. Akasaka, *J. Am. Chem. Soc.* **2012**, *134*, 16103-16106.
122. J. Mateos-Gil, L. Rodriguez-Perez, M. Moreno Oliva, G. Katsukis, C. Romero-Nieto, M. A. Herranz, D. M. Guldi, N. Martín, *Nanoscale* **2015**, *7*, 1193-1200.

The supramolecular reactivity of π-exTTF has also been investigated in several examples.[123] In π-exTTF-crown ether tweezers the affinity of the receptors towards C_{60} arises from an interplay of π-π, n-π and CH-π interactions that results in a remarkable binding constant (log K_a = 7.0 in PhCN) at room temperature (Figure 41e).[124] To gain control in the supramolecular organization of π-exTTF-based architectures, the design of covalently linked peptides of different lengths has also been explored (Figure 41d).[125] These π-exTTF-peptides have enabled the spontaneous self-assembly of SWCNTs into well-ordered structures of different scales.[126]

Considering these precedents, in this PhD work we intended to develop molecular receptors for graphene based on π-exTTF units.

4.2.2. Synthesis of π-exTTF-pyrene conjugates

To ensure a strong binding of the π-exTTF units to the graphene basal plane, two pyrene receptors **11** and **21**, containing one (PyexTTF) or three (3PyexTTF) pyrene units, have been synthesized (Figure 42).

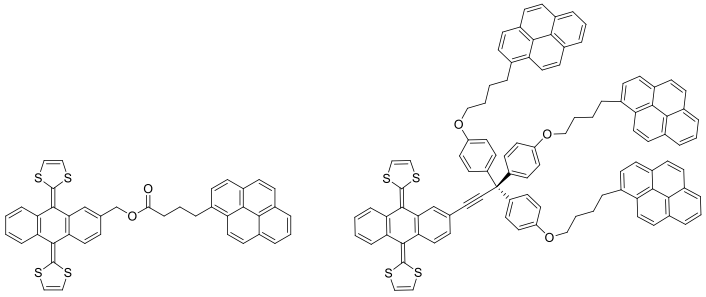

11 **21**

Figure 42. Structure of the π-exTTF derivatives for the non-covalent functionalization of graphene.

The common step in the synthesis of derivatives **11** and **21** is the Horner-Wadsworth-Emmons reaction between the dimethyl-(1,3-dithiol-2-yl)-phosphonate **5** and an anthraquinone derivative. To achieve this, it is necessary

123. E. M. Perez, B. M. Illescas, M. A. Herranz, N. Martín, *New J. Chem.* **2009**, *33*, 228-234.
124. L. Moreira, J. Calbo, R. M. Krick Calderon, J. Santos, B. M. Illescas, J. Arago, J.-F. Nierengarten, D. M. Guldi, E. Orti, N. Martín, *Chem. Sci.* **2015**, *6*, 4426-4432.
125. J. L. López, C. Atienza, A. Insuasty, J. López-Andarias, C. Romero-Nieto, D. M. Guldi, N. Martín, *Angew. Chem. Int. Ed.* **2012**, *51*, 3857-3861.
126. J. López-Andarias, J. L. López, C. Atienza, F. G. Brunetti, C. Romero-Nieto, D. M. Guldi, N. Martín, *Nat. Commun.* **2014**, *5*, 3763.

the synthesis of the phosphonate following a procedure well known in the bibliography (Scheme 1).[127] Commercially available vinylene trithiocarbonate **1** was treated successively in four reaction steps: S-methylation, reduction with $NaBH_4$, treatment with HBF_4 and phosphonylation with trimethylphosphite, to yield the desired product.

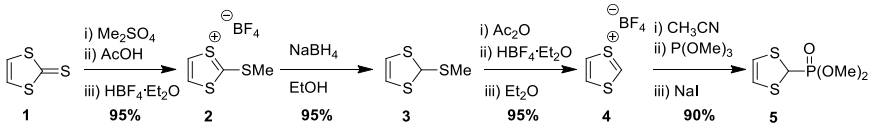

Scheme 1. Synthesis of phosphonate **5**.

The addition of *n*-BuLi over phosphonate **5** generated a very reactive carbanion that reacted with the protected 2-hydroxymethylanthraquinone **7** to yield the derivative **8** (Scheme 2). After cleavage of the protective group, the π-exTTF derivative **11** was obtained by a esterification reaction between the 4-(1-pyrenyl)butyric acid **10** and the 2-(hydroxymethyl)-9,10-bis(1,3-dithiol-2-ylidene)-9,10-dihydroanthracene **9** in the presence of 1,3-dicyclohexylcarbodiimide (DCC) and (dimethylamino)-pyridine (DMAP).[128]

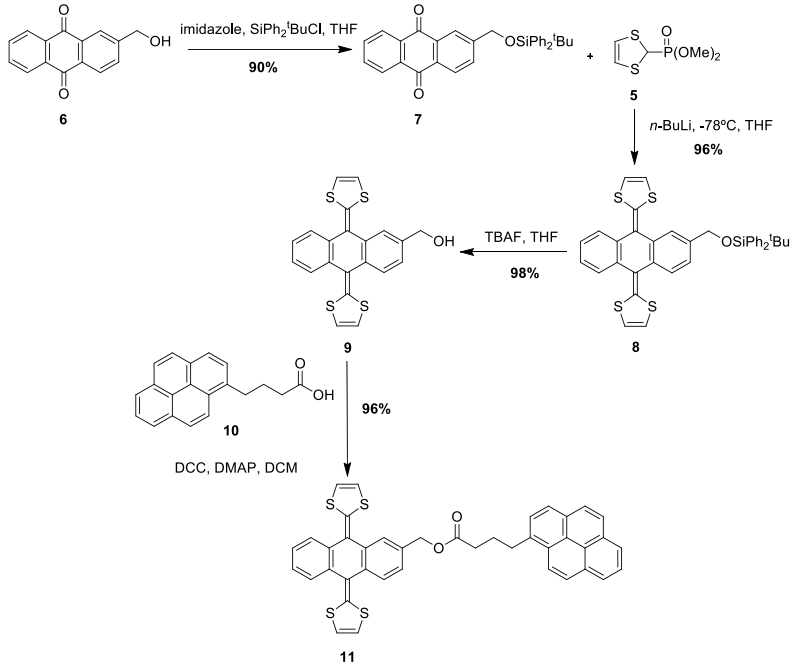

Scheme 2. Synthesis of the π-exTTF derivative **11.**

127. A. J. Moore, M. R. Bryce, *Synthesis* **1991**, 26-28.
128. M. Á. Herranz, C. Ehli, S. Campidelli, M. Gutiérrez, G. L. Hug, K. Ohkubo, S. Fukuzumi, M. Prato, N. Martín, D. M. Guldi, *J. Am. Chem. Soc.* **2008**, *130*, 66-73.

The synthesis of 3PyexTTF **21** was carried out following the sequence of reactions collected in Scheme 3.

The terminal alkyne **13**[129] and the iodo-π-exTTF derivative **16**[130] were synthesized according to the previously described procedures. Compound **17** was obtained by the Sonogashira coupling between these two precursors in the presence of $Pd(PPh_3)_4$, CuI and triethylamine. The treatment of molecule **17** with BBr_3 allowed to obtain trisphenol **18** quantitatively, which by subsequent etherification with the 4-(1-pyrenyl)-1-butanol tosylate **20** afforded the desired final product **21**. All products were fully characterized by ^1H and ^{13}C-NMR, FTIR, mass spectrometry and UV-Vis spectroscopy. The detailed description of the synthesis and characterization can be found in the experimental section.

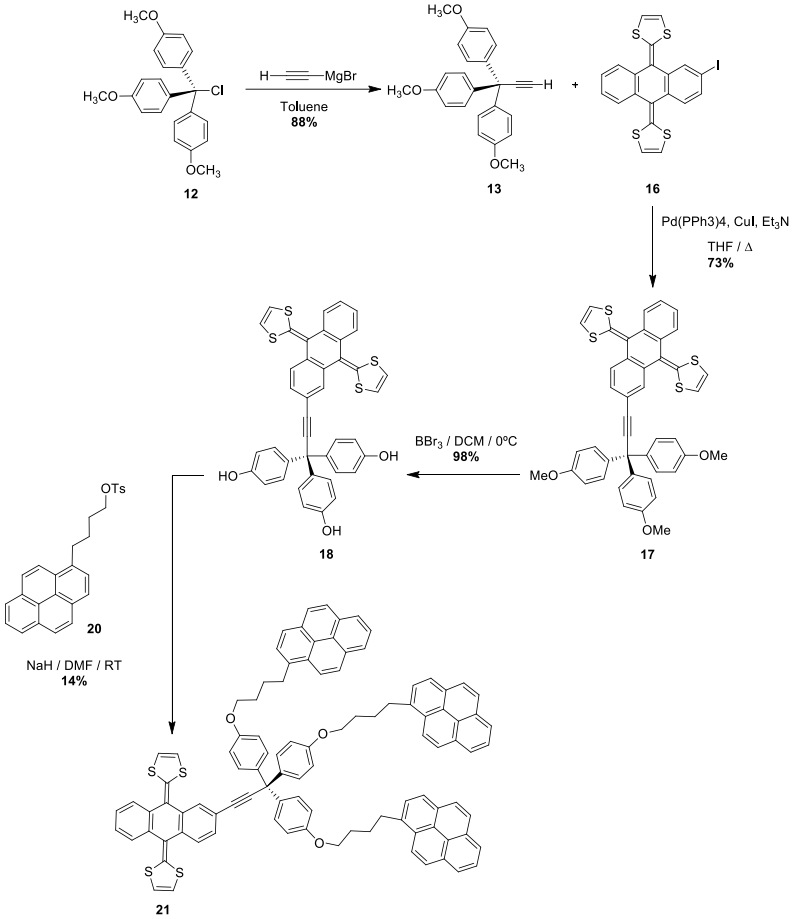

Scheme 3. Synthesis of the π-exTTF derivative **21**.

129. P. D. Jones, T. E. Glass, *Tetrahedron* **2004**, *60*, 11057-11065.
130. M. C. Díaz, B. M. Illescas, C. Seoane, N. Martín, *J. Org. Chem.* **2004**, *69*, 4492-4499.

The iodo-π-exTTF derivative **16**, necessary in the synthesis of the tripodal compound **21**, was synthesized using the reaction conditions described in Scheme 4. 2-Iodoanthraquinone **15** was obtained by the treatment of compound **14** with KNO_2, CuI and HI at 35 °C.[131] To obtain the iodo-π-exTTF derivative **16**, the same reaction conditions used to synthesize **8** were employed, although in this case the Horner-Wadsworth-Emmons reaction takes place between phosphonate **5** and the 2-iodoanthraquinone **15**.[130]

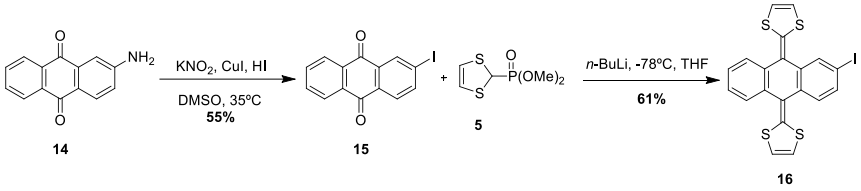

Scheme 4. Synthesis of π-exTTF derivative **16.**

In Figure 43 are presented the ^{1}H-NMR spectra of intermediates **13**, **17** and **18**.

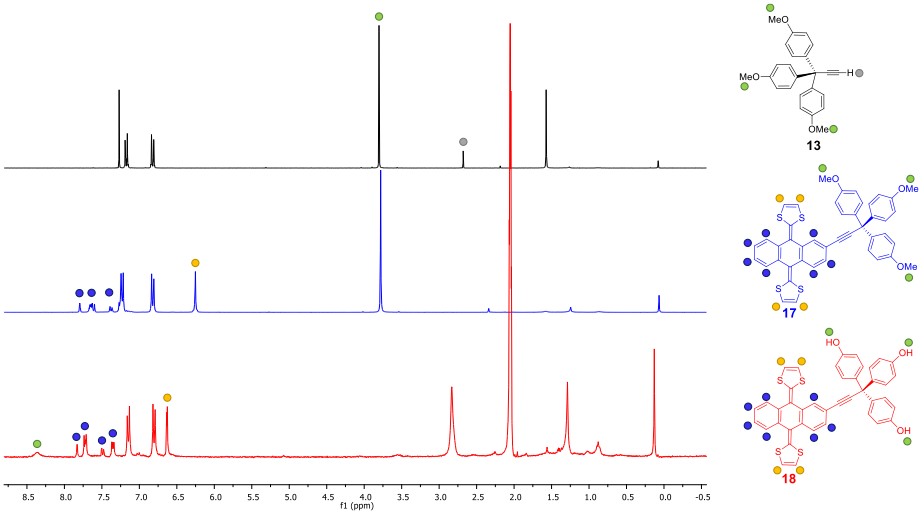

Figure 43. ^{1}H-NMR spectra (300 MHz, 298 K) of **13** (black), **17** (blue) in $CDCl_3$ and **18** (red) in acetone-d_6. The principal changes during the synthesis are denoted with colored bullets.

It can be observed that the synthesis of trisphenol **18** was achieved successfully, since the singlet at 2.68 ppm, corresponding to the terminal alkyne **13**, disappears after the Sonogashira coupling. Furthermore, the signals associated to the skeleton of π-exTTF clearly appear in compounds **17** and **18**. Thus, at ca.

131. W. Baik, W. Luan, H. J. Lee, C. H. Yoon, S. Koo, B. H. Kim, *Can. J. Chem.* **2005**, *83*, 213-219.

6.62-6.28 ppm are found the signals of the 1,3-dithiole rings, whereas the signals of the anthracene backbone appear between 7.82-7.28 ppm. The singlet at 3.81 ppm assigned to the methoxy groups of **13** and **17** vanishes for **18** and a broad signal corresponding to the hydroxyl groups appears at 8.39 ppm instead.

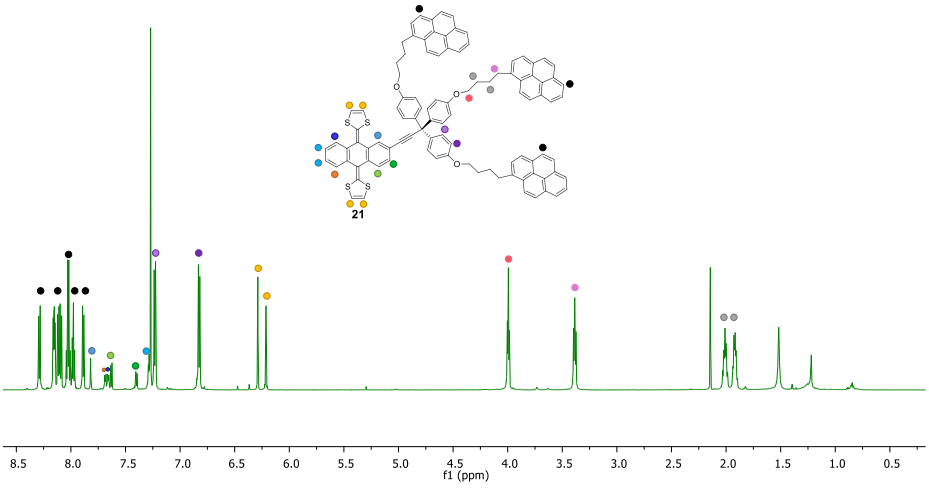

Figure 44. ^{1}H-NMR spectrum ($CDCl_3$, 300 MHz, 298 K) of the final product **21**. Representative signals are depicted by colored bullets.

The ^{1}H-NMR spectrum of 3PyexTTF **21** is shown in Figure 44. The signals corresponding to the aliphatic chains and to the pyrene units can be observed in addition to the π-exTTF characteristic signals mentioned in Figure 43, confirming the synthesis of the desired final product.

4.2.3. Study of the solution interactions between π-exTTF derivatives and FLG

Before accomplishing the non-covalent functionalization of FLG with the π-exTTF-pyrene systems **11** and **21**, it is necessary to study if any interactions exist between them. These studies were carried out by UV-Vis and fluorescence titrations, which consist in the addition of increasing quantities of FLG in NMP to a solution of known concentration of the desired system. In both cases, the measurements were performed in NMP at 25 °C.

Firstly, the UV-Vis titrations were carried out. To determine if the π-exTTF moiety and the pyrene unit interact with the graphene surface, the studies were accomplished with 4-(1-pyrenyl)-1-butanol and 9,10-bis(1,3-dithiol-2-ylidene)-9,10-dihydroanthracene (π-exTTF) as references.

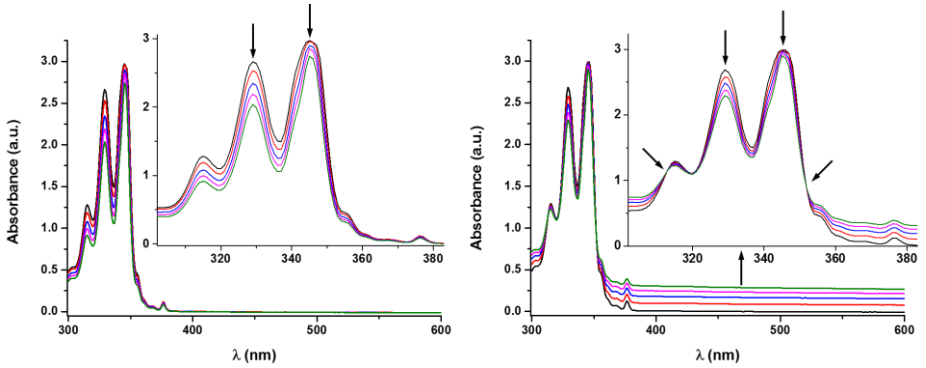

Figure 45. UV-Vis spectra obtained during the dilution (left) and titration (right) with FLG of 4-(1-pyrenyl)-1-butanol ($1.27 \cdot 10^{-4}$ M). Each addition corresponds to 50 μL.

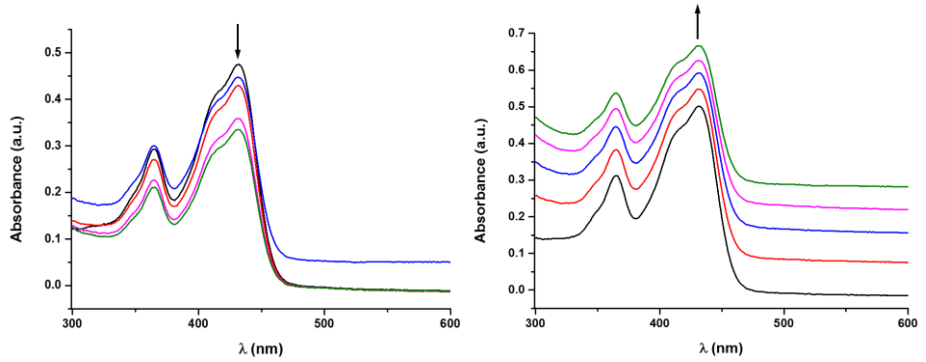

Figure 46. UV-Vis spectra obtained during the dilution (left) and titration (right) with FLG of π-exTTF ($3.94 \cdot 10^{-5}$ M). Each addition corresponds to 50 μL.

For each titration different behaviors are observed. In the case of 4-(1-pyrenyl)-1-butanol (Figure 45), spectral changes associated with the addition of FLG were noticed. The pyrene bands with maxima at 329 and 345 nm, decreased in intensity and two pseudo-isosbestic points appear at 313 and 351 nm, respectively. These changes suggest the interaction of 4-(1-pyrenyl)-1-butanol with FLG. However, in the titration experiment with π-exTTF (Figure 46) no changes were observed in the spectra, indicating the absence of appreciable interactions with FLG.

Once that the studies were carried out with the independent reference units, the evaluation of the interactions between PyexTTF **11** and 3PyexTTF **21** with FLG was accomplished.

In order to confirm that all the changes observed in the titrations are not due to dilution, control experiments have been carried out. These control experiments

consist in the addition of equal amounts of NMP without FLG to a solution of known concentration of the desired system.

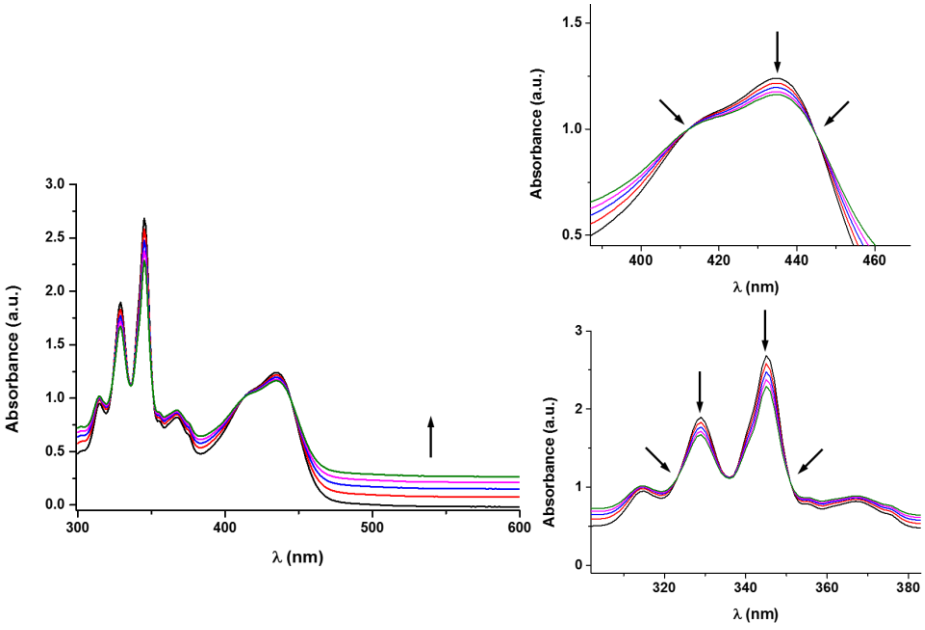

Figure 47. UV-Vis spectra obtained upon titration of PyexTTF **11** ($5.87 \cdot 10^{-5}$ M) with FLG. Each addition corresponds to 50 µL.

For PyexTTF **11**, it can be noticed a similar behavior to that of 4-(1-pyrenyl)-1-butanol (Figure 47). We observed a decrease in the intensity of the pyrene bands as well as for the π-exTTF characteristic absorption band at 435 nm with the addition of FLG. Moreover, these spectral changes are accompanied by the appearance of several pseudo-isosbestic points (323, 351, 412 and 445 nm), which suggest the interaction between FLG and the whole molecule.[91,132]

On the other hand, in the titration experiments for 3PyexTTF **21**, it is observed the increase of the absorbance in the region between 400-600 nm and no significant changes for the absorption band of π-exTTF (Figure 48). However, the pyrene maxima decrease their intensity and, again, two pseudo-isosbestic points appear at 311 and 351 nm, respectively. All these data suggest that, in this case, only the pyrene units might be interacting with FLG.

132. a) E. M. Pérez, L. Sánchez, G. Fernández, N. Martín, *J. Am. Chem. Soc.* **2006**, *128*, 7172-7173. b) E. M. Perez, N. Martín, *Chem. Soc. Rev.* **2008**, *37*, 1512-1519.

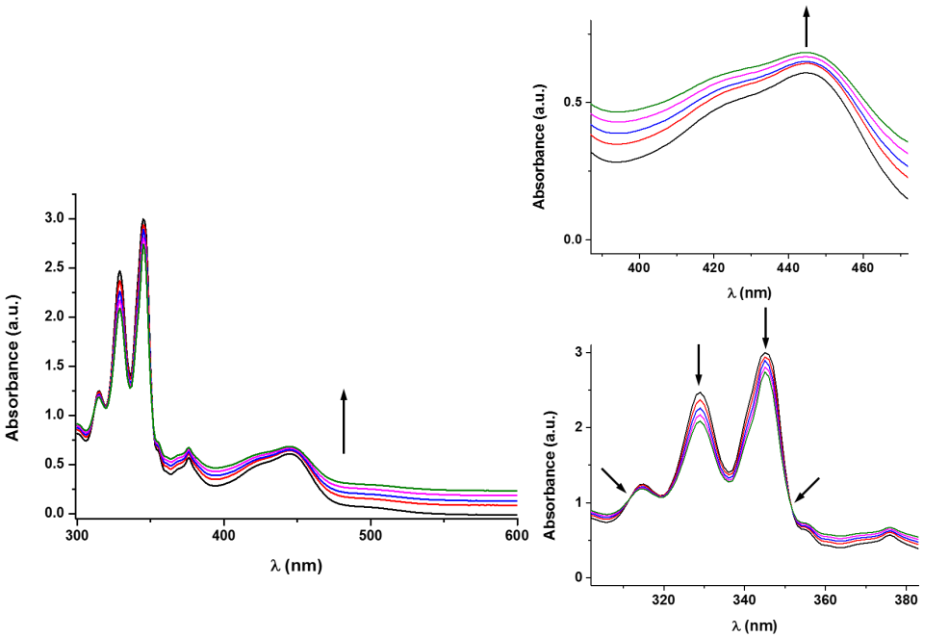

Figure 48. UV-Vis spectra obtained upon titration of 3PyexTTF **21** ($2.39 \cdot 10^{-5}$ M) with FLG. Each addition corresponds to 50 µL.

To corroborate the interaction between FLG and the pyrene moieties of molecules **11** and **21**, the systems were further investigated by fluorescence titrations.

Pyrene is a sensitive fluorescent probe that displays an assembly of monomeric fluorescence peaks (377-396 nm) and an additional band (called excimer) at ~ 480 nm when two fluorophores are spatially proximal.[133]

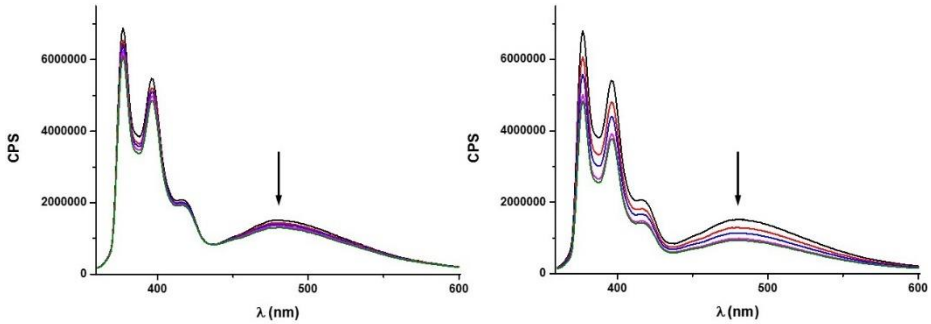

Figure 49. Fluorescence spectra obtained upon dilution (left) and titration (right) with FLG of PyexTTF **11** ($2.94 \cdot 10^{-5}$ M). Each addition corresponds to 50 µL (λ_{exc} = 344 nm).

133. A. T. Haedler, H. Misslitz, C. Buehlmeyer, R. Q. Albuquerque, A. Köhler, H.-W. Schmidt, *ChemPhysChem* **2013**, *14*, 1818-1829.

In the fluorescence measurements for PyexTTF **11**, an emission quenching is noticed with the increasing addition of FLG (Figure 49). This emission is attenuated in a 40% in relation to its original intensity. Comparing the titration experiment with the control one (dilution), the greater quenching in the former suggests an interaction between FLG and the studied system.

In the case of 3PyexTTF **21**, the experiments showed the same trend that in the previous case (Figure 50). Moreover, the maximum emission of the pyrene excimer shifts to lower wavelengths with the addition of increasing quantities of FLG, from 486 to 483 nm. This fact could be explained by the disruption of the non-covalent interaction among the pyrene rings when the molecule is interacting with FLG.

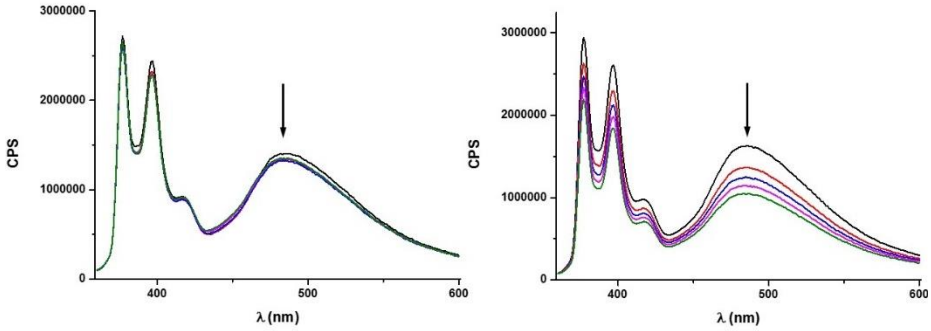

Figure 50. Fluorescence spectra obtained upon dilution (left) and titration (right) with FLG of 3PyexTTF **21** ($6.83 \cdot 10^{-6}$ M). Each addition corresponds to 50 μL (λ_{exc} = 344 nm).

Once that the interactions between PyexTTF **11** and 3PyexTTF **21** with FLG have been corroborated, the synthesis of the supramolecular hybrids took place.

4.2.4. Synthesis of non-covalent FLG/π-exTTF hybrids

The synthesis of the supramolecular complexes of FLG and the π-exTTF receptors was carried out following a procedure that combines sonication, filtration and washings steps. In particular, the desired molecule was suspended in a FLG dispersion previously exfoliated in NMP. This mixture was sonicated during 30 minutes and subsequently filtered and washed with DCM to remove the excess of organic molecule. The washings were repeated until the filtrate was transparent (see experimental section for specific details). The solids obtained were characterized by several techniques to confirm the non-covalent functionalization of FLG with the monopodal or tripodal π-exTTF receptors **11** and **21** (Figure 51).

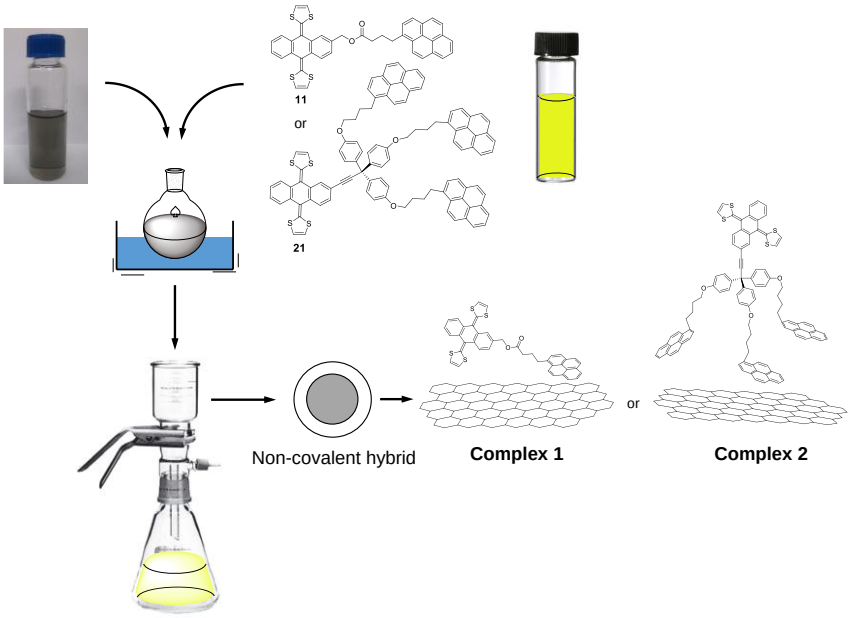

Figure 51. Schematic representation of the procedure followed in the synthesis of the non-covalent FLG/π-exTTF hybrids.

UV-Vis spectroscopy is a very useful technique to determine if the supramolecular modification has taken place successfully, because it allows to observe the characteristic absorption bands of pyrene and π-exTTF.

In Figure 52 (left), the spectra of the starting FLG, PyexTTF **11** and PyexTTF/FLG (**complex 1**) are shown. For these, the characteristic pyrene peaks at 329 and 345 nm can be discerned, respectively. Moreover, at 432 nm it can be intuited a broad band symptomatic of the presence of the π-exTTF units. The peak positions coincide with the maxima of the organic molecule, thus confirming the presence of this in the complex.

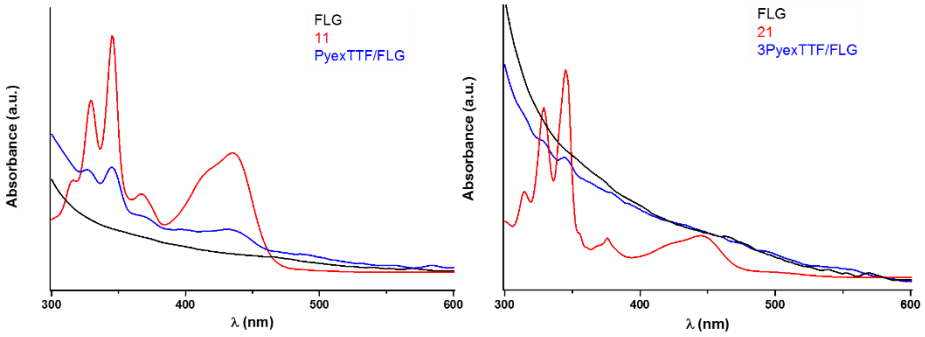

Figure 52. Left: UV-Vis spectra of FLG, PyexTTF **11** and **complex 1** in NMP. Right: UV-Vis spectra of FLG, 3PyexTTF **21** and **complex 2** in NMP.

In the case of 3PyexTTF/FLG (**complex 2**), the spectrum has a similar trend to that of PyexTTF/FLG (**complex 1**) and it can be observed the characteristic two peaks of the pyrene moieties. So, again the UV-Vis spectrum verifies the non-covalent functionalization of graphene. The absorption band of the π-exTTF in the case of the tripodal derivative (**21**) is less intense that in the monovalent one (**11**), which makes difficult the assignment of bands corresponding to this fragment (Figure 52, right).

In order to evaluate in a quantitative manner the functionalization degree of FLG with the monopodal and tripodal receptors, TGA analyses were performed on the obtained supramolecular complexes. In Figure 53 is depicted the TGA of the supramolecular **complex 1** under air conditions. The complex undergoes a 35% weight loss, which corresponds approximately to a ratio of 1 PyexTTF (**11**) per 107 carbon atoms. Besides, the thermal behavior of the organic molecule is shown, presenting a maximum in its first derivative curve at 300 °C, that matches with the desorption in the supramolecular complex.

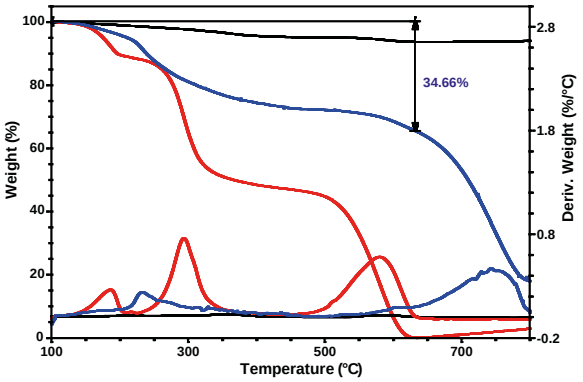

Figure 53. TGA weight loss and first derivative curves under air conditions of FLG (black), PyexTTF **11** (red) and **complex 1** (blue).

In the case of **complex 2**, the observed weight loss is around 32%, which means that there is around 1 3PyexTTF (**21**) per 264 carbon atoms. This lower functionalization degree can be attributed to the greater size of the organic compound. One of these molecules requires more space than one of the monovalent derivatives to interact with FLG. Again, the desorption of the supramolecular complex coincides with the first derivative maximum of the molecule (Figure 54).

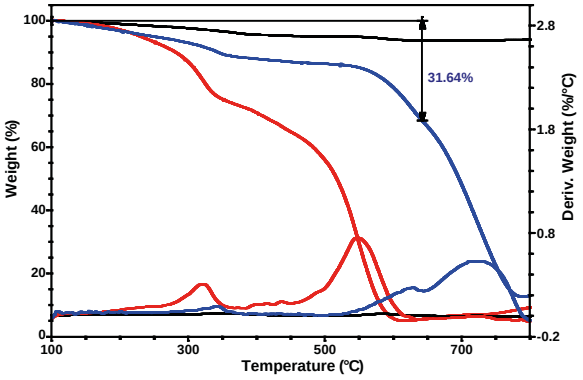

Figure 54. TGA weight loss and first derivative curves under air conditions of FLG (black), 3PyexTTF **21** (red) and **complex 2** (blue).

As expected, the supramolecular complexes **1** and **2** maintain the decomposition pattern of the monopodal and tripodal π-exTTF-based receptors, although with a small increase of the temperature decomposition maxima (see derivative curves in Figure 53 and Figure 54), which indicates a thermal stabilization of the whole system due to the non-covalent binding to FLG.

As it has been discussed above, Raman spectroscopy can be employed to determine how the non-covalent functionalization influences FLG properties and structure. In Figure 55, the Raman spectra for both PyexTTF and 3PyexTTF supramolecular complexes with FLG are shown. At a first glance, it is observed that the rate of defects (D band) does not increase after the functionalization, which is reasonable considering that no covalent bonds are formed upon supramolecular functionalization. Following with the G band, this is shifted to lower frequencies in the complexes when compared to FLG. The interaction of FLG with the pyrene-π-exTTF receptors causes its n-doping.[86,115] In the case of **complex 1**, this shift is slightly greater (9 cm^{-1}) than for **complex 2** (7 cm^{-1}), which suggests different interactions for each organic molecule. Furthermore, the I_{2D}/I_G ratio also varies with the doping degree,[134] being smaller for higher doping degrees (greater shift), as it can be observed in the inset of Figure 55.

134. Das. A, Pisana. S, Chakraborty. B, Piscanec. S, S. K. Saha, U. V. Waghmare, K. S. Novoselov, H. R. Krishnamurthy, A. K. Geim, A. C. Ferrari, A. K. Sood, *Nat. Nanotechnol.* **2008**, *3*, 210-215.

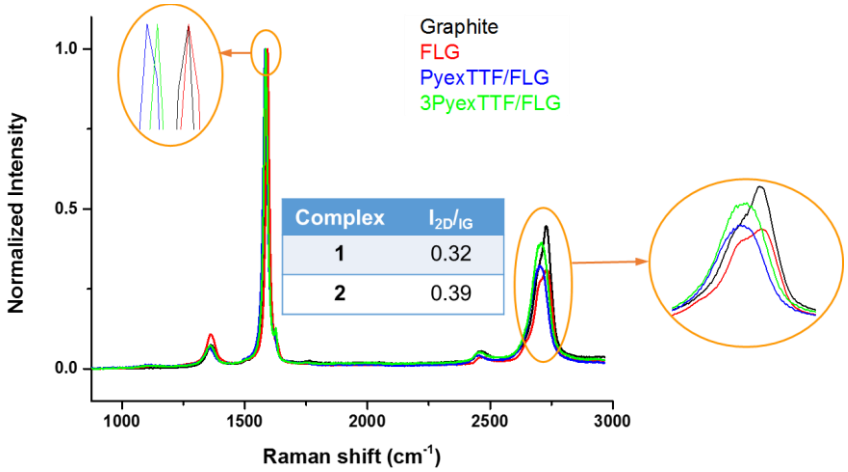

Figure 55. Raman spectra (λ_{exc} = 532 nm) of graphite, FLG and complexes **1** and **2**.

The morphology of the supramolecular complexes was investigated making use of TEM analysis. The re-aggregation of graphene flakes after the functionalization and washing process is prevented by the incorporation of the organic molecules, since TEM analysis reveals a nanomaterial disintegrated and with regular flakes that randomly stacked onto each other (Figure 56). Besides, the dimensions of these flakes do not seem to have decreased during the sonication process.

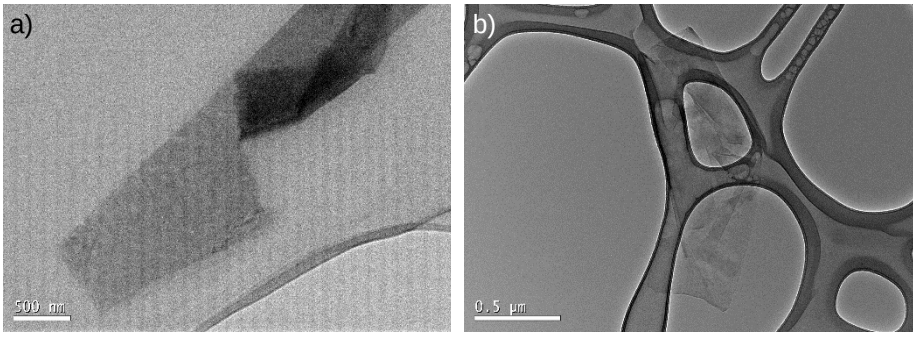

Figure 56. FLG after the non-covalent functionalization. a) **complex1**, and b) **complex 2**.

X-ray photoelectron spectroscopy (XPS) permits to determine the elemental composition of the nanomaterial surface relating the binding energy with the different elements, the electronic state and type of hybridization.[135]

135. M. E. Lipińska, S. L. H. Rebelo, M. F. R. Pereira, J. A. N. F. Gomes, C. Freire, J. L. Figueiredo, *Carbon* **2012**, *50*, 3280-3294.

In the XPS survey spectra of the FLG supramolecular complexes with monopodal and tripodal pyrene-π-exTTFs (Figure 57 and Figure 58), in addition to the core level contributions of C 1s at 284.6 eV and O 1s at 532.6 eV, photoelectrons collected from the S 2p at around 160 eV are observed.

In the insert spectra shown in Figure 57, it is observed the peak corresponding to sulfur in PyexTTF/FLG (**complex 1**), which appears shifted to lower binding energies compared with PyexTTF **11**. This shift suggests a charge transfer from the PyexTTF molecule to graphene. Similar results have been obtained for π-exTTF derivatives interacting with Au (111) surfaces.[136]

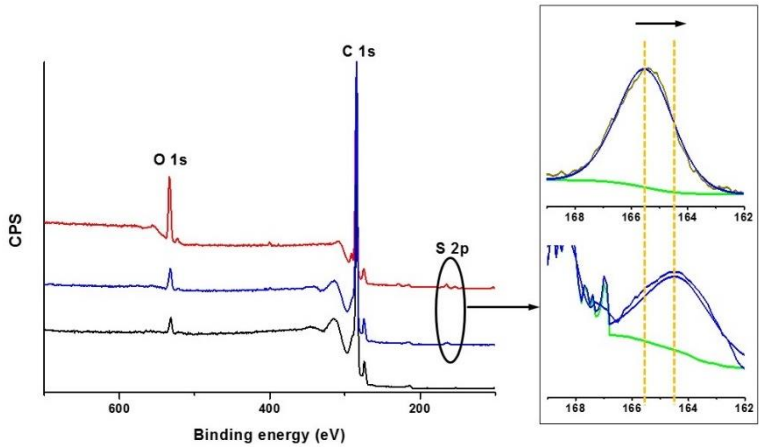

Figure 57. XPS analysis of FLG (black), PyexTTF **11** (red) and **complex 1** (blue). Detailed inset of the sulfur band of **11** (upper graph) compared to **complex 1** (lower graph).

On the other hand, for 3PyexTTF/FLG (**complex 2**) the sulfur peak is also observed, but in this case the value of the binding energy is not significantly shifted respect to the organic molecule **21**, meaning that the π-exTTF in the tripodal derivative does not seem to interact with the graphene surface, maybe because of its distant position from it, which agrees with the results of the UV-Vis titrations.

136. C. Urban, D. Écija, Y. Wang, M. Trelka, I. Preda, A. Vollmer, N. Lorente, A. Arnau, M. Alcamí, L. Soriano, N. Martín, F. Martín, R. Otero, J. M. Gallego, R. Miranda, *J. Phys. Chem. C* **2010**, *114*, 6503-6510.

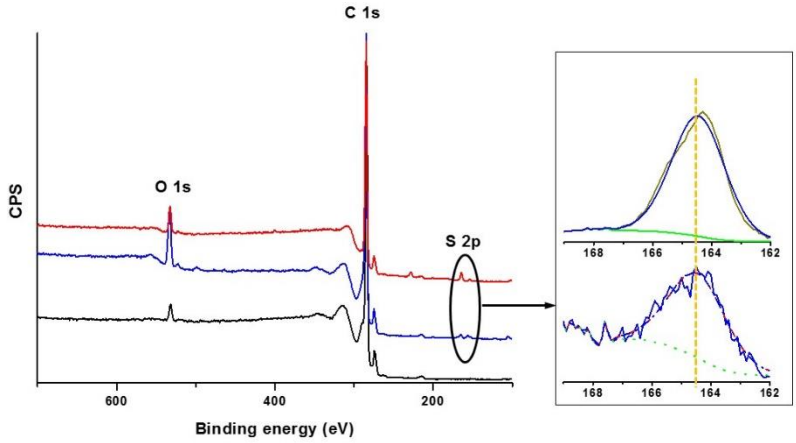

Figure 58. XPS analysis of FLG (black), 3PyexTTF **21** (red) and **complex 2** (blue). Detailed inset of the sulfur band of **21** (upper graph) compared to **complex 2** (lower graph).

The conclusions obtained from XPS also agree with the different shifts observed in Raman spectroscopy for both complexes.

4.2.5. Preparation of graphene/π-exTTF modified electrodes. Applications in biosensing

The electrochemical behavior of PyexTTF **11** and 3PyexTTF **21** onto graphene surfaces was also studied in collaboration with the group of Prof. Encarnación Lorenzo at UAM. The measurements were carried out in three different graphene/glassy carbon modified electrodes: graphene oxide/glassy carbon electrode (GO/GC), graphene oxide electrochemically reduced/glassy carbon electrode (GO-ER/GC) and pristine graphene/glassy carbon electrode (Graphene/GC) (see preparation methods for modified GC electrodes in the experimental section).

The non-covalent functionalization of these electrodes was carried out immersing them in a solution of **11** or **21** (0.36 mM in THF) during 15 hours. After this period of time, the electrodes were washed with THF to remove the molecules non-directly adsorbed on the electrode surface. To verify that the functionalization was successfully carried out, the cyclic voltammograms (CVs) of these electrodes were recorded using an electrochemical cell containing clean electrolyte (0.1 M tetrabutylammonium perchlorate, TBAP, in DMF) (Figure 59).

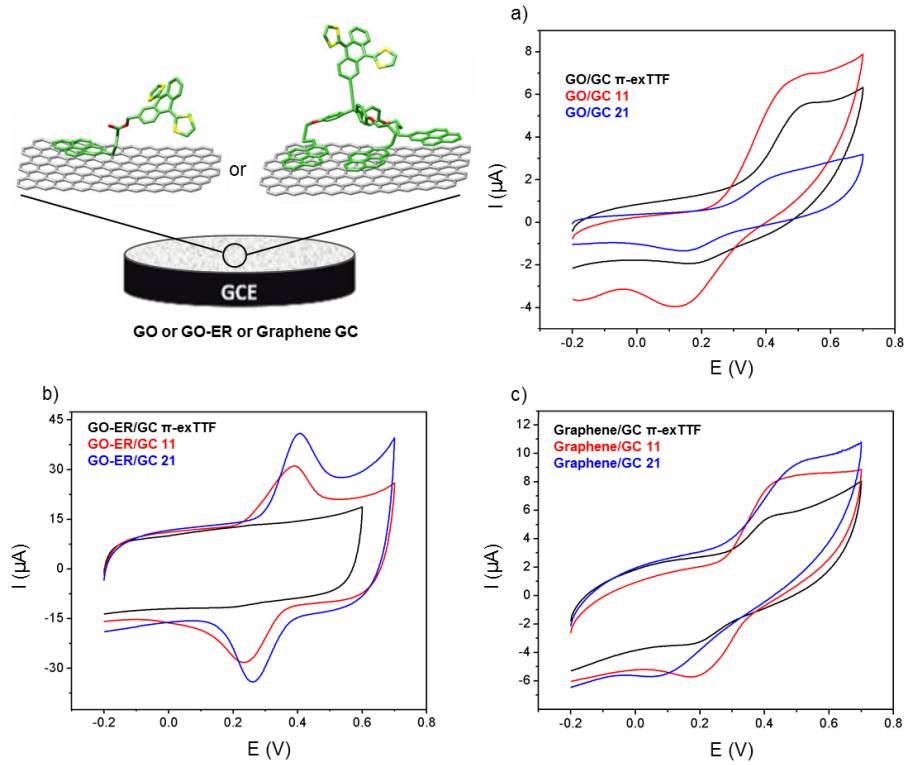

Figure 59. Schematic representation of the modified electrodes. Cyclic voltammograms of a) GO/GC, b) GO-ER/GC and c) Graphene/GC modified with π-exTTF (black), PyexTTF **11** (red) and 3PyexTTF **21** (blue) in 0.1 M TBAP/DMF at 100 mV/s.

In all cases, the redox couple associated with the oxidation/reduction of the π-exTTF moiety is evident, meaning that the molecules are adsorbed onto the electrode surface. The π-exTTF molecule was employed as reference to compare with the electrodes modified with **11** and **21**. The differences observed in the current intensity can be explained by the interactions between the organic compounds and the surface of the electrodes. Graphene oxide (Figure 59a) is a hydrophilic material due to the oxygenated groups present on its surface, so the affinity of the molecules coated with pyrenes is smaller than the one of the π-exTTF. On the other hand, pristine graphene and graphene oxide electrochemically reduced are more hydrophobic because of the higher π-conjugated surface, which allows the π-π interactions between the pyrene units and the electrodes (Figure 59b and c). In fact, for these two electrodes almost no signal was observed for the π-exTTF, so the adsorption takes place by the pyrene moieties present in PyexTTF **11** and 3PyexTTF **21**.

Once demonstrated that **11** and **21** adsorb onto the electrodes surface, Laviron analyses were performed to determine if there were differences in the electron transfer rates between both molecules.[137] The values obtained for the transfer coefficient (α) and the heterogeneous charge transfer rate constant (k^o) are summarized in Table 2.

Table 2. Heterogeneous charge transfer rate constant (k^o), transfer coefficient (α) and differential peak potential (ΔE_p) of PyexTTF **11** and 3PyexTTF **21** adsorbed onto different electrodes in 0.1 M TBAP/DMF.

Modified electrode	k^o (s^{-1})	α	ΔEp (V)
11/GO/GC	4.68	0.659	58
21/GO/GC	3.51	0.388	40
11/GO-ER/GC	9.62	0.506	23
21/GO-ER/GC	6.02	0.667	12
11/Graphene/GC	0.78	0.387	85
21/Graphene/GC	0.29	0.652	102

In all cases, the value of k^o is higher for the monovalent derivative, which suggests that the tripodal derivative is adsorbed through the pyrene units with the π-exTTF moiety far away from the electrode surface in comparison with the monovalent molecule, making difficult the electron transfer between them. These results agree with previous investigations on the heterogeneous rate constants of electron transfer in monopodal and tripodal pyrene systems containing redox-active Co(tpy) complexes.[82]

In addition, the study of the dependence of the adsorption process with the time allows to determine the surface coverage (Γ) of the electrodes. For this, the modified electrodes were immersed in the solutions of π-exTTF derivatives **11** or **21** during different times. The surface coverage was calculated making use of the equation $\Gamma = Q_{ox}/nFA$, where *F* is the Faraday constant (96485 C/mol), *n* is the number of the electrons transferred in the redox process (n = 2), Q_{ox} is the charge associated with the oxidation and *A* is the area of the electrode (0.07 cm^2). The value of Q_{ox} is obtained by the integration of the oxidation peak current in the cyclic voltammograms. In Figure 60, the surface coverage as a function of the adsorption time for each electrode is represented.

137. E. Laviron, *J. Electroanal. Chem.* **1979**, *101*, 19-28.

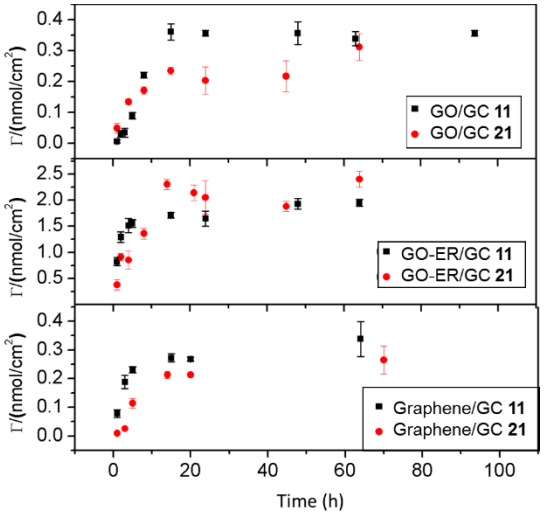

Figure 60. Surface concentration as a function of the adsorption time for PyexTTF **11** (black) and 3PyexTTF **21** (red) for each electrode.

It is noticed that the surface coverage is noticeably higher for the GO-ER/CG electrode than for the others. Although no significant differences are observed for the two pyrene receptors.

The kinetic stability of the adsorbed molecules was also evaluated. Due to the higher surface coverage of the GO-ER/CG electrode, these experiments were carried out with this electrode. The modified electrode was transferred to a clean electrolyte solution and was submitted to several CVs along the time. In Figure 61, the desorption behavior for molecules **11** and **21** is shown. The presence of three pyrene units in the tripodal derivative **21** allows a stronger interaction with the electrode surface and subsequently a lower desorption rate than in the case of the monopodal derivative **11**, giving a stable layer with a high surface coverage along the time.

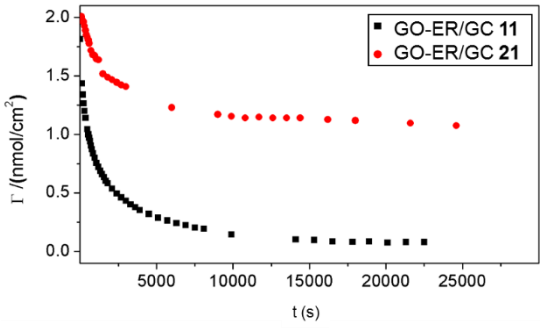

Figure 61. Surface coverage *vs.* desorption time of modified GO-ER/GC electrode by adsorption of PyexTTF **11** (black) and 3PyexTTF **21** (red) 0.36 mM/THF during 15 hours into 0.1 M TBAP/DMF.

In addition to the fundamental electrochemical characterization of the modified electrodes, the development of an enzymatic biosensor was achieved. PyexTTF/GO-ER/GC electrodes were used to prepare it, since these electrodes exhibit a higher surface coverage than the others and a better electrochemical response in aqueous media.

Horseradish Peroxidase (HRP) was immobilized by cross-linking with glutaraldehyde onto the PyexTTF/GO-ER/GC electrode. Once the enzyme was immobilized, cyclic voltammetry measurements were carried out in a 0.1 M phosphate buffer solution (PBS) (pH = 6.5) with increasing amounts of H_2O_2 (Figure 62).

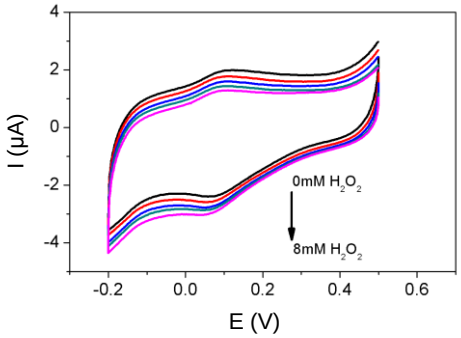

Figure 62. Cyclic voltammograms at 10 mV/s of HRP/PyexTTF/GO-ER/GC at 0.1 M PBS (pH = 6.5) at increasing amounts of H_2O_2 (from 0 mM to 8 mM).

As observed in Figure 62, the intensity of the reduction peak increases and the one of the oxidation peak decreases at higher concentrations of H_2O_2. These measurements were repeated in the absence of the enzyme and no response was obtained, meaning that PyexTTF **11** acts as electrochemical mediator. In fact, **11** is able to reduce the HRP_{ox} oxidized by H_2O_2 to HRP_{red} and the signal obtained in the measurements is the reduction of the oxidized form of the HRP enzyme.

The detection limit of the biosensor is 1.4 μM, and was obtained by electrostatic chronoamperometry (Figure 63a). Furthermore it presents a good linear response (Figure 63b) and can operate at very low potentials.

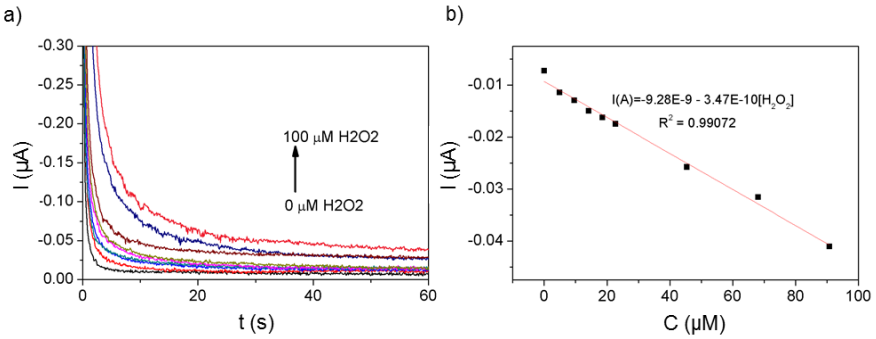

Figure 63. a) Chronoamperometry at 0.0 V of HRP/PyexTTF/GO-ER/GC at 0.1 M PBS (pH = 6.5) at increasing amounts of H_2O_2 (from 0 μM to 100 μM), c) Linear fit of current intensity chronoamperometry *vs.* H_2O_2 concentration.

These properties make HRP/PyexTTF/GO-ER/GC a good sensing platform, which could be employed in other biosensors that coupled other enzymes that generate H_2O_2 as Lactate oxidase or Glucose oxidase.

4.3. NON-COVALENT FUNCTIONALIZATION OF GRAPHENE WITH PORPHYRIN-BASED RECEPTORS

4.3.1. Porphyrins

Porphyrins are electron-donor chromophores based on a macrocyclic system with 18 π-electrons. The parent porphyrin ring, porphine (P), consists of four pyrrole rings linked by four methine bridges (Figure 64). The substitution of the pyrrole *exo*-hydrogens (*β*-pyrrolic position), the methine hydrogens (*meso* position) and the two inner NH (hydrogen bonding/metal coordination), allows to obtain a great number of porphyrin derivatives with different electronic and optical properties.

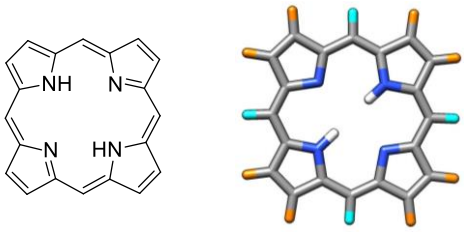

Figure 64. Porphyrin structure. *β*-pyrrolic (orange), *meso* (light blue) and inner N/NH (blue) positions.

In their absorption spectra, porphyrins present characteristic intense bands between 380 and 420 nm, known as Soret bands, and arising from π-π* transitions from the ground state to the second excited singlet state. Besides, between 500 and 650 nm appear the Q bands, less intense than the former, and originated from π-π* transitions from the ground state to the first excited singlet state. Metalloporphyrins can be differentiated from the free-base by their absorption spectra, since the metalated porphyrins present two Q bands meanwhile the free-base porphyrin has four, as a consequence of its lower symmetry.[138]

Porphyrins have been used extensively as molecular materials due to their optical and electronic properties. Particularly in the field of organic electronics, their absorption spectra in the visible range, their electron-donor character, their large conjugated π-system and their self-assembly ability, have provided interesting systems for photoinduced electron transfer and charge transport.[139]

138. M. Gouterman, *The Porphyrins*, Academic Press, New York, **1978**.
139. a) H. Imahori, T. Umeyama, K. Kurotobi, Y. Takano, *Chem. Commun.* **2012**, *48*, 4032-4045. b) T. Hasobe, *J. Phys. Chem. Lett* **2013**, *4*, 1771-1780. c) T. Umeyama, H. Imahori, *J. Phys. Chem. C* **2013**, *117*, 3195-3209.

Several remarkable examples in which porphyrins are combined with different carbon nanostructures are depicted in Figure 65 and briefly discussed in the following lines.

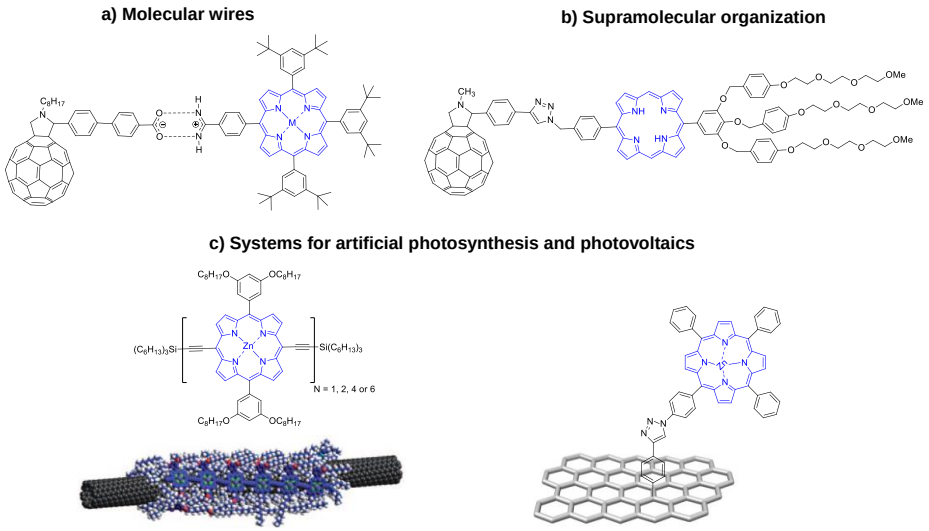

Figure 65. Porphyrin-based nanomaterials for organic electronics.

Many examples considering fullerenes and porphyrins have been explored in donor-acceptor systems. However, the concept of supramolecular wires based on these two units has recently been investigated in our research group.[140] The molecular wires are non-covalent hybrids formed by different C_{60}-*p*-phenylene oligomers with a terminal carboxylate and a zinc porphyrin bearing an amidinium moiety (Figure 65a), the interaction between the molecules is particularly stable due to the synergy between hydrogen bonds and electrostatic forces. The study of the influence of the oligomeric bridge length was accomplished by transient absorption experiments; where it was found that the photoexcitation of the porphyrin leads to an electron transfer between this one and C_{60} derivatives. In addition, charge-separation and recombination rates depend on the oligomer length, being smaller for the longer oligomers. The obtained attenuation factor (β = 0.07 ± 0.01 Å^{-1}), is one of the lowest values reported for molecular wires. Other example of charge transport in dyads formed by fullerenes and porphyrins was reported by Aida and co-workers.[141] The self-assembly of an enantiopure covalent dyad (Figure 65b) allowed to

140. S. Vela, S. Bauroth, C. Atienza, A. Molina-Ontoria, D. M. Guldi, N. Martín, *Angew. Chem. Int. Ed.* **2016**, *55*, 15076-15080.
141. Y. Hizume, K. Tashiro, R. Charvet, Y. Yamamoto, A. Saeki, S. Seki, T. Aida, *J. Am. Chem. Soc.* **2010**, *132*, 6628-6629.

obtain long nanofibers with an ambipolar charge-transport character. However, the racemic product forms spherical assemblies with a poor photocurrent response, so chirality is important in order to obtain materials able to transport charge carriers efficiently.

Porphyrins have also been used to functionalize CNTs and graphene. Anderson and co-workers developed porphyrin-CNT complexes making use of the non-covalent modification with different porphyrin oligomers.[142] UV-Vis and fluorescence studies showed the great affinity of the tetrameric and hexameric porphyrin oligomers for CNTs. Furthermore, photoluminescence excitation maps revealed a stronger binding with (8,6) and (7,5) tubes, and an energy transfer from the porphyrin oligomers to the CNTs.

On the other hand, the covalent functionalization of carbon nanostructures also allows to obtain photoactive materials. In fact, Zhang and co-workers reported the synthesis of a graphene nanoconjugated (Figure 65c) using a "click" reaction between graphene bearing phenylacetylene groups and an azide-terminated zinc porphyrin.[143] The photo-induced electron transfer properties of these nanoconjugates were studied in a photoelectrochemical cell. In these measurements, it was observed the corresponding photocurrent when the electrode was illuminated, due to the charge transfer from the porphyrin to graphene.

Inspired by these results and pyrene's ability to bind graphene, we decided to explore the preparation of mono- and tripodal pyrene-porphyrin hybrids in the search for novel non-covalent porphyrin/graphene systems.

4.3.2. Synthesis of porphyrin-pyrene conjugates

In order to accomplish the non-covalent functionalization of FLG, we designed similar receptors to those of the π-exTTF family presented in the previous section (Figure 66). Furthermore, we carried out the synthesis of the free-base porphyrins and those incorporating Ni and Zn metals.

142. J. K. Sprafke, S. D. Stranks, J. H. Warner, R. J. Nicholas, H. L. Anderson, *Angew. Chem. Int. Ed.* **2011**, *50*, 2313-2316.
143. H.-X. Wang, K.-G. Zhou, Y.-L. Xie, J. Zeng, N.-N. Chai, J. Li, H.-L. Zhang, *Chem. Commun*. **2011**, *47*, 5747-5749.

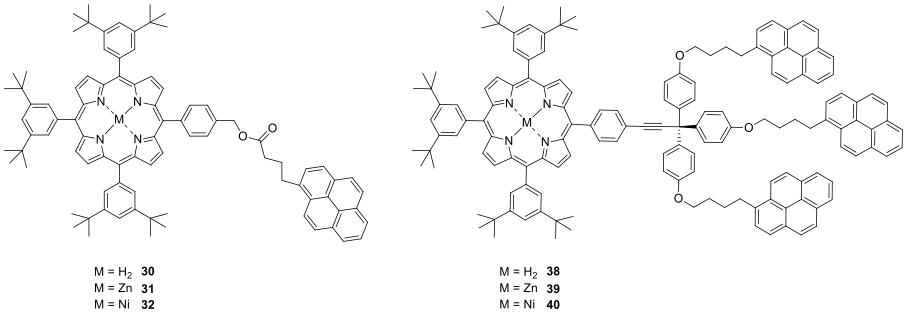

Figure 66. Structure of the pyrene-porphyrin derivatives designed for the non-covalent functionalization of FLG.

In a first step, it is necessary to synthesize the porphyrin derivatives with an asymmetrical pattern in their meso positions. In both cases, we have carried out a statistical condensation under Lindsey conditions; pyrrole with two different aldehydes in 4:3:1 ratio; to obtain the A_3B porphyrins (Scheme 5).[144] In this reaction, the six possible regioisomers are obtained and this is the reason of the low yields generally obtained.

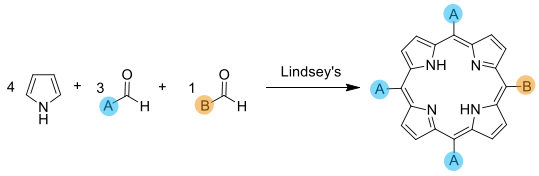

Scheme 5. Synthesis of A_3B porphyrin by Lindsey's methodology.

The 3,5-di-*tert*-butylbenzaldehyde **24** (A-CHO) was synthesized from 3,5-di-*tert*-butyltoluene **22** by radicalic halogenation to yield 3,5-di-*tert*-butyl(bromomethyl)benzene **23**, that was subsequently oxidized with hexamethylenetetramine (HMTA), following the previously described procedure in the bibliography (Scheme 6).[145]

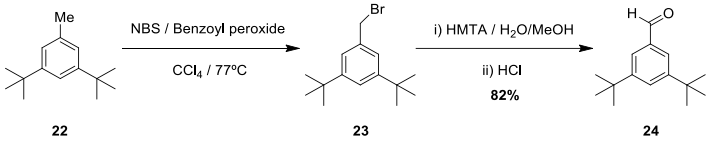

Scheme 6. Synthesis of 3,5-di-*tert*-butylbenzaldehyde **24** (A-CHO).

144. a) J. S. Lindsey, I. C. Schreiman, H. C. Hsu, P. C. Kearney, A. M. Marguerettaz, *J. Org. Chem.* **1987**, *52*, 827-836. b) P. D. Rao, S. Dhanalekshmi, B. J. Littler, J. S. Lindsey, *J. Org. Chem.* **2000**, *65*, 7323-7344.
145. M. J. Plater, S. Aiken, G. Bourhill, *Tetrahedron* **2002**, *58*, 2405-2413.

As B-CHO components, it was necessary to prepare two different aldehydes for the synthesis of the monopodal or tripodal systems, respectively.

The synthesis of pyrene derivative **27** was carried out by two synthetic steps (Scheme 7).

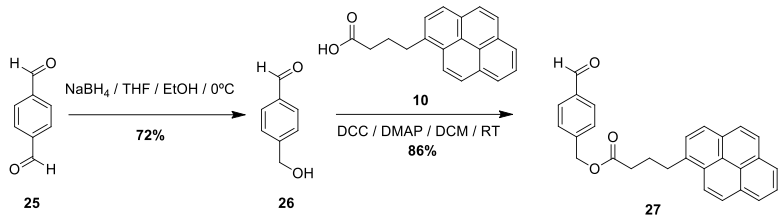

Scheme 7. Synthesis of compound **27** (B-CHO) for the monopodal systems.

The reduction of one of the aldehydes of terephthalaldehyde allowed to obtain 4-hydroxymethylbenzaldehyde **26**,[146] whose posterior reaction with 4-(1-pyrenyl)butyric acid **10** in the presence of DCC and DMAP provided the desired compound.

For the synthesis of the tripodal porphyrins **38**-**40**, it was necessary to synthesize a tripodal B-CHO component (Scheme 8). Aldehyde **34** was obtained by a Sonogashira coupling between 4-iodobenzaldehyde (**33**) and the alkyne **13**[129] in the presence of $Pd(PPh_3)_4$ as catalyst, CuI and Et_3N.

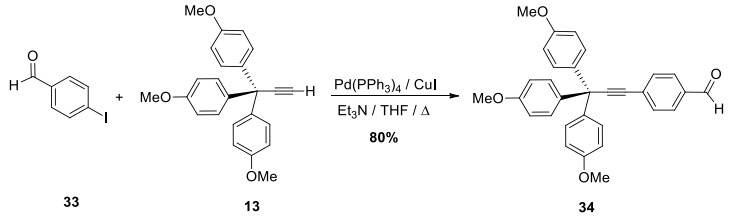

Scheme 8. Synthesis of aldehyde **34** (B-CHO) for the tripodal systems.

The complete synthesis of the free-base porphyrins **30** and **35** is depicted in Scheme 9.

146. N. M. Loim, E. S. Kelbyscheva, *Russ. Chem. Bull.* **2004**, *53*, 2080-2085.

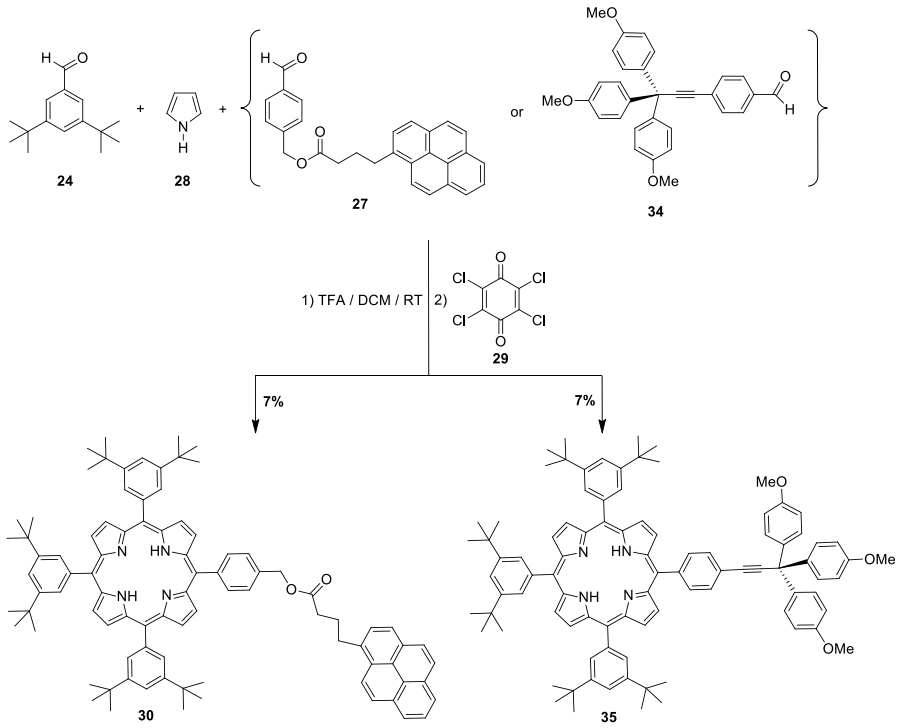

Scheme 9. Synthesis of A_3B porphyrins **30** and **35**.

The mixture of 3,5-di-*tert*-butylbenzaldehyde **24**, pyrrole **28** and aldehyde **27** or **34** in the presence of TFA, and its posterior treatment with *p*-chloranil **29**, led to the free base porphyrins **30** and **35** in moderate yields.

The treatment of porphyrin **30** with the acetate salts of Zn or Ni afforded the metalloporphyrins **31** and **32** (Scheme 10) in excellent yields, following a similar procedure to those previously described in the bibliography.[147]

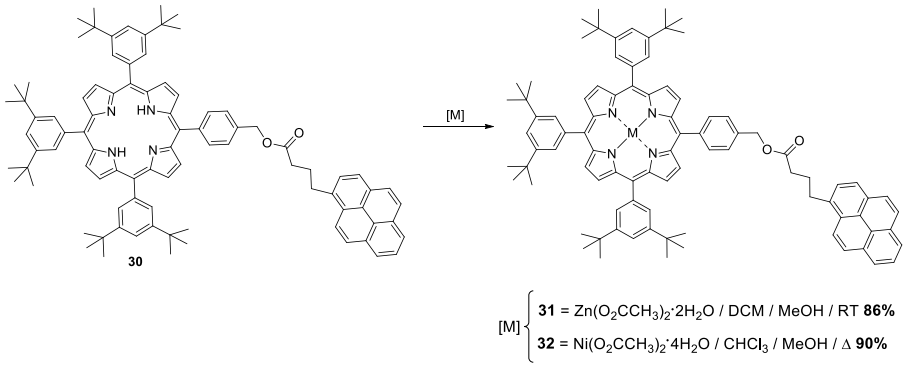

Scheme 10. Synthesis of final products **31** and **32**.

147. R. Kumar, M. Sankar, *Inorg. Chem.* **2014**, *53*, 12706-12719.

From the ^{1}H-NMR spectra of the pyrene-porphyrin derivatives, it can be observed that the synthesis of these three molecules was achieved successfully. The three compounds present similar signals in all the spectra, at around 9.04-8.73 ppm appear the β-pyrrolic protons and between 8.4-7.6 ppm the aromatic signals of the pyrene and benzene rings. Besides, the signals corresponding to the methylene group of the ester at ca. ~ 5.5 ppm, the alkyl chain (3.58-2.29 ppm) and the *tert*-butyl groups (at around 1.5 ppm) are observed, which implies that the condensation between the two aldehydes (**24** and **27**) and the pyrrole **28** took place.

The evidence for the metalation in compounds **31** and **32** is the disappearance of the upfield signal at -2.68 ppm corresponding to the internal NH protons of the free base porphyrin. As an example, the ^{1}H-NMR of molecule **31** is shown in Figure 67.

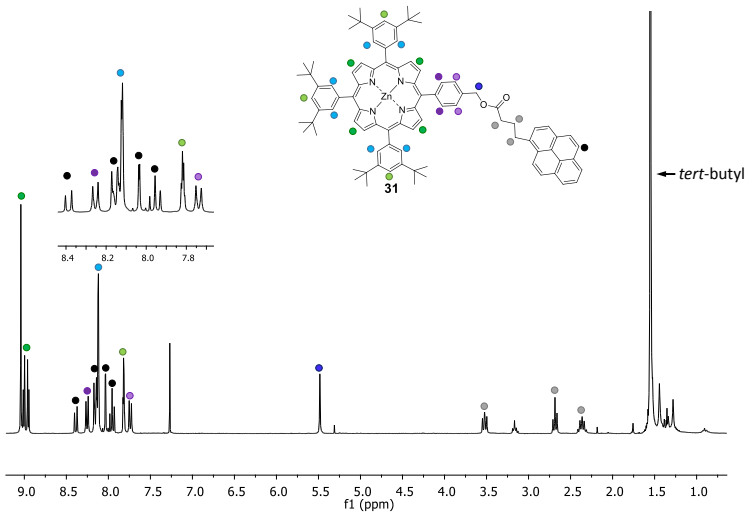

Figure 67. ^{1}H-NMR ($CDCl_3$, 300 MHz, 298 K) of **31**. Representative signals are depicted by colored bullets.

The treatment of porphyrin **35** with boron tribromide yielded the corresponding deprotected porphyrin **36** quantitatively. Its deprotonation in the presence of K_2CO_3 led to the phenoxide anion that by a nucleophilic attack to 1-(4-bromobutyl)pyrene (**37**)[148] afforded the final 3PyH$_2$P product **38**. The metalloporphyrins, 3PyZnP **39** and 3PyNiP **40**, were obtained by the reaction of **38** with the acetate salts of Zn or Ni.

148. A. V. Safronov, N. I. Shlyakhtina, T. A. Everett, M. R. VanGordon, Y. V. Sevryugina, S. S. Jalisatgi, M. F. Hawthorne, *Inorg. Chem.* **2014**, *53*, 10045-10053.

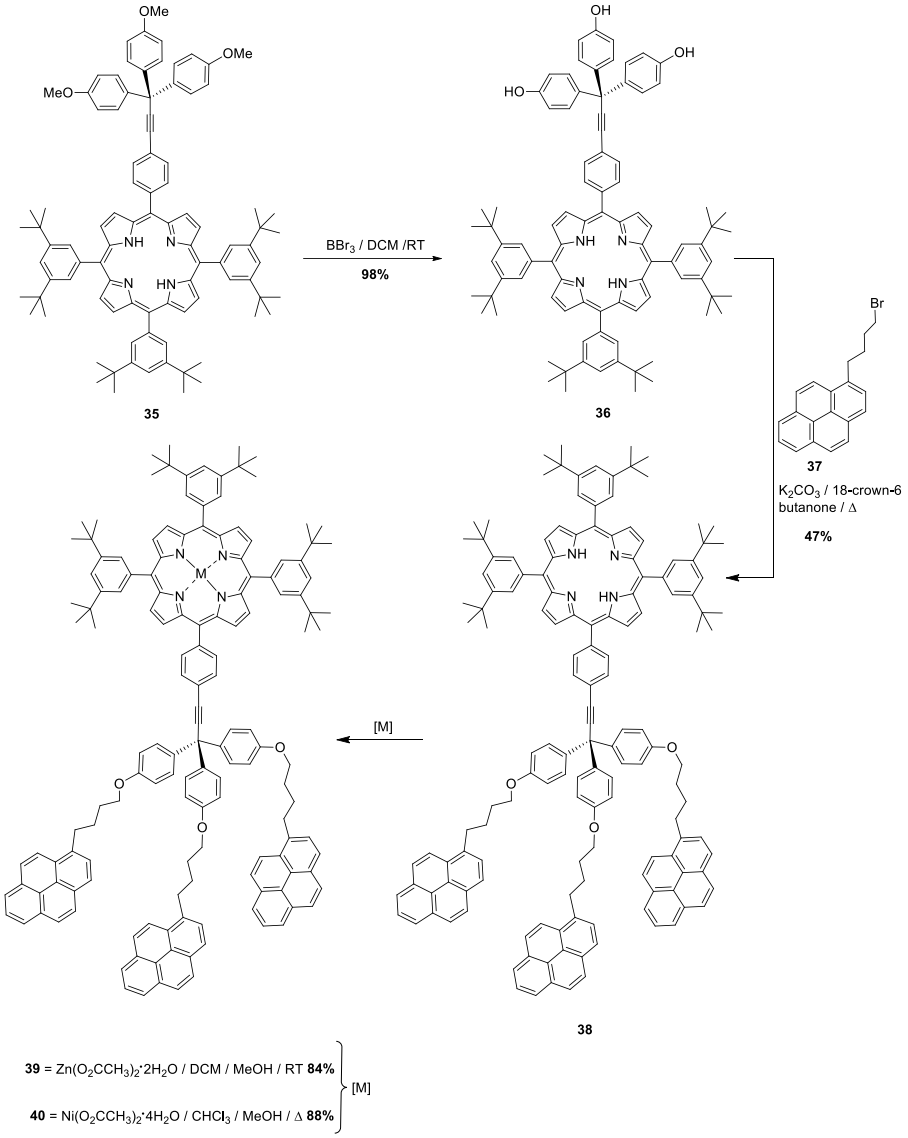

Scheme 11. Synthesis of tripodal porphyrin derivatives **38**, **39** and **40**.

All products were satisfactorily characterized by the standard analytical and spectroscopic techniques. As in the monopodal series, the ^{1}H-NMR spectra for the three final molecules are very similar, the most remarkable difference being the presence or the absence of the signal at -2.70 ppm corresponding to the internal NH protons (as a result of the ring current effect of the aromatic porphyrin ring). In Figure 68, the ^{1}H-NMR spectrum of **38** is shown as representative example.

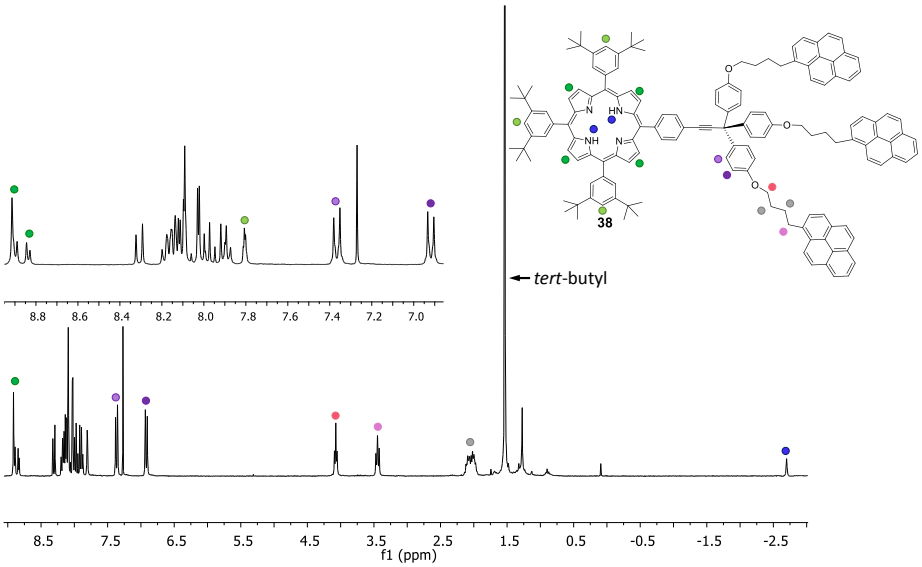

Figure 68. ^{1}H-NMR ($CDCl_3$, 300 MHz, 298 K) of **38**. Representative signals are depicted by colored bullets.

Once that the target molecules were synthesized, it was studied if these systems were able to self-assemble in solution. For this reason ^{1}H-NMR studies at variable concentration were carried out with PyZnP **31** as model system (Figure 69). The study was performed starting from a concentrated solution of **31** (40 mM) that was diluted a 50% and subsequently diluted another 50%. For each dilution the spectrum was recorded.

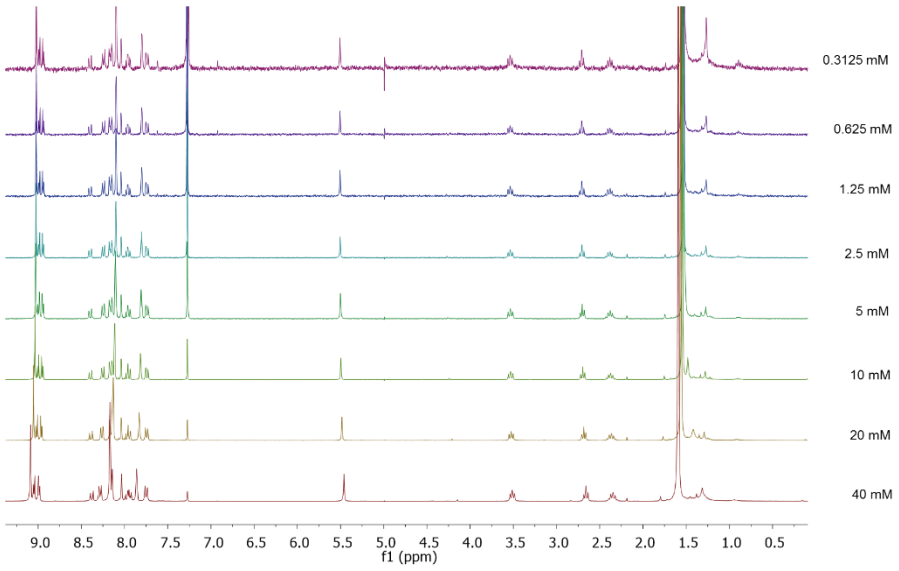

Figure 69. ^{1}H-NMR spectra ($CDCl_3$, 300 MHz, 298 K) of **31** at variable concentration.

As the concentration increases, all the signals present a slight shielding and broadening. In the aromatic region it can be observed that the β-pyrrolic protons are shifted downfield and the pyrene signals have the opposite behavior (Figure 70). In this last set of signals, the broadening is more evident.

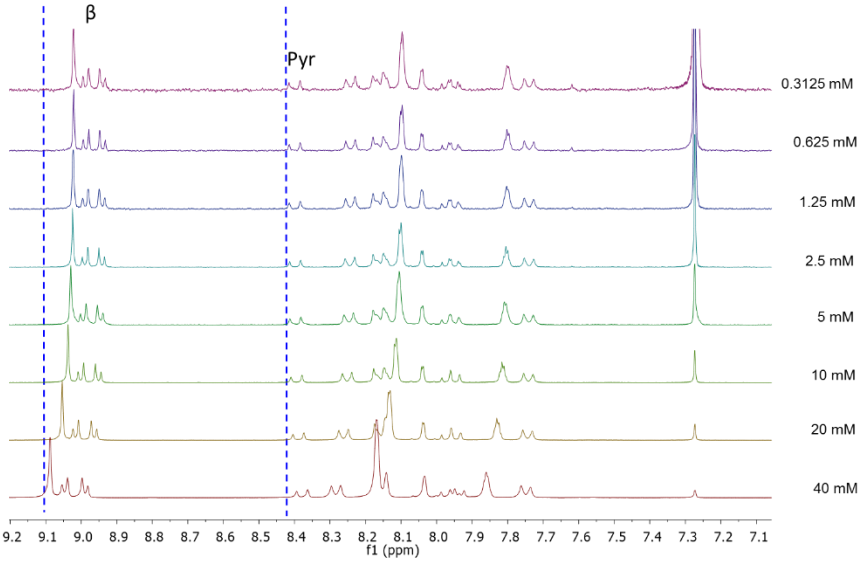

Figure 70. Partial ^{1}H-NMR spectra (300 MHz, 298 K) in $CDCl_3$ of the aromatic region of system **31**.

In Figure 71 are shown the signals corresponding to the methylene group, the alkyl chain and the *tert*-butyl groups of porphyrin **31**. All set of signals experience small shifts with the concentration increase, although the *tert*-butyl groups shift in the opposite direction to the other signals (downfield *vs.* upfield).

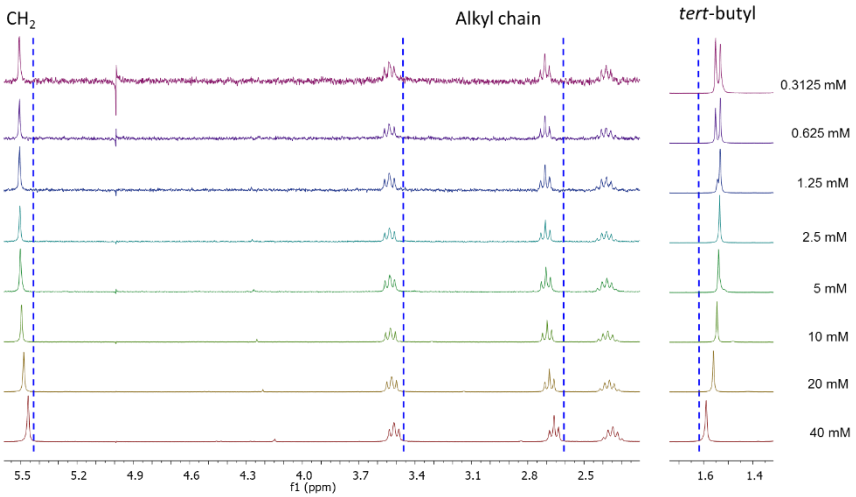

Figure 71. Partial ^{1}H-NMR spectra (300 MHz, 298 K) in $CDCl_3$ of the aliphatic region of systems **31**.

When the chemical shift of the signals is represented *vs*. concentration, for example the β-pyrrolic and *tert*-butyl protons (Figure 72), it can be observed a clear linear tendency. This behavior suggests a weak interaction between the molecules, but the working range of concentrations in ^{1}H-NMR does not allow to carry out more in depth investigations.

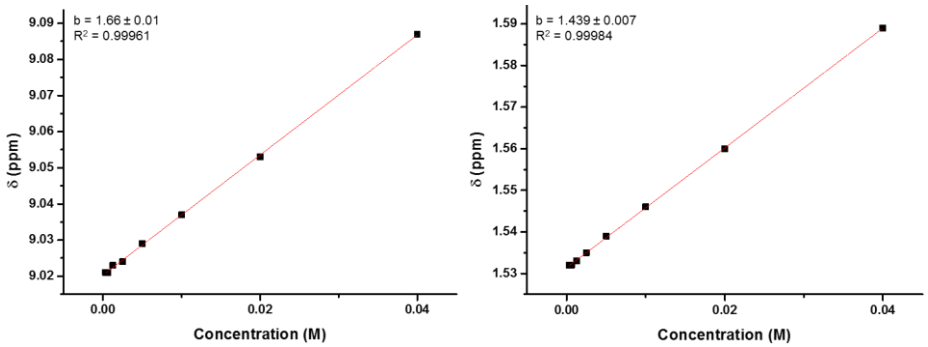

Figure 72. Concentration *vs.* chemical shift for the β-pyrrolic (left) and the *tert*-butyl (right) protons of system **31**.

The characterization of the pyrene-porphyrin series by UV-Vis spectroscopy and cyclic voltammetry allowed to investigate the opto-electronic properties of these molecules and to estimate the band-gap (energetic difference between HOMO and LUMO orbitals) for each system. The UV-Vis spectra of the two different families, the monopodal porphyrins (**30**-**32**) and the tripodal porphyrins (**38**-**40**) are shown in Figure 73.

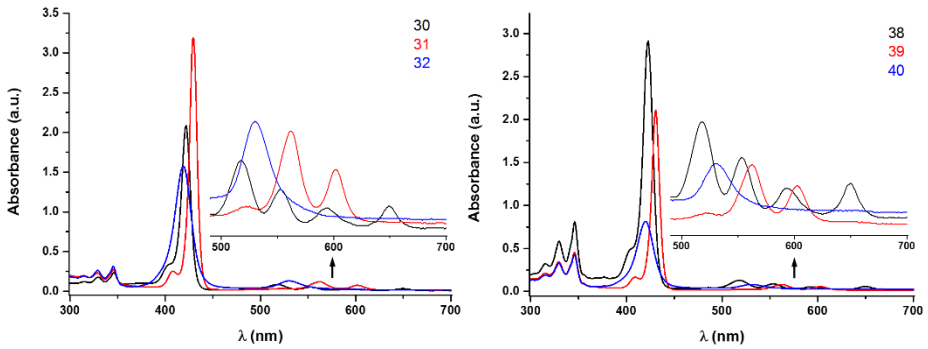

Figure 73. Left: UV-Vis spectra of compounds **30**, **31** and **32**. Right: UV-Vis spectra of compounds **38**, **39** and **40**.

As it was discussed above, the presence of the metal modifies the optical and electronic properties of porphyrins. When Zn is the central atom of the structure, the Soret band (429 nm) is red shifted around 7 nm compared to the free-base porphyrin (422 nm). The number of Q bands is also modified

decreasing from four to two respect to the free base porphyrin. In the case of Ni, the Soret band is blue shifted 3 nm and only one Q band is observed.

In spite of the different structure of the monopodal or tripodal series of molecules, there is not a great variation in the optical characteristics of the porphyrins **30**-**32** *vs.* **38**-**40** (Table 3).

From the onset of the spectra (lowest energy absorption), the optical band-gap can be estimated considering that band-gap (eV) ≈ 1240 / onset (nm).[149] The value for these compounds is comprised between 1.84 and 2.02 eV (Table 3).

Table 3. Summary of the optical properties of compounds **30**-**32** and **38**-**40** obtained from the UV-Vis spectra in NMP.

Compound	Soret Band (nm)	Onset (nm)	Band-gap (eV)
30	422	672	1.85
31	429	629	1.97
32	419	615	2.02
38	423	675	1.84
39	431	632	1.96
40	420	614	2.02

The electrochemical characterization of the two pyrene-porphyrin series was carried out by cyclic voltammetry (CV) measurements in *o*-DCB/CH_3CN. For all systems, two quasi-reversible one electron reductions are observed for porphyrins, while two quasi-reversible one electron oxidations are only clearly seen for PyZnP **31**. In addition, the pyrene irreversible oxidation is also discernible in all systems when scanned up to + 1.0 V, being the current intensity of this wave greater for the tripodal derivatives (**38**-**40**) because of the three pyrene units present in them (Figure 74).

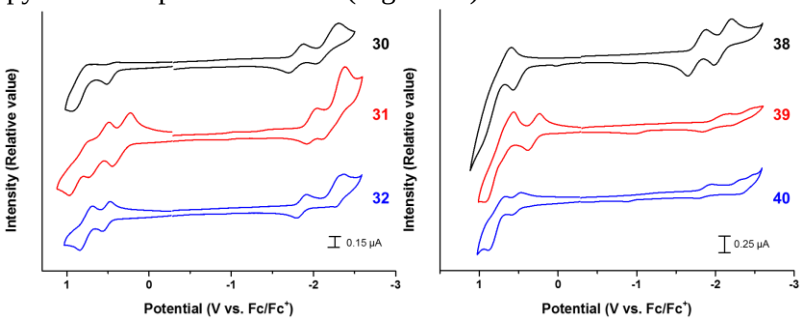

Figure 74. Cyclic voltammograms of **30**-**32** (left) and **38**-**40** (right), obtained in *o*-DCB/CH_3CN (5/1) solutions containing 0.1 M $TBAPF_6$ and using $Ag/AgNO_3$ as reference electrode, glassy carbon as working electrode and a Pt wire as counter electrode. Scan rate: 100 mV/s.

149. S. Yang, L. Dunsch, *J. Phys. Chem. B* **2005**, *109*, 12320-12328.

The values of the half-wave potentials ($E^{1/2} = (E^{pa}+E^{pc})/2$, where E^{pa} and E^{pc} are the anodic and cathodic peaks, respectively) and the HOMO-LUMO gap ($\Delta E_{gap} = E^{1/2}{}_{ox,1} - E^{1/2}{}_{red,1}$) for each compound are summarized in Table 4. It has to be noticed that for both families of compounds, the donor-acceptor behavior is similar, being the Zn derivatives (**31** and **39**) the ones with a better donor ability, and with poorer acceptor properties (harder to reduce). The free base porphyrins (**30** and **38**) are the best acceptor compounds of the series due to their more accessible reduction potentials and the Ni systems (**32** and **40**) are the weakest's donors of each series.

The HOMO-LUMO gaps obtained by electrochemistry are in accordance to those obtained from absorption spectroscopy.

Table 4. Summary of the electrochemical data for compounds **30**-**32** and **38**-**40** (*o*-DCB/CH_3CN *vs.* Fc/Fc^+).

Compound	$E^{1/2}{}_{ox,1}$ (mV)	$E^{1/2}{}_{ox,2}$ (mV)	$E^{1/2}{}_{red,1}$ (mV)	$E^{1/2}{}_{red,2}$ (mV)	ΔE_{gap} (V)
30	496	842	-1769	-2128	2.27
31	309	663	-1985	-2279	2.29
32	505	782	-1843	-2302	2.35
38	496	781	-1784	-2113	2.28
39	301	759	-1971	-2287	2.27
40	532	800	-1861	-2255	2.39

4.3.3. Study of the solution interactions between porphyrin derivatives and FLG

Before carrying out the non-covalent functionalization of FLG with the porphyrin derivatives, UV-Vis titrations were accomplished to determine the potential interactions between FLG and the monopodal and tripodal porphyrin derivatives. In order to confirm that all the changes observed in the titrations are not due to dilution, control experiments have been carried out in all of them.

Firstly, the UV-Vis titrations were achieved with symmetric porphyrin reference samples, to investigate if their large aromatic systems were able to interact with the basal plane of FLG.

When increasing amounts of FLG are added to a solution of the study molecule, spectral changes are noticed. The absorption of the Soret band at 419 nm decreases and two pseudo-isosbestic points appear at 405 and 432 nm, respectively. These changes suggest an interaction between the porphyrin and

FLG. It has to be noticed that the same behavior was observed for all the symmetric porphyrins (free base, Zn and Ni), in spite of only the titration experiments for the Ni porphyrin are shown (Figure 75).

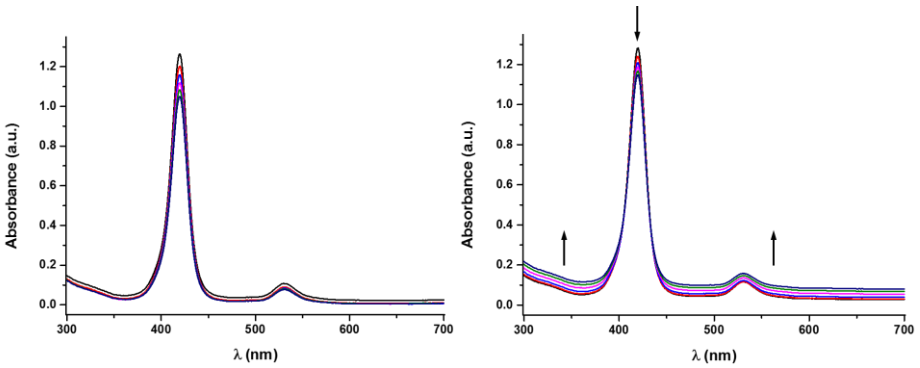

Figure 75. UV-Vis spectra obtained during the dilution (left) and titration (right) with FLG of a symmetric Ni porphyrin ($5.53 \cdot 10^{-6}$ M). Each addition corresponds to 50 µL.

Right after, these same studies were carried out with the monovalent (**30**-**32**) and tripodal (**38**-**40**) porphyrin derivatives.

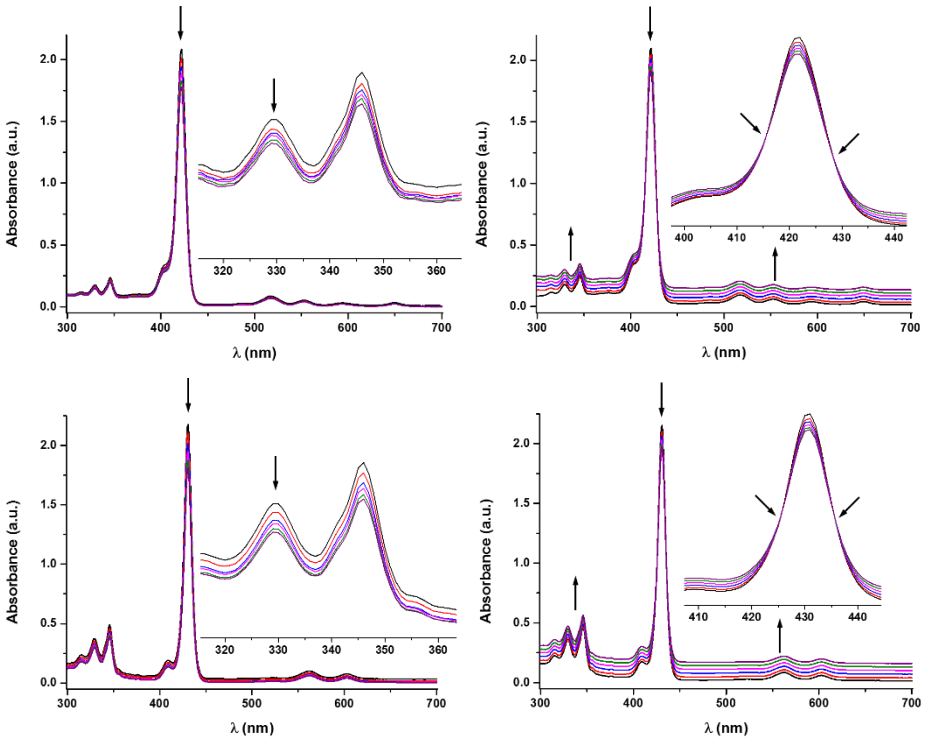

Figure 76. Upper: UV-Vis spectra obtained during the dilution (left) and titration (right) with FLG of PyH_2P **30** ($6.07 \cdot 10^{-6}$ M). Lower: UV-Vis spectra obtained during the dilution (left) and titration (right) with FLG of 3PyZnP **39** ($3.36 \cdot 10^{-6}$ M). Each addition corresponds to 50 µL.

In Figure 76, the UV-Vis titrations for systems **30** and **39** are shown. For both molecules it is observed that the absorption of the Soret band decreases with the addition of FLG. Moreover, in the two cases, two pseudo-isosbestic points appear at 415 and 428 nm for **30** and at 425 and 436 nm for **39**, respectively. These changes in the spectra during the measurements and the presence of the isosbestic points, suggest an interaction between the molecules and FLG and the existence of an equilibrium process for this interaction.[84,89] The same trend was observed for the other compounds of each family.

On the other hand, in collaboration with the group of Prof. D. M. Guldi at Erlangen-Nürnberg University, preliminary transient absorption measurements have been carried out.

For these measurements, the synthesis of the supramolecular complexes **3**-**8** (Figure 80) was performed by a sequential enrichment of a solution of the porphyrin derivatives (**30**-**32** and **38**-**40**) in THF with graphite. This dispersion was sonicated and centrifuged, and subsequently new graphite was added. Finally, a centrifugation step was applied in order to separate the unexfoliated graphite and the instable material from the stable supernatant.

In the case of complexes **3**-**5**, transient absorption measurements were performed for all of them at an excitation wavelength of 387 nm. In the case of PyH_2P/FLG and PyNiP/FLG (complexes **3** and **5**), the global analysis performed with Glotaran[150] yielded no signs of an electron transfer reaction between the porphyrin and the basal plane of graphene. For PyZnP/FLG (**complex 4**), the transient absorption spectra showed, in comparison with the pure molecule, features of the porphyrin cation signature in the region from 600 to 800 nm (Figure 77).

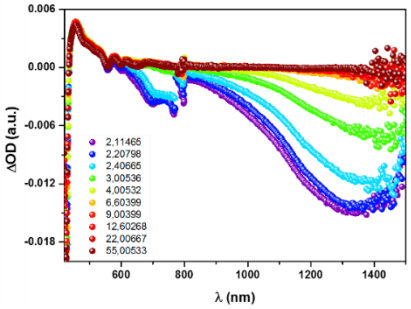

Figure 77. Transient absorption spectra of **complex 4** in THF and at an excitation wavelength of 387 nm (time steps in ps are showed in the scale bar).

150. J. J. Snellenburg, S. P. Laptenok, R. Seger, K. M. Mullen, I. H. M. van Stokkum, *J. Stat. Soft.* **2012**, *49*, 1-22.

This can be visualized by comparing the transient absorption spectra at 4 ps of both, PyZnP **31** and PyZnP/FLG (**complex 4**), with the cation absorption signature obtained by applying a voltage of 0.4 V and the global fit of the hybrid. (Figure 78, left). These spectra reveal that **complex 4** differs greatly in its absorption features compared to **31**. On the other hand, it resembles nicely the cation signature obtained by spectroelectrochemistry (SEC), meaning that the electron transfer from the porphyrin moiety to graphene takes place. In Figure 78 (right) are depicted the population diagrams of the different states. As it can be observed, the charge separation happens within a few picoseconds, while the charge recombination appears in the range of a few hundred picoseconds. The regular singlet and triplet features correspond to the times of PyZnP **31** (around 2 ns and over 8 ns exceeding the time range for these type of measurements).

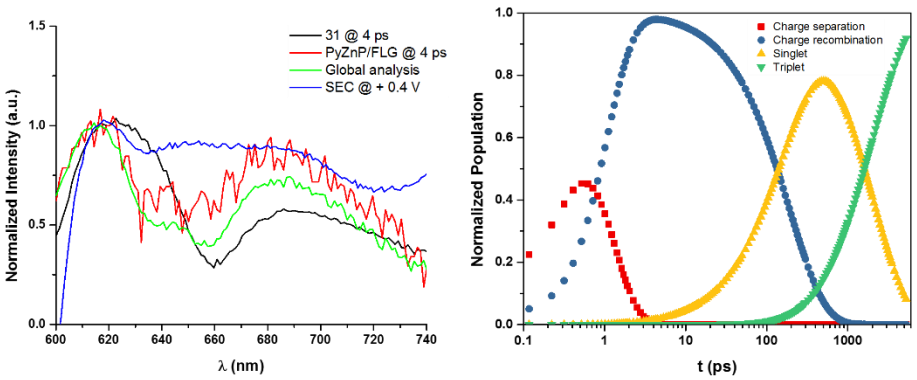

Figure 78. Left: transient absorption spectra at 4 ps of **31** (black), **complex 4** (red), the global analysis fit attributed to the charge separated state (green) and SEC (blue) in THF. Right: Population of the charge separation (red), charge recombination (blue), singlet (yellow) and triplet (green) states.

For complexes **6**-**8**, in the transient absorption measurements there is no sign of any cation features. As example in Figure 79 are depicted the transient absorption spectra at different time delays of 3PyH$_2$P **38** and 3PyH$_2$P/FLG (**complex 6**), no noticeable difference is observed between both spectra, which implies that no charge transfer reaction occurs in this case. A similar behavior is observed for the other two complexes. These results might be due to the longer distance existing between the porphyrin unit in the tripodal derivatives and the basal plane of graphene.

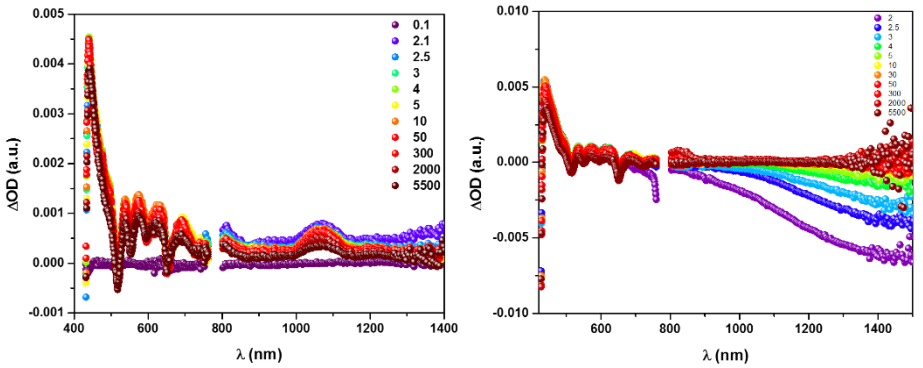

Figure 79. Transient absorption spectra of 3PyH$_2$P **38** (left) and **complex 6** (right) in THF, obtained upon femtosecond flash photolysis (387 nm) with different time delays.

4.3.4. Synthesis of non-covalent FLG/porphyrin hybrids

The FLG/pyrene-porphyrin supramolecular complexes were synthesized following the same procedure previously used for the π-exTTF-based family (see experimental section for details). After the anchoring of the pyrene receptors to FLG under sonication, the complexes were isolated by filtration on PTFE membranes and extensive washing (Figure 80).

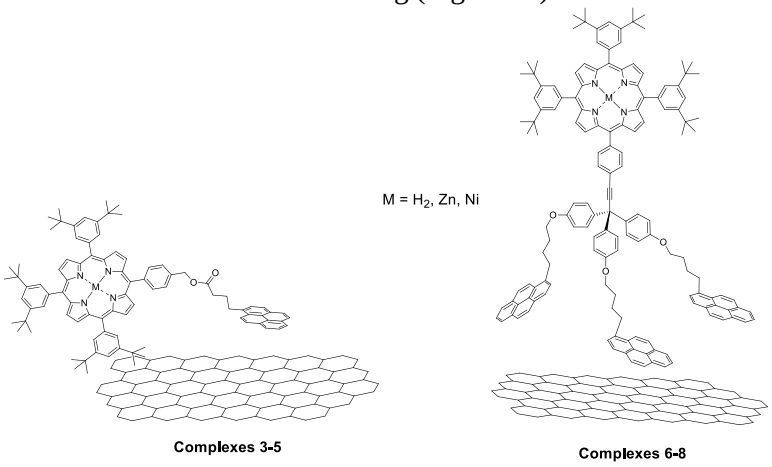

Figure 80. Supramolecular FLG/pyrene-porphyrin hybrids.

Due to the strong characteristic absorption of the Soret band, it is easy to determine if the non-covalent functionalization of FLG with the porphyrin derivatives has been achieved successfully by UV-Vis spectroscopy.

In Figure 81, the spectra of the starting FLG, the PyNiP **32** and the supramolecular **complex 5** are shown. For this later, it can be observed the graphene absorption pattern and the Soret band of the Ni porphyrin at 419 nm,

which implies that the modification has taken place. For the other two porphyrin compounds, **30** and **31**, the spectra of the complexes **3** and **4** present similar characteristics, with no appreciable shifts of the Soret bands when compared to those of the molecular precursors.

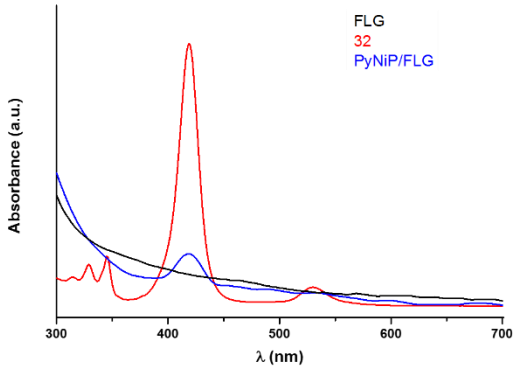

Figure 81. UV-Vis spectra of FLG, PyNiP **32** and **complex 5** in NMP.

The non-covalent functionalization of FLG with tripodal derivatives **38**, **39** and **40**, provided very similar conclusions after analysis of the UV-Vis spectra. As an example, the spectrum of **complex 6** is presented in Figure 82. Again, the Soret band of the porphyrin can be observed at 423 nm, demonstrating the successful modification of FLG.

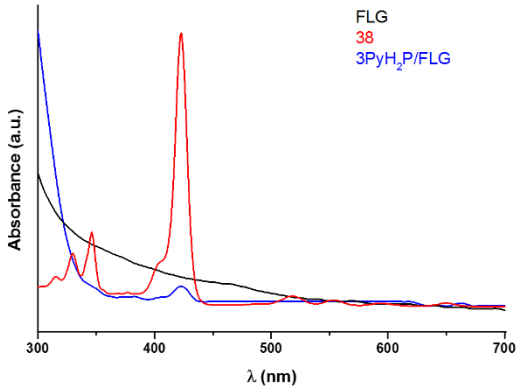

Figure 82. UV-Vis spectra of FLG, $3PyH_2P$ **38** and **complex 6** in NMP.

It is not strange that the bands corresponding to pyrene are not observed in all these cases, considering their lower intensity in comparison with the Soret band.

Thermogravimetric analysis provides insights onto the stability of the formed complexes and the functionalization degree. FLG is thermally stable when heated up to 900 °C in an inert atmosphere. Samples of FLG after the anchoring of the monopodal or tripodal porphyrin molecules showed a weight loss

between 300-600 °C, with a small increase of the temperature decomposition maxima, whereas the molecular precursors present maxima, in their first derivative curves, at around 460 °C, that matches with the desorption in the supramolecular complexes. As an example, in Figure 83 are shown the TGA curves of the FLG, PyNiP **32** and PyNiP/FLG (**complex 5**).

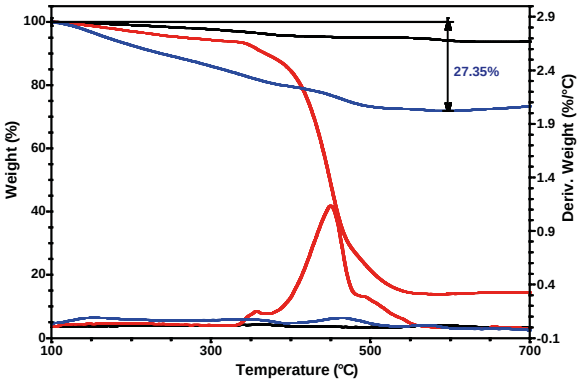

Figure 83. TGA weight loss and first derivative curves under inert conditions of FLG (black), PyNiP **32** (red) and **complex 5** (blue).

When complexes formed by porphyrin derivatives with the same central atom are compared, the weight loss for the hybrids of the tripodal derivatives is slightly higher (Figure 84). **Complex 3** undergoes a 21% weight loss, which corresponds to an approximate ratio of 1 PyH_2P **30** per 390 carbon atoms. For **complex 6**, the weight loss is around 24%, meaning that there is 1 $3PyH_2P$ **38** per 529 carbon atoms, approximately. The lower functionalization degree of **complex 6** can be attributed to the greater size of the tripodal compound.

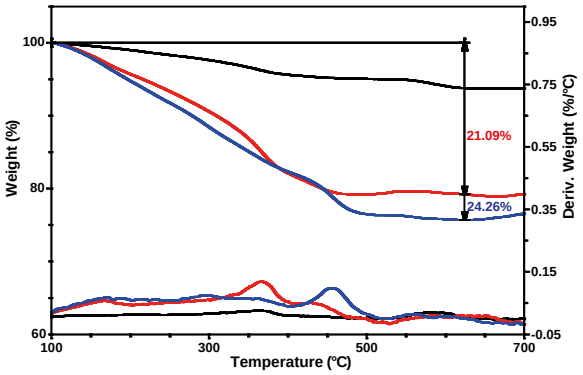

Figure 84. TGA weight loss and first derivative curves under inert conditions of FLG (black), **complex 3** (red) and **complex 6** (blue).

In order to investigate the quality of the FLG supramolecular complexes and their electronic characteristics compared with the pristine material, **complexes 3-8** were studied by Raman spectroscopy. In the monopodal pyrene-porphyrin supramolecular hybrids (Figure 85), the G band is shifted to lower frequencies for all new materials when compared with FLG. This shift is of 12, 8 and 5 cm^{-1} for **complex 3**, **complex 5** and **complex 4**, respectively.

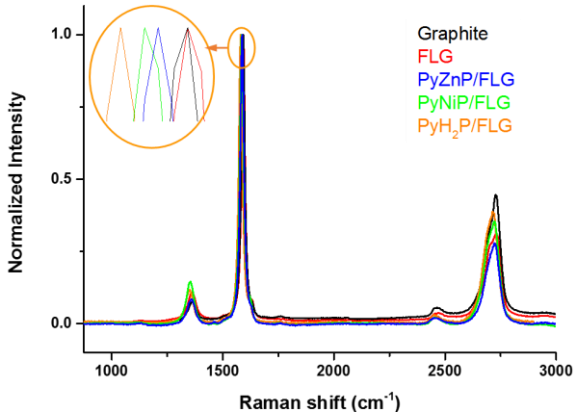

Figure 85. Raman spectra (λ_{exc} = 532 nm) of graphite, FLG and complexes **3-5**.

This behavior can be related with the electronic characteristics of the pyrene-porphyrin molecules and could be explained by the difference in energy between the Fermi level of FLG and the LUMO orbitals of the molecular receptors. The work function of graphene is about 4.5 eV,[23] and the LUMO energies of the monopodal porphyrins **30-32** *vs.* vacuum can be estimated from the first reduction potential in the CV using the expression: E_{LUMO} = -5.1 eV - E_{CV} *vs.* (Fc/Fc^+) (Table 5).[151]

As it can be observed, the greater shift of the G band corresponds with the lower ΔE between FLG and PyH_2P **30**, which suggests a smaller loss in the exciton energy and a higher transference. Whereas the smallest shift is found for PyZnP/FLG (**complex 4**), whose LUMO orbital is located further, being the loss in the exciton energy bigger and, therefore, the transference decreases.[152]

151. G. Sforazzini, E. Orentas, A. Bolag, N. Sakai, S. Matile, *J. Am. Chem. Soc.* **2013**, *135*, 12082-12090.
152. a) C. X. Guo, H. B. Yang, Z. M. Sheng, Z. S. Lu, Q. L. Song, C. M. Li, *Angew. Chem. Int. Ed.* **2010**, *49*, 3014-3017. b) H. Xin, S. Subramaniyan, T.-W. Kwon, S. Shoaee, J. R. Durrant, S. A. Jenekhe, *Chem. Mater.* **2012**, *24*, 1995-2001.

Table 5. Summary of the E_{LUMO} values for compounds **30**-**32** and estimated differences in energy between graphene's work function and LUMO orbitals.

Compound	$E^{1/2}_{red,1}$ (V)	E_{LUMO} (eV)	ΔE (eV)
30	-1.769	-3.331	1.169
31	-1.985	-3.115	1.385
32	-1.843	-3.257	1.243

In the case of the supramolecular nanohybrids built from the tripodal compounds, the shift of the G band does not follow a tendency related with the electronic characteristics of the molecular receptors. The shift for **complex 7** and **8** is 8 cm^{-1}, while for the **complex 6** is 6 cm^{-1} (Figure 86). The results suggest that the porphyrin's nature has no influence on the interactions between FLG and the tripodal pyrene-porphyrin systems. The presence of the pyrene units seem to provoke the G frequency doping by π-π stacking forces regardless the presence of electro-donating groups in the receptor structure.

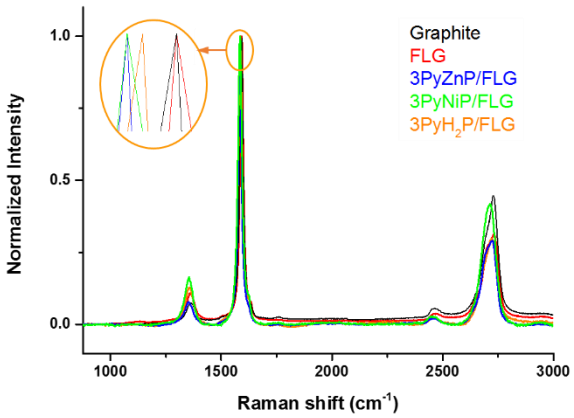

Figure 86. Raman spectra (λ_{exc} = 532 nm) of graphite, FLG and complexes **6**-**8**.

In this sense, it is known that pyrene units tend to interact with carbon surfaces and their derivatives suffer an oxidative electropolymerization reaction, which can be used for its adsorption onto these surfaces.[153] For this reason, consecutive cyclic voltammograms were recorded with a glassy carbon electrode for all porphyrin derivatives, allowing, in a certain way, to shed light on the interaction between these systems and FLG.

153. a) A. Le Goff, B. Reuillard, S. Cosnier, *Langmuir* **2013**, *29*, 8736-8742. b) M. Kohmoto, H. Ozawa, L. Yang, T. Hagio, M. Matsunaga, M.-a. Haga, *Langmuir* **2016**, *32*, 4141-4152.

In Figure 87, the consecutive cyclic voltammograms for PyNiP **32** and 3PyH_2P **38** are shown, revealing that both behaviors are very different. In the case of the monovalent derivative all the peaks can be observed, whereas the adsorption of the molecule takes place. However, for the tripodal compound, the redox peaks corresponding to the porphyrin disappear with the same number of scans. These results suggest that during the adsorption of the tripod, the porphyrin unit is located far from the electrode and the electron transfer associated with its redox processes is not observed. In the case of the monopodal derivative, in spite of the adsorption, the porphyrin unit remains near to the electrode, which allows the diffusion of the electrons.

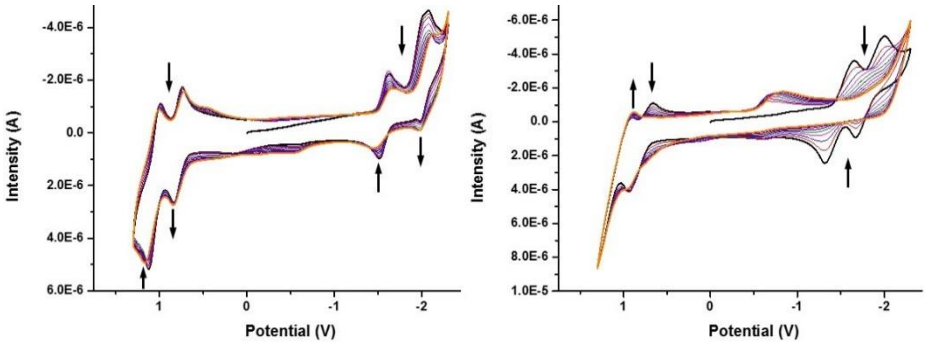

Figure 87. Consecutive cyclic voltammograms of **32** (left) and **38** (right), obtained in *o*-DCB/CH_3CN (5/1) solutions containing 0.1 M $TBAPF_6$ and using $Ag/AgNO_3$ as reference electrode, glassy carbon as working electrode and a Pt wire as counter electrode. Scan rate: 100 mV/s.

These findings could explain the difference in the Raman spectra for all the nanohybrids, since the porphyrin unit is far from the surface in the tripodal derivatives and their interaction with the basal plane of graphene takes place through the pyrene units.

Finally, by TEM analysis it was confirmed that graphene remains partially exfoliated after the non-covalent functionalization with the porphyrin derivatives. In Figure 88 are shown representative images for **complex 4** and **complex 7**. In both cases large graphene sheets are observed. However, the re-aggregation and unordered restacking of the solution well exfoliated FLG/supramolecular complexes, happens upon solvent evaporation.

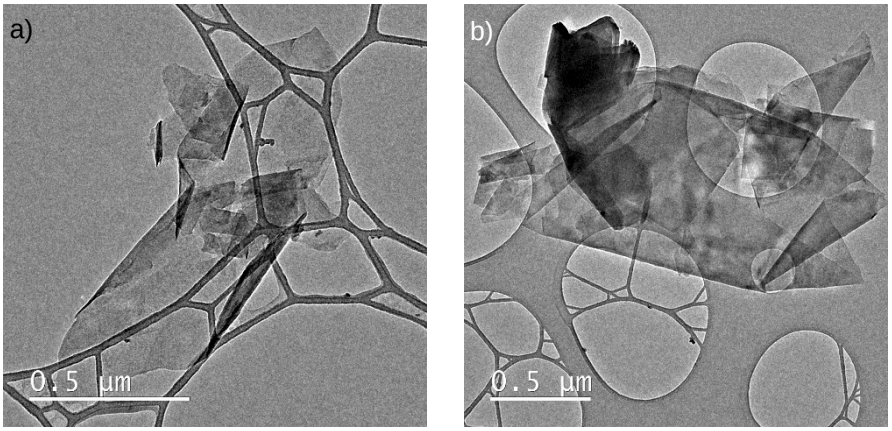

Figure 88. TEM images of a) **complex 4** and b) **complex 7**.

4.4. NON-COVALENT FUNCTIONALIZATION OF GRAPHENE WITH C_{60}-BASED RECEPTORS

4.4.1. Fullerene C_{60}

Fullerenes are a family of carbon allotropes consisting of molecules formed by carbon atoms arranged in the shape of hollow spheres. The most abundant fullerene is the one composed of 60 carbon atoms. [60]Fullerene is a π-electron carbon cluster with a truncated icosahedron geometry (I_h), which is composed of 20 hexagons and 12 pentagons, where the centers of the pentagons are at the corners of an icosahedron and share their edges with adjacent hexagons in a structure that resembles a soccer ball (Figure 89).[2a]

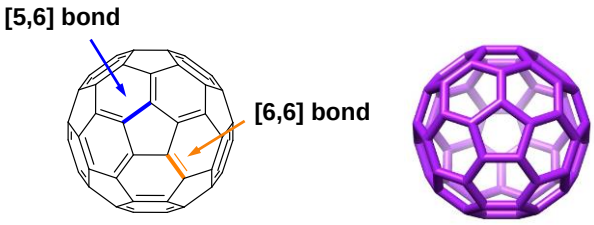

Figure 89. Schematic representation of [60]fullerene structure.

In C_{60} all carbon atoms are sp^2-hybridized and participate in two types of bonds: those between two hexagons, the [6,6], measuring 1.38 Å and presenting a double bond character and those between a pentagon and a hexagon, the [5,6], measuring 1.45 Å and a simple bond character (Figure 89).

C_{60} is characterized by its electron accepting behavior, which makes it able to accept, reversibly, up to six electrons.[154] However, its oxidation is more difficult, most studies on the anodic electrochemistry of C_{60} indicate an irreversible behavior close to the solvent window.[154] Furthermore, C_{60} presents various absorption bands in the UV-Vis region, being a good chromophore. Other important feature of this singular molecule, is its small reorganization energy, inducing a fast charge separation and a slower charge recombination in electron transfer processes.[155]

On the other hand, one of the major drawbacks of C_{60} is its poor solubility in common solvents, so its functionalization is necessary to be implemented for applications in different fields. C_{60} derivatives retain the basic photophysic and

154. a) Q. Xie, E. Perez-Cordero, L. Echegoyen, *J. Am. Chem. Soc.* **1992**, *114*, 3978-3980. b) L. Echegoyen, L. E. Echegoyen, *Acc. Chem. Res.* **1998**, *31*, 593-601.
155. D. M. Guldi, M. Prato, *Acc. Chem. Res.* **2000**, *33*, 695-703.

electrochemical characteristics of the raw material with an increase of their absorption in the UV-Vis region when appropriately modified.[156]

Due to their remarkable properties fullerene-based materials have been used in several fields, especially as electroactive materials in organic electronics, for devices such as field effect transistors and solar cells (Figure 90). Some representative examples, related with the work developed in our research group, are briefly discussed in the following.

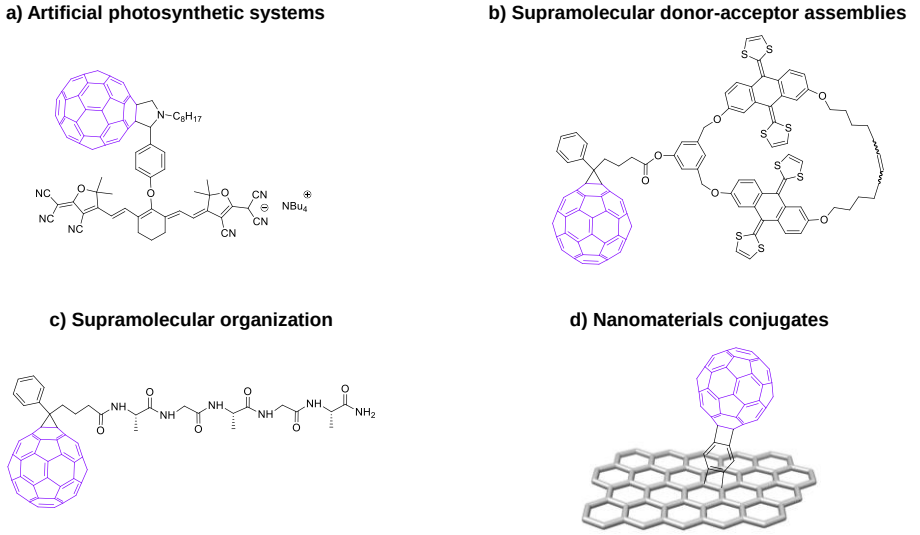

Figure 90. Some of the applications of C_{60}-based materials in organic electronics and supramolecular chemistry.

Several synthetic strategies have been pursued toward artificial photosynthetic and photovoltaic model systems using C_{60} as electron acceptor. For example, anionic fullerene-heptamethine conjugates absorbing as far as 900 nm have been reported (Figure 90a).[157] The main characteristic of this dyad is that the photoexcitation of the cyanine unit leads to a charge transfer from its higher singlet excited state to the C_{60} moiety. The formation of the radical ion pair cyanine-fullerene and, therefore, the charge separation was determined by transient absorption experiments.

156. a) D. M. Guldi, N. Martín, *Fullerenes: From Synthesis to Optoelectronic Properties*, Springer, **2002**. b) G. Accorsi, N. Armaroli, *J. Phys. Chem. C* **2010**, *114*, 1385-1403.
157. C. Villegas, E. Krokos, P.-A. Bouit, J. L. Delgado, D. M. Guldi, N. Martín, *Energy Environ. Sci.* **2011**, *4*, 679-684.

The synthesis of donor-acceptor supramolecular polymers based in the interactions between π-exTTF and C_{60} have been investigated (Figure 90b).[158] The use of a macrocyclic host covalently linked to C_{60} generates a large supramolecular polymer with a high binding constant (log K_a = 5.1 ± 0.5 in $CHCl_3$). As a consequence of that, even at low concentrations, the ratio of monomer is very small. In the UV-Vis spectra recorded at different concentrations, a charge transfer band is observed due to the electronic communication between the two units. The morphology of the polymer was investigated by AFM analysis, which showed long and straight fibers with lengths reaching several microns.

The supramolecular organization of fullerenes has also been achieved by using pentapeptide biomolecular templates (Figure 90c).[159] These molecules organize forming ordered nanofibers of several micrometers length, based on hydrogen bond and π-π interactions. These results are particularly relevant for the assembly of fullerenes in different devices, where the achieved organization could be crucial for the device operation.

C_{60} has further been used in the functionalization of CNTs and graphene. These are all-carbon based nanoconjugates materials. In a recent example, the synthesis of a fullerene-graphene nanoconjugate was reported (Figure 90d).[160] The characterization of this new material was accomplished by several techniques, but the more relevant evidences of the covalent anchoring are obtained by FTIR, Raman and XPS analysis. In fact, in the FTIR spectrum of the nanoconjugate, the characteristic bands of C_{60} are observed. The shake-up satellite peaks of C_{60} are shown in XPS and the G band of graphene was found upshifted in the Raman spectrum of the new material compared with that of graphene, suggesting an electronic communication between graphene and C_{60}.

In the next section, we will present our results related with the development of supramolecular receptors for graphene based on the C_{60} core, for the construction of new all-carbon non-covalent hybrids.

158. H. Isla, E. M. Pérez, N. Martín, *Angew. Chem. Int. Ed.* **2014**, *53*, 5629-5633.
159. A. Insuasty, C. Atienza, J. L. Lopez, N. Martín, *Chem. Commun.* **2015**, *51*, 10506-10509.
160. D. Garcia, L. Rodriguez-Perez, M. A. Herranz, D. Pena, E. Guitian, S. Bailey, Q. Al-Galiby, M. Noori, C. J. Lambert, D. Perez, N. Martín, *Chem. Commun.* **2016**, *52*, 6677-6680.

4.4.2. Synthesis of C_{60}-pyrene conjugates

Similarly to the synthetic methodologies developed in the previous series (π-exTTF, porphyrins), pyrene anchoring groups were incorporated in the structure of C_{60} to favor the attachment to FLG. The pyrene-fullerene dyads **41** and **48** (Figure 91) were obtained by a 1,3-dipolar cycloaddition reaction between the corresponding pyrene-based aldehydes with *N*-octylglycine and C_{60}, following the procedure reported by Prato and co-workers.[161]

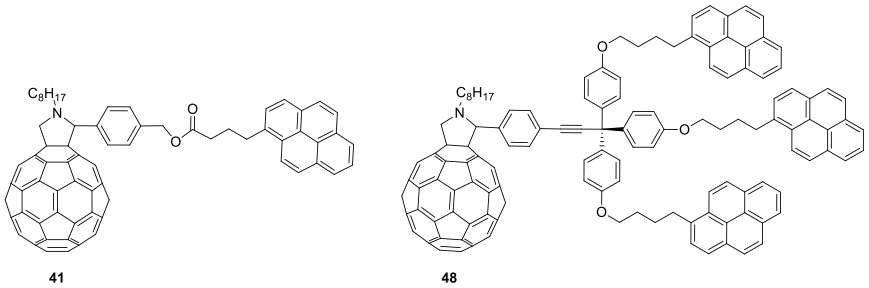

Figure 91. Structure of the C_{60} derivatives for the non-covalent functionalization of graphene.

The synthesis of the pyrene-aldehyde **27** has been described previously (Scheme 7). The preparation of the tripodal aldehyde **47** was carried out following the synthetic route described in Scheme 12.

The Sonogashira coupling between the terminal alkyne **13** and ethyl 4-bromobenzoate **42**, in the presence of $Pd(PPh_3)_2Cl_2$, CuI and Et_3N, provided compound **43** in a good yield. The subsequent treatment of **43** with boron tribromide at 0 °C removed the methoxy substituents yielding the trisphenol derivative **44**.[162] The reaction of this compound with the 4-(1-pyrenyl)-1-butanol tosylate **20** in the presence of K_2CO_3 as base afforded the tripodal derivative **45**. The consecutive treatment of this ethylbenzoate derivative with DIBAL-H and PCC allowed to synthesize the desired aldehyde **47** through the intermediate alcohol **46**. The direct reduction of the ester group of **45** was not found to work properly.

161. a) M. Maggini, G. Scorrano, M. Prato, *J. Am. Chem. Soc.* **1993**, *115*, 9798-9799. b) M. Prato, M. Maggini, *Acc. Chem. Res.* **1998**, *31*, 519-526.
162. J. A. Mann, T. Alava, H. G. Craighead, W. R. Dichtel, *Angew. Chem. Int. Ed.* **2013**, *52*, 3177-3180.

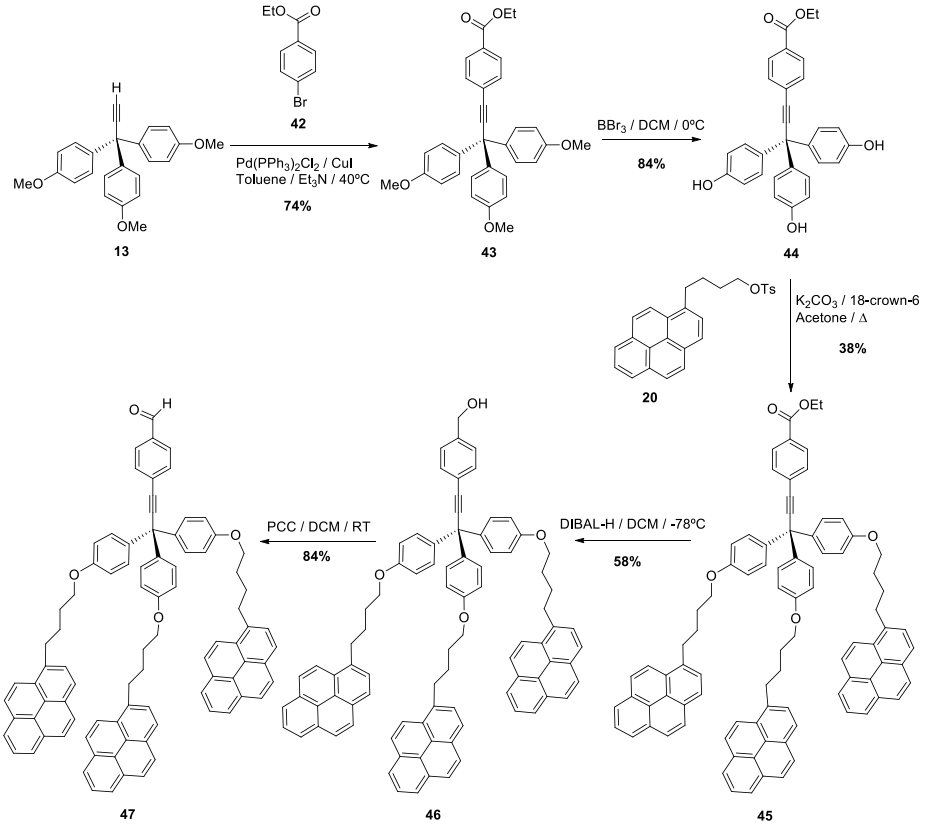

Scheme 12. Synthesis of the tripodal aldehyde **47**.

Finally, fulleropyrrolidines **41** and **48** were synthesized by the in situ generation of the respective azomethine ylides by Prato reaction between aldehyde **27** or **47**, *N*-octylglycine and C_{60}, in toluene at reflux with moderate yields (35-38%) (Scheme 13).

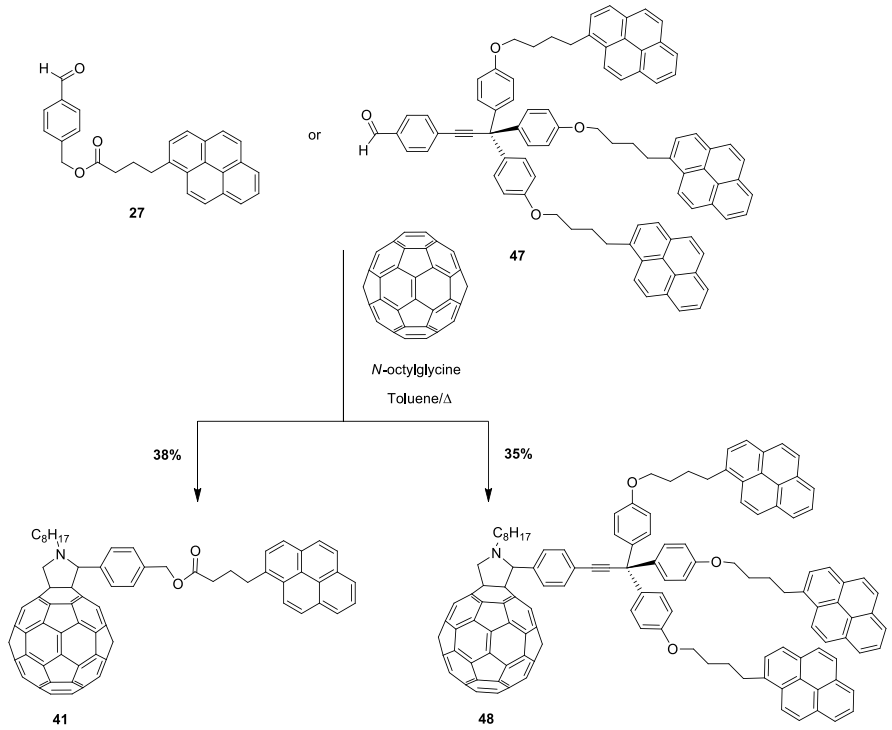

Scheme 13. Synthesis of the C_{60} derivatives **41** and **48**.

All compounds were fully characterized by the standard analytical and spectroscopic techniques. The ^{1}H-NMR spectra of the final products **41** and **48** are shown below (Figure 92). For both compounds, the pyrrolidine proton doublets and singlet are observed, between 5.10-4.10 ppm in the case of PyC_{60} **41** and between 4.95-3.85 ppm for $3PyC_{60}$ **48**. These resonances confirm the successful synthesis of the target molecules, since their presence imply the covalent linkage between the precursors of the Prato reaction. In addition, the signals of the pyrene units are evident in both spectra at around 8.25-7.80 ppm, and in the aliphatic region of the spectra the protons of the alkyl chains can also be observed.

The ^{13}C-NMR of the dyads show that although the resonances observed were less than expected due to the superposition of several signals, the number of resonances reveals the lack of symmetry in these compounds. The signals for the sp^3 carbons of the pyrrolidine ring and for the [6,6] junction of the C_{60} framework are observed in the region between 84.4-65.9 ppm. The structure was further confirmed by exact MALDI-TOF-MS spectrometry, which showed the molecular ions for **41** and **48** at m/z 1252.3163 (calculated 1252.3171) and 2033.6756 (calculated 2033.6686), respectively.

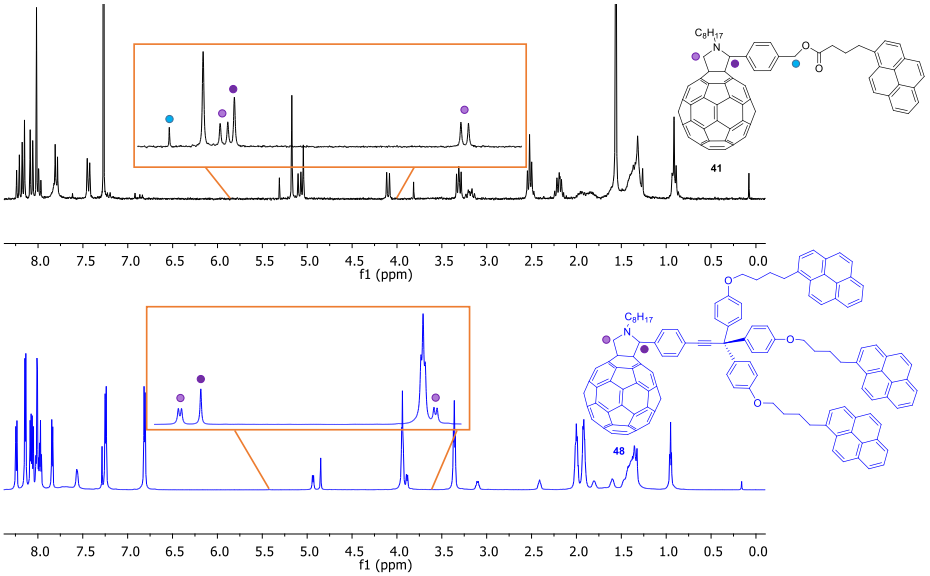

Figure 92. ^{1}H-NMR spectra ($CDCl_3$, 300 MHz, 298 K) of the final compounds **41** and **48**.

4.4.3. Study of the supramolecular interactions between different pyrene-based systems

a) Interactions between complementary electronic systems

Inspired by the different electronic properties that the systems endowed with one pyrene unit present (Figure 93), and the many examples reported in bibliography about supramolecular interactions between porphyrins and C_{60} or π-exTTF and C_{60},[163] we decided to study if these systems were able to form donor-acceptor ensembles.

Furthermore, the previous results obtained in the self-assembly investigations of PyZnP **31**, motivated us to explore if the affinity between our pyrene-based molecules can be improved from the interplay between π-π and charge-transfer interactions.

163. L. Moreira, B. M. Illescas, N. Martín, *J. Org. Chem.* **2017**, *82*, 3347-3358.

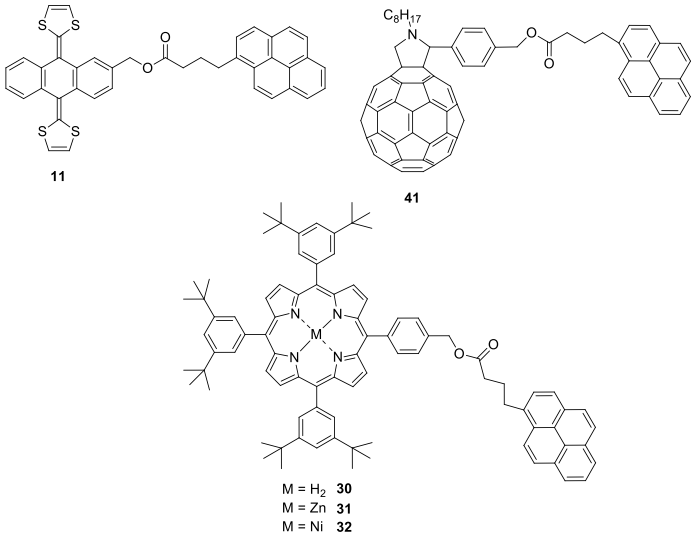

Figure 93. Structures of the different systems synthesized with one pyrene unit.

The complexation studies were carried out by ^{1}H-NMR titrations, performed under the same conditions. In order to keep constant the concentration of the host (**11**, or **30**-**32**, 2.5 mM in $CDCl_3$), a solution of this one was used as solvent to prepare the guest solution (**41**), avoiding dilution factors. After each addition, ^{1}H-NMR spectra were recorded.

In a first series, titration experiments were accomplished between PyZnP **31** and PyC_{60} **41**. As the concentration of the C_{60} derivative increases, several signals present a slight shielding (Figure 94).

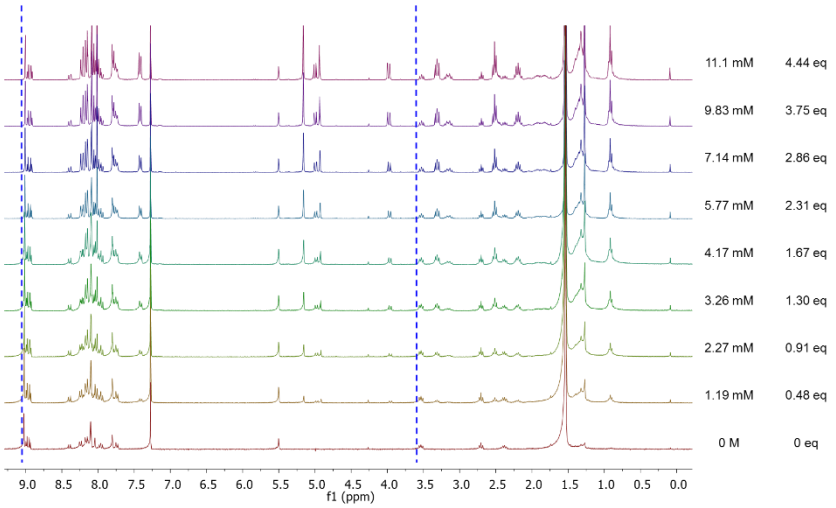

Figure 94. ^{1}H-NMR titration (300 MHz, 298 K) of system **31** with increasing amounts of **41** in $CDCl_3$.

To obtain the value of the binding constant considering a 1:1 binding model, only the signals unequivocally belonging to the porphyrin are fitted to equation 1,[164] using Origin Pro 9.0.

$$\Delta\delta = \Delta\delta_{max}\frac{K[G]-K[H]-1+\sqrt{(K[G]+K[H]+1)^2-4K^2[G][H]}}{K[G]-K[H]+1+\sqrt{(K[G]+K[H]+1)^2-4K^2[G][H]}} \qquad \textbf{Equation 1}$$

Where Δδ is the chemical shift variation between one addition and the next, K is the binding constant, and [G] and [H] are the concentrations of the guest and the host respectively.

In Figure 95 is observed the variation of the signals between 9.1 and 7.7 ppm when increasing amounts of **41** are added. β-pyrrolic protons present the higher Δδ (0.024 ppm).

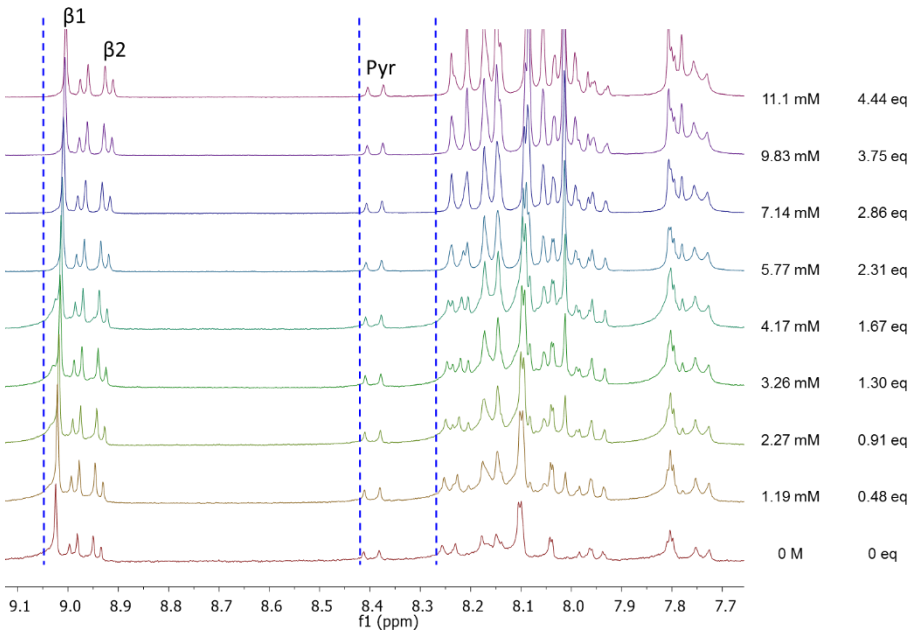

Figure 95. Partial ^{1}H-NMR titration ($CDCl_3$, 300 MHz, 298 K) of **31** with **41**, corresponding to the porphyrin core and pyrene protons.

Due to the complexity of the spectra when the concentration of PyC_{60} **41** increases, the signals that can be unequivocally assigned to the porphyrin are the β-pyrrolic protons, the higher signal of the pyrene protons at 8.41 ppm and the peaks corresponding to the alkyl chain at ca. 3.54 ppm are also clearly

164. P. Thordarson, in *Supramolecular Chemistry: From Molecules to Nanomaterials*, John Wiley & Sons, Ltd, **2012**.

distinguishable. For this reason, these signals were fitted to equation 1 (Figure 96).

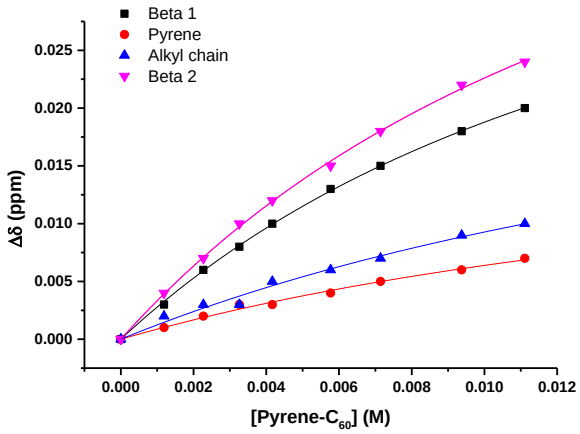

Figure 96. Data fitting for signals change in the ^{1}H-NMR spectra upon the addition of **41** to **31**.

In Table 6 are summarized the values of the binding constant obtained for each signal and the fitting error.

Table 6. Binding constant values for each followed signal during the ^{1}H-NMR titration between systems **31** and **41**.

Signal	K value	Fitting error	Log K	R^2
Beta 1	73	±4	1.86	0.9996
Beta 2	72	±6	1.86	0.9992
Pyrene	51	±15	1.71	0.9920
Alkyl chain	47	±19	1.67	0.9853

The obtained values for the binding constant are in accordance with previous results obtained in our group.[165] For example, the π-stacking between a C_{60} derivative and a Zn porphyrin (Figure 97) provided a value of log K = 1.3 (K = 20). The slight increase in the value of the binding constant for the systems described here, could be due to the additional π-π stacking forces between pyrene units.

165. L. Moreira, J. Calbo, B. M. Illescas, J. Aragó, I. Nierengarten, B. Delavaux-Nicot, E. Ortí, N. Martín, J.-F. Nierengarten, *Angew. Chem. Int. Ed.* **2015**, *54*, 1255-1260.

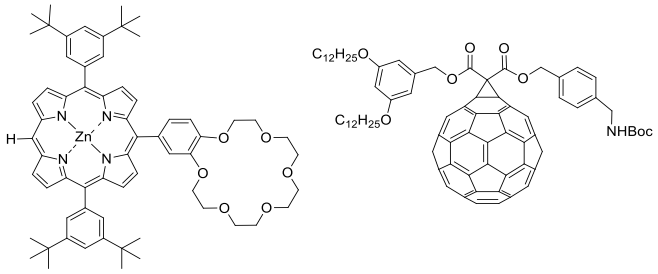

Figure 97. Structure of the porphyrin and C_{60} molecules previously investigated in complexation assays.

Once evaluated the interaction between PyZnP **31** and PyC_{60} **41**, the same analysis was carried out with the other two pyrene-porphyrin derivatives **30** and **32**, in order to study the influence of the central atom in the interaction.

In the case of PyH_2P **30** a similar behavior to that of **31** was observed when increasing amounts of **41** are added (Figure 98). However, the chemical shifts observed are smaller than in the case of **31**. In the case of the β-pyrrolic protons $\Delta\delta = 0.01$ ppm.

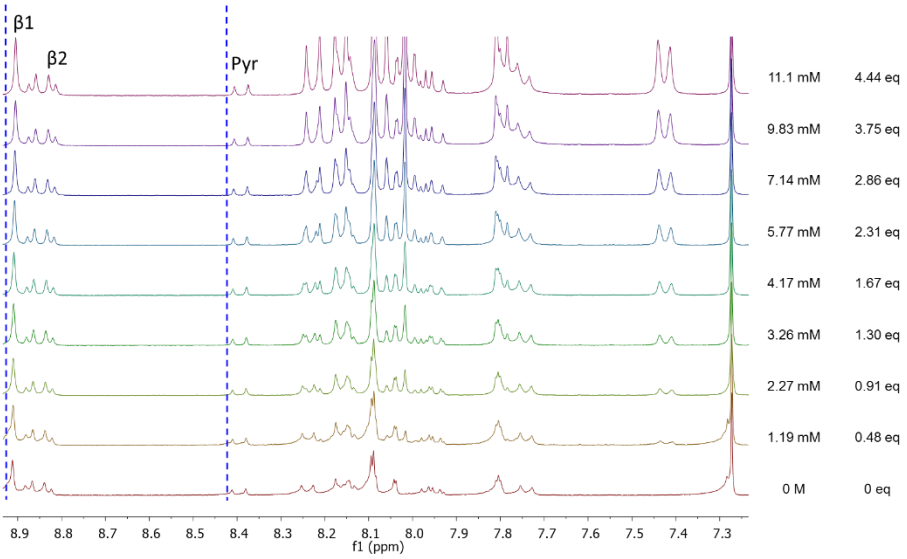

Figure 98. Partial ^{1}H-NMR titration ($CDCl_3$, 300 MHz, 298 K) of **30** with increasing amounts of **41**, corresponding to the porphyrin and pyrene protons.

The same signals that in the previous case were considered for the fitting to equation 1. However, the variation of the chemical shift of the pyrene protons did not converge, for that reason the fitting with these protons chemical shifts was not considered (Figure 99).

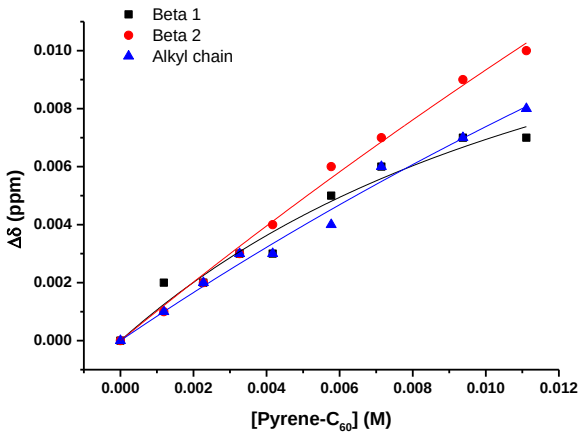

Figure 99. Data fitting for signals change in the ^{1}H-NMR spectra upon the addition of **41** to **30**.

The value of the binding constant obtained for each signal and the fitting error are summarized in Table 7.

Table 7. Binding constant values for each followed signal during the ^{1}H-NMR titration between systems **30** and **41**.

Signal	K value	Fitting error	Log K	R^2
Beta 1	84	±43	1.92	0.96149
Beta 2	11	±7	1.04	0.99443
Alkyl chain	17	±13	1.23	0.98476

It is noticed the great difference between the values of the binding constants obtained for each signal and the magnitude of the fitting error. The better results are obtained for the fitting with the beta 2 protons, which provide a value of log K = 1.04 (K = 11).

For PyNiP **32**, the observed behavior when increasing amounts of **41** are added, is a bit different if it is compared with systems **31** and **30**. As it is shown in Figure 100, the variation of the chemical shift of the β-pyrrolic protons is very small (Δδ = 0.003 ppm), while in the case of the pyrene protons or *t*-butyl protons this variation is higher, of about 0.015 ppm. It has to be noticed that for the previous systems the *t*-butyl protons were not affected by the addition of **41**, however, in this case, these protons are notably affected. Moreover, the signal is splitted when the concentration of **41** increases, being possible to distinguish the two different types of *t*-butyl protons present in the molecule.

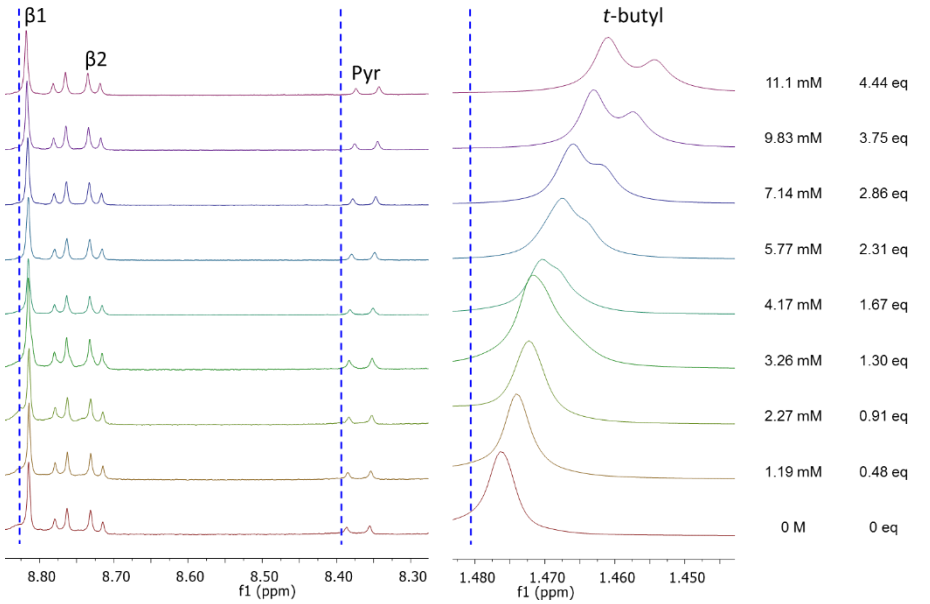

Figure 100. Partial ^{1}H-NMR titration ($CDCl_3$, 300 MHz, 298 K), corresponding to the porphyrin, pyrene and *t*-butyl protons, for the addition of **41** to **32**.

In this case, due to the small variation of the chemical shift for the β-pyrrolic protons (< 0.005 ppm), the signals that have been fitted to equation 1 are the corresponding to the pyrene, alkyl chain and *t*-butyl protons groups (Figure 101).

In Table 8 are summarized the values of the binding constant obtained for each signal and the fitting error.

Table 8. Binding constant values for each followed signal during the ^{1}H-NMR titration between systems **32** and **41**.

Signal	K value	Fitting error	Log K	R^2
Pyrene	2	±9	0.30	0.98684
Alkyl chain	17	±9	1.23	0.99183
***t*-butyl**	8	±7	0.90	0.99389

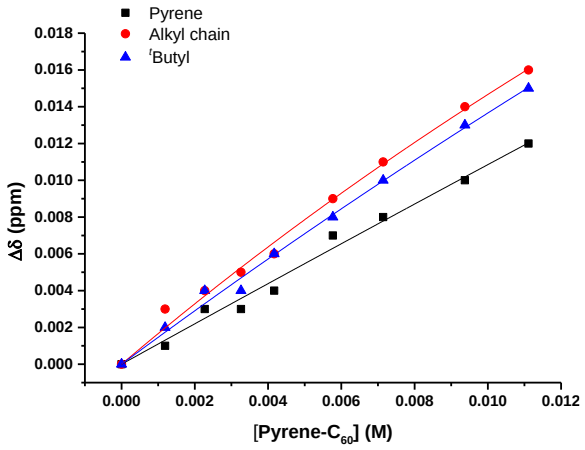

Figure 101. Data fitting for signals change in the ^{1}H-NMR spectra upon the addition of **41** to **32**.

The data fitting yields results in the same line that in the previous case, with binding constants of a similar order of magnitude.

The association between porphyrins and C_{60} is governed by van der Waals forces,[166] but other effects can influence the strength of this association. Such forces are coordinative bond formation, charge transfer, electrostatic interactions and solvation.[167] Comparing the values of the binding constants obtained in our series, it is clear that the central atom influences the interaction.

For PyZnP **31**, the higher binding constant could be due to the free coordination site that allows to zinc porphyrin to form 1:1 complexes,[168] its greater number of electrons compared with the free porphyrin[165] and its better donor character (Table 4). On the other hand, the lower value of the binding constant for the PyNiP **32** can be attributed to the strong interaction between the electrons of Ni and the π-electrons of the porphyrin.[138] The shorter length for the Ni-N bond deforms the structure in addition[169] and it could explain the differences observed in the ^{1}H-NMR titration for this system. Furthermore, this molecule is the worst donor of the series.

166. P. D. W. Boyd, M. C. Hodgson, C. E. F. Rickard, A. G. Oliver, L. Chaker, P. J. Brothers, R. D. Bolskar, F. S. Tham, C. A. Reed, *J. Am. Chem. Soc.* **1999**, *121*, 10487-10495.
167. D. Sun, F. S. Tham, C. A. Reed, L. Chaker, P. D. W. Boyd, *J. Am. Chem. Soc.* **2002**, *124*, 6604-6612.
168. M. Nappa, J. S. Valentine, *J. Am. Chem. Soc.* **1978**, *100*, 5075-5080.
169. H.-H. Tsai, M. C. Simpson, *J. Phys. Chem. A* **2004**, *108*, 1224-1232.

Once that the ability of the porphyrin systems (**30**-**32**) to form supramolecular ensembles with PyC_{60} **41** was confirmed, we also performed this analysis with PyexTTF **11**. π-exTTF can establish charge-transfer, π-π and van der Waals interactions with the convex surface of C_{60}. However, even though theoretical calculations indicate that one single molecule of π-exTTF could associate C_{60}, this does not happen experimentally.[132b] In a further step, we wanted to evaluate if the presence of the pyrene unit covalently linked to the π-exTTF core can increase the binding affinity for C_{60} derivatives, in particular PyC_{60} **41**, by π-π stacking interactions.

The ^{1}H-NMR titrations of PyexTTF **11** with **41** were carried out under the same conditions to those described above. A solution of **11** (2.5 mM) was used as solvent to prepare the guest solution (**41**), in order to keep constant the concentration of the host avoiding dilution factors (Figure 102).

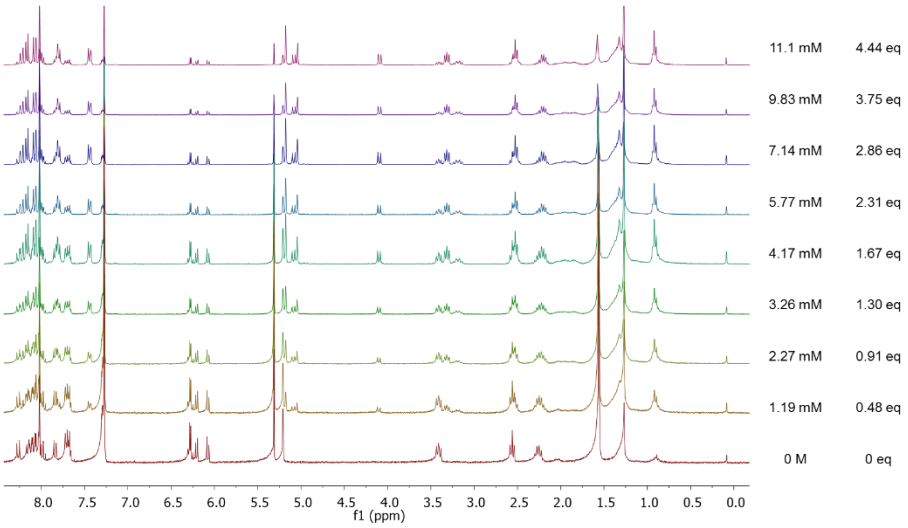

Figure 102. ^{1}H-NMR titration ($CDCl_3$, 300 MHz, 298 K) of system **11** with increasing amounts of **41**.

When increasing amounts of PyC_{60} **41** are added, the only signals that present a significant shift (>0.005 ppm) are the ones corresponding to the 1,3-dithiole rings, being the variation $\Delta\delta$ = 0.006 ppm (Figure 103).

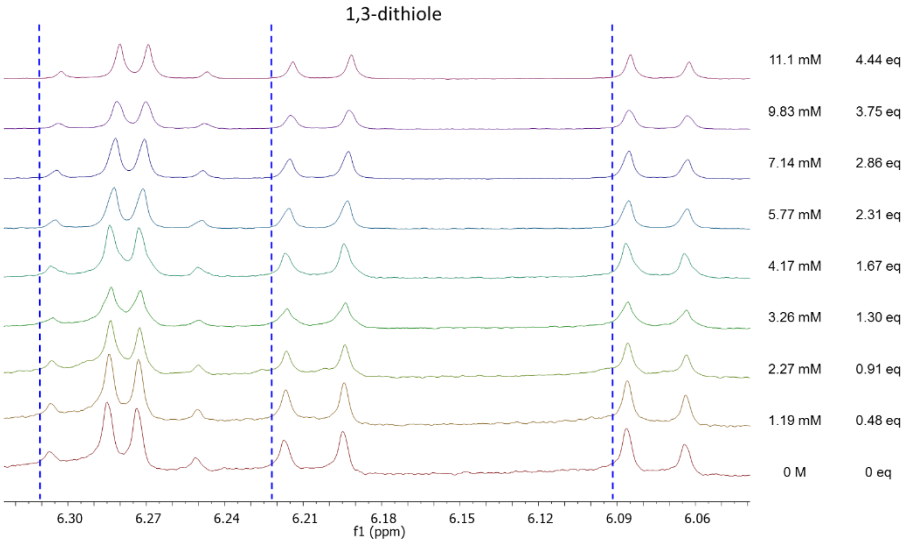

Figure 103. Partial ^{1}H-NMR titration ($CDCl_3$, 300 MHz, 298 K) of **11** with **41**, corresponding to the 1,3-dithiole rings protons.

When the data obtained were tried to fit to equation 1, it was observed a lineal behavior and the fitting error for this system is very large, which implies that the interaction between PyexTTF **11** and PyC_{60} **41** is much weaker than the interaction with the porphyrin systems, and that ^{1}H-NMR spectroscopy is not an appropriate technique to estimate the magnitude of such interaction.

b) Self-assembly interactions

Since the study of the self-assembly behavior of PyZnP **31** evidenced a weak interaction between these molecules, it was decided to carry out the same concentration dependent ^{1}H-NMR experiments with the tripodal derivative **48**, since it was expected that the presence of three pyrene units could increase the π-π stacking interactions (Figure 104).

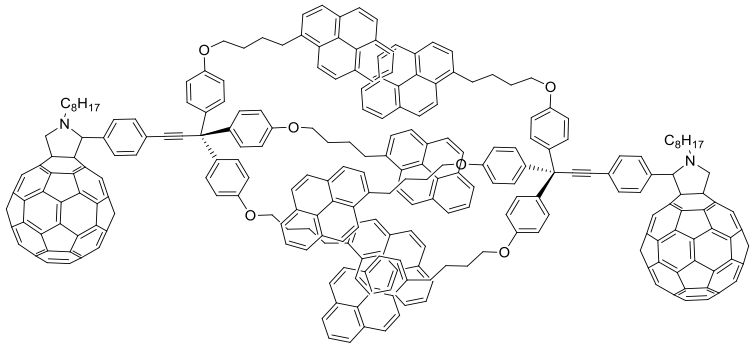

Figure 104. Cartoon representing the potential assembly formed by $3PyC_{60}$ **48**.

The concentration dependent ^{1}H-NMR experiments were performed by dilution of a concentrated solution of **48** (40 mM, in $CDCl_3$). For each spectrum the solution was diluted a 50% (Figure 105).

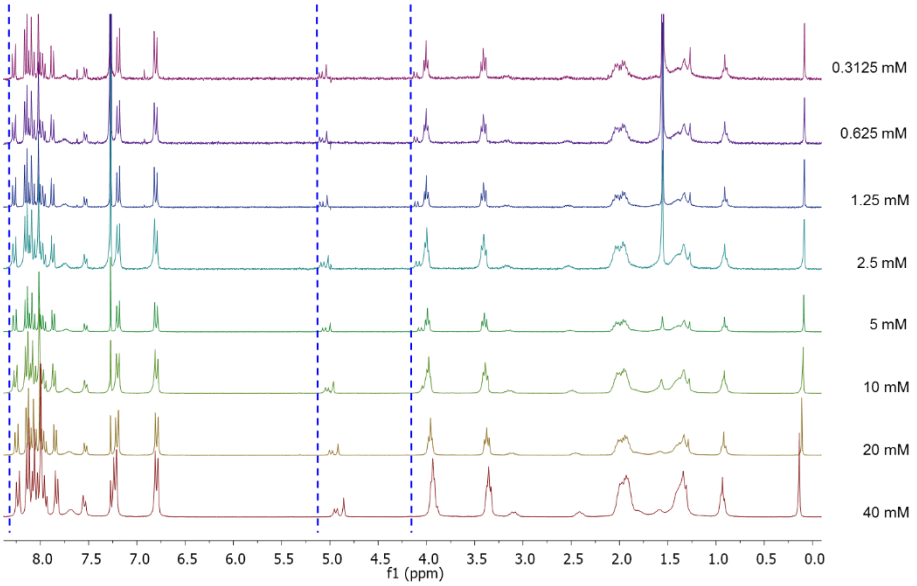

Figure 105. ^{1}H-NMR ($CDCl_3$, 300 MHz, 298 K) spectra at variable concentration for $3PyC_{60}$ **48**.

As the concentration increases, all the signals present a slight shielding and a broadening. The majority of the signals are shifted upfield (Figure 106), which suggests the formation of aggregates through π-π interactions.[132a,170]

The protons of the fulleropyrrolidine are more affected than the aromatic protons by the increase in concentration, being the shift for the former around 0.18 ppm and for the latter of 0.04 ppm.

The representation of the chemical shift *vs*. concentration leads to a nonlinear behavior (see below), which implies that, in this case, the interactions are strong enough to be determined by ^{1}H-NMR spectroscopy. Besides, this nonlinear trend allows to calculate the binding constant for the present system.

170. a) G. Fernández, E. M. Pérez, L. Sánchez, N. Martín, *Angew. Chem. Int. Ed.* **2008**, *47*, 1094-1097. b) E. M. Perez, N. Martín, *Chem. Soc. Rev.* **2015**, *44*, 6425-6433.

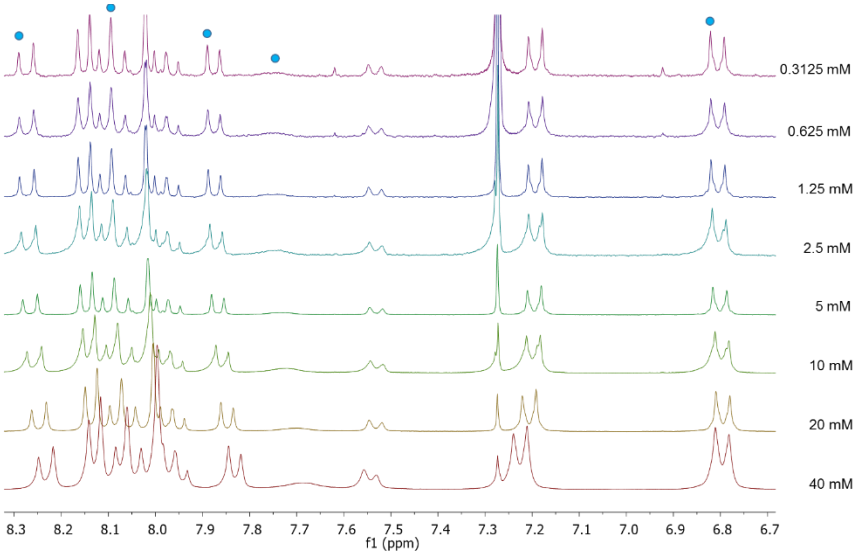

Figure 106. Partial ^{1}H-NMR spectra ($CDCl_3$, 300 MHz, 298 K) of the aromatic region for $3PyC_{60}$ **48**. The signals used to calculate the binding constant are denoted by blue dots.

The value of the binding constant was calculated using the next equation: [171]

$$\delta_{obs} = \delta_m + (\delta_m - \delta_d)\frac{(1+8KC)^{1/2}-1}{(1+8KC)^{1/2}+1} \qquad \textbf{Equation 2}$$

Where δ_{obs} is the experimental shift, δ_m is the shift of the monomer, δ_d is the shift of the aggregate (dimer), K is the binding constant and C is the concentration. In Table 9 are summarized the K values for each signal and the fitting error. In addition to the signals highlighted in Figure 106, all the pyrrolidine protons and the triplet of the alkyl chain at 3.36 ppm were used to calculate the binding constant.

Table 9. Binding constant values for each followed signal during the concentration dependent ^{1}H-NMR experiments for system **48**.

Protons	K value, fitting error and R^2		
Pyrene	9 ± 1 R^2 =0.99749	10 ± 2 R^2=0.99661	7 ± 5 R^2=0.96088
Aromatic ring	8 ± 6 R^2 = 0.93652		
Aromatic ring tripod	42 ± 10 R^2 = 0.9894		
Pyrrolidine	11.0 ± 0.3 R^2 =0.99987	10.5 ± 0.3 R^2=0.99988	9.9 ± 0.6 R^2=0.99952
Alkyl chain	9.1 ± 0.5 R^2 = 0.99965		

171. Y. Liu, Z. Fan, H.-Y. Zhang, C.-H. Diao, *Org. Lett.* **2003**, *5*, 251-254.

The data fit to equation 2 for one of the pyrene protons is shown in Figure 107. The nonlinear behavior of the chemical shift *vs.* concentration discussed above is also represented.

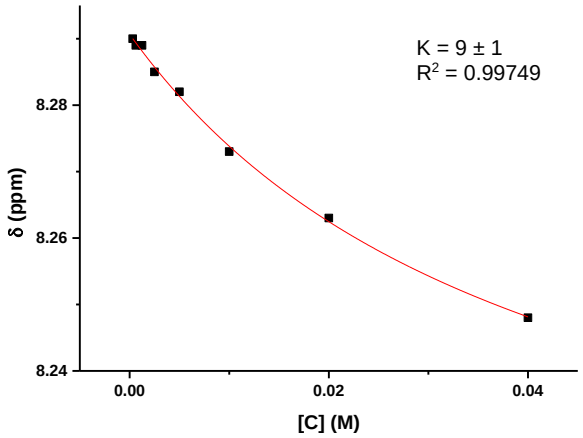

Figure 107. Data fitting for the pyrene signal change in the concentration dependent ^{1}H-NMR experiments.

Variable temperature ^{1}H-NMR experiments were performed at a concentration of 5 mM and modifying the temperature from 328 to 228 K. As the temperature decreased, the well-defined sharp signals evolved to broad ones and are shifted upfield (Figure 108), in agreement with the results obtained in the concentration dependent experiments.

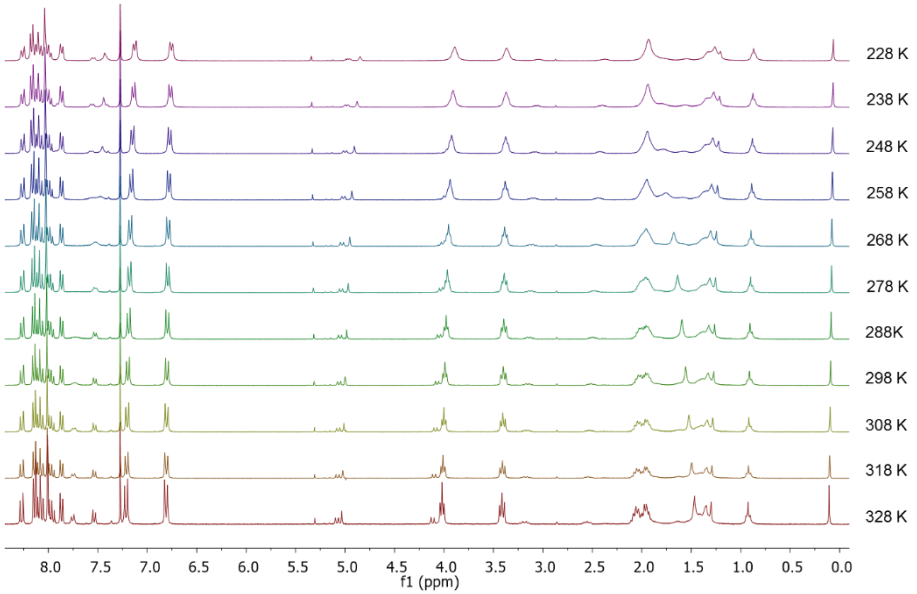

Figure 108. ^{1}H-NMR spectra ($CDCl_3$, 300 MHz) at variable temperature for $3PyC_{60}$ **48**.

The shifts observed for the different signals are smaller than in the case of the concentration dependent experiments, except in the case of the signals corresponding to the aromatic ring located near to the pyrrolidine and the rings of the tripodal skeleton denoted with blue dots in Figure 109, which suggests that these protons have a different contribution at lower temperatures. Furthermore, it has to be noticed that the binding constant obtained for the proton at 6.80 ppm (aromatic ring tripod) is higher than the others, implying a stronger contribution that could explain this behavior.

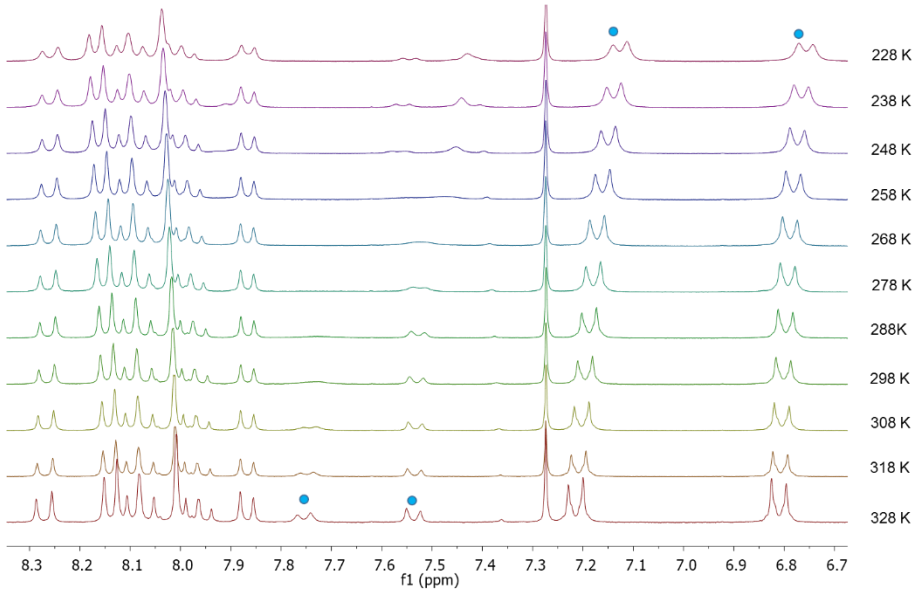

Figure 109. Partial ^{1}H-NMR spectra (CDCl3, 300 MHz) of the aromatic region for 3PyC_{60} **48**.

In order to determine the protons that participate in the interactions, a ROESY experiment was carried out for a solution of **48**, whose concentration was 20 mM. These experiments allow to observe what protons are close in the space, at distances lower than 5 Å. Taking this into account and the diameter of C_{60} (1 nm), the protons nearest to that of the fulleropyrrolidine are the first protons of the octyl chain and the protons of the aromatic ring bonded to it. So any other proton that shows a correlation signal should be spatially close and reports a possible interaction. In Figure 110 is shown the ROESY spectrum for **48**, the signals marked with squares are correlations through the space, the protons are far away in the molecule although correlate by ROESY, which could explain why all the signals are shifted upfield in the different dependent ^{1}H-NMR experiments.

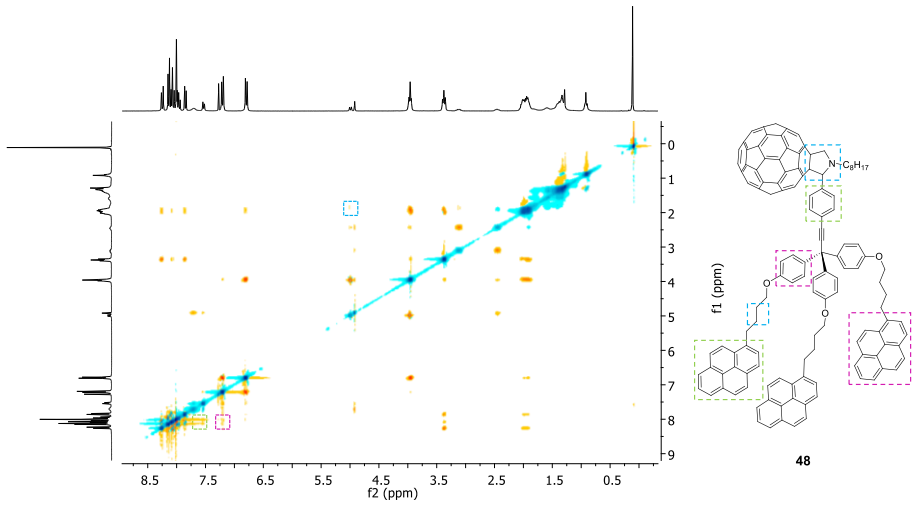

Figure 110. ROESY spectrum for 3PyC$_{60}$ **48** (20 mM).

Diffusion-ordered NMR spectroscopy (DOSY) experiments were performed at two different concentrations of **48** (2.5 and 20 mM) to determine if the diffusion coefficient was modified with the concentration and provided other evidence for the self-association. As expected the diffusion coefficient decreased from 4.09×10^{-6} to 3.03×10^{-6} in the concentrated solution, suggesting the presence of larger size species. By MALDI-TOF mass spectrometry, in spite of the high molecular weight of **48** (m/z 2035), the peak corresponding to the dimer mass is also observed.

The morphology of the aggregates was studied by different microscopic techniques such as AFM, SEM and confocal microscopy (Figure 111). For all of them, a solution of **48** (~ 10^{-6} M) was drop-casted onto mica (AFM) or glass (SEM and confocal microscopy). The images displayed spherical aggregates of around 100 nm of width. In addition, confocal microscopy showed that these aggregates exhibit a blue fluorescence, characteristic of pyrene compounds, when the sample is excited at 405 nm (Figure 111d).

With all the results obtained by the different techniques: concentration and temperature dependent ^{1}H-NMR experiments, ROESY and DOSY spectroscopy, mass spectrometry and microscopy, the self-association in small aggregates, most probably dimeric structures, of 3PyC$_{60}$ **48** can be confirmed.

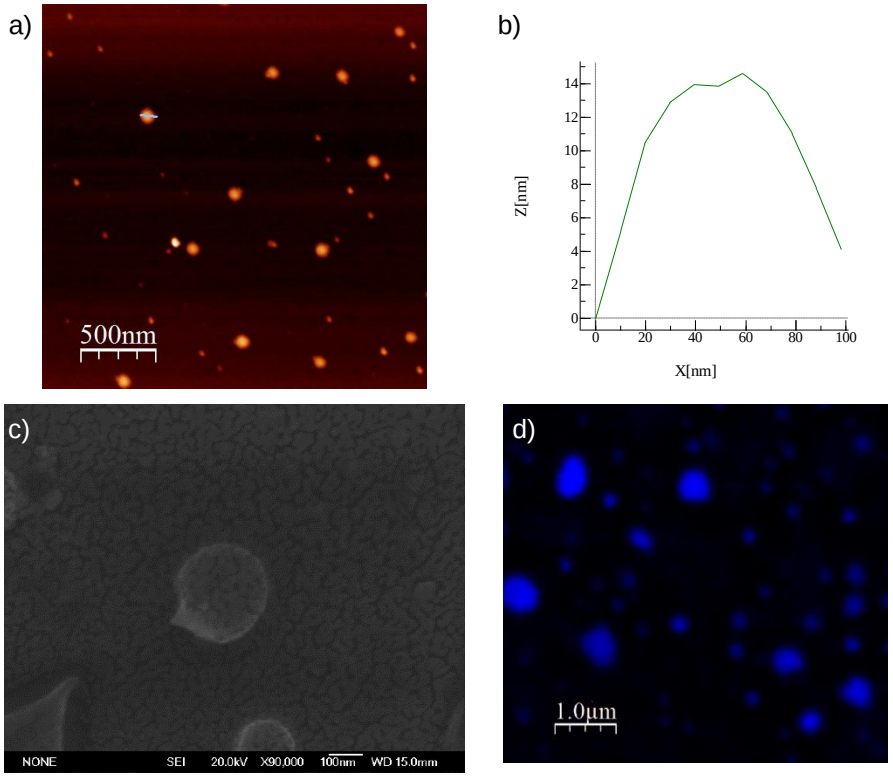

Figure 111. a) AFM image of a drop-cast chloroform solution of **48**. b) Profile of the structure show in a) (blue line). c) SEM image obtained for the same solution of **48**. d) Confocal microscopy image of a drop-cast chloroform solution of **48** (λ_{exc} = 405 nm).

4.4.4. Study of the solution interactions between C_{60} derivatives and FLG

The non-covalent functionalization of FLG with the pyrene-C_{60} derivatives **41** and **48**, was also investigated. First of all, as in the cases of the π-exTTF and porphyrin-based receptors, UV-Vis and fluorescence titrations were carried out in order to determine the interactions between these two molecular receptors and FLG in solution.

In order to confirm that all the changes observed in the titrations are not due to dilution, control experiments have been carried out in all of them.

In Figure 112, the UV-Vis titration of PyC_{60} **41** is shown. When increasing amounts of FLG are added, the intensity of the pyrene bands decreases at the same time that the absorbance between 400 and 600 nm increases, with the appearance of a pseudo-isosbestic point at 355 nm.

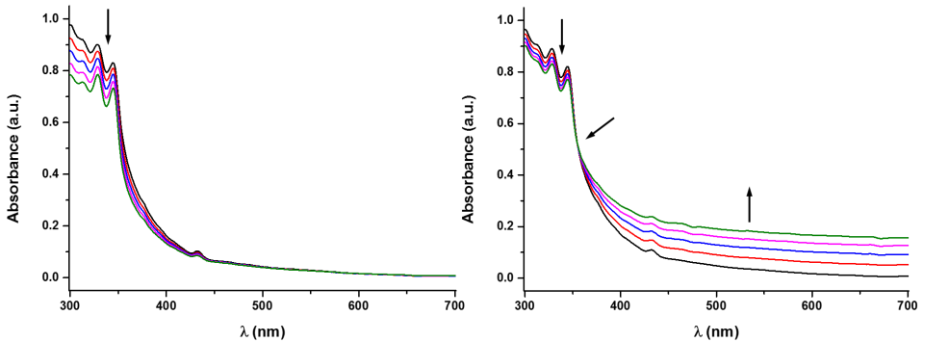

Figure 112. UV-Vis spectra obtained during the dilution (left) and titration (right) with FLG of PyC_{60} **41** ($3 \cdot 10^{-5}$ M). Each addition corresponds to 50 µL.

In the case of $3PyC_{60}$ **48**, the titration experiment presents a similar trend. The difference is the appearance of two pseudo-isosbestic points, instead of one, located at 310 and 350 nm, respectively (Figure 113). These values are very similar to those obtained for 3PyexTTF **21** (311 and 351 nm), suggesting the same behavior for both tripodal derivatives. Besides, the differences between both pyrene-C_{60} derivatives agree with the expected distinct behavior for them.

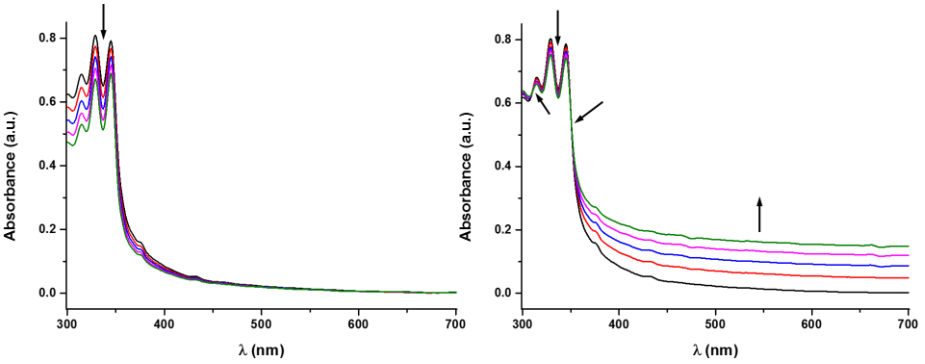

Figure 113. UV-Vis spectra obtained during the dilution (left) and titration (right) with FLG of $3PyC_{60}$ **48** ($1.52 \cdot 10^{-5}$ M). Each addition corresponds to 50 µL.

The presence of the pseudo-isosbestic points in both cases suggest an interaction between the organic molecules and FLG, in addition to an equilibrium process for this interaction.

In order to corroborate the interaction between the pyrene-C_{60} derivatives and FLG, fluorescence titrations were also carried out (Figure 114). For both molecular systems, **41** and **48**, when increasing amounts of FLG are added, a similar emission quenching of the pyrene fluorescence is observed (15%).

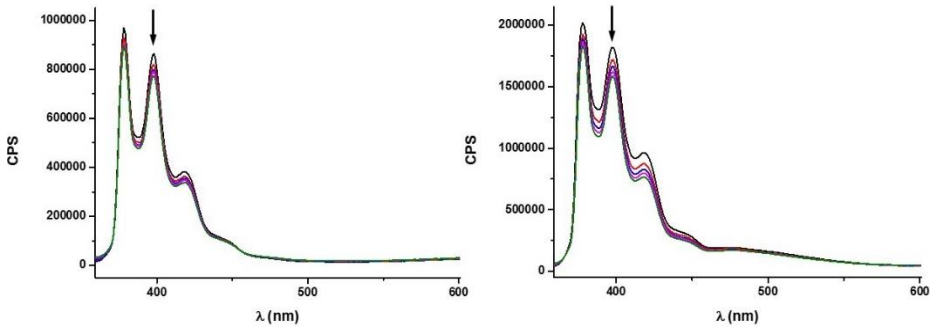

Figure 114. Left: Fluorescence spectra obtained upon titration of PyC_{60} **41** ($3 \cdot 10^{-5}$ M) with FLG. Each addition corresponds to 50 μL. Right: Fluorescence spectra obtained upon titration of $3PyC_{60}$ **48** ($1.52 \cdot 10^{-5}$ M) with FLG. Each addition corresponds to 50 μL (λ_{exc} = 344 nm).

This quenching of the fluorescence implies an interaction between the pyrene units present in the organic molecules and the basal plane of graphene.

4.4.5. Synthesis of non-covalent FLG/C_{60} hybrids

Once that the interaction between the organic molecules and FLG has been confirmed by the UV-Vis and fluorescence titrations, the non-covalent functionalization was carried out. As in the previous cases, a combination of sonication, filtration and washing steps allowed to obtain the FLG/pyrene-C_{60} non-covalent complexes **9** and **10** (Figure 115, see experimental section for details), which were characterized by several complementary techniques in order to corroborate that the supramolecular modification took place satisfactorily.

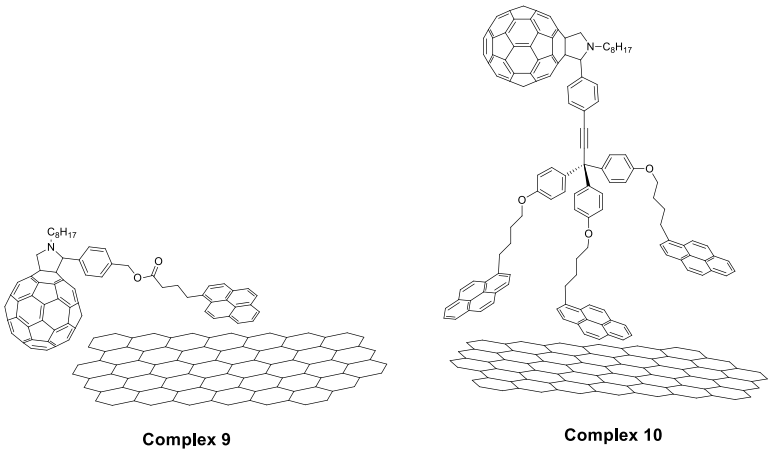

Figure 115. Supramolecular FLG/pyrene-C_{60} hybrids

Due to the characteristic absorption of the pyrene moieties, UV-Vis spectroscopy is a very useful technique to determine if the non-covalent functionalization of FLG with the pyrene-C_{60} derivatives has taken place. In Figure 116 are shown the UV-Vis spectra obtained for each complex, where two bands corresponding to pyrene units, together with the absorption pattern of graphene are observed, confirming the supramolecular modification.

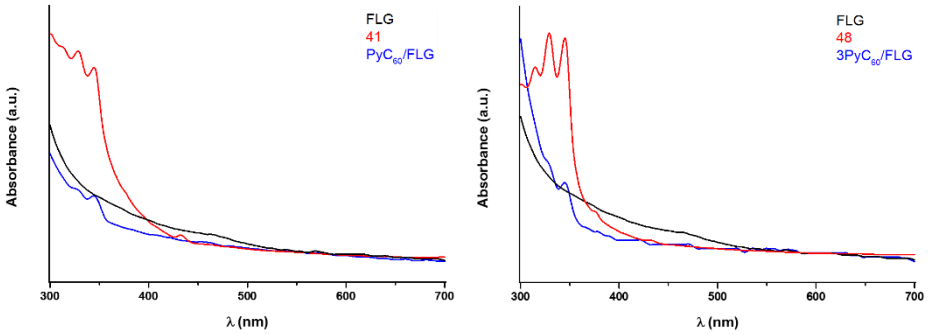

Figure 116. Left: UV-Vis spectra of FLG, PyC_{60} **41** and **complex 9** in NMP. Right: UV-Vis spectra of FLG, $3PyC_{60}$ **48** and **complex 10** in NMP.

Making use of FTIR spectroscopy, the non-covalent functionalization of FLG can be complementary confirmed. In Figure 117 the FTIR spectra of FLG, **41** and **complex 9** are shown. For this last one, the graphene skeletal in-plane vibrations at 1583 cm^{-1}, the vibrational band at 1736 cm^{-1} of the carbonyl group from the ester in **41**, and the characteristic vibrational peak of C_{60} at 527 cm^{-1}, also confirm the successful FLG modification. In the FTIR spectrum of **complex 10**, similar characteristics are observed.

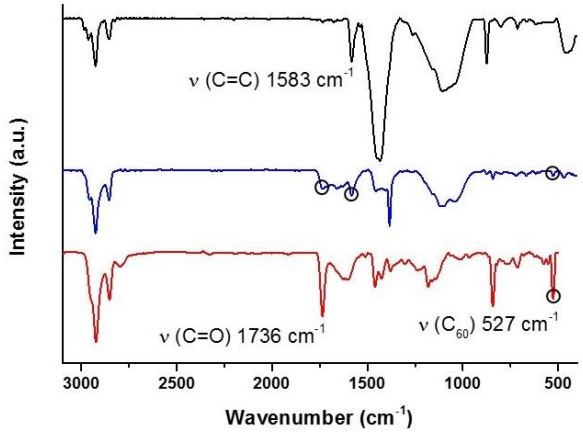

Figure 117. FTIR spectra of FLG (black), **complex 9** (blue) and **41** (red).

By TGA analysis is possible to determine the functionalization degree of the complexes in a quantitative manner (Figure 118). For **complex 9**, the experimented weight loss is around 9%, which corresponds to an approximate ratio of 1 PyC_{60} (**41**) per 1062 atoms of carbon. In the case of **complex 10**, the weight loss is higher (17%) and can be estimated that there is 1 $3PyC_{60}$ (**48**) per 811 atoms of carbon approximately. It is known that the presence of three pyrene units should lead to a more stable complex for a similar surface coverages,[82] although the functionalization degree obtained for this series is lower than in the previous cases. The differences between complexes **9** and **10** should arise from the weakest interaction with FLG in the case of **complex 9** (see theoretical investigations in section 4.5)

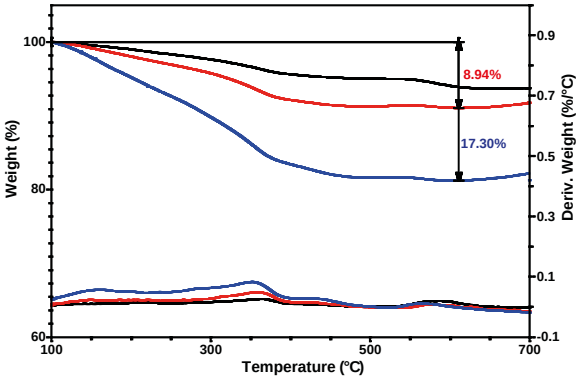

Figure 118. TGA weight loss and first derivative curves under inert conditions of FLG (black), **complex 9** (red) and **complex10** (blue).

Raman spectroscopy has been employed to examine the electronic characteristics of the obtained complexes and if their structures have been modified during the non-covalent functionalization. As expected, the I_D/I_G ratio does not increase after the supramolecular modification of FLG, meaning that its structure has not suffered any alteration (cutting, covalent modification) during this process (Figure 119). For the G band, it is surprisingly found a shift to lower frequencies for both complexes. Considering the electron-withdrawing ability of C_{60}, we expected the Raman G-band frequency to shift upwards compared with FLG due to the p-doping effect of C_{60}. However, these findings suggest that for both complexes the interaction mainly takes place through the pyrene moieties, a similar result has been reported recently.[172] Comparing **complex 9** with **complex 10**, the shift of the G band is higher for the last one

172. S. Qu, M. Li, L. Xie, X. Huang, J. Yang, N. Wang, S. Yang, *ACS Nano* **2013**, *7*, 4070-4081.

(insert in Figure 119), since the attachment to FLG via the pyrene "feet", acting as donor groups, causes a stronger electronic interaction in the tripodal system.

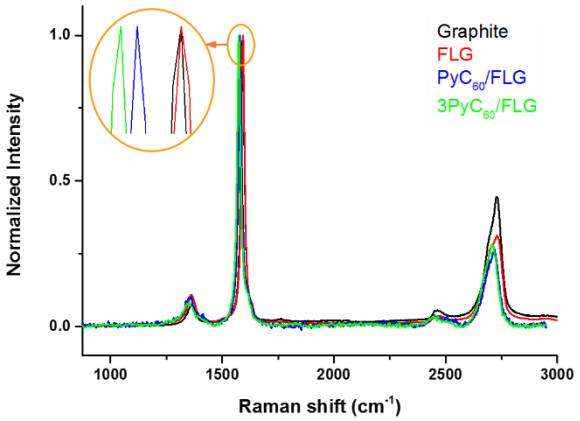

Figure 119. Raman spectra (λ_{exc} = 532 nm) of graphite, FLG, **complex 9** and **complex 10**.

In order to further demonstrate the different binding behavior to FLG of the monopodal and tripodal systems, consecutive cyclic voltammograms were recorded onto the surface of a glassy carbon electrode, where compounds **41** and **48** were adsorbed upon consecutive cycles (Figure 120).

In the case of PyC_{60} **41**, when the number of scans increases and the adsorption of the molecule takes place, all the redox processes are clearly observed. Whereas, in $3PyC_{60}$ **48**, for the same number of scans, the reductions associated with the C_{60} unit disappear. As in the previous π-exTTF and porphyrin-based systems, for the monovalent derivative the electroactive unit remains near the electrode due to the flexibility of the alkyl chain, and the electrons can diffuse to it, in spite of the adsorption. However, in the case of **48**, the C_{60} moiety is located far away from the electrode and the adsorption of the pyrene units completely covers the electrode and prevents the electron transport.

With these results, it is possible to say that for both complexes the interactions take place through the pyrene units and the adhesion of the tripodal system to the carbon surface is stronger than the monopodal system, something in somehow, in accordance with the Raman results.

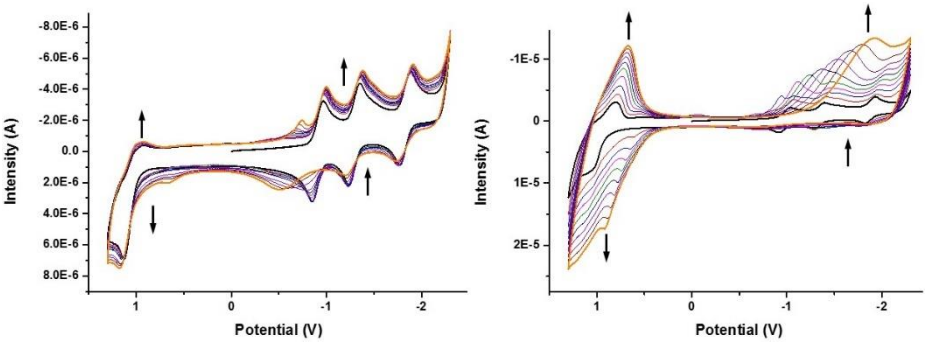

Figure 120. Consecutive cyclic voltammograms of **41** (left) and **48** (right), obtained in *o*-DCB/CH_3CN (5/1) solutions containing 0.1 M $TBAPF_6$ and using $Ag/AgNO_3$ as reference electrode, glassy carbon as working electrode and a Pt wire as counter electrode. Scan rate: 100 mV/s.

Finally, by TEM analysis, the morphology of the non-covalent hybrids was studied. In Figure 121, representative TEM images obtained for **complex 9** are shown. It is observed that, after the supramolecular modification, the material is still formed by few layers and the re-aggregation is prevented by the presence of the organic molecules.

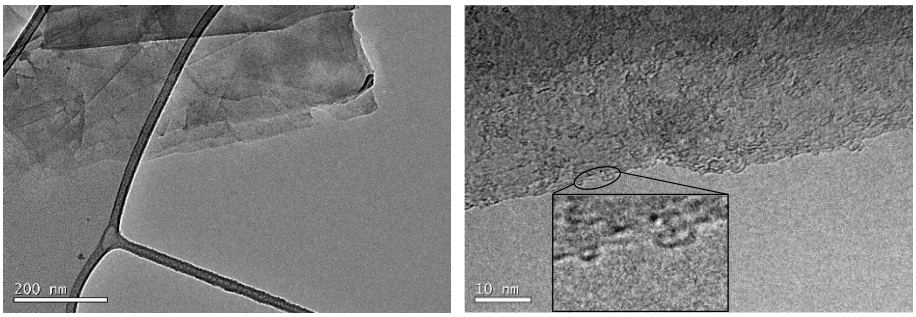

Figure 121. TEM images obtained after the non-covalent functionalization of FLG with PyC_{60} **41**.

In addition, when the images are obtained at 10 nm magnification, in the edges of FLG is detected the presence of small round shape forms with diameters at around 1 nm, confirming the presence of C_{60} in the sample and the non-covalent functionalization of FLG.

4.5. THEORETICAL STUDIES ON THE NON-COVALENT FUNCTIONALIZATION OF GRAPHENE WITH MONOPODAL AND TRIPODAL RECEPTORS

In order to shed light into the non-covalent interactions between the monopodal or tripodal pyrene-based receptors and FLG, a comprehensive theoretical analysis has been carried out in collaboration with the group of Prof. Enrique Ortí at Universidad de Valencia, using molecular mechanics calculations by means of the general MM3 force field[173] using Tinker 7.1.[174] Long molecular dynamics simulations were carried out for the supramolecular assembly of the different receptors with a graphene monolayer large enough to bear the biggest tripodal derivatives. The dynamics simulations were performed in gas phase, without periodic conditions and at room temperature (298 K) during 10 ns with a time step of 1 fs. The graphene sheet was frozen during the simulation. To better understand the non-covalent interaction along the time, the characteristic intramolecular geometry parameters of the receptors were analyzed in the dynamics (Figure 122).

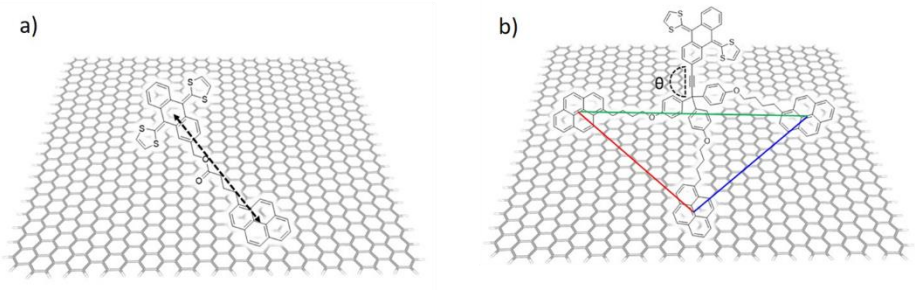

Figure 122. Characteristic intramolecular geometry parameters measured along the molecular dynamics for the monopodal (a) and tripodal (b) pyrene derivatives. Geometry parameters are defined as the distance between the centroids of pyrene and the counterpart moiety (π-exTTF, C_{60} or H_2P) for monopodal systems, and between the centroids of the pyrene feet in the tripodal derivatives. The tilting angle θ is defined as the angle between the sp^3 carbon connecting the three legs, the first *sp* carbon of the triple C≡C bond and the centroid of the head moiety (π-exTTF, C_{60} or H_2P).

In Figure 123 is depicted the evolution of the intramolecular distance between pyrene and the electroactive moiety in the monopodal derivatives. Theoretical calculations predict two well-differentiated regimes for these systems depending on the distance between the two units: the conformations in which the two moieties are separated by more than 14 Å —see e.g. 0–2.5 and 3.0–10.0

173. N. L. Allinger, Y. H. Yuh, J. H. Lii, *J. Am. Chem. Soc.* **1989**, *111*, 8551-8566.
174. J. W. Ponder, *TINKER Version 7.1* **2015**, http://dasher.wustl.edu/tinker.

ns in **11**, > 7 ns in **41**, and > 1.5 ns in **30**, and folded structures with shorter pyrene-counterpart distances of around 10 Å (Figure 123).

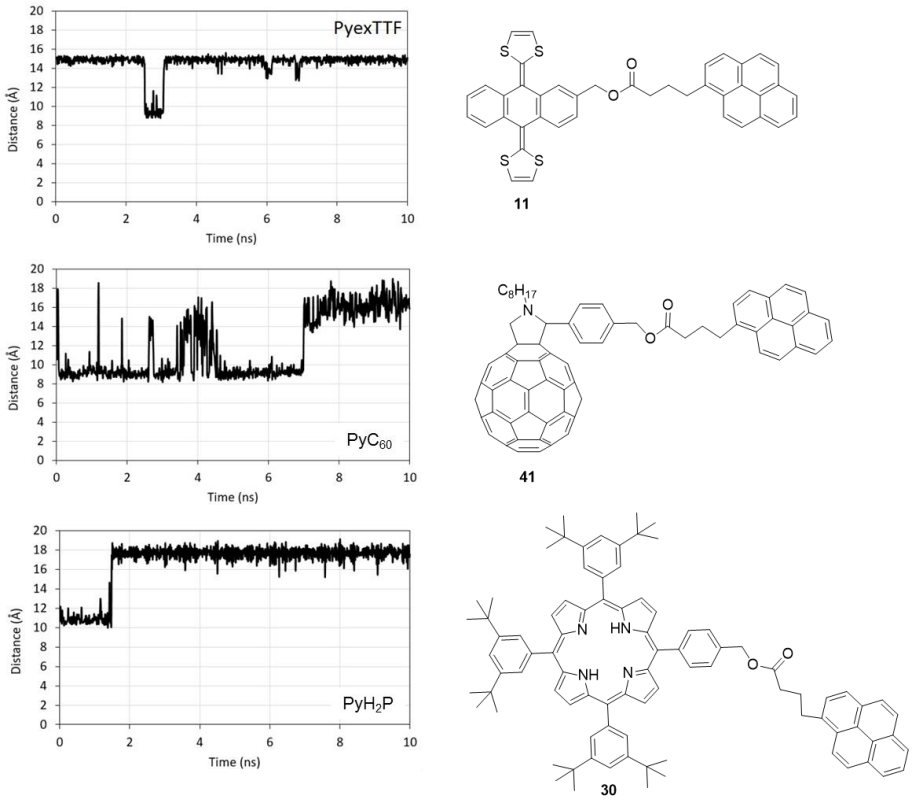

Figure 123. Evolution of the intramolecular distance between pyrene and the counterpart (π-exTTF, C_{60} or H_2P) along the long molecular dynamics simulation in the monopodal pyrene-based receptor/graphene assemblies.

As an example, the two possible conformations for the monopodal PyexTTF **11** are shown in Figure 124.

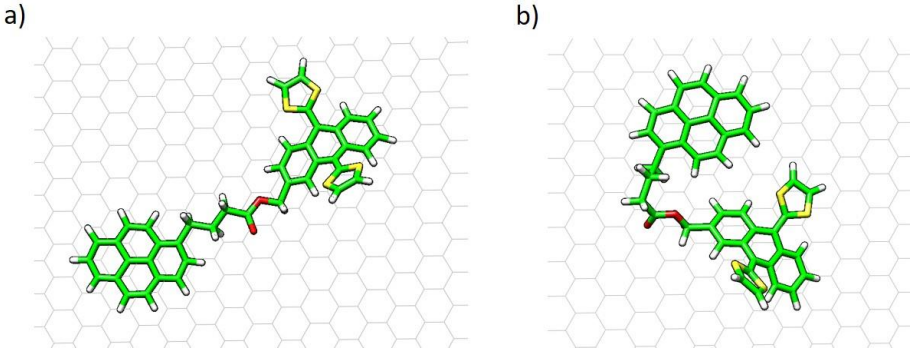

Figure 124. a) Extended and b) folded conformations for the monopodal PyexTTF/graphene assembly.

In the case of the tripodal derivatives, the evolution of the intramolecular distances between the three pyrene units (Figure 125) indicates that the extended conformation in which the three pyrene feet are well separated between each other (~20 Å) barely exists along the simulation (see e.g. 0–0.5 ns in $3PyH_2P$). In contrast, conformations in which one foot remains close to one vicinal pyrene are predicted as the most visited structures along the dynamics simulation. Interestingly, in the case of $3PyC_{60}$, the distance between two pyrene units (red in Figure 125) is maintained after 1 ns simulation. At this time, the fullerene ball interacts with the graphene sheet and separates two pyrene units at a fixed distance of ~18 Å (see also Figure 129b).

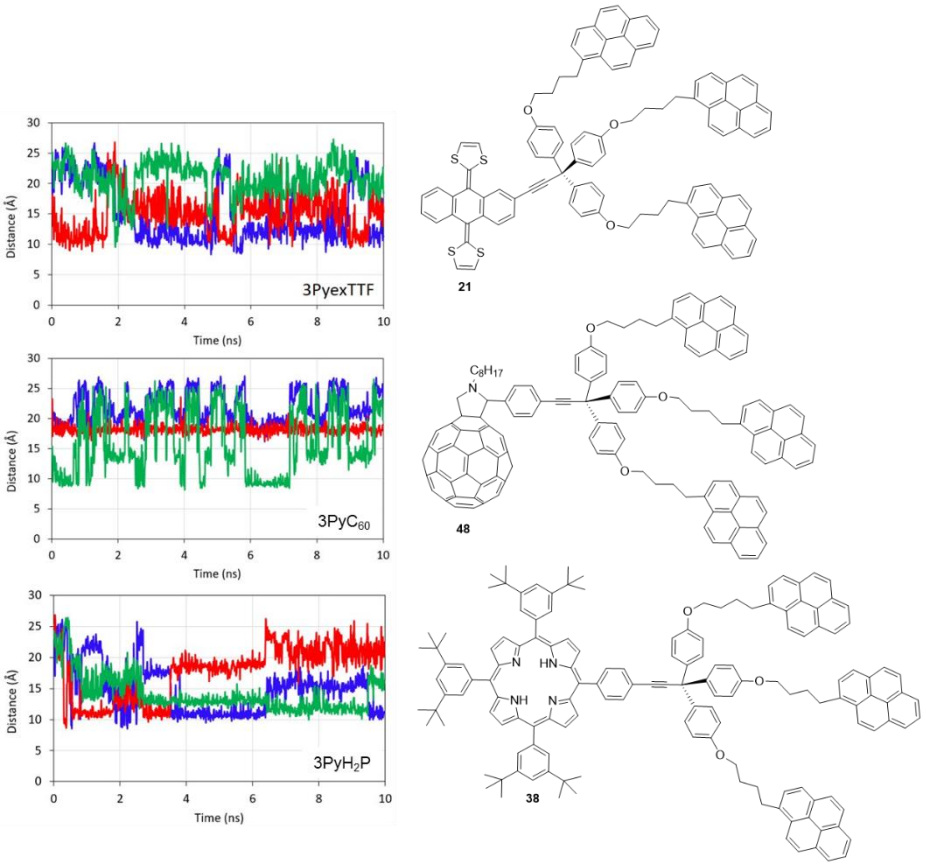

Figure 125. Evolution of the intramolecular distances between the three pyrene units along the long molecular dynamics simulation in the tripodal pyrene-based receptor/graphene assemblies. See Figure 122b to identify the colors used for geometry parameter specifications.

Finally, the tilting angle of the head moiety (π-exTTF, C_{60} or H_2P) with respect to the triple C≡C bond (Figure 122b) was measured along the molecular

dynamics simulation (Figure 126). Theoretical calculations predict a rapid evolution of the angle from 160–180º to 100–140º indicating that the head moiety is able to interact favorably with one of the pyrene feet by means of noncovalent interactions. This tilting angle is particularly small in the case of $3PyC_{60}$ (Figure 126) due to a strong supramolecular interaction between the fullerene ball and the graphene sheet (Figure 129b). After 6.3 ns in $3PyH_2P$, the tilting angle turns to 160-180º describing the detachment of one pyrene-based foot from the graphene sheet due to the strong interaction of the porphyrin moiety with graphene.

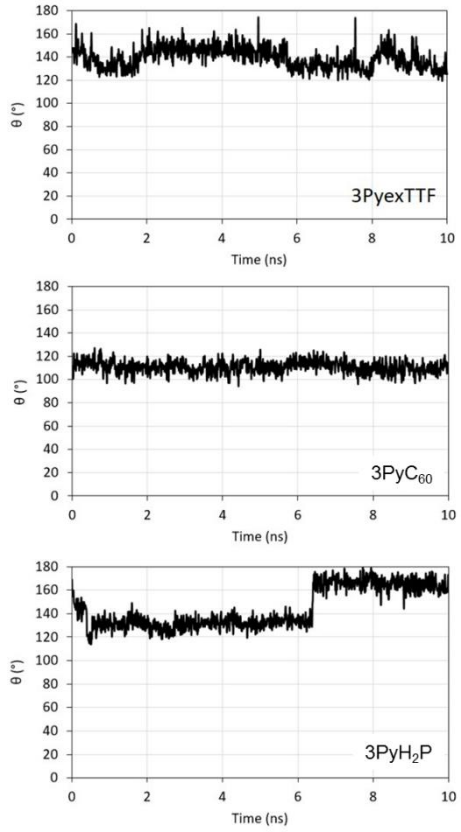

Figure 126. Evolution of the tilting angle θ of the head moiety (π-exTTF, C_{60} or H_2P) with respect to the triple C≡C bond along the long molecular dynamics simulation in the tripodal pyrene-based receptor/graphene assemblies. See Figure 122b.

In order to quantify the supramolecular interaction between the pyrene-based receptors and graphene, representative snapshots of the molecular dynamics were extracted and their geometries were optimized using the MM3 force field keeping the atoms of the graphene sheet frozen. Minimum-energy geometry for

PyexTTF (Figure 127a and Figure 128a) indicates stabilizing π–π interactions between pyrene and graphene in the 3.2–3.6 Å range together with short CH···π (2.6–2.9 Å) and O···π (3.4–3.6 Å) contacts between the aliphatic chain and graphene. Interestingly, the π-exTTF unit interacts with graphene by means of a mixed supramolecular interaction involving π–π, CH···π and S···π forces (Figure 127a). This conformation has been reported as the most stable arrangement for the supramolecular interaction between π-exTTF and graphene by means of high-level revPBE0-D3/cc-pVTZ theoretical calculations.[91]

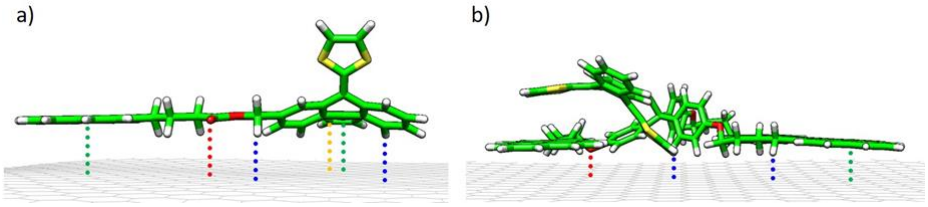

Figure 127. Representation of the different noncovalent interactions stabilizing the supramolecular recognition of monopodal (a) and tripodal (b) π-exTTF-based receptors/graphene assemblies. Color coding: CH···π (blue), O···π (red), S···π (yellow) and π–π (green).

In the case of 3PyexTTF (Figure 127b and Figure 128b), theoretical calculations predict for the minimum-energy structure short π–π interactions in the 3.3–3.7 Å range between the three pyrene units and graphene, as in the case of the analogous monopodal derivative. In addition, CH···π and O···π contacts are calculated at 2.6–3.0 and 3.2–3.5 Å, respectively, between the leg connectors and graphene. Finally, although highly tilted from perpendicularity, the π-exTTF moiety is only able to interact with graphene by two CH···π interactions calculated at 2.8–3.0 Å (Figure 127b).

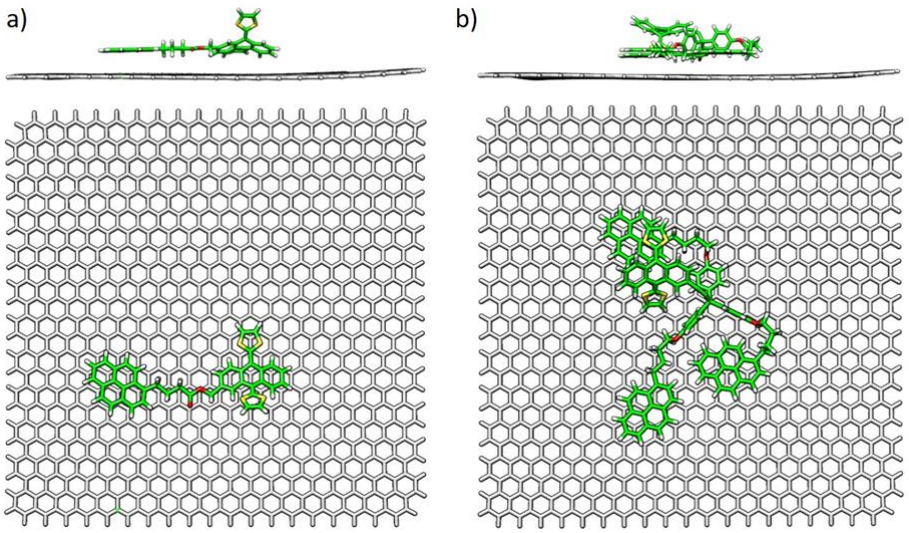

Figure 128. Side and top views of the minimum-energy geometry calculated at the MM3 level for a representative structure of the supramolecular assembly of graphene with monopodal (a) and tripodal (b) π-exTTF-based receptors.

In the monopodal and tripodal C_{60}-based receptors, the supramolecular recognition with graphene is similar to that obtained for the previous π-exTTF-based derivatives. In PyC_{60}, a short interaction between the fullerene ball and graphene is predicted around 3.0 Å, together with a large number of CH···π contacts in the range of 2.6–3.0 Å (Figure 129a). Moving to $3PyC_{60}$, the fullerene head is able to interact with graphene through both the C_{60} ball with short π–π interactions (2.9–3.1 Å) and the long aliphatic chain with CH···π contacts calculated at 2.8–3.1 Å (Figure 129b).

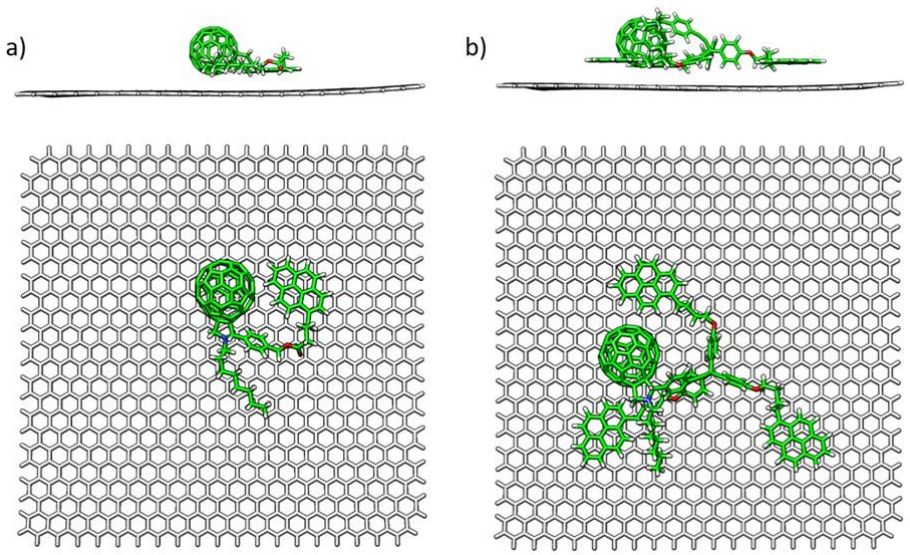

Figure 129. Side and top views of the minimum-energy geometry calculated at the MM3 level for a representative structure of the supramolecular assembly of graphene with monopodal (a) and tripodal (b) C_{60}-based receptors.

The minimum-energy geometry predicted for PyH_2P/graphene assembly indicates similar supramolecular interactions in the pyrene branch as described before for the other systems. In this case, the porphyrin interacts with the graphene sheet by means of a large surface of contacts of π–π (3.2–3.9 Å) and CH···π (2.7–3.1 Å) nature (Figure 130a). In the case of the tripodal analogue $3PyH_2P$, the porphyrin is predicted to interact with one pyrene foot but reaches the graphene sheet through its peripheral *tert*-butyl benzene groups with small CH···π interactions in the 2.9–3.2 Å range (Figure 130b).

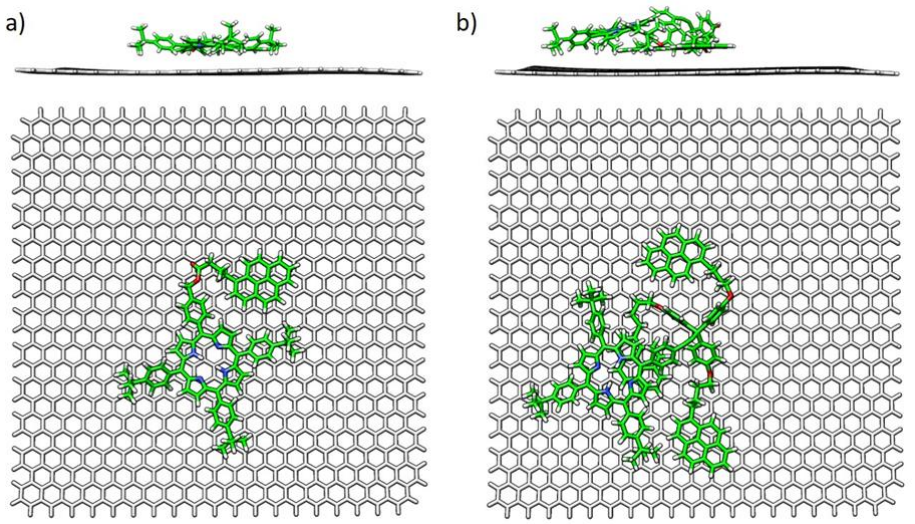

Figure 130. Side and top views of the minimum-energy geometry calculated at the MM3 level for a representative structure of the supramolecular assembly of graphene with monopodal (a) and tripodal (b) porphyrin-based receptors.

Interaction energies for the different receptors/graphene arrangements were calculated at the MM3 level using the representative minimum-energy geometries described above for the monopodal and tripodal systems (Table 10). Deformation energies were not considered.* Theoretical calculations predict for the monopodal derivatives a large interaction energy (E_{int}) with graphene of more than –50 kcal/mol in all cases. The E_{int} of PyexTTF is calculated the smallest among the series due to the small surface of interaction between the nonplanar π-exTTF unit and the graphene sheet. Interestingly, PyC_{60} remains in between, with an E_{int} of almost –70 kcal/mol. The extra stabilization of PyC_{60} with respect to PyexTTF is not only ascribed to the $C_{60}\cdots$graphene interaction but also to the large number of $CH\cdots\pi$ contacts between the long aliphatic chain and the sheet (Figure 129a). PyH_2P/graphene is calculated with a large E_{int} of –97 kcal/mol owing to the extended surface of porphyrin$\cdots$graphene interaction.

Moving to the tripodal systems, theoretical calculations predict larger interaction energies with graphene compared to the monopodal derivatives. Among the three tripodal receptors, the smallest E_{int} is computed for 3PyexTTF due to the small interaction between π-exTTF and graphene (Figure 127b).

* Density Functional Theory calculations demonstrated that the deformation energy provoked by the tilting of the head units in the tripodal host/graphene recognition amounts only 7 kcal/mol at the B3LYP/6-31G** level of theory.

Despite the larger E_{int} predicted in the monopodal PyH_2P compared to the C_{60} analogue, the tripodal $3PyC_{60}$ and $3PyH_2P$ systems present almost identical interaction energies. The supramolecular interaction of porphyrin only through its peripheral *tert*-butyl groups in $3PyH_2P$/graphene, on the one hand, and the short $C_{60}\cdots$graphene contacts predicted for the $3PyC_{60}$ derivative, on the other hand, explains the trends theoretically predicted in the E_{int} (Table 10). As a reference, the interaction energy of a pyrene unit over graphene amounts to –23.4 kcal/mol at the same level of theory. For the monopodal derivatives, it is logical that E_{int} is calculated significantly larger due to the presence of other supramolecular interactions originated from the counterpart (π-exTTF, C_{60} or H_2P) and the chain linking both fragments. In the case of the tripodal systems, E_{int} is calculated significantly larger than three times the pyrene interaction (–23.4 x 3 = –70.2) in all cases (Table 10). These results suggest that all the supramolecular forces described above for the tripodal derivatives with graphene, involving both the pyrene legs, the head moiety and the saturated chain linker, are relevant for the final stabilization of the receptor/graphene complex.

Table 10. Interaction energies calculated for the receptor/graphene assemblies at the MM3 level of theory for representative minimum-energy structures.

Host	E_{int} (kcal/mol)
PyexTTF	–58.0
PyC_{60}	–72.3
PyH_2P	–98.3
3PyexTTF	–115.4
$3PyC_{60}$	–129.1
$3PyH_2P$	–131.2

The supramolecular interaction between the monopodal and tripodal systems with graphene was finally analyzed in terms of the intermolecular contact area between the receptor and the graphene sheet. The intermolecular contact area was calculated using Chimera 1.7[175] as (surface of host + surface of guest – surface of complex)/2, where the area refers to solvent-excluded molecular surfaces. Figure 131 shows a nice correlation between the intermolecular contact area and the interaction energy calculated for the different systems with

175. E. F. Pettersen, T. D. Goddard, C. C. Huang, G. S. Couch, D. M. Greenblatt, E. C. Meng, T. E. Ferrin, *J. Comput. Chem.* **2004**, *25*, 1605-1612.

graphene as expected from the dispersion nature of the interactions involving the supramolecular self-assembly.

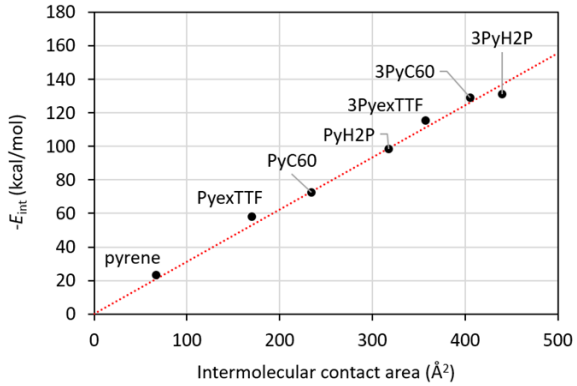

Figure 131. Relationship between the intermolecular contact area and the interaction energy for the receptors/graphene assemblies.

5. CONCLUSIONS

5. CONCLUSIONS

The research developed in this PhD work has provided valuable information on the construction of supramolecular aggregates between a complete series of molecular receptors and FLG. The results obtained can be summarized in the following bullet points:

- In the search for an optimum solvent in the exfoliation of graphite, three different solvents were tested: NMP, *o*-DCB and DMF. Under the same conditions of sonication and centrifugation, it was observed that DMF was not able to stabilize the graphene layers, providing dispersions with a high degree of sedimentation. For this reason this solvent was discarded for the exfoliation of graphite. In the case of NMP and *o*-DCB, homogeneous dispersions without sedimentation were obtained and further studied by TEM. In both solvents graphite was efficiently exfoliated, although the aggregates obtained in *o*-DCB were formed with a higher number of layers than in the case of NMP, evidencing a lower exfoliation degree. Finally, Raman spectroscopy carried out with the material obtained in the exfoliation with NMP allowed to estimate that the material is composed by approximately three layers of graphene (FLG), allowing to conclude that the optimum solvent for the exfoliation of graphite is NMP.
- In addition, the sonication time influence in the exfoliation efficiency was studied. Using NMP as solvent and keeping the same centrifugation conditions, three different times were employed for the sonication: 2.5, 18 and 24 hours. It was observed that for longer sonication times the concentration of the dispersions increases, even though TEM showed that the dimensions of the flakes decreased and that these smaller flakes tend to agglomerate. This finding can be explained by the fact that the solvent around the layers is proportional to the sphere described by the flake, meaning that for smaller flakes the solvent around them is lower and the concentration increases. The election of the exfoliation conditions depends on the subsequent application of the obtained material, in our case we decided to work with less concentrated dispersions, but with higher flake dimensions, in order to facilitate the non-covalent functionalization of FLG.
- A complete series of receptors, containing one or three pyrene anchoring groups, was designed and synthesized following common organic synthetic strategies that provided the desired molecules with good yields. Furthermore, three different families of molecular receptors, endowed with

π-exTTF, porphyrin (free base, Zn, or Ni) and C_{60} electroactive units, were prepared and thoroughly characterized.

- The non-covalent interactions between the different families of pyrene-based receptors were studied by ^{1}H-NMR experiments. For the monopodal derivatives, ^{1}H-NMR titrations were performed adding increasing amounts of the PyC_{60} derivative **41** to a solution of the porphyrins (PyH_2P, PyZnP and PyNiP) **30**-**32** or PyexTTF **11** derivatives, with the aim to determine if these systems were able to form donor-acceptor ensembles in solution. In the case of the porphyrin derivatives it was observed that the interaction and the value of the binding constant depend on the central atom present in the porphyrin unit. For the PyexTTF derivative the interaction is much weaker than for the porphyrin systems. On the other hand, concentration and temperature dependent ^{1}H-NMR experiments were performed for $3PyC_{60}$ **48**, in order to investigate its self-assembly. In both experiments the aromatic signals are shifted upfield, suggesting the formation of aggregates through π-π stacking interactions.

- The studies in solution of the possible interactions between the different molecular receptors and FLG showed that all the systems interact with the basal plane of graphene. In UV-Vis titrations, when increasing amounts of FLG were added, changes in the spectra were observed for all the monopodal and tripodal derivatives. In addition, these changes are accompanied by the presence of pseudo-isosbestic points that hint to an equilibrium process for this interaction. For the π-exTTF and C_{60} families, fluorescence titrations were performed with the aim to corroborate the interaction of the pyrene units present in all the molecular receptors. When increasing amounts of FLG were added, the quenching of the pyrene emission was observed in all the systems, being this attenuation similar for all of them.

- The synthesis of the supramolecular complexes of FLG and the molecular receptors was carried out following a procedure that combines sonication, filtration and washings steps. Afterwards, the formation of the non-covalent hybrids was confirmed by several analytical, spectroscopic and microscopic techniques. In the *UV-Vis* spectrum of each complex the characteristic bands of the organic molecule are observed, the pyrene bands at 329 and 345 nm in the complexes formed by the π-exTTF and C_{60} derivatives, and the Soret band at around 425 nm in the complexes formed by the porphyrin derivatives. The functionalization degree was determined by *TGA*, being in

general higher for the monopodal derivatives due to their smaller size. Moreover, the supramolecular complexes present a slight stabilization in the temperature desorption when they are compared with the organic molecules, due to the non-covalent interaction with FLG. In the *Raman* spectra of all complexes, a shift of the G band to lower frequencies when compared with FLG is observed. These findings suggest that the interaction of the different systems with the basal plane of graphene modifies its electronic properties through π-π stacking interactions in all cases. *XPS* spectroscopy allowed to determine that in the case of PyexTTF/FLG (**complex 1)** and 3PyexTTF/FLG (**Complex 2**), the interaction with FLG is different for each compound. The peak corresponding to sulfur in **complex 1** is shifted to lower binding energies when is compared with the organic molecule **11**, suggesting a charge transfer from the π-exTTF unit to FLG. However, in **complex 2** there is no appreciable shift of the sulfur peak. These results agree with the different shifts observed in Raman spectroscopy for both complexes.

- The more probable conformations for the receptors in their interaction with graphene were investigated by molecular mechanics calculations, and their geometries optimized in order to quantify the supramolecular binding. For all systems, the most probable conformation is the one which maximizes the π interactions between the whole molecule and the basal plane of graphene. In the case of the monopodal derivatives, both the pyrene and the π-exTTF, P, or C_{60} units interact with the graphene surface, whereas in the tripodal derivatives implies the approach of two pyrene units and partially the π-exTTF, P, or C_{60} units interact with the graphene surface. These results, together with the interaction energies calculated, shed light on the shifts observed in Raman spectroscopy for the G band.
- The electrochemical behavior of PyexTTF **11** and 3PyexTTF **21** was studied in three different graphene-based modified glassy carbon (GC) electrodes: with graphene oxide (GO/GC), with electro-reduced graphene oxide (GO-ER/GC) and with pristine graphene (Graphene/GC). The non-covalent functionalization of these electrodes with PyexTTF **11** and 3PyexTTF **21** allowed to determine the different affinity of these molecules for the distinct surfaces, being bigger for the GO-ER/GC and Graphene/GC electrodes due to their higher π-conjugated surface and their hydrophobic character. By Laviron analyses it was determined the electron transfer rate for both systems, and in all the electrodes the value of the heterogeneous charge

transfer rate constant is greater for the monopodal derivative PyexTTF **11**, indicating that for the tripodal derivative 3PyexTTF **21** the π-exTTF unit is located far away from the electrode surface. These results agree with the previously obtained by Raman and XPS spectroscopy, and with the theoretical calculations. In addition, the surface coverage and the kinetic stability were also studied, and it was observed that in spite of its higher size and the lower surface coverage, the tripodal derivative 3PyexTTF **21** allows to obtain more stable layers due to the presence of the three pyrene units. Moreover, PyexTTF/GO-ER/GC modified electrodes were used to develop an enzymatic biosensor due to their higher surface coverage and their better electrochemical response in aqueous media. The HRP enzyme was immobilized onto the electrode and its response *vs.* increasing amounts of H_2O_2 was studied. It was observed that the monopodal derivative PyexTTF **11** acts as an electrochemical mediator in this biosensor, which is able to operate at very low potentials with a good linear response.

- In the case of the porphyrin families, the electronic communication in the non-covalent hybrids was preliminary investigated by transient absorption spectroscopy. For the monopodal derivatives, the spectral features of the porphyrin cation were observed for the PyZnP/FLG complex, due to the electron transfer from the porphyrin unit to graphene. In the case of the tripodal derivatives, no evidences of the cation features in the non-covalent hybrids were obtained, although further investigations are being carried out.

6. EXPERIMENTAL SECTION

6. EXPERIMENTAL SECTION

Materials

All reagents were purchased from commercial sources and used without further purification with the exception of pyrrole, which was filtered through an Al_2O_3 gel column prior to use to remove polymers. Solvents were dried and distilled using standard techniques.[176] Those reactions requiring an inert atmosphere were carried out using Argon as source.

The graphite used for graphene exfoliation was purchased from TIMCAL (TIMREX SFG15, ρ = 2.26 g/cc, particle size = 8.80 μm, surface area = 9.50 m^2/g, ash ≤ 0.100%, interlaminar distance = 0.3354-0.3358 nm).

Vacuum filtrations of graphene materials were carried out with polycarbonate track etched (PCTE) (pore size = 0.2 μm, Φ = 47 cm) and polytetrafluoroethylene (PTFE) (pore size = 0.2 μm, Φ = 47 cm) membranes.

π-exTTF, used as reference in different analysis, was synthesized using the procedure previously described in the bibliography.[127] Symmetric porphyrins used as references in different analysis were obtained from the regioisomeric mixture isolated in the statistical condensation of compounds **30** and **35**.

General techniques

Analytical thin-layer chromatography (TLC): was performed using aluminum coated Merck Kieselgel 60 F254 plates to check the evolution of reactions. Visualization was made by UV light (λ = 254 or 365 nm).

Purification of crude reaction mixtures: was achieved by flash column chromatography or gravity-fed column chromatography using silica gel.

NMR spectra: were recorded on a Bruker DPX-300, Bruker AV-500 or Bruker AVIII-700 at 298 K, using partially deuterated solvents as internal standards. Chemical shifts (δ) are expressed in ppm and are referred to the residual peak of the solvent. Spin multiplicities are reported as singlet (s), doublet (d), triplet (t), quartet (q), multiplet (m) and broad (br), with proton-proton coupling constants (*J*) given in Hz.

FT-IR spectra: were recorded on a Bruker TENSOR 27 (ATR device, 7500-370 cm^{-1}), with a resolution of 1 cm^{-1}.

176. W. L. F. Armarego, C. L. L. Chai, *Purification of Laboratory Chemicals*, Elsevier, **2003**.

Mass spectra: were realized by the mass spectra services at the Universidad Complutense de Madrid and at the Universidad Autónoma de Madrid. Electronic Impact measurements (EI) were recorded using a HP 5989A apparatus (70 eV, 200 ºC). MALDI-TOF measurements were recorded utilizing a BRUKER-REFLEX III apparatus (matrix: dithranol, N_2 laser at 337 nm) or Brucker Ultraflex III apparatus (matrix: *trans*-2-[3-(4-*tert*-Butylphenyl)-2-methyl-2-propenylidene]malononitrile (DCTB)).

UV-Vis-NIR spectra: were recorded with a Shimadzu Spectrophotometer UV-3600 at 298 K, with a resolution of 1 nm.

Fluorescence spectra: were recorded with a Fluoromax-4 spectrofluorometer (HORIBA) at 298 K.

Raman spectra: were recorded on a NT-MDT in Via Microscope at room temperature using an exciting laser source of 532 nm.

Thermogravimetric analyses (TGA): were carried out with a thermobalance TA-TGA-Q-500 under N_2 or air atmosphere, depending on the sample. The sample (≈ 0.5 mg) was introduced inside a platinum crucible and equilibrated at 90 ºC followed by a 10 ºC/min ramp between 90 and 1000 ºC.

XPS analysis: were performed on a SPECS GmbH (PHOIBOS 150 9MCD) spectrometer operating in the constant analyzer energy mode. A non monochromatic aluminium X-ray source (1486.61 eV) was used with a power of 200 W and voltage of 12 kV. Pass energies of 75 and 25 eV were used for acquiring both survey and high resolution spectra, respectively. Survey data were acquired from kinetic energies of 1487-400 eV with an energy step of 1 eV and 100 ms dwell time per point. *SpecsLab Version 2.48* software was used for spectrometer control and data handling. The semi-quantitative analysis were performed from the C 1s (284.3 eV) signal. The samples were introduced as pellets of 8 mm diameter.

Transmission electron microscopy (TEM): was performed on a JEOL JEM 2100, with an acceleration voltage of 200 kV equipped with a camera CCD ORIUS SC1000 (model 832) and the microanalysis were performed by XEDS (OXFORD INCA). The samples were dispersed in NMP and dropped onto a holey carbon copper grid (200 mesh), the solvent was removed in a vacuum oven during 48 hours.

Scanning electron microscopy (SEM): was performed on a JEOL JSM 6335F, working at 10 kV. Samples were deposited by drop-casting on a glass plate,

dried in a vacuum oven during 48 hours and metallized with Au prior to observation.

Atomic force microscopy (AFM): was performed under ambient conditions using SPM Nanoscope IIIa multimode working on tapping mode with a RTESPA tip (Veeco) at a working frequency of B235 KHz. Height and phase images were simultaneously obtained. The samples were prepared by drop-casting or spin coating on freshly cleaved mica and were dried under ambient conditions for 24 hours and later in a vacuum oven during 48 hours.

Confocal microscopy: was performed under ambient conditions on a OLYMPUS FV1200, with three confocal detectors and seven lasers. The samples were prepared by drop-casting on a glass plate and measured with an exciting laser source of 405 nm.

Cyclic voltammetry: was carried out on a potentiostat/galvanostat AUTOLAB with PGSTAT30 equipped with a software GPES for windows version 4.8 in a conventional three compartment cell. Platinum wire was used as the counter electrode and the working electrode was a glassy carbon electrode. The reference electrode was a silver/silver ion electrode (0.01 M $AgNO_3$, 0.1 M tetrabutylammonium hexafluorophosphate ($TBAPF_6$)/CH_3CN). CVs were recorded using a scan rate of 100 mV/s. The samples were dissolved in *o*-DCB/CH_3CN (5/1) and the solutions were purged for 20 min. with argon prior to the electrochemical measurements.

The measurements carried out by the group of Prof. Encarnación Lorenzo at UAM were performed with a potentiostat AUTOLAB PGSTAT128N using the software package GPES 4.9. For conventional three electrode experiments, a homemade single compartment electrochemical cell was employed. Glassy carbon (GC) electrodes were used as working electrodes and Pt wire as counter electrode. Specific calomel electrode (1M LiCl for organic media from Radiometer Analytical) and sodium saturated calomel electrode were used as reference electrodes for experiments in organic solvents and aqueous environment, respectively. Prior to the experiments all solutions were deoxygenated by bubbling nitrogen for 5 min. All experiments were carried out at room temperature.

GC electrodes were modified with graphene by three different strategies as follows:

- Graphene Oxide/Glassy Carbon electrode (GO/GC): was prepared by drop-casting 5 μL of the synthesized graphene oxide[67,177] onto a glassy carbon electrode and left to dry.
- Graphene Oxide Electrochemically Reduced/Glassy Carbon electrode (GO-ER/GC): was assembled by drop-casting 5 μL of the synthesized graphene oxide onto glassy carbon electrode and left to dry. Then, the electrode was immersed in a buffer solution of pH 5, 0.1 M acetic acid/potassium acetate, and 15 cyclic voltammetry scans were applied between 0 and -1.5 V at 50 mV/s. After the repetitive scans the electrode was rinsed with Milli-Q water and left to dry.[178]
- Pristine Graphene/Glassy Carbon electrode (Graphene/GC): was prepared by successively deposition of 5 drops (10 μL) of the synthesized pristine graphene onto a glassy carbon electrode and left to dry in a vacuum desiccator. In this case, graphene was exfoliated in DMF following the procedure described later.

The PyexTTF/GO-ER/GC modified electrode was prepared by the adsorption of PyexTTF **11** from solution during 15 hours. A 0.36 mM **11**/THF solution was used to prepare the developed biosensor. 2.5 μL of a solution containing 12.1 U of HRP/μL in PBS at pH 6.5 was deposited onto the PyexTTF/GO-ER/GC electrode, after that 2.5 μL of 2.5% glutaraldehyde solution was added and left to dry in order to cross-link the HRP on the electrode surface. Biosensor response to H_2O_2 was obtained by chronoamperometry at 0.0 V.

Transient absorption measurements: were performed with the transient absorption pump probe system HELIOS from ultrafast systems. To generate laser pulses with a pulse width of 150 fs and a wavelength of 775 nm a CPD-2110 titanium:sapphire laser system from Clark-MXR Inc. was utilized.

177. a) W. S. Hummers, R. E. Offeman, *J. Am. Chem. Soc.* **1958**, *80*, 1339. b) E. Casero, A. M. Parra-Alfambra, M. D. Petit-Domínguez, F. Pariente, E. Lorenzo, C. Alonso, *Electrochemistry Communications* **2012**, *20*, 63-66. c) E. Casero, C. Alonso, L. Vázquez, M. D. Petit-Domínguez, A. M. Parra-Alfambra, M. de la Fuente, P. Merino, S. Álvarez-García, A. de Andrés, F. Pariente, E. Lorenzo, *Electroanalysis* **2013**, *25*, 154-165.
178. H.-L. Guo, X.-F. Wang, Q.-Y. Qian, F.-B. Wang, X.-H. Xia, *ACS Nano* **2009**, *3*, 2653-2659.

6.1. SYNTHESIS OF ORGANIC COMPOUNDS

2-(Methylthio)-1,3-dithiolium tetrafluoroborate (2)[127]

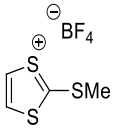

1,3-Dithiole-2-thione **1** (5.29 g, 39.39 mmol) was suspended in Me_2SO_4 (39.4 mL, 416.40 mmol), heated at 95 ºC during 30 minutes and then left to cool to 0 ºC. At this temperature, glacial acetic acid (8 mL) was added and kept stirring during 10 minutes. $HBF_4 \cdot Et_2O$ (5.4 mL, 39.39 mmol) was added and the solution was stirred during 20 extra minutes, followed by the addition of diethyl ether (125 mL) to yield a precipitate that was filtered and washed with diethyl ether (95%).

^{1}H-NMR (DMSO-d_6, 300 MHz), δ: 8.73 (s, 2H), 3.17 (s, 3H).

2-(Methylthio)-1,3-dithiole (3)[127]

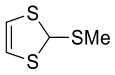

$NaBH_4$ (0.28 g, 7.41 mmol) was slowly added to a 0 ºC cooled solution of 2-(methylthio)-1,3-dithiolium tetrafluoroborate **2** (1.72 g, 7.29 mmol) in absolute ethanol under Ar atmosphere and the mixture was kept stirring during 2 hours. The solvent was removed under reduced pressure, washed with water and extracted with DCM. The organic layer was dried over $MgSO_4$, filtered and taken to dryness to yield the desired product as a dark oil (95%).

^{1}H-NMR ($CDCl_3$, 300 MHz), δ: 6.12 (s, 1H), 6.07 (s, 2H), 2.20 (s, 3H).

1,3-Dithiolium tetrafluoroborate (4)[127]

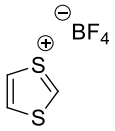

To a solution of 2-(methylthio)-1,3-dithiole **3** (0.77 g, 5.12 mmol) in acetic anhydride (12.5 mL) at 0 ºC, $HBF_4 \cdot Et_2O$ (0.7 mL, 5.22 mmol) was added dropwise. The solution was stirred during 15 minutes, afterwards diethyl ether (125 mL) was added. The mixture was stirred again during 30 minutes to yield a white solid that was filtered and washed with diethyl ether (95%).

^{1}H-NMR (DMSO-d_6, 300 MHz), δ: 6.79 (s, 1H), 9.37 (s, 2H).

Dimethyl-(1,3-dithiol-2-yl)-phosphonate (5)[127]

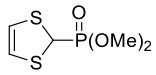

To a solution of 1,3-dithiolium tetrafluoroborate **4** (0.63 g, 3.31 mmol) in acetonitrile, $P(OMe)_3$ (0.40 mL, 3.31 mmol) and NaI (0.48 g, 3.31 mmol) were added successively, stirring the resultant mixture at room temperature during 2 hours. The crude reaction solvent was then removed under reduced pressure, washed with water and extracted with DCM. The organic layer was dried over $MgSO_4$, filtered and the solvent was removed to yield the desired product as a dark oil (90%).

^{1}H-NMR ($CDCl_3$, 300 MHz), δ: 5.98 (s, 2H), 4.73 (d, 1H, *J* = 4.5 Hz), 3.75 (d, 6H, *J* = 10.5 Hz).

2-(((*Tert*-butyldiphenylsilyl)oxy)methyl)anthraquinone (7)[179]

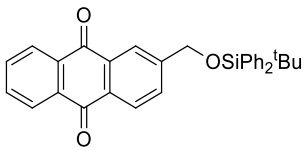

2-Hydroxymethylanthraquinone **6** (1.00 g, 4.20 mmol) was dissolved in 50 mL of anhydrous THF and, under Ar atmosphere, imidazole (1.43 g, 21.00 mmol) and *tert*-butyldiphenylsilane chloride (1.3 mL, 5.03 mmol) were added. The reaction mixture was kept stirring overnight. Then, the solvent was removed under reduced pressure and the residue was dissolved in DCM and washed with water. The organic layer was dried with $MgSO_4$ and filtered, the solvent was then evaporated to yield a crude that was purified by silica gel column chromatography, using a hexane/DCM (2/1) mixture as eluent. The final product was obtained as a pale yellow solid (90%).

^{1}H-NMR ($CDCl_3$, 300 MHz), δ: 8.33-8.25 (m, 4H), 7.83-7.79 (m, 3H), 7.73-7.70 (m, 4H), 7.47-7.38 (m, 6H), 4.92 (s, 2H), 1.16 (s, 9H).

179. G. J. Marshallsay, M. R. Bryce, *J. Org. Chem.* **1994**, *59*, 6847-6849.

2-(((*Tert*-butyldiphenylsylyl)oxy)methyl)-9,10-bis(1,3-dithiol-2-ylidene)-9,10-dihydroanthracene (8)[180]

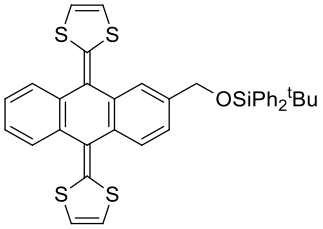

A volume of 2.0 mL of *n*-BuLi (1.6 M in hexane, 3.20 mmol) was added to a solution of dimethyl (1,3-dithiol-2yl)phosphonate **5** (0.58 g, 2.75 mmol) in anhydrous THF (100 mL) at -78 ºC and under Ar atmosphere. The mixture was kept stirring during 45 minutes at the same temperature. Then, 2-(((*tert*-butyldiphenylsilyl)oxy)methyl)anthraquinone **7** (0.22 g, 0.47 mmol) was dissolved in anhydrous THF (100 mL) and added dropwise. The mixture was kept at -78 ºC during 1 hour and then was left to reach room temperature overnight. The solvent was removed under reduced pressure and the crude was washed with water (100 mL) and extracted with DCM (3 x 100 mL). The combined organic layers were washed with water (2 x 100 mL) and a saturated NaCl aqueous solution (2 x 100 mL), dried over $MgSO_4$ and filtered. The solvent was removed and the residue was purified by silica gel column chromatography using a hexane/DCM (2/1) mixture as eluent. The final product was obtained as a yellow solid (96%).

^{1}H-NMR ($CDCl_3$, 300 MHz), δ: 8.25-8.14 (m, 7H), 8.03-7.72 (m, 10H), 6.79 (s, 4H), 4.83 (m, 2H), 1.16 (s, 9H).

2-(Hydroxymethyl)-9,10-bis(1,3-dithiol-2-ylidene)-9,10-dihydroanthracene (9)[180]

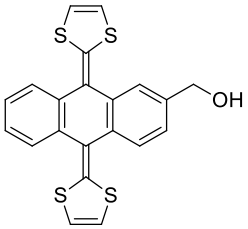

To a solution of 2-(((*tert*-butyldiphenylsilyl)oxy)methyl)-9,10-bis(1,3-dithiol-2-ylidene)-9,10-dihydroanthracene **8** (0.29 g, 0.50 mmol) in anhydrous THF, a

180. S. González, N. Martín, D. M. Guldi, *J. Org. Chem.* **2003**, *68*, 779-791.

volume of 0.16 mL of TBAF (1.0 M in THF, 0.54 mmol) was added under Ar atmosphere. The mixture was kept stirring during 2 hours at room temperature. After this time, the reaction mixture was washed with water and extracted with DCM. The organic layer was dried over $MgSO_4$, filtered and the solvent was removed under reduced pressure. The residue was purified by silica gel column chromatography, using DCM as eluent, to yield a yellow solid (98%).

^{1}H-NMR ($CDCl_3$, 300 MHz), δ: 7.66-7.57 (m, 4H), 7.36-7.23 (m, 3H), 6.74-6.73 (m, 4H), 5.29 (t, 1H, *J* = 5.6 Hz), 4.54 (d, 2H, *J* = 5.6 Hz).

9,10-Bis(1,3-dithiol-2-ylidene)-9,10-(dihydroanthracen-2-yl)methyl 4-(pyren-1-yl)butanoate (PyexTTF, 11)[128]

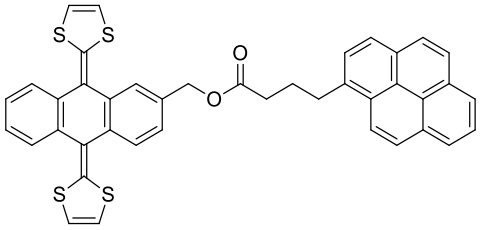

2-(Hydroxymethyl)-9,10-bis(1,3-dithiol-2-ylidene)-9,10-dihydroanthracene **9** (0.35 g, 0.85 mmol) and 4-(1-pyrenyl)butyric acid **10** (0.35 g, 1.20 mmol) were dissolved in 20 mL of DCM. The mixture was stirred for 10 minutes at 0 ºC (ice/water bath) under Ar atmosphere. Then 1,3-dicyclohexylcarbodiimide (DCC) (0.25 g, 1.20 mmol) and 4-(dimethylamino)pyridine (DMAP) (0.01 g, 0.12 mmol) in 5 mL of DCM were added, and the mixture was stirred for another 15 minutes at 0 ºC. The cooling bath was then removed, and the solution was allowed to warm to room temperature. After being stirred for 24 hours under Ar atmosphere, the reaction mixture was washed with water (3 x 50 mL). The organic layer was dried over $MgSO_4$, filtered and evaporated. The residue was purified by silica gel column chromatography, using a hexane/AcOEt (3/1) mixture as eluent, to yield a yellow solid (96%).

^{1}H-NMR ($CDCl_3$, 300 MHz), δ: 8.17 (d, 1H, *J* = 9.30 Hz), 8.14-7.94 (m, 7H), 7.83 (d, 1H, *J* = 8.06 Hz), 7.72-7.65 (m, 4H), 7.31-7.26 (m, 3H), 6.26 (1H, AB, J_{AB} = 6.80 Hz), 6.24 (1H, AB, J_{AB} = 6.80 Hz), 6.18 (1H, AB, J_{AB} = 6.60 Hz), 6.06 (1H, AB, J_{AB} = 6.60 Hz), 5.21 (s, 2H), 3.40 (t, 2H, *J* = 7.80 Hz), 2.56 (t, 2H, *J* = 7.80 Hz), 2.24 (q, 2H, J = 7.80 Hz).

3,3,3-Tris(4-methoxyphenyl)propine (13)[129]

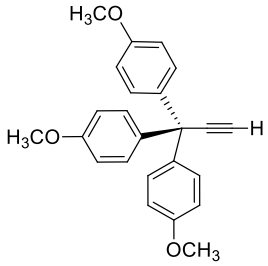

A solution of 4,4',4''-trimethoxytrityl chloride **12** (1g, 2.71 mmol) in anhydrous toluene was subjected to N_2-vacuum cycles and cooled at -78 ºC. After that, the solution remained under Ar atmosphere and ethynylmagnesium bromide (0.5 M in THF, 5.81 mmol) was added drop by drop. The reaction was allowed to warm to room temperature and was stirred 3 additional hours. Afterwards, it was quenched with saturated aqueous NH_4Cl and extracted with AcOEt. The organic layer was dried with $MgSO_4$, filtered and evaporated. The residue was purified by silica gel column chromatography, using a hexane/DCM (3/2) mixture as eluent, to yield a white solid (88%).

^{1}H-NMR ($CDCl_3$, 300 MHz), δ: 7.18 (d, 6H, J = 8.9 Hz), 6.82 (d, 6H, J = 8.9 Hz), 3.80 (s, 9H), 2.68 (s, 1H).

2-Iodoanthraquinone (15)[131]

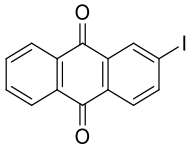

To a solution of 2-aminoanthraquinone **14** (2.23 g, 10 mmol), KNO_2 (3.4 g, 40 mmol) and CuI (0.57 g, 3 mmol) in DMSO (25 mL), a solution of HI (5.25 mL, 40 mmol) in DMSO (25 mL) was added dropwise at 35 ºC. The reaction mixture was stirred during 30 minutes. After this time, a K_2CO_3 aqueous solution was added to reach neutral pH. The product precipitate, water (300 mL) was added and the solid was filtered and dried. The crude reaction mixture was purified by silica gel column chromatography, using a hexane/DCM (1/2) mixture as eluent, to yield a yellow solid (55%).

^{1}H-NMR ($CDCl_3$, 300 MHz), δ: 8.61 (d, 1H, J = 1.7 Hz), 8.31-8.23 (m, 2H), 8.14 (dd, 1H, J_1 = 8.3 Hz, J_2 = 1.7 Hz), 7.97 (d, 1H, J = 8.3 Hz), 7.85-7.77 (m, 2H).

2-Iodo-9,10-bis(1,3-dithiol-2-yliden)-9,10-dihydroanthracene (16)[130]

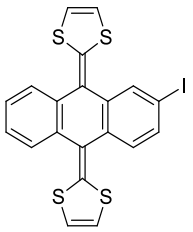

A volume of 13.09 mL of *n*-BuLi (1.6 M in hexane, 20.95 mmol) was added to a solution of dimethyl(1,3-dithiol-2yl)phosphonate **5** (3.81 g, 17.95 mmol) in anhydrous THF (30 mL) at -78 ºC and under Ar atmosphere. The mixture was kept stirring during 45 minutes at the same temperature. Then, 2-iodoanthraquinone **15** (1 g, 2.99 mmol) was dissolved in anhydrous THF (20 mL) and added dropwise. The mixture was kept at -78 ºC during 1 hour and then was left to reach room temperature overnight. The solvent was removed under reduced pressure and the crude was washed with water (100 mL) and extracted with DCM (3 x 100 mL). The organic layer was dried over $MgSO_4$ and filtered. The solvent was removed under reduced pressure and the residue was purified by silica gel column chromatography using a hexane/DCM (3/1) mixture as eluent. The final product was obtained as a yellow solid (61%).

^{1}H-NMR ($CDCl_3$, 300 MHz), δ: 8.01 (d, 1H, J = 1.6 Hz), 7.71-7.66 (m, 2H), 7.60 (dd, 1H, J_1 = 8.2 Hz, J_2 = 1.6 Hz), 7.43 (d, 1H, J = 8.2 Hz), 7.32-7.28 (m, 2H), 6.33 (s, 2H), 6.31 (s, 2H).

2-(3,3,3-Tris(4-methoxyphenyl)-1-propynyl)-9,10-bis(1,3-dithiol-2-yliden)-9,10-dihydroanthracene (17)

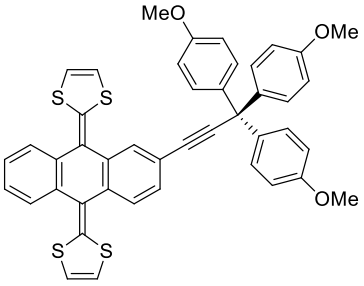

To a solution of 2-iodo-9,10-bis(1,3-dithiol-2-yliden)-9,10-dihydroanthracene **16** (0.28 g, 0.56 mmol) in anhydrous THF (20 mL), 3,3,3-tris(4-methoxyphenyl)propine **13** (0.100 g, 0.28 mmol), $Pd(PPh_3)_4$ (40%), CuI (40%) and Et_3N (0.12 mL, 0.84 mmol) were added. The reaction was refluxed under

Ar atmosphere overnight. After cooling to room temperature, AcOEt was added. The organic layer was washed with NH_4Cl solution (50 mL), water (2 x 50 mL) and NaCl solution (2 x 50 mL), and then dried with $MgSO_4$. The solvent was removed under reduced pressure and the crude was purified by silica gel column chromatography using a hexane/DCM (2/1) mixture as eluent. The final product was obtained as a yellow solid (73%).

^{1}H-NMR (300 MHz, $CDCl_3$), δ: 7.82 (d, 1H, J = 1.4 Hz), 7.73–7.60 (m, 3H), 7.40 (dd, 1H, J_1 = 8.0 Hz, J_2 = 1.4 Hz), 7.31–7.28 (m, 2H), 7.26-7.23 (m, 6H), 6.86-6.83 (m, 6H), 6.28 (s, 4H), 3.81 (s, 9H).

^{13}C-NMR (75 MHz, $CDCl_3$), δ: 158.7, 138.5, 136.9, 136.8, 135.8, 135.6, 135.4, 130.5, 129.5, 128.7, 128.3, 126.5, 125.4, 125.3, 122.2, 121.8, 121.6, 117.7, 113.7, 96.9, 85.2, 55.7, 54.6.

FT-IR ($CHCl_3$), ν (cm^{-1}): 2924, 2853, 1605, 1580, 1547, 1506, 1459, 1411, 1298, 1250, 1177, 1112, 1034, 828, 804, 757, 643, 588.

UV-Vis ($CHCl_3$), λ_{max} (nm) (ε): 371 (19557), 438 (26937).

MALDI-TOF-MS (m/z) calculated for $C_{44}H_{32}O_3S_4$ $[M]^+$: 736.1234, found: 736.1216.

2-(3,3,3-Tris(4-hydroxyphenyl)-1-propynyl)-9,10-bis(1,3-dithiol-2-yliden)-9,10-dihydroanthracene (18)

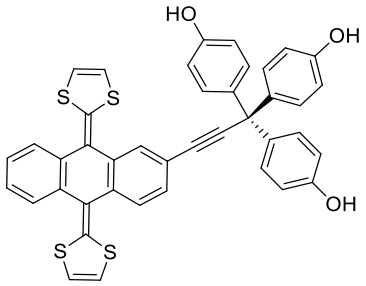

To a solution of 2-(3,3,3-tris(4-methoxyphenyl)-1-propynyl)-9,10-bis(1,3-dithiol-2-yliden)-9,10-dihydroanthracene **17** (0.1 g, 0.13 mmol) in anhydrous DCM (20 mL) at 0 ºC and under Ar atmosphere, BBr_3 (9.5 mL, 9.5 mmol) was added. The yellow solution turned brown immediately. The reaction mixture was maintained under these conditions for 6 hours. The reaction was worked up by addition of MeOH and H_2O. The precipitate was filtered under vacuum using a PTFE membrane. The final product was isolated as an orange solid quantitatively.

^{1}H-NMR (300 MHz, Acetone-d_6), δ: 8.39 (s, 3H), 7.83 (d, 1H, J = 1.5 Hz), 7.72 (m, 3H), 7.48 (dd, 1H, J_1 = 8.0, J_2 =1.5 Hz), 7.37-7.34 (m, 2H), 7.15 (d, 6H, J = 8.7 Hz), 6.80 (d, 6H, J = 8.7 Hz), 6.62 (s, 2H), 6.61 (s, 2H).

^{13}C-NMR (75 MHz, Acetone-d_6), δ: 157.1, 138.3, 137.9, 136.6, 136.2, 130.9, 129.7, 128.6, 127.1, 126.1, 125.9, 122.2, 121.9, 121.5, 118.6, 115.5, 98.3, 85.1, 55.0.

FT-IR (Acetone), ν (cm^{-1}): 3360, 3064, 2960, 2922, 2851, 1701, 1600, 1549, 1509, 1456, 1411, 1367, 1260, 1228, 1170, 834, 802, 758, 650.

UV-Vis (Acetone), λ_{max} (nm) (ε): 370 (6349), 435 (8348).

MALDI-TOF-MS (m/z) calculated for $C_{41}H_{26}O_3S_4$ $[M]^+$: 694.0765, found: 695.0834 $[M+H]^+$.

4-(1-Pyrenyl)-1-butanol tosylate (20)[82]

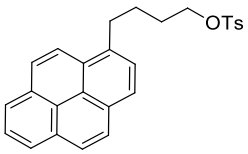

To a solution of 4-(1-pyrenyl)-1-butanol **19** (0.3 g, 1.09 mmol) and a catalytic amount of DMAP (2.5 mg) in anhydrous DCM (30 mL) was added trimethylamine (10 mL). The reaction mixture was cooled to -10 ºC and a solution of *p*-toluenesulfonyl chloride (0.32 g, 1.64 mmol) in anhydrous DCM was added drop by drop. The reaction mixture was allowed to react under these conditions during 3 days. The organic layer was washed with water (3 x 20 mL), dried over $MgSO_4$ and the solvent was removed under reduce pressure. The residue was purified by silica gel column chromatography using a hexane/ AcOEt (4/1) mixture as eluent. The final product was obtained as a white solid (87%).

^{1}H-NMR (300 MHz, $CDCl_3$), δ: 8.21-7.75 (m, 9H), 7.73 (d, 2H, J = 8 Hz), 7.23 (d, 2H, J = 8 Hz), 4.08 (t, 2H, J = 6 Hz), 3.31 (t, 2H, J = 7 Hz), 2.35 (s, 3H), 1.96-1.74 (m, 4H).

2-(3,3,3-Tris(4-(4-(1-pyrenyl)butoxy)phenyl)-1-propynyl)-9,10-bis(1,3-dithiol-2-yliden)-9,10-dihydroanthracene (3PyexTTF, 21)

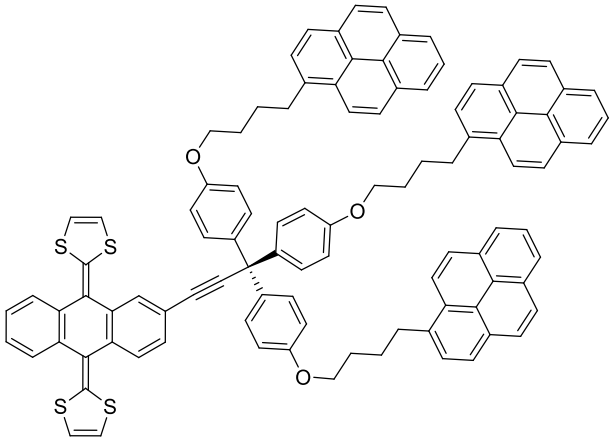

To a solution of 2-(3,3,3-tris(4-hydroxyphenyl)-1-propynyl)-9,10-bis(1,3-dithiol-2-yliden)-9,10-dihydroanthracene **18** in dry DMF (0.095 g, 0.14 mmol, 4 mL) was added slowly NaH (95%, 0.049 g, 2.05 mmol) as a solid under argon atmosphere. The solution turned dark after the addition of the base. After two hours, a solution of 4-(1-pyrenyl)-1-butanol tosylate **20** (0.26 g, 0.62 mmol) in 3 mL of dry DMF was added. The reaction mixture was stirred at room temperature overnight. The solution was extracted with DCM and water, the organic layer was dried with Na_2SO_4 and the solvent was removed under reduced pressure. The residue was purified by silica gel column chromatography using a gradient from hexane/AcOEt (4/1) to DCM/hexane (3/1) as eluent. The final product was isolated as a yellow solid (14%).

^{1}H-NMR (700 MHz, $CDCl_3$), δ: 8.29 (d, 3H, *J* = 9.2 Hz), 8.18-7.96 (m, 21H), 7.89 (d, 3H, *J* = 7.7 Hz), 7.82 (d, 1H, *J* = 1.5 Hz), 7.71-7.61 (m, 3H), 7.40 (dd, 1H, J_1 = 7.9, J_2 = 1.5 Hz), 7.30–7.27 (m, 2H), 7.23 (d, 6H, *J* = 8.8 Hz), 6.83 (d, 6H, *J* = 8.8 Hz), 6.29 (s, 2H), 6.21 (s, 2H), 3.99 (t, 6H, *J* = 6.2 Hz), 3.39 (t, 6H, *J* = 7.7 Hz), 2.01 (m, 6H), 1.96– 1.88 (m, 6H).

^{13}C-NMR (175 MHz, $CDCl_3$), δ: 157.8, 138.1, 136.6, 136.4, 135.3, 131.4, 130.9, 130.1, 129.8, 129.1, 128.6, 127.8, 127.5, 127.3, 126.6, 126.0, 125.8, 125.1, 125.0, 124.9, 124.8, 124.7, 123.4, 121.8, 121.3, 117.3, 117.0, 113.8, 96.6, 84.7, 67.7, 54.1, 33.2, 30.9, 29.3, 28.3.

FT-IR ($CHCl_3$), ν (cm^{-1}): 2955, 2920, 2853, 1728, 1604, 1546, 1506, 1464, 1379, 1288, 1246, 1173, 1119, 845, 763.

UV-Vis (NMP), λ_{max} (nm) (ε): 315 (45787), 329 (91575), 345 (111355), 376 (20879), 445 (21978).

MALDI-TOF-MS (m/z) calculated for $C_{101}H_{74}O_3S_4$ [M^+]: 1462.4521 found: 1462.4519.

3,5-Di-*tert*-butyl(bromomethyl)benzene (23)[145]

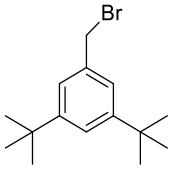

A mixture of 3,5-di-*tert*-butyltoluene **22** (90 g, 440 mmol), NBS (135 g, 660 mmol) and benzoyl peroxide (1 g, 40 mmol) in CCl_4 (800 mL) was refluxed for 3 hours. The solution was cooled down, filtered and concentrated under reduced pressure. The crude residue **23** was used without further purification in the next step.

3,5-Di-*tert*-butylbenzaldehyde (24)[145]

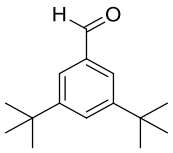

A mixture of compound **23** (125 g, 440 mmol) and hexamethylenetetramine (HMTA) (256 g, 1.83 mol) in MeOH/H_2O (500 mL, 1/1) was refluxed for 4 hours. Concentrated aqueous HCl (150 mL) was added dropwise and the mixture was refluxed for 30 minutes. The solution was cooled down and extracted with DCM, the solvent was removed under reduced pressure and the residue was recrystallized from EtOH/H_2O to obtain the product as a white solid (82%).

^{1}H-NMR (300 MHz, $CDCl_3$) δ: 10.00 (s, 1H), 7.71 (m, 3H), 1.35 (s, 18H).

4-Hydroxymethylbenzaldehyde (26)[146]

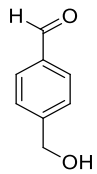

Terephthalaldehyde **25** (1 g, 7.45 mmol) was dissolved in a mixture of 95% EtOH and THF. To the resulting stirred solution, $NaBH_4$ (0.07 g, 1.86 mmol) was added at -5 ºC in small portions. The mixture was stirred for 6 hours while the temperature was maintained at 0 ºC. The reaction mixture was then adjusted to pH 5 with 1M HCl. The solvent was evaporated under reduced pressure, then H_2O was added and the solution was extracted with AcOEt. The organic layer was dried with Na_2SO_4 and the solvent evaporated under reduced pressure. The crude of reaction was purified by silica gel column chromatography using a hexane/AcOEt (3/2) mixture as eluent. The product was isolated as a white solid (72%).

^{1}H-NMR (300 MHz, $CDCl_3$), δ: 9.81 (s, 1H), 7.70 (d, 2H *J* = 8.0 Hz), 7.39 (d, 2H, *J* = 8.0 Hz), 4.65 (s, 2H), 4.13 (s, 1H).

4-Formylbenzyl 4-(pyren-1-yl)butanoate (27)

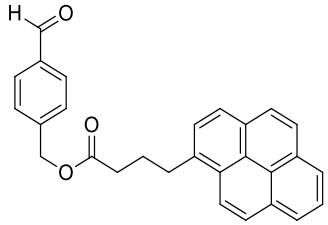

A solution of 4-hydroxymethylbenzaldehyde **26** (0.43 g, 3.15 mmol) and 4-(1-pyrenyl)butyric acid **10** (1.36 g, 4.73 mmol) in DCM at 0 ºC was stirred for 10 minutes under Ar atmosphere. Then DCC (0.98 g, 4.73 mmol) and DMAP (0.054 g, 0.44 mmol) in 10 mL of DCM were added and the mixture was stirred for another 15 minutes at 0 ºC. The cooling bath was then removed, and the solution was allowed to react at room temperature 24 hours. The reaction mixture was washed with water. The organic layer was dried with Na_2SO_4 and the solvent was removed under reduced pressure. The residue was purified by silica gel column chromatography using a DCM/hexane (8/3) mixture as eluent. The product was isolated as a yellow solid (86%).

^{1}H-NMR (300 MHz, $CDCl_3$) δ: 9.94 (s, 1H), 8.24 (d, 1H, *J* = 9.3 Hz), 8.19-7.95 (m, 7H), 7.82 (d, 1H, *J* = 7.8 Hz), 7.76 (d, 2H, *J* = 8.1 Hz), 7.38 (d, 2H, *J* = 8.1 Hz), 5.12 (s, 2H), 3.42–3.33 (m, 2H), 2.54 (t, 2H, *J* = 7.3 Hz), 2.30–2.18 (m, 2H).

^{13}C-NMR (75 MHz, $CDCl_3$) δ 191.8, 173.1, 142.6, 135.9, 135.5, 131.4, 130.9, 130.0, 129.9, 128.8, 128.1, 127.5, 127.5, 127.4, 126.8, 125.9, 125.1, 125.0, 124.9, 124.8, 124.8, 123.3, 65.3, 33.8, 32.7, 26.7.

FT-IR ($CHCl_3$), ν (cm^{-1}): 2925, 2854, 1731, 1692, 1609, 1579, 1509, 1489, 1456, 1434, 1417, 1380, 1305, 1245, 1208, 1182, 1159, 1142, 1100, 1065, 1033, 1007, 972, 909, 843, 818, 781, 760, 721, 709, 682, 621, 588.

UV-Vis ($CHCl_3$), λ_{max} (nm) (ε): 314 (12588), 329 (27529), 345 (32824).

EI-MS (m/z) calculated for $C_{28}H_{22}O_3$ [M^+]: 406.1569 found: 406.1563.

4[10,15,20-Tris(3,5-di-*tert*-butylphenyl)porphyrin-5-yl]benzyl 4-(pyren-1-yl)butanoate (PyH_2P, 30)

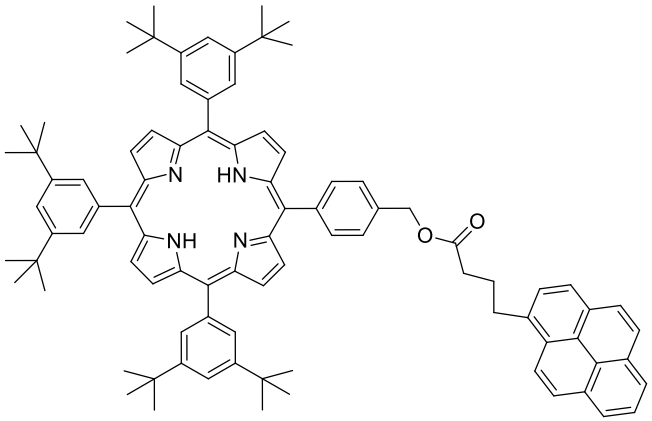

A solution of 3,5-di-*tert*-butylbenzaldehyde **24** (1.11 g, 5.12 mmol), 4-formylbenzyl 4-(pyren-1-yl)butanoate **27** (0.69 g, 1.71 mmol) and pyrrole **28** (0.47 mL, 6.83 mmol) in dry DCM (340 mL) was degassed under argon for 1 hour. After this period of time, trifluoroacetic acid (TFA) (0.1 mL, 1.02 mmol) was added drop by drop. After the addition of TFA the solution turned black with the time. The mixture was allowed to react under room temperature overnight. To obtain the desired porphyrin, *p*-chloranil **29** (0.19 g, 0.77 mmol) was added and the mixture was refluxed 2 hours. After the oxidation, and at room temperature, 0.5 mL of Et_3N were added to quench the reaction. The solution changed from green to red. Then, the solvent was removed under reduced pressure and the solid was purified by silica gel column chromatography using a gradient from hexane/DCM (2/1) to (1/1) as eluent. The product was obtained as a purple solid (7%).

^{1}H-NMR (300 MHz, $CDCl_3$) δ: 8.93 (s, 4H), 8.90 (d, 2H, J_{AB} = 4.8 Hz), 8.85 (d, 2H, J_{AB} = 4.8 Hz), 8.40 (d, 1H J = 9.3 Hz), 8.26 (d, 2H J = 8.0 Hz), 8.20 – 8.13 (m, 4H), 8.10 (t, 6H, J =1.7 Hz), 8.07-7.90 (m, 4H), 7.82 (t, 3H, J = 1.7 Hz), 7.75 (d, 2H, J = 8.0 Hz), 5.51 (s, 2H), 3.58–3.50 (m, 2H), 2.71 (t, 2H, J = 7.2 Hz), 2.46–2.32 (m, 2H), 1.54 (s, 54H), -2.68 (s, 2H).

^{13}C-NMR (75 MHz, $CDCl_3$) δ: 173.6, 148.7, 143.5, 142.5, 141.3, 135.7, 135.3, 134.7, 131.4, 130.9, 130.1, 129.9, 129.7, 128.9, 127.5, 126.8, 126.5, 125.9, 125.0, 124.9, 124.8, 124.6, 123.4, 121.5, 121.0, 118.9, 53.5, 35.1, 34.1, 32.9, 31.8, 26.9.

FT-IR ($CHCl_3$), ν (cm^{-1}): 2960, 2927, 2860, 1739, 1684, 1592, 1516, 1469, 1428, 1395, 1363, 1253, 1154, 977, 912, 844, 800, 756.

UV-Vis (NMP), λ_{max} (nm) (ε): 315 (19769), 329 (29654), 346 (39539), 422 (342669), 517 (14827), 552 (8237), 594 (4942), 649, (4942).

MALDI-TOF-MS (m/z) calculated for $C_{89}H_{94}N_4O_2$ [M^+]: 1250.7377 found: 1250.7319.

4{Zinc (II) [10,15,20-tris(3,5-di-*tert*-butylphenyl)porphyrin-5-yl]benzyl} 4-(pyren-1-yl)butanoate (PyZnP, 31)

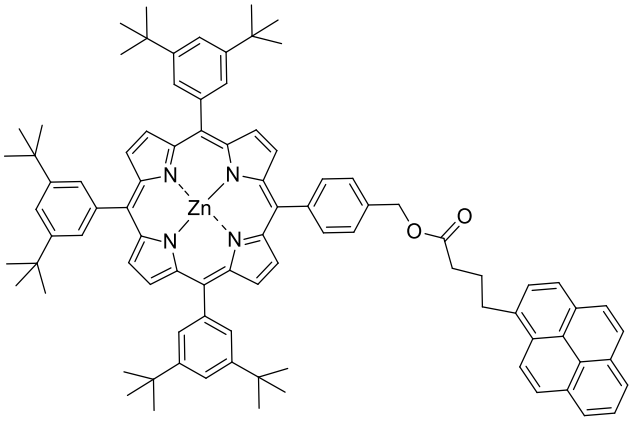

A solution of **30** in DCM (0.075 g, 0.06 mmol) was mixed with a solution of $Zn(O_2CCH_3)_2{\cdot}2H_2O$ (0.04 g, 0.18 mmol) in MeOH. The reaction mixture was allowed to react at room temperature overnight, then the solvent was removed under reduced pressure and the crude was purified by preparative TLC using as eluent a gradient from hexane/DCM (3/1) to (7/3). The product was isolated as a purple solid (86%).

^{1}H-NMR (300 MHz, $CDCl_3$) δ: 9.04 (s, 4H), 9.00 (d, 2H, J_{AB} = 4.7 Hz), 8.95 (d, 2H, J_{AB} = 4.7 Hz), 8.39 (d, 1H, *J* = 9.3 Hz), 8.25 (d, 2H, *J* = 8.0 Hz), 8.18-8.13 (m, 4H), 8.12 (d, 6H, *J* = 1.7 Hz), 8.09-7.91 (m, 4H), 7.82 (t, 3H, *J* = 1.7 Hz), 7.74 (d, 2H, *J* = 8.0 Hz), 5.48 (s, 2H), 3.58 – 3.46 (m, 2H), 2.69 (t, 2H, *J* = 7.2 Hz), 2.43 – 2.29 (m, 2H), 1.55 (s, 54H).

^{13}C-NMR (75 MHz, $CDCl_3$) δ: 173.7, 150.6, 150.5, 150.1, 148.7, 143.2, 141.9, 135.8, 135.2, 134.6, 132.4, 132.3, 131.7, 131.5, 131.0, 130.1, 129.9, 129.7, 128.9, 127.6, 126.8, 126.5, 125.9, 125.0, 124.9, 123.5, 122.7, 122.6, 120.9, 66.4, 35.2, 34.1, 33.0, 31.9, 27.0.

FT-IR ($CHCl_3$), ν (cm^{-1}): 2959, 2868, 1738, 1592, 1521, 1469, 1425, 1391, 1362, 1288, 1247, 1214, 1067, 1001, 931, 889, 845, 797, 716.

UV-Vis (NMP), λ_{max} (nm) (ε): 314 (42398), 329 (51170), 345 (60672), 429 (780702), 561 (26316), 601 (16082).

MALDI-TOF-MS (m/z) calculated for $C_{89}H_{92}N_4O_2Zn$ [M+]: 1312.6512 found: 1312.6506.

4{Niquel (II) [10,15,20-tris(3,5-di-*tert*-butylphenyl)porphyrin-5-yl]benzyl} 4-(pyren-1-yl)butanoate (PyNiP, 32)

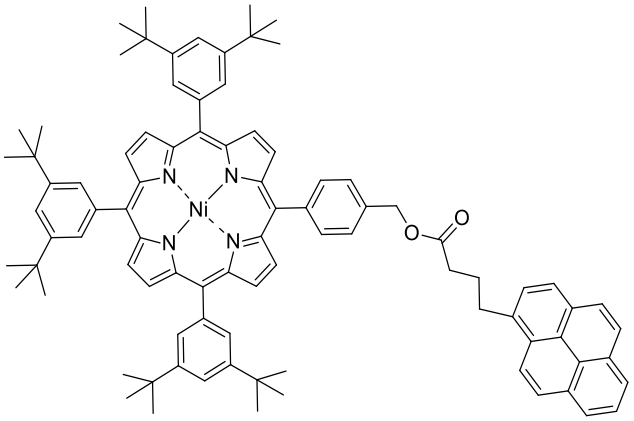

Compound **30** (0.07 g, 0.06 mmol) was dissolved in MeOH (1 mL) and $CHCl_3$ (9 mL), and $Ni(O_2CCH_3)_2{\cdot}4H_2O$ (0.14 g, 0.6 mmol) was added. The mixture was degassed under Argon during 20 minutes, and then heated to reflux for 24 hours. After this time the solvent was removed under reduced pressure and the crude was purified by silica gel column chromatography using a hexane/DCM (8/2) mixture as eluent. The product was isolated as a red solid (90%).

^{1}H-NMR (300 MHz, $CDCl_3$) δ: 8.83 (s, 4H), 8.78 (d, 2H, J_{AB} = 5.0 Hz), 8.73 (d, 2H, J_{AB} = 5.0 Hz), 8.37 (d, 1H, *J* = 9.3 Hz), 8.19 – 8.11 (m, 4H), 8.08-7.91 (m, 6H), 7.89 (d, 6H, *J* = 1.8 Hz), 7.73 (t, 3H, J = 1.8 Hz), 7.67 (d, 2H, *J* = 8.0 Hz), 5.44 (s, 2H), 3.55 – 3.47 (m, 2H), 2.67 (t, 2H, *J* = 7.2 Hz), 2.42 – 2.29 (m, 2H), 1.48 (s, 54H).

^{13}C-NMR (75 MHz, $CDCl_3$) δ: 172.4, 147.9, 141.8, 141.7, 141.3, 140.1, 138.9, 134.6, 134.3, 132.8, 131.4, 130.7, 130.4, 129.9, 129.0, 127.8, 127.6, 126.4, 125.7, 125.6, 124.8, 123.9, 123.8, 122.3, 120.0, 119.2, 116.8, 65.2, 34.0, 33.0, 31.8, 30.6, 25.8.

FT-IR ($CHCl_3$), ν (cm^{-1}): 2925, 2855, 1739, 1463, 1366, 1259, 1010, 796, 754, 719.

UV-Vis (NMP), λ_{max} (nm) (ε): 314 (34545), 329 (47273), 345 (56364), 419 (287273), 530 (23636).

MALDI-TOF-MS (m/z) calculated for $C_{89}H_{92}N_4NiO_2$ [M+]: 1306.6574 found: 1306.6512.

4-(3,3,3-Tris(4-methoxyphenyl)-1-propynyl)benzaldehyde (34)

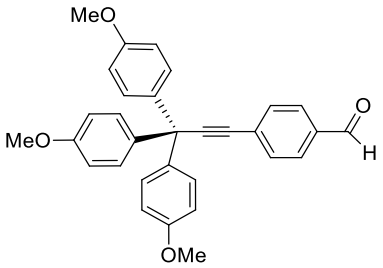

A solution of 4-iodobenzaldehyde **33** (0.65 g, 2.80 mmol), $Pd(PPh_3)_4$ (0.08 g, 0.07 mmol) and CuI (0.01 g, 0.07 mmol) in dry THF was deoxygenated during 30 minutes. Subsequently, a solution of 3,3,3-tris(4-methoxyphenyl)propine **13** (0.5 g, 1.40 mmol) in dry THF and Et_3N (0.6 mL, 4.19 mmol) were added. The reaction mixture was refluxed overnight. Then, the solvent was removed under reduced pressure and the crude was purified by silica gel column chromatography using a hexane/AcOEt (8/2) mixture as eluent. The product was isolated as a pale yellow solid (80%).

^{1}H-NMR (300 MHz, $CDCl_3$) δ: 9.89 (s, 1H), 7.73 (d, 2H, *J* = 8.2 Hz), 7.54 (d, 2H, *J* = 8.2 Hz), 7.12 (d, 6H, *J* = 8.9 Hz), 6.75 (d, 6H, *J* = 8.9 Hz), 3.70 (s, 9H).

^{13}C-NMR (75 MHz, $CDCl_3$) δ: 191.6, 158.5, 137.6, 135.3, 132.2, 130.1, 129.6, 113.4, 100.8, 83.9, 55.3, 54.3.

FT-IR ($CHCl_3$), ν (cm^{-1}): 2930, 2836, 2222, 1700, 1603, 1506, 1461, 1414, 1387, 1300, 1250, 1207, 1177, 1115, 1034, 829, 756, 719, 589.

UV-Vis ($CHCl_3$), λ_{max} (nm) (ε): 288 (15020).

EI-MS (m/z) calculated for $C_{31}H_{26}O_4$ [M+]: 462.1831, found: 462.1826.

5-(4-(3,3,3-Tris(4-methoxyphenyl)-1-propynyl)phenyl)-10,15,20-tris(3,5-di-*tert*-butylphenyl)porphyrin (35)

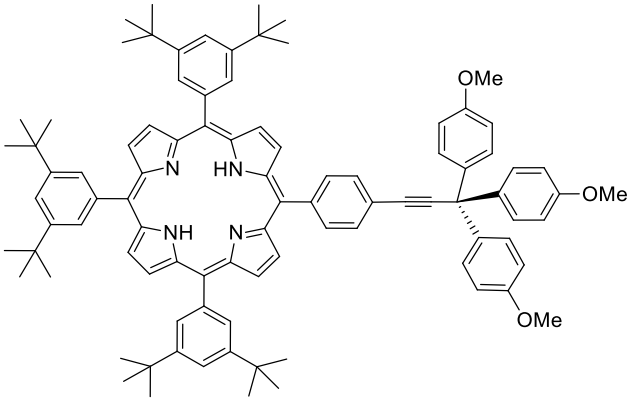

A solution of 3,5-di-*tert*-butylbenzaldehyde **24** (0.94 g, 4.33 mmol), 4-(3,3,3-tris(4-methoxyphenyl)-1-propynyl)benzaldehyde **34** (0.67 g, 1.44 mmol) and pyrrole **28** (0.40 mL, 5.77 mmol) in dry DCM (340 mL) was degassed under argon for 1 hour. After this period of time, TFA (0.09 mL, 0.87 mmol) was added drop by drop. Following the addition of TFA the solution turned black with the time. The mixture was allowed to react under room temperature overnight. To complete the porphyrin formation, *p*-chloranil **29** (0.16 g, 0.65 mmol) was added and the mixture was refluxed 2 hours. After the oxidation, and at room temperature, 0.5 mL of Et_3N were added to quench the reaction. The solution changed from green to red. Then, the solvent was removed under reduced pressure and the solid was purified by silica gel column chromatography using a hexane/DCM (7/3) mixture as eluent. The product was obtained as a purple solid (7%).

^{1}H-NMR (300 MHz, $CDCl_3$) δ: 9.04 (d, 4H, *J* = 3.6 Hz), 8.98 (d, 1H, *J* = 4.7 Hz), 8.93 (d, 2H, *J* = 3.6 Hz), 8.87 (d, 1H, *J* = 4.7 Hz), 8.23 (d, 2H, *J* = 7.9 Hz), 8.12 (m, 6H), 7.92 (d, 2H, *J* = 7.9 Hz), 7.83 (t, 3H, *J* = 1.8 Hz), 7.41 (d, 6H, *J* = 8.8 Hz), 6.95 (d, 6H, *J* = 8.8 Hz), 3.87 (s, 9H), 1.56 (s, 54H), -2.67 (s, 2H).

^{13}C-NMR (75 MHz, $CDCl_3$) δ: 158.4, 150.6, 150.5, 150.0, 148.8, 148.6, 141.8, 138.3, 134.4, 134.3, 132.4, 132.2, 131.5, 130.3, 129.9, 129.7, 129.6, 123.1, 122.6, 121.5, 121.0, 120.9, 113.4, 97.2, 84.8, 55.3, 54.3, 35.1, 31.8.

FT-IR ($CHCl_3$), ν (cm^{-1}): 2961, 2904, 2868, 2834, 1710, 1592, 1506, 1476, 1463, 1441, 1425, 1394, 1363, 1340, 1296, 1248, 1220, 1176, 1114, 1069, 1037, 1001, 972, 948, 931, 909, 883, 859, 825, 800, 775, 732, 716, 646, 588.

UV-Vis ($CHCl_3$), λ_{max} (nm) (ε): 422 (131967), 452 (45902), 548 (4918), 588 (1639), 617 (820), 671 (5738).

MALDI-TOF-MS (m/z) calculated for $C_{92}H_{98}N_4O_3$ [M+]: 1306.7639 found: 1306.7633.

5-(4-(3,3,3-Tris(4-hydroxyphenyl)-1-propynyl)phenyl)-10,15,20-tris(3,5-di-*tert*-butylphenyl)porphyrin (36)

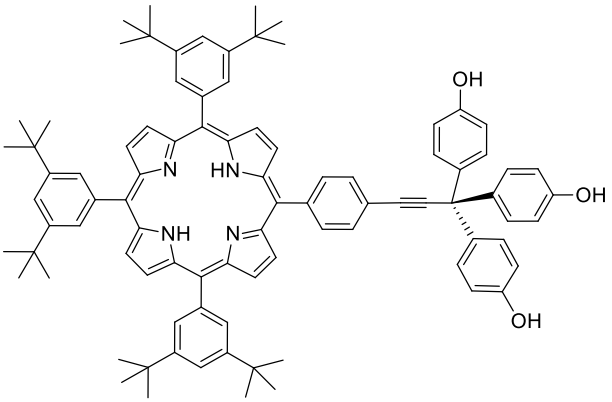

To a solution of **35** (0.05 g, 0.04 mmol) in dry DCM at 0 ºC was added BBr_3 (0.82 mL, 0.82 mmol). The reaction mixture was allowed to react at room temperature during 3 hours. After this time the reaction was quenched with MeOH and Et_3N. The reaction mixture was subsequently extracted with H_2O and DCM. The product was isolated as a purple solid quantitatively.

^{1}H-NMR (500 MHz, $CDCl_3$) δ: 8.90 (d, 6H, *J* = 5.6 Hz), 8.84 (d, 2H, *J* = 4.6 H), 8.19 (d, 2H, *J* = 8.1 Hz), 8.09 (m, 6H), 7.88 (d, 2H, *J* = 8.1 Hz), 7.82 – 7.78 (m, 3H), 7.32 (d, 6H, *J* = 8.7 Hz), 6.84 (d, 6H, *J* = 8.7 Hz), 1.53 (s, 54H), -2.70 (s, 2H).

^{13}C-NMR (125 MHz, $CDCl_3$) δ: 154.8, 149.1, 142.7, 141.7, 141.6, 138.7, 134.8, 130.8, 130.3, 130.2, 130.1, 121.9, 121.4, 115.4, 115.3, 97.5, 85.2, 54.7, 35.5, 32.1.

FT-IR ($CHCl_3$), ν (cm^{-1}): 3394, 3247, 2958, 2863, 2677, 2485, 1728, 1594, 1508, 1468, 1396, 1363, 1247, 1172, 1071, 1019, 976, 909, 836, 803, 733, 588.

UV-Vis ($CHCl_3$), λ_{max} (nm) (ε): 422 (488432), 452 (20566), 518 (17995), 554 (12853), 593 (7712), 649 (7712).

MALDI-TOF-MS (m/z) calculated for $C_{89}H_{92}N_4O_3$ [M+]: 1264.7169 found: 1264.7164.

1-(4-Bromobutyl)pyrene (37)[148]

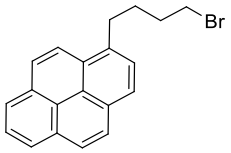

A solution of PPh_3 (0.72 g, 2.73 mmol) in 5 mL of dry DCM was slowly added dropwise to a solution of 4-(1-pyrenyl)-1-butanol **19** (0.25 g, 0.91 mmol) and CBr_4 (0.60 g, 1.82 mmol) in 10 mL of dry DCM and at 0 ºC. The reaction mixture was stirred at room temperature during 3 hours. After this time the solvent was removed under reduced pressure and the solid was purified by silica gel column chromatography using a hexane/DCM (3/1) mixture as eluent. The product was obtained as a greenish-brown solid (80%).

^{1}H-NMR (300 MHz, $CDCl_3$), δ: 8.29 (d, 1H, *J* = 9.3 Hz), 8.23 – 8.09 (m, 4H), 8.07 – 7.97 (m, 3H), 7.88 (d, 1H, *J* = 7.8 Hz), 3.49 (t, 2H, *J* = 6.0 Hz), 3.39 (t, 2H, *J* = 7.0 Hz), 2.05 (m, 4H).

5-(4-(3,3,3-Tris(4-(4-(1-pyrenyl)butoxy)phenyl)-1-propynyl)phenyl)-10,15,20-tris(3,5-di-*tert*-butylphenyl)porphyrin (3PyH$_2$P, 38)

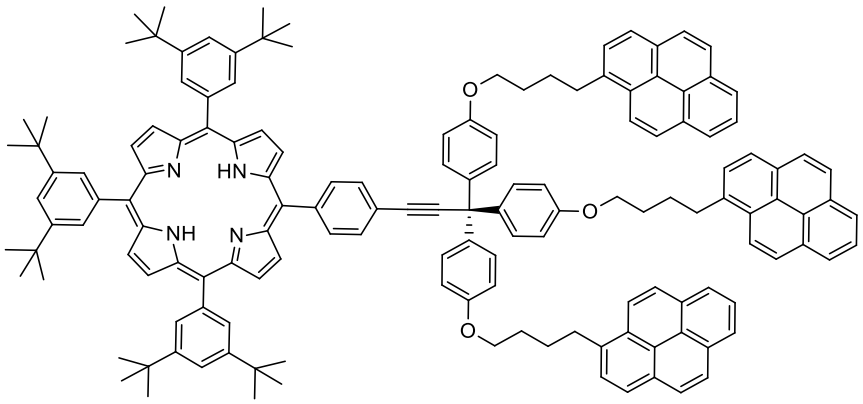

A solution of **36** (0.07 g, 0.06 mmol), K_2CO_3 (0.07 g, 0.51 mmol) and 18-crown-6 (1.5 mg, 0.006 mmol) in butanone (4 mL) was degassed under Ar and subsequently heated under reflux for 1 hour. After this time, 1-(4-bromobutyl)pyrene **37** (0.09 g, 0.25 mmol) was added dissolved in 2 mL of butanone dropwise. The reaction was allowed to react under these conditions two days. The solvent was removed under reduced pressure and the solid was purified by silica gel column chromatography using a hexane/DCM (7/3) mixture as eluent. The product was isolated as a purple solid (47%).

^{1}H-NMR (300 MHz, $CDCl_3$) δ: 8.90 (d, 6H, *J* = 7.2 Hz), 8.84 (d, 2H, *J* = 4.8 Hz), 8.31 (d, 3H, *J* = 9.3 Hz), 8.21–7.86 (m, 34H), 7.81 (t, 3H, *J* = 1.6 Hz), 7.37 (d, 6H, *J* = 8.8 Hz), 6.92 (d, 6H, *J* = 8.8 Hz), 4.07 (t, 6H, *J* = 6.0 Hz), 3.45 (t, 6H, J = 7.4 Hz), 2.15 – 1.93 (m, 12H), 1.54 (s, 54H), -2.70 (s, 2H).

^{13}C-NMR (75 MHz, $CDCl_3$) δ: 157.9, 148.7, 138.1, 136.6, 131.5, 130.9, 130.2, 129.8, 128.7, 127.5, 127.3, 126.6, 125.8, 124.8, 124.7, 123.4, 121.6, 121.5, 121.0, 114.0, 99.2, 67.7, 35.1, 33.2, 31.7, 29.3, 28.3.

FT-IR ($CHCl_3$), ν (cm^{-1}): 2958, 2927, 2863, 1701, 1669, 1652, 1593, 1556, 1505, 1472, 1427, 1395, 1363, 1297, 1246, 1178, 1110, 1024, 976, 907, 841, 803, 727, 609.

UV-Vis (NMP), λ_{max} (nm) (ε): 315 (42838), 330 (78983), 346 (109772), 423 (389558), 518 (17403), 553 (12048), 594 (6693), 650 (8032).

MALDI-TOF-MS (m/z) calculated for $C_{149}H_{140}N_4O_3$ [M+]: 2033.0925, found: 2033.0944.

Zinc (II) 5-(4-(3,3,3-tris(4-(4-(1-pyrenyl)butoxy)phenyl)-1-propynyl)phenyl)-10,15,20-tris(3,5-di-*tert*-butylphenyl)porphyrin (3PyZnP, 39)

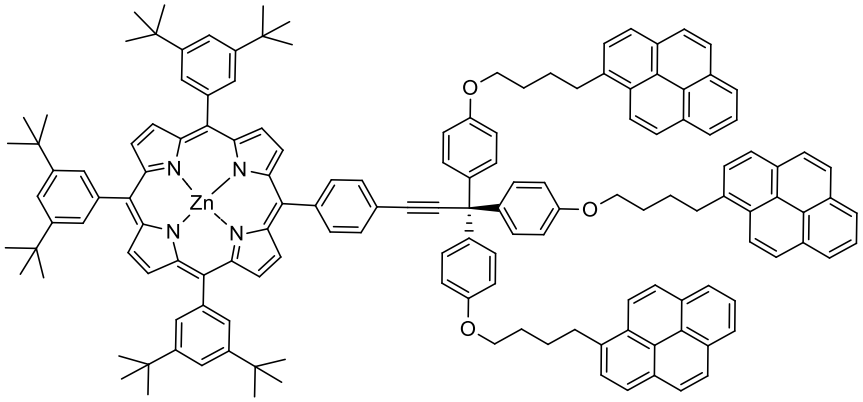

A solution of porphyrin **38** in DCM (0.06 g, 0.03 mmol) was mixed with a solution of $Zn(O_2CCH_3)_2{\cdot}2H_2O$ (0.02 g, 0.08 mmol) in MeOH. The reaction mixture was allowed to react at room temperature overnight, then the solvent was removed under reduced pressure and the crude was purified by silica gel column chromatography using a hexane/DCM (7/3) mixture as eluent. The product was isolated as a purple solid (84%).

^{1}H-NMR (300 MHz, $CDCl_3$) δ: 9.04 (s, 4H), 9.02 (d, 2H, J_{AB} = 4.8 Hz), 8.96 (d, 2H, J_{AB} = 4.8 Hz), 8.30 (d, 3H, *J* = 9.3 Hz), 8.22–7.87 (m, 34H), 7.82 (d,

3H, *J* = 1.7 Hz), 7.39 (d, 6H, *J* = 8.8 Hz), 6.93 (d, 6H, *J* = 8.8 Hz), 4.07 (t, 6H, *J* = 6.0 Hz), 3.44 (t, 6H, *J* = 7.4 Hz), 2.05 (m, 12H), 1.55 (s, 54H).

^{13}C-NMR (75 MHz, $CDCl_3$) δ: 157.9, 148.6, 141.8, 138.2, 136.6, 131.5, 130.9, 130.3, 129.9, 128.7, 127.5, 127.3, 126.6, 125.8, 124.8, 124.7, 123.4, 114.0, 97.3, 67.8, 54.4, 35.1, 33.2, 31.8, 29.3, 28.3.

FT-IR ($CHCl_3$), ν (cm^{-1}): 2924, 2855, 1724, 1598, 1507, 1463, 1368, 1294, 1247, 1177, 1004, 840, 719.

UV-Vis (NMP), λ_{max} (nm) (ε): 315 (62500), 329 (104167), 346 (136905), 431 (627976), 562 (23810), 602 (17857).

MALDI-TOF-MS (m/z) calculated for $C_{149}H_{138}N_4O_3Zn$ [M+]: 2095.0060, found: 2095.0055.

Niquel (II) 5-(4-(3,3,3-tris(4-(4-(1-pyrenyl)butoxy)phenyl)-1-propynyl)phenyl)-10,15,20-tris(3,5-di-*tert*-butylphenyl)porphyrin (3PyNiP, 40)

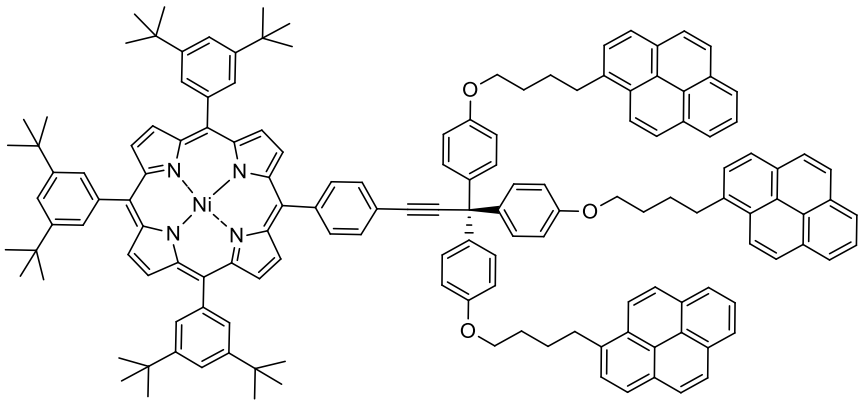

Compound **39** (0.03 g, 0.01 mmol) was dissolved in MeOH (1 mL) and $CHCl_3$ (9 mL), and $Ni(O_2CCH_3)_2{\cdot}4H_2O$ (0.04 g, 0.14 mmol) was added. The mixture was degassed under Ar during 20 minutes, and then heated to reflux for 24 hours. After this time the solvent was removed under reduced pressure and the crude was purified by silica gel column chromatography using a hexane/DCM (6/4) mixture as eluent. The product was isolated as a red solid (88%).

^{1}H-NMR (300 MHz, $CDCl_3$) δ: 8.81 (s, 4H), 8.78 (d, 2H, J_{AB} = 5.0 Hz), 8.71 (d, 2H, J_{AB} = 5.0 Hz), 8.30 (d, 3H, *J* = 9.3 Hz), 8.18–7.77 (m, 34H), 7.72 (s, 3H), 7.32 (d, 6H, *J* = 8.9 Hz), 6.89 (d, 6H, *J* = 8.9 Hz), 4.06 (t, 6H, *J* = 6.0 Hz), 3.44 (t, 6H, *J* = 7.4 Hz), 2.03 (m, 12H), 1.47 (s, 54H).

^{13}C-NMR (125 MHz, $CDCl_3$) δ: 156.8, 147.9, 141.8, 138.9, 137.0, 135.6, 130.4, 129. 9, 129.2, 127.7, 127.6, 126.5, 126.2, 125.6, 124.8, 123.8, 123.7, 122.4, 120.1, 112.9, 97.3, 66.7, 34.0, 32.1, 30.7, 28.7, 27.3.

FT-IR ($CHCl_3$), ν (cm^{-1}): 2958, 2926, 2857, 1708, 1648, 1598, 1507, 1466, 1396, 1363, 1250, 1178, 1077, 1010, 895, 839, 803, 609.

UV-Vis (NMP), λ_{max} (nm) (ε): 315 (28401), 329 (49327), 346 (64275), 420 (122571), 530 (11958).

MALDI-TOF-MS (m/z) calculated for $C_{149}H_{138}N_4O_3Ni$ [M+]: 2089.0122, found: 2089.0112.

***N*-octyl-2-{4-[6-(pyren-1-yl)-2-oxa-3-oxo-hexyl]phenyl}pyrrolidino[3,4:1,2][60]fullerene (PyC_{60}, 41)**

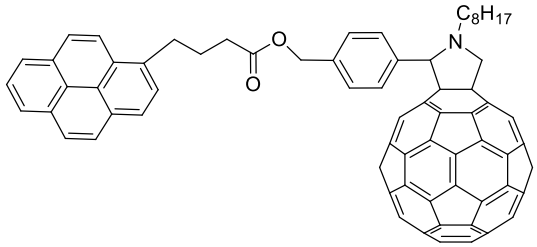

N-octylglycine (0.14 g, 0.74 mmol) and 4-formylbenzyl 4-(pyren-1-yl)butanoate **27** (0.07 g, 0.18 mmol) were added to a solution of C_{60} (0.20 g, 0.28 mmol) in toluene (100 mL). The resulting solution was heated overnight at reflux under Ar atmosphere. The solvent was removed under reduced pressure and the crude was purified by silica gel column chromatography using as eluent a gradient from C_2S to C_2S/toluene (1/1). The product was isolated as a brown solid (38%).

^{1}H-NMR (700 MHz, $CDCl_3$) δ: 8.22 (d, 1H, *J* = 9.2 Hz), 8.19-7.97 (m, 8H), 7.80 (d, 2H, *J* = 7.7 Hz), 7.44 (d, 2H, *J* = 7.7 Hz), 5.20 – 5.14 (m, 2H), 5.08 (d, 1H, *J* = 9.3 Hz), 5.04 (s, 1H), 4.10 (d, 1H, *J* = 9.3 Hz), 3.33 – 3.29 (m, 2H), 3.18 (m, 1H), 2.55 – 2.49 (m, 3H), 2.23 – 2.16 (m, 2H), 1.99 – 1.91 (m, 1H), 1.88 – 1.79 (m, 1H), 1.50 – 1.28 (m, 10H), 0.91 (t, 3H, *J* = 7.0 Hz).

^{13}C-NMR (175 MHz, $CDCl_3$) δ: 173.3, 156.5, 154.2, 153.4, 153.3, 147.3, 146.6, 146.4, 146.3, 146.2, 146.1, 146.0, 145.8, 145.6, 145.5, 145.4, 145.3, 145.2, 145.1, 144.7, 144.4, 144.3, 143.0, 142.9, 142.6, 142.5, 142.4, 142.3, 142.2, 142.1, 142.0, 141.8, 141.6, 141.3, 140.1, 139.8, 139.3, 137.6, 136.8, 136.5, 136.2, 135.8, 135.6, 131.4, 130.9, 130.0, 128.8, 127.5, 127.4, 126.8, 125.9,

125.1, 125.0, 124.8, 123.3, 82.3, 76.6, 68.9, 66.9, 65.9, 53.2, 34.0, 32.7, 32.0, 29.7, 29.3, 28.4, 27.5, 26.9, 22.7, 14.2.

FT-IR (KBr), ν (cm^{-1}): 2923, 2852, 2796, 1736, 1605, 1511, 1460, 1426, 1379, 1301, 1238, 1182, 1025, 967, 843, 714, 576, 553, 527.

UV-Vis (NMP), λ_{max} (nm) (ε): 313 (30667), 329 (30000), 344 (27667), 432 (3333).

MALDI-TOF-MS (m/z) calculated for $C_{97}H_{41}NO_2$ [M+]: 1252.3171 found: 1252.3163.

Ethyl 4-[3,3,3-tris(4-methoxyphenyl)-1-propynyl]benzoate (43)[162]

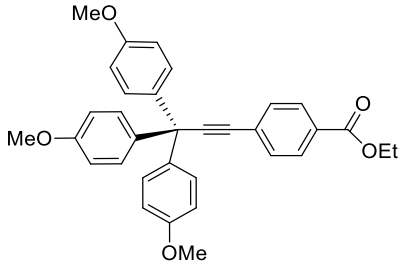

A schlenk tube was charged with 3,3,3-tris(4-methoxyphenyl)propine **13** (0.39 g, 1.10 mmol), $Pd(PPh_3)_2Cl_2$ (0.03 g, 0.05 mmol) and CuI (0.02 g, 0.09 mmol). The mixture was subjected to three argon/vacuum cycles. Subsequently, dry toluene (20 mL), Et_3N (0.4 mL) and ethyl 4-bromobenzoate **42** (0.15 mL, 0.93 mmol), were added to the reaction flask and the mixture was subjected again with three argon/vacuum cycles. The reaction mixture was heated to 40 ºC overnight. The crude was purified by silica gel column chromatography using a hexane/AcOEt (8/2) mixture as eluent. The product was isolated as a pale brown solid (74%).

^{1}H-NMR (300 MHz, $CDCl_3$) δ: 8.03 (d, 2H, *J* = 8.3 Hz), 7.59 (d, 2H, *J* = 8.3 Hz), 7.27 (d, 6H, *J* = 8.8 Hz), 6.88 (d, 6H, *J* = 8.8 Hz), 4.41 (q, 2H, *J* = 7.1 Hz), 3.83 (s, 9H), 1.43 (t, 3H, *J* = 7.1 Hz).

Ethyl 4-[3,3,3-tris(4-hydroxyphenyl)-1-propynyl]benzoate (44)[162]

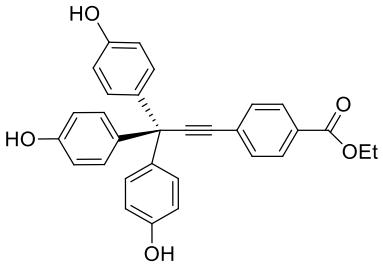

To a solution of **43** (0.07 g, 0.15 mmol) in dry DCM and at 0 ºC was added BBr_3 (4 mL, 4 mmol). The reaction mixture was allowed to react at room temperature during 3 hours. After this time, the reaction was quenched with MeOH and the solvent was removed under reduced pressure. The crude was purified by silica gel column chromatography using a hexane/AcOEt (1/1) mixture as eluent. The product was isolated as a red solid (84%).

^{1}H-NMR (300 MHz, acetone-d_6) δ: 8.38 (s, 3H), 8.01 (d, 2H, *J* = 8.4 Hz), 7.65 (d, 2H, *J* = 8.4 Hz), 7.13 (d, 6H, *J* = 8.7 Hz), 6.80 (d, 6H, *J* = 8.7 Hz), 4.35 (q, 2H, *J* = 7.1 Hz), 1.36 (t, 3H, *J* = 7.1 Hz).

Ethyl 4-{3,3,3-tris[4-(4-(pyren-1-yl)butoxy)phenyl]-1-propynyl}benzoate (45)

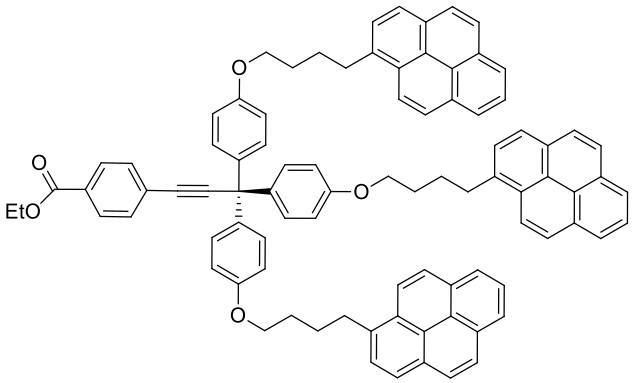

A solution of tris(phenol) **44** (0.09 g, 0.20 mmol), K_2CO_3 (0.25 g, 1.85 mmol) and 18-crown-6 (0.05 g, 0.18 mmol) in acetone was degassed under Ar and heated at reflux during 1 hour. After this time, 4-(1-pyrenyl)-1-butanol tosylate **20** (0.31 g, 0.72 mmol) was added in 5 mL of acetone drop by drop. The reaction was allowed to react under these conditions 3 days. The solvent was removed under reduced pressure and the solid was purified by silica gel column chromatography using a hexane/AcOEt (4/1) mixture as eluent. The product was isolated as a white solid (38%).

^{1}H-NMR (500 MHz, $CDCl_3$) δ: 8.28 (d, 3H, *J* = 9.2 Hz), 8.18-7.95 (m, 23H), 7.88 (d, 3H, *J* = 7.8 Hz), 7.54 (m, 2H), 7.19 (d, 6H, *J* = 8.8 Hz), 6.83 (d, 6H, *J* = 8.8 Hz), 4.38 (q, 2H, *J* = 7.2 Hz), 4.02 (t, 6H, *J* = 6.2 Hz), 3.42 (t, 6H, *J* = 7.6 Hz), 2.05 (m, 6H), 1.97 (m, 6H), 1.40 (t, 3H, *J* = 7.2 Hz).

^{13}C-NMR (125 MHz, $CDCl_3$) δ: 167.0, 158.3, 138.0, 137.0, 131.9, 131.8, 131.3, 130.5, 130.2, 129.8, 129.7, 129.6, 129.1, 128.9, 127.9, 127.7, 127.0, 126.2, 125.5, 125.4, 125.3, 125.2, 125.1, 123.8, 114.3, 100.0, 84.3, 68.1, 61.5, 54.6, 52.6, 33.6, 30.1, 29.7, 28.7, 14.7.

]FT-IR ($CHCl_3$), ν (cm^{-1}): 2930, 2863, 1718, 1604, 1503, 1466, 1438, 1395, 1242, 1175, 1106, 1020, 961, 900, 838, 764, 729, 612.

UV-Vis ($CHCl_3$), λ_{max} (nm) (ε): 314 (38732), 329 (87324), 345 (119366).

MALDI-TOF-MS (m/z) calculated for $C_{90}H_{72}O_5$ [M+]: 1232.5380, found: 1232.5490.

4-{3,3,3-tris[4-(4-(pyren-1-yl)butoxy)phenyl]-1-propynyl}benzylic alcohol (46)

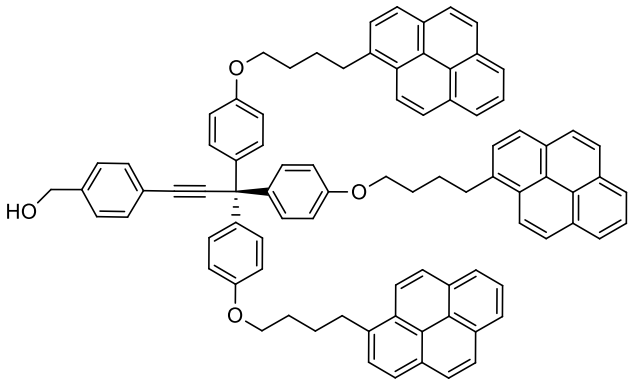

To a solution of ester **45** (0.08 g, 0.06 mmol) in dry DCM at -78 ºC and under Ar, was added DIBAL-H (0.07 mL, 0.07mmol) drop by drop. After 2 hours, MeOH (0.5 mL) was added to the reaction mixture and then was extracted with ether and HCl (1M), the solvent was removed under reduced pressure and the crude was purified by silica gel column chromatography using a hexane/AcOEt (1/1) mixture as eluent. The product was isolated as a white solid (58%).

^{1}H-NMR (500 MHz, $CDCl_3$) δ: 8.28 (d, 3H, *J* = 9.2 Hz), 8.18-7.95 (m, 21H), 7.88 (d, 3H, *J* = 7.8 Hz), 7.50 (d, 2H, *J* = 8.1 Hz), 7.30 (d, 2H, *J* = 8.1 Hz), 7.24 (d, 6H, *J* = 8.8 Hz), 6.84 (d, 6H, *J* = 8.8 Hz), 4.68 (s, 2H), 4.01 (t, 6H, *J* = 6.2 Hz), 3.41 (t, 6H, *J* = 7.6 Hz), 2.10 – 2.00 (m, 6H), 1.99 – 1.91 (m, 6H).

^{13}C-NMR (125 MHz, $CDCl_3$) δ: 158.2, 141.0, 138.4, 137.0, 132.2, 131.9, 131.3, 130.5, 130.3, 129.1, 127.9, 127.7, 127.1, 127.0, 126.2, 125.5, 125.4, 125.3, 125.2, 125.1, 123.8, 123.5, 114.3, 96.8, 84.7, 68.1, 65.4, 54.5, 33.6, 29.7, 28.7.

FT-IR ($CHCl_3$), ν (cm^{-1}): 3455, 3040, 2931, 2864, 1604, 1502, 1466, 1388, 1295, 1241, 1175, 1108, 1036, 905, 837, 726, 644, 615.

UV-Vis ($CHCl_3$), λ_{max} (nm) (ε): 314 (37698), 329 (83730), 345 (111508).

MALDI-TOF-MS (m/z) calculated for $C_{88}H_{70}O_4$ [M+]: 1190.5274, found: 1190.5284.

4-{3,3,3-tris[4-(4-(pyren-1-yl)butoxy)phenyl]-1-propynyl}benzaldehyde (47)

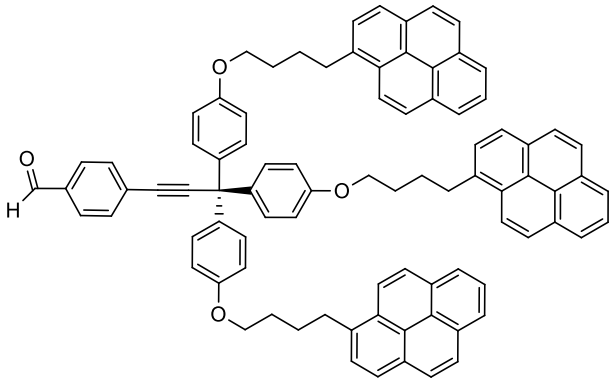

To a solution of alcohol **46** (0.07 g, 0.06 mmol) in DCM and at room temperature, was added PCC (0.03 g, 0.12 mmol). The mixture was allowed to react under these conditions overnight. After this time, the solvent was removed under reduced pressure and the crude was purified by silica gel column chromatography using a hexane/AcOEt (2/1) mixture as eluent. The product was isolated as a white solid (84%).

^{1}H-NMR (300 MHz, $CDCl_3$) δ: 9.99 (s, 1H), 8.28 (d, 3H, *J* = 9.3 Hz), 8.19-7.93 (m, 21H), 7.88 (d, 3H *J* = 7.8 Hz), 7.81 (d, 2H, *J* = 8.2 Hz), 7.62 (d, 2H, *J* = 8.2 Hz), 7.19 (d, 6H, *J* = 8.8 Hz), 6.83 (d, 6H, *J* = 8.8 Hz), 4.02 (t, 6H, *J* = 6.0 Hz), 3.42 (t, 6H, *J* = 7.4 Hz), 2.01 (m, 12H).

^{13}C-NMR (75 MHz, $CDCl_3$) δ: 191.5, 157.9, 137.5, 136.6, 135.2, 132.2, 131.5, 130.9, 130.1, 129.9, 129.5, 128.7, 127.5, 127.3, 126.6, 125.8, 125.1, 124.9, 124.8, 124.7, 123.4, 114.0, 100.9, 88.9, 67.7, 54.3, 33.2, 29.7, 28.3.

FT-IR ($CHCl_3$), ν (cm^{-1}): 2926, 2857, 1699, 1603, 1505, 1466, 1387, 1297, 1246, 1177, 1110, 1040, 964, 902, 841, 757, 717, 618.

UV-Vis ($CHCl_3$), λ_{max} (nm) (ε): 313 (28571), 329 (48485), 345 (70563).

MALDI-TOF-MS (m/z) calculated for $C_{88}H_{68}O_4$ [M+]: 1188.5118, found: 1188.5156.

***N*-octyl-2-(4-(3,3,3-tris(4-(4-(1-pyrenyl)butoxy)phenyl)-1-propynyl)phenyl)pyrrolidino[3,4:1,2][60]fullerene (3PyC$_{60}$, 48)**

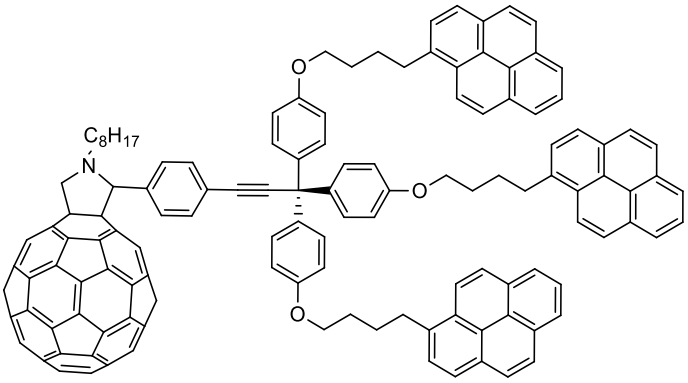

N-octylglycine (0.06 g, 0.34 mmol) and **47** (0.1 g, 0.08 mmol) were added to a solution of C_{60} (0.09 g, 0.13 mmol) in toluene (100 mL). The resulting solution was heated overnight at reflux and under Ar atmosphere. The solvent was removed under reduced pressure and the crude was purified by silica gel column chromatography using as eluent a gradient from C_2S to C_2S/toluene (3/1). The product was isolated as a brown solid (35%).

^{1}H-NMR (700 MHz, $CDCl_3$) δ: 8.22 (d, 3H, *J* = 9.2 Hz), 8.17-7.91 (m, 21H), 7.82 (d, 3H, *J* = 7.7 Hz), 7.71 (s, 2H), 7.55 (s, 2H), 7.23 (d, 6H, *J* = 8.6 Hz), 6.80 (d, 6H, *J* = 8.6 Hz), 4.92 (d, 1H, *J* = 9.1 Hz), 4.83 (s, 1H), 3.92 (t, 6H, *J* = 5.9 Hz), 3.87 (d, 1H, *J* = 9.1 Hz), 3.35 (t, 6H, *J* = 7.6 Hz), 3.09 (m, 1H), 2.40 (s, 1H), 1.98 (m, 6H), 1.95 – 1.85 (m, 6H), 1.79 (d, 1H, *J* = 4.7 Hz), 1.59 (s, 1H), 1.50 – 1.25 (m, 10H), 0.94 (t, 3H, *J* = 6.8 Hz).

^{13}C-NMR (175 MHz, $CDCl_3$) δ: 157.8, 156.3, 153.9, 153.1, 147.1, 146.5, 146.2, 146.1, 146.0, 145.9, 145.8, 145.7, 145.5, 145.3, 145.1, 145.0, 144.9, 144.5, 144.4, 144.2, 142.9, 142.7, 142.5, 142.3, 142.1, 142.0, 141.9, 141.8, 141.7, 141.6, 141.4, 141.3, 139.9, 139.7, 139.5, 137.9, 137.3, 136.7, 136.6, 136.4, 135.7, 135.5, 131.9, 131.5, 130.9, 130.1, 129.9, 129.4, 128.7, 127.6, 127.3, 126.6, 125.8, 125.2, 125.1, 124.9, 124.8, 123.8, 123.4, 113.9, 97.0, 84.4, 82.2, 76.4, 68.8, 67.7, 66.7, 54.2, 53.1, 33.2, 32.1, 29.8, 29.4, 29.3, 28.4, 28.3, 27.7, 22.8, 14.3.

FT-IR (KBr), ν (cm^{-1}): 2925, 2856, 1605, 1504, 1463, 1383, 1299, 1244, 1178, 1114, 1040, 840, 760, 714, 616, 585, 553, 527.

UV-Vis (NMP), λ_{max} (nm) (ε): 315 (45395), 329 (53289), 345 (51974), 433 (3289).

MALDI-TOF-MS (m/z) calculated for $C_{157}H_{87}NO_3$ [M+]: 2033.6686, found: 2033.6756.

6.2. SYNTHESIS OF FLG NON-COVALENT HYBRIDS

Chemical exfoliation of graphite

Graphite (0.2 g) was dispersed in NMP (100 mL) and sonicated at room temperature during 150 minutes at a low-power sonication bath, to obtain homogeneous aggregates. This dispersion was then centrifuged at 500 rpm for 45 minutes. After this process, the supernatant was isolated on vials with a Pasteur pipette. The FLG dispersion was kept in solution for further reactions.

General procedure for the synthesis of monopodal non-covalent hybrids

A sample of 4 mg of the monopodal derivative (compounds **11**, **30**, **31**, **32** and **41**) was mixed with 20 mL of the FLG dispersion previously obtained in NMP ($1.6x10^{-4}$ M, molecule concentration). This mixture was sonicated during 30 min. After this time, the mixture was filtered on a PTFE membrane and washed with dichloromethane until the filtrate was transparent to afford the corresponding supramolecular complex.

General procedure for the synthesis of tripodal non-covalent hybrids

A sample of 7 mg of the tripodal derivative (compounds **21, 38, 39, 40** and **48**) was mixed with 20 mL of the FLG dispersion previously obtained in NMP ($1.6x10^{-4}$ M, molecule concentration). This mixture was sonicated during 30 min. After this time, the mixture was filtered on a PTFE membrane and washed with dichloromethane until the filtrate was transparent to afford the corresponding supramolecular complex.

PyexTTF/FLG (Complex 1)

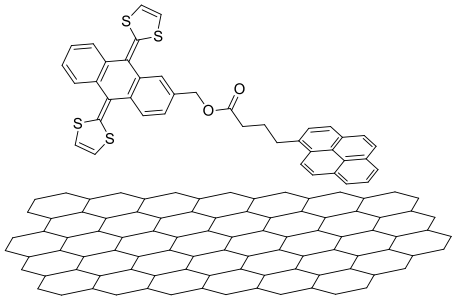

FT-IR (KBr), ν (cm^{-1}): 2957, 2924, 2855, 1736, 1702, 1585, 1458, 1385, 1113, 1049, 867, 804, 669.

TGA (Air atmosphere): weight loss and temperature desorption (organic groups): 34.7%, 603 ºC.

Raman: I_D/I_G = 0.07.

UV-Vis (NMP), λ_{max} (nm): 329, 345, 432.

XPS: % atomic: C (284.6 eV) = 95.4, O (532.6 eV) = 4.47, S (163.6 eV) = 0.13.

3PyexTTF/FLG (Complex 2)

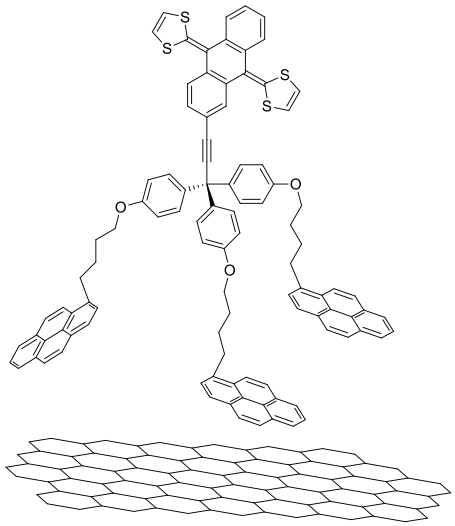

FT-IR (KBr), ν (cm^{-1}): 2956, 2925, 2854, 1740, 1682, 1582, 1455, 1434, 1385, 1214, 1157, 1034, 875, 772, 722, 667.

TGA (Air atmosphere): weight loss and temperature desorption (organic groups): 31.6%, 628 ºC.

Raman: I_D/I_G = 0.07.

UV-Vis (NMP), λ_{max} (nm): 329, 345.

XPS: % atomic: C (284.6 eV) = 90.12, O (533.6 eV) = 9.64, S (164.6 eV) = 0.23.

PyH_2P/FLG (Complex 3)

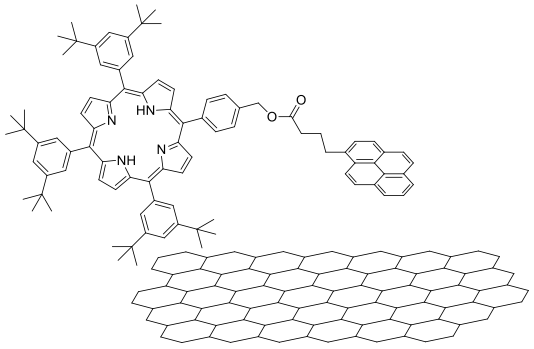

FT-IR (KBr), ν (cm^{-1}): 2924, 2853, 1739, 1638, 1581, 1460, 1400, 1384, 1162, 1117.

TGA (N_2 atmosphere): weight loss and temperature desorption (organic groups): 21.1%, 432 ºC.

Raman: I_D/I_G = 0.12.

UV-Vis (NMP), λ_{max} (nm): 421.

PyZnP/FLG (Complex 4)

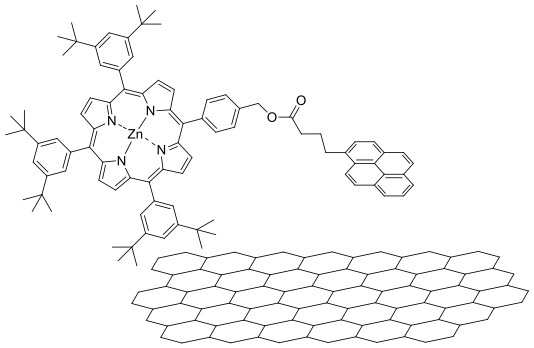

FT-IR (KBr), ν (cm^{-1}): 2925, 2855, 1740, 1582, 1543, 1459, 1385, 1161, 1116, 672.

TGA (N_2 atmosphere): weight loss and temperature desorption (organic groups): 31.6%, 569 ºC.

Raman: I_D/I_G = 0.08.

UV-Vis (NMP), λ_{max} (nm): 429.

PyNiP/FLG (Complex 5)

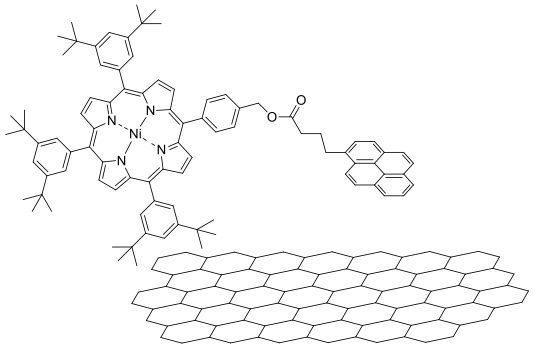

FT-IR (KBr), ν (cm^{-1}): 2924, 2854, 1738, 1587, 1456, 1403, 1163, 1113, 799, 670.

TGA (N_2 atmosphere): weight loss and temperature desorption (organic groups): 27.4%, 463 ºC.

Raman: I_D/I_G = 0.15.

UV-Vis (NMP), λ_{max} (nm): 419.

3PyH_2P/FLG (Complex 6)

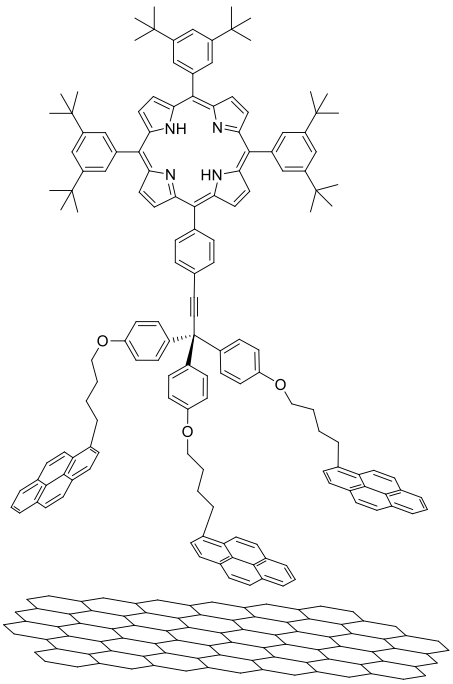

FT-IR (KBr), ν (cm^{-1}): 2925, 2853, 1742, 1623, 1580, 1459, 1141, 1121, 669, 603.

TGA (N_2 atmosphere): weight loss and temperature desorption (organic groups): 24.3%, 459 ºC.

Raman: I_D/I_G = 0.13.

UV-Vis (NMP), λ_{max} (nm): 423.

3PyZnP/FLG (Complex 7)

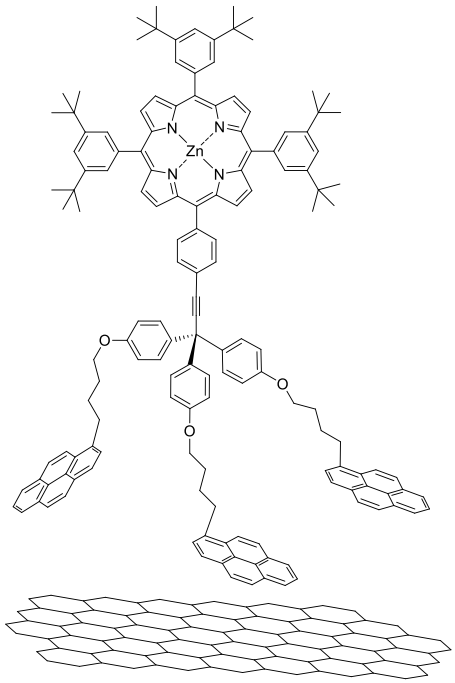

FT-IR (KBr), ν (cm^{-1}): 2924, 2854, 1742, 1591, 1456, 1233, 1156, 670, 648.

TGA (N_2 atmosphere): weight loss and temperature desorption (organic groups): 27.6%, 441 ºC.

Raman: I_D/I_G = 0.08.

UV-Vis (NMP), λ_{max} (nm): 430.

3PyNiP/FLG (Complex 8)

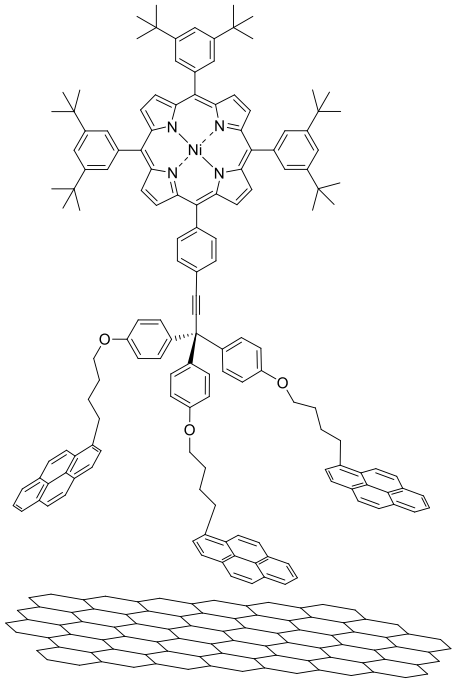

FT-IR (KBr), ν (cm^{-1}): 2924, 2854, 1741, 1435, 1086, 875, 713, 669.

TGA (N_2 atmosphere): weight loss and temperature desorption (organic groups): 16.2%, 438 ºC.

Raman: I_D/I_G = 0.16.

UV-Vis (NMP), λ_{max} (nm): 420.

PyC_{60}/FLG (Complex 9)

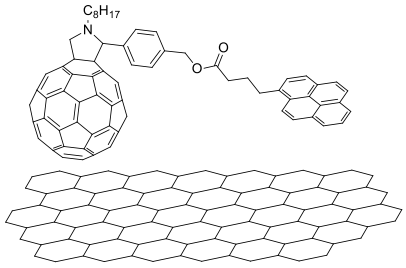

FT-IR (KBr), ν (cm^{-1}): 2956, 2925, 2855, 1736, 1583, 1457, 1384, 1121, 1098, 1039, 843, 721, 667, 527, 470.

TGA (N_2 atmosphere): weight loss and temperature desorption (organic groups): 8.9%, 426 ºC.

Raman: I_D/I_G = 0.10.

UV-Vis (NMP), λ_{max} (nm): 327, 345.

3PyC$_{60}$/FLG (Complex 10)

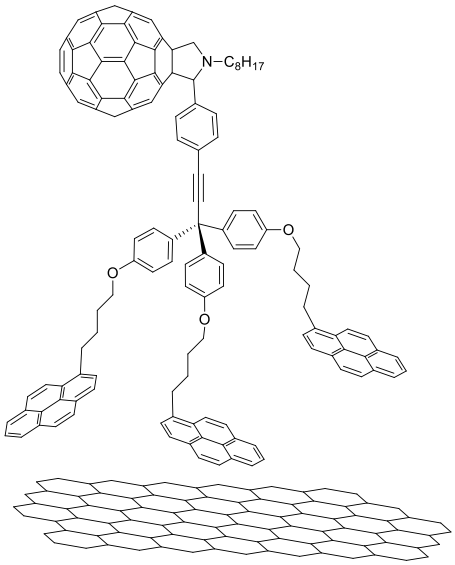

FT-IR (KBr), ν (cm^{-1}): 2926, 2855, 1582, 1432, 1384, 1247, 1110, 1034, 841, 655, 527, 470.

TGA (N_2 atmosphere): weight loss and temperature desorption (organic groups): 17.3%, 429 ºC.

Raman: I_D/I_G = 0.08.

UV-Vis (NMP), λ_{max} (nm): 328, 345.

BIBLIOGRAPHY

BIBLIOGRAPHY

1. a) E. H. L. Falcao, F. Wudl, *Carbon Allotropes: Beyond Graphite and Diamond*, *J. Chem. Technol. Biotechnol.* **2007**, *82*, 524-531. b) J. L. Delgado, M. A. Herranz, N. Martín, *The Nano-Forms of Carbon*, *J. Mater. Chem.* **2008**, *18*, 1417-1426.

2. a) H. W. Kroto, J. R. Heath, S. C. O'Brien, R. F. Curl, R. E. Smalley, *C_{60}: Buckminsterfullerene*, *Nature* **1985**, *318*, 162-163. b) J. R. Heath, R. F. Curl, R. E. Smalley, *The UV Absorption Spectrum of C_{60} (Buckminsterfullerene): A Narrow Band at 3860 Å*, *J. Chem. Phys.* **1987**, *87*, 4236-4238.

3. S. Iijima, *Helical Microtubules of Graphitic Carbon*, *Nature* **1991**, *354*, 56-58.

4. a) S. Iijima, T. Ichihashi, *Single-shell Carbon Nanotubes of 1-nm Diameter*, *Nature* **1993**, *363*, 603-605. b) D. S. Bethune, C. H. Klang, M. S. de Vries, G. Gorman, R. Savoy, J. Vazquez, R. Beyers, *Cobalt-catalysed Growth of Carbon Nanotubes with Single-Atomic-Layer Walls*, *Nature* **1993**, *363*, 605-607.

5. K. S. Novoselov, A. K. Geim, S. V. Morozov, D. Jiang, Y. Zhang, S. V. Dubonos, I. V. Grigorieva, A. A. Firsov, *Electric Field Effect in Atomically Thin Carbon Films*, *Science* **2004**, *306*, 666-669.

6. T. Akasaka, F. Wudl, S. Nagase, *Chemistry of Nanocarbons*, John Wiley&Sons, Chichester, **2010**.

7. a) D. M. Guldi, B. M. Illescas, C. M. Atienza, M. Wielopolski, N. Martín, *Fullerene for Organic Electronics*, *Chem. Soc. Rev.* **2009**, *38*, 1587-1597. b) K. A. Mazzio, C. K. Luscombe, *The Future of Organic Photovoltaics*, *Chem. Soc. Rev.* **2015**, *44*, 78-90.

8. A. Montellano, T. Da Ros, A. Bianco, M. Prato, *Fullerene C_{60} as A Multifunctional System for Drug and Gene Delivery*, *Nanoscale* **2011**, *3*, 4035-4041.

9. A. Muñoz, D. Sigwalt, B. M. Illescas, J. Luczkowiak, L. Rodríguez-Pérez, I. Nierengarten, M. Holler, J.-S. Remy, K. Buffet, S. P. Vincent, J. Rojo, R. Delgado, J.-F. Nierengarten, N. Martín, *Synthesis of Giant Globular Multivalent Glycofullerenes as Potent Inhibitors in A Model of Ebola Virus Infection*, *Nat. Chem.* **2016**, *8*, 50-57.

10. D. M. Guldi, N. Martín, *Carbon Nanotubes and Related Structures*, Wiley-VCH, Weinheim, **2010**.

11. R. H. Baughman, A. A. Zakhidov, W. A. d. Heer, *Carbon Nanotubes: The Route Towards Application*, *Science* **2002**, *297*, 787-792.

12. M. F. L. De Volder, S. H. Tawfick, R. H. Baughman, A. J. Hart, *Carbon Nanotubes: Present and Future Commercial Applications*, *Science* **2013**, *339*, 535-539.

13. J. N. Coleman, U. Khan, Y. K. Gun'ko, *Mechanical Reinforcement of Polymers Using Carbon Nanotubes*, *Adv. Mater.* **2006**, *18*, 689-706.

14. L. Dai, D. W. Chang, J.-B. Baek, W. Lu, *Carbon Nanomaterials for Advanced Energy Conversion and Storage*, *Small* **2012**, *8*, 1130-1166.

15. A. K. Geim, *Graphene: Status and Prospects*, *Science* **2009**, *324*, 1530-1534.

16. S. Bae, H. Kim, Y. Lee, X. Xu, J.-S. Park, Y. Zheng, J. Balakrishnan, T. Lei, H. Ri Kim, Y. I. Song, Y.-J. Kim, K. S. Kim, B. Ozyilmaz, J.-H. Ahn, B. H. Hong, S. Iijima, *Roll-to-Roll Production of 30-Inch Graphene Films for Transparent Electrodes*, *Nat. Nanotechnol.* **2010**, *5*, 574-578.

17. Y. D. Kim, H. Kim, Y. Cho, J. H. Ryoo, C.-H. Park, P. Kim, Y. S. Kim, S. Lee, Y. Li, S.-N. Park, Y. Shim Yoo, D. Yoon, V. E. Dorgan, E. Pop, T. F. Heinz, J. Hone, S.-H. Chun, H. Cheong, S. W. Lee, M.-H. Bae, Y. D. Park, *Bright Visible Light Emission from Graphene*, *Nat. Nanotechnol.*, **2015**, *10*, 676-681.

18. a) K. S. Kim, Y. Zhao, H. Jang, S. Y. Lee, J. M. Kim, K. S. Kim, J.-H. Ahn, P. Kim, J.-Y. Choi, B. H. Hong, *Large-Scale Pattern Growth of Graphene Films for Stretchable Transparent Electrodes*, *Nature* **2009**, *457*, 706-710. b) A. H. Castro Neto, F. Guinea, N. M. R. Peres, K. S. Novoselov, A. K. Geim, *The Electronic Properties of Graphene*, *Rev. Mod. Phys.* **2009**, *81*, 109-162.

19. M. L. Mueller, X. Yan, B. Dragnea, L.-s. Li, *Slow Hot-Carrier Relaxation in Colloidal Graphene Quantum Dots*, *Nano Lett.* **2011**, *11*, 56-60.

20. T. Ohta, A. Bostwick, T. Seyller, K. Horn, E. Rotenberg, *Controlling The Electronic Structure of Bilayer Graphene*, *Science* **2006**, *313*, 951-954.

21. L. Jiao, L. Zhang, X. Wang, G. Diankov, H. Dai, *Narrow Graphene Nanoribbons from Carbon Nanotubes*, *Nature* **2009**, *458*, 877-880.

22. H. Liu, Y. Liu, D. Zhu, *Chemical Doping of Graphene*, *J. Mater. Chem.* **2011**, *21*, 3335-3345.

23. H.-X. Wang, Q. Wang, K.-G. Zhou, H.-L. Zhang, *Graphene in Light: Design, Synthesis and Applications of Photo-Active Graphene and Graphene-Like Materials*, *Small* **2013**, *9*, 1266-1283.

24. a) X. Huang, Z. Yin, S. Wu, X. Qi, Q. He, Q. Zhang, Q. Yan, F. Boey, H. Zhang, *Graphene-Based Materials: Synthesis, Characterization, Properties, and Applications*, *Small* **2011**, *7*, 1876-1902. b) X. Wan, Y. Huang, Y. Chen, *Focusing on Energy and Optoelectronic Applications: A Journey for Graphene and Graphene Oxide at Large Scale*, *Acc. Chem. Res.* **2012**, *45*, 598-607.

25. a) L. Dai, *Functionalization of Graphene for Efficient Energy Conversion and Storage*, *Acc. Chem. Res.* **2013**, *46*, 31-42. b) N. Martín, *Carbon Nanoforms for Photovoltaics: Myth or Reality?*, *Adv. Energy Mater.* **2017**, *7*, 1601102.

26. D. D. L. Chung, *Review Graphite*, *J. Mater. Sci.* **2002**, *37*, 1475-1489.

27. R. E. Peierls, *Quelques Propriétés Typiques Des Corps Solides*, *Ann. Inst. Henri Poincare* **1935**, *5*, 177-222.

28. L. D. Landau, *Theory of Phase Transformations. I*, *Phys. Z. Sowjetunion* **1937**, *11*, 26.

29. J. C. Meyer, A. K. Geim, M. I. Katsnelson, K. S. Novoselov, T. J. Booth, S. Roth, *The Structure of Suspended Graphene Sheets*, *Nature* **2007**, *446*, 60-63.

30. S. Eigler, A. Hirsch, *Chemistry with Graphene and Graphene Oxide: Challenges for Synthetic Chemists*, *Angew. Chem. Int. Ed.* **2014**, *53*, 7720-7738.

31. A. K. Geim, K. S. Novoselov, *The Rise of Graphene*, *Nat. Mater.* **2007**, *6*, 183-191.

32. S. Stankovich, D. A. Dikin, R. D. Piner, K. A. Kohlhaas, A. Kleinhammes, Y. Jia, Y. Wu, S. T. Nguyen, R. S. Ruoff, *Synthesis of Graphene-Based Nanosheets Via Chemical Reduction of Exfoliated Graphite Oxide*, *Carbon* **2007**, *45*, 1558-1565.

33. D. R. Dreyer, S. Park, C. W. Bielawski, R. S. Ruoff, *The Chemistry of Graphene Oxide*, *Chem. Soc. Rev.* **2010**, *39*, 228-240.

34. C. Gómez-Navarro, R. T. Weitz, A. M. Bittner, M. Scolari, A. Mews, M. Burghard, K. Kern, *Electronic Transport Properties of Individual Chemically Reduced Graphene Oxide Sheets*, *Nano Lett.* **2007**, *7*, 3499-3503.

35. X. Yang, X. Dou, A. Rouhanipour, L. Zhi, H. J. Räder, K. Müllen, *Two-Dimensional Graphene Nanoribbons*, *J. Am. Chem. Soc.* **2008**, *130*, 4216-4217.

36. C. Berger, Z. Song, X. Li, X. Wu, N. Brown, C. Naud, D. Mayou, T. Li, J. Hass, A. N. Marchenkov, E. H. Conrad, P. N. First, W. A. de Heer, *Electronic Confinement and Coherence in Patterned Epitaxial Graphene*, *Science* **2006**, *312*, 1191-1196.

37. a) V. Leon, M. Quintana, M. A. Herrero, J. L. G. Fierro, A. d. l. Hoz, M. Prato, E. Vazquez, *Few-Layer Graphenes from Ball-Milling of Graphite with Melamine*, *Chem. Commun.* **2011**, *47*, 10936-10938. b) E. Vazquez, F. Giacalone, M. Prato, *Non-Conventional Methods and Media for The Activation and Manipulation of Carbon Nanoforms*, *Chem. Soc. Rev.* **2014**, *43*, 58-69.

38. Y. Hernandez, V. Nicolosi, M. Lotya, F. M. Blighe, Z. Sun, S. De, I. T. McGovern, B. Holland, M. Byrne, Y. K. Gun'Ko, J. J. Boland, P. Niraj, G. Duesberg, S. Krishnamurthy, R. Goodhue, J. Hutchison, V. Scardaci, A. C. Ferrari, J. N. Coleman, *High-Yield Production of Graphene by Liquid-Phase Exfoliation of Graphite*, *Nat. Nanotechnol.* **2008**, *3*, 563-568.

39. F. Torrisi, T. Hasan, W. Wu, Z. Sun, A. Lombardo, T. S. Kulmala, G.-W. Hsieh, S. Jung, F. Bonaccorso, P. J. Paul, D. Chu, A. C. Ferrari, *Inkjet-Printed Graphene Electronics*, *ACS Nano* **2012**, *6*, 2992-3006.

40. T. J. Mason, J. P. Lorimer, *Applied Sonochemistry*, Wiley-VCH, Weinheim, **2002**.

41. Y. Hernandez, M. Lotya, D. Rickard, S. D. Bergin, J. N. Coleman, *Measurement of Multicomponent Solubility Parameters for Graphene Facilitates Solvent Discovery*, *Langmuir* **2010**, *26*, 3208-3213.

42. C. E. Hamilton, J. R. Lomeda, Z. Sun, J. M. Tour, A. R. Barron, *High-Yield Organic Dispersions of Unfunctionalized Graphene*, *Nano Lett.* **2009**, *9*, 3460-3462.

43. A. B. Bourlinos, V. Georgakilas, R. Zboril, T. A. Steriotis, A. K. Stubos, *Liquid-Phase Exfoliation of Graphite Towards Solubilized Graphenes*, *Small* **2009**, *5*, 1841-1845.

44. Z. Sun, X. Huang, F. Liu, X. Yang, C. Rosler, R. A. Fischer, M. Muhler, W. Schuhmann, *Amine-Based Solvents for Exfoliating Graphite to Graphene Outperform The Dispersing Capacity of N-methyl-pyrrolidone and Surfactants*, *Chem. Commun.* **2014**, *50*, 10382-10385.

45. X. Zhang, A. C. Coleman, N. Katsonis, W. R. Browne, B. J. van Wees, B. L. Feringa, *Dispersion of Graphene in Ethanol Using A Simple Solvent Exchange Method*, *Chem. Commun.* **2010**, *46*, 7539-7541.

46. a) J. Shen, J. Wu, M. Wang, P. Dong, J. Xu, X. Li, X. Zhang, J. Yuan, X. Wang, M. Ye, R. Vajtai, J. Lou, P. M. Ajayan, *Surface Tension Components Based Selection of Cosolvents for Efficient Liquid Phase Exfoliation of 2D Materials*, *Small* **2016**, *12*, 2741-2749. b) U. Halim, C. R. Zheng, Y. Chen, Z. Lin, S. Jiang, R. Cheng, Y. Huang, X. Duan, *A Rational Design of Cosolvent Exfoliation of Layered Materials by Directly Probing Liquid–Solid Interaction*, *Nat. Commun.* **2013**, *4*, 2213. c) Y. Min, S. Zhigang, Z. Xiaojing, M. Shulin, *Achieving Concentrated Graphene Dispersions in Water/Acetone Mixtures by The Strategy of Tailoring Hansen Solubility Parameters*, *J. Phys. D: Appl. Phys.* **2013**, *46*, 025301.

47. U. Khan, A. O'Neill, M. Lotya, S. De, J. N. Coleman, *High-Concentration Solvent Exfoliation of Graphene*, *Small* **2010**, *6*, 864-871.

48. U. Khan, H. Porwal, A. O'Neill, K. Nawaz, P. May, J. N. Coleman, *Solvent-Exfoliated Graphene at Extremely High Concentration*, *Langmuir* **2011**, *27*, 9077-9082.

49. D. Parviz, F. Irin, S. A. Shah, S. Das, C. B. Sweeney, M. J. Green, *Challenges in Liquid-Phase Exfoliation, Processing, and Assembly of Pristine Graphene*, *Adv. Mater.* **2016**, *28*, 8796-8818.

50. A. C. Ferrari, J. C. Meyer, V. Scardaci, C. Casiraghi, M. Lazzeri, F. Mauri, S. Piscanec, D. Jiang, K. S. Novoselov, S. Roth, A. K. Geim, *Raman Spectrum of Graphene and Graphene Layers*, *Phys. Rev. Lett.* **2006**, *97*, 187401.

51. J. C. Meyer, A. K. Geim, M. I. Katsnelson, K. S. Novoselov, D. Obergfell, S. Roth, C. Girit, A. Zettl, *On The Roughness of Single- and Bi-Layer Graphene Membranes*, *Solid State Commun.* **2007**, *143*, 101-109.

52. C. Vallés, C. Drummond, H. Saadaoui, C. A. Furtado, M. He, O. Roubeau, L. Ortolani, M. Monthioux, A. Pénicaud, *Solutions of Negatively Charged Graphene Sheets and Ribbons*, *J. Am. Chem. Soc.* **2008**, *130*, 15802-15804.

53. K. S. Novoselov, D. Jiang, F. Schedin, T. J. Booth, V. V. Khotkevich, S. V. Morozov, A. K. Geim, *Two-Dimensional Atomic Crystals*, *Proc. Natl. Acad. Sci. U. S. A.* **2005**, *102*, 10451-10453.

54. K. S. Subrahmanyam, S. R. C. Vivekchand, A. Govindaraj, C. N. R. Rao, *A Study of Graphenes Prepared by Different Methods: Characterization, Properties and Solubilization*, *J. Mater. Chem.* **2008**, *18*, 1517-1523.

55. M. Shtein, I. Pri-Bar, M. Varenik, O. Regev, *Characterization of Graphene-Nanoplatelets Structure Via Thermogravimetry*, *Anal. Chem.* **2015**, *87*, 4076-4080.

56. X. Wang, P. F. Fulvio, G. A. Baker, G. M. Veith, R. R. Unocic, S. M. Mahurin, M. Chi, S. Dai, *Direct Exfoliation of Natural Graphite into Micrometre Size Few Layers Graphene Sheets Using Ionic Liquids*, *Chem. Commun.* **2010**, *46*, 4487-4489.

57. D. Nuvoli, L. Valentini, V. Alzari, S. Scognamillo, S. B. Bon, M. Piccinini, J. Illescas, A. Mariani, *High Concentration Few-Layer Graphene Sheets Obtained by Liquid Phase Exfoliation of Graphite in Ionic Liquid*, *J. Mater. Chem.* **2011**, *21*, 3428-3431.

58. R. Bari, G. Tamas, F. Irin, A. J. A. Aquino, M. J. Green, E. L. Quitevis, *Direct Exfoliation of Graphene in Ionic Liquids with Aromatic Groups*, *Colloids Surf. A* **2014**, *463*, 63-69.

59. M. Matsumoto, Y. Saito, C. Park, T. Fukushima, T. Aida, *Ultrahigh-Throughput Exfoliation of Graphite into Pristine 'Single-Layer' Graphene Using Microwaves and Molecularly Engineered Ionic Liquids*, *Nat. Chem.* **2015**, *7*, 730-736.

60. M. Lotya, Y. Hernandez, P. J. King, R. J. Smith, V. Nicolosi, L. S. Karlsson, F. M. Blighe, S. De, Z. Wang, I. T. McGovern, G. S. Duesberg, J. N. Coleman, *Liquid Phase Production of Graphene by Exfoliation of Graphite in Surfactant/Water Solutions*, *J. Am. Chem. Soc.* **2009**, *131*, 3611-3620.

61. M. Lotya, P. J. King, U. Khan, S. De, J. N. Coleman, *High-Concentration, Surfactant-Stabilized Graphene Dispersions*, *ACS Nano* **2010**, *4*, 3155-3162.

62. S. Vadukumpully, J. Paul, S. Valiyaveettil, *Cationic Surfactant Mediated Exfoliation of Graphite into Graphene Flakes*, *Carbon* **2009**, *47*, 3288-3294.

63. A. B. Bourlinos, V. Georgakilas, R. Zboril, T. A. Steriotis, A. K. Stubos, C. Trapalis, *Aqueous-Phase Exfoliation of Graphite in The Presence of Polyvinylpyrrolidone for The Production of Water-Soluble Graphenes*, *Solid State Commun.* **2009**, *149*, 2172-2176.

64. Y. T. Liang, M. C. Hersam, *Highly Concentrated Graphene Solutions Via Polymer Enhanced Solvent Exfoliation and Iterative Solvent Exchange*, *J. Am. Chem. Soc.* **2010**, *132*, 17661-17663.

65. L. Xu, J.-W. McGraw, F. Gao, M. Grundy, Z. Ye, Z. Gu, J. L. Shepherd, *Production of High-Concentration Graphene Dispersions in Low-Boiling-Point Organic Solvents by Liquid-Phase Noncovalent Exfoliation of Graphite with A Hyperbranched Polyethylene and Formation of Graphene/Ethylene Copolymer Composites*, *J. Phys. Chem. C* **2013**, *117*, 10730-10742.

66. I. Uysal Unalan, C. Wan, S. Trabattoni, L. Piergiovanni, S. Farris, *Polysaccharide-Assisted Rapid Exfoliation of Graphite Platelets into High Quality Water-Dispersible Graphene Sheets*, *RSC Adv.* **2015**, *5*, 26482-26490.

67. Y. Xu, H. Bai, G. Lu, C. Li, G. Shi, *Flexible Graphene Films Via The Filtration of Water-Soluble Noncovalent Functionalized Graphene Sheets*, *J. Am. Chem. Soc.* **2008**, *130*, 5856-5857.

68. D.-W. Lee, T. Kim, M. Lee, *An Amphiphilic Pyrene Sheet for Selective Functionalization of Graphene*, *Chem. Commun.* **2011**, *47*, 8259-8261.

69. D. Parviz, S. Das, H. S. T. Ahmed, F. Irin, S. Bhattacharia, M. J. Green, *Dispersions of Non-Covalently Functionalized Graphene with Minimal Stabilizer*, *ACS Nano* **2012**, *6*, 8857-8867.

70. S. Das, F. Irin, H. S. Tanvir Ahmed, A. B. Cortinas, A. S. Wajid, D. Parviz, A. F. Jankowski, M. Kato, M. J. Green, *Non-Covalent Functionalization of Pristine Few-Layer Graphene Using Triphenylene Derivatives for Conductive Poly (Vinyl Alcohol) Composites*, *Polymer* **2012**, *53*, 2485-2494.

71. S. Sampath, A. N. Basuray, K. J. Hartlieb, T. Aytun, S. I. Stupp, J. F. Stoddart, *Direct Exfoliation of Graphite to Graphene in Aqueous Media with Diazaperopyrenium Dications*, *Adv. Mater.* **2013**, *25*, 2740-2745.

72. L. Zhang, Z. Zhang, C. He, L. Dai, J. Liu, L. Wang, *Rationally Designed Surfactants for Few-Layered Graphene Exfoliation: Ionic Groups Attached to Electron-Deficient π-Conjugated Unit Through Alkyl Spacers*, *ACS Nano* **2014**, *8*, 6663-6670.

73. V. Georgakilas, M. Otyepka, A. B. Bourlinos, V. Chandra, N. Kim, K. C. Kemp, P. Hobza, R. Zboril, K. S. Kim, *Functionalization of Graphene: Covalent and Non-Covalent Approaches, Derivatives and Applications*, *Chem. Rev.* **2012**, *112*, 6156-6214.

74. L. Rodriguez-Perez, M. A. Herranz, N. Martín, *The Chemistry of Pristine Graphene*, *Chem. Commun.* **2013**, *49*, 3721-3735.

75. a) A. Ciesielski, P. Samorì, *Supramolecular Approaches to Graphene: From Self-Assembly to Molecule-Assisted Liquid-Phase Exfoliation*, *Adv. Mater.* **2016**, *28*, 6030-6051. b) A. Ciesielski, P. Samori, *Graphene Via Sonication Assisted Liquid-Phase Exfoliation*, *Chem. Soc. Rev.* **2014**, *43*, 381-398.

76. X. An, T. Simmons, R. Shah, C. Wolfe, K. M. Lewis, M. Washington, S. K. Nayak, S. Talapatra, S. Kar, *Stable Aqueous Dispersions of Noncovalently Functionalized Graphene from Graphite and Their Multifunctional High-Performance Applications*, *Nano Lett.* **2010**, *10*, 4295-4301.

77. X. An, T. W. Butler, M. Washington, S. K. Nayak, S. Kar, *Optical and Sensing Properties of 1-Pyrenecarboxylic Acid-Functionalized Graphene Films Laminated on Polydimethylsiloxane Membranes*, *ACS Nano* **2011**, *5*, 1003-1011.

78. J. Malig, C. Romero-Nieto, N. Jux, D. M. Guldi, *Integrating Water-Soluble Graphene into Porphyrin Nanohybrids*, *Adv. Mater.* **2012**, *24*, 800-805.

79. G. Katsukis, J. Malig, C. Schulz-Drost, S. Leubner, N. Jux, D. M. Guldi, *Toward Combining Graphene and QDs: Assembling CdTe QDs to Exfoliated Graphite and Nanographene in Water*, *ACS Nano* **2012**, *6*, 1915-1924.

80. A. Roth, M.-E. Ragoussi, L. Wibmer, G. Katsukis, G. d. l. Torre, T. Torres, D. M. Guldi, *Electron-Accepting Phthalocyanine-Pyrene Conjugates: Towards Liquid Phase Exfoliation of Graphite and Photoactive Nanohybrid Formation with Graphene*, *Chem. Sci.* **2014**, *5*, 3432-3438.

81. A. Perry, S. J. Green, D. W. Horsell, S. M. Hornett, M. E. Wood, *A Pyrene-appended Spiropyran for Selective Photo-Switchable Binding of Zn(II): UV–Visible and Fluorescence Spectroscopy Studies of Binding and Non-Covalent Attachment to Graphene, Graphene Oxide and Carbon Nanotubes*, *Tetrahedron* **2015**, *71*, 6776-6783.

82. J. A. Mann, J. Rodríguez-López, H. D. Abruña, W. R. Dichtel, *Multivalent Binding Motifs for The Noncovalent Functionalization of Graphene*, *J. Am. Chem. Soc.* **2011**, *133*, 17614-17617.

83. J. A. Mann, W. R. Dichtel, *Improving The Binding Characteristics of Tripodal Compounds on Single Layer Graphene*, *ACS Nano* **2013**, *7*, 7193-7199.

84. C. B. Kc, G. N. Lim, F. D'Souza, *Charge Separation in Graphene-decorated Multimodular Tris(pyrene)–Subphthalocyanine–Fullerene Donor–Acceptor Hybrids*, *Angew. Chem. Int. Ed.* **2015**, *54*, 5088-5092.

85. N. V. Kozhemyakina, J. M. Englert, G. Yang, E. Spiecker, C. D. Schmidt, F. Hauke, A. Hirsch, *Non-Covalent Chemistry of Graphene: Electronic Communication with Dendronized Perylene Bisimides*, *Adv. Mater.* **2010**, *22*, 5483-5487.

86. R. Voggu, B. Das, C. S. Rout, C. N. R. Rao, *Effects of Charge Transfer Interaction of Graphene with Electron Donor and Acceptor Molecules Examined Using Raman Spectroscopy and Cognate Techniques, J. Phys. Condens. Matter.* **2008**, *20*, 472204.

87. A. Ghosh, K. V. Rao, S. J. George, C. N. R. Rao, *Noncovalent Functionalization, Exfoliation, and Solubilization of Graphene in Water by Employing A Fluorescent Coronene Carboxylate*, *Chem. Eur. J.* **2010**, *16*, 2700-2704.

88. J. Malig, A. W. I. Stephenson, P. Wagner, G. G. Wallace, D. L. Officer, D. M. Guldi, *Direct Exfoliation of Graphite with A Porphyrin - Creating Functionalizable Nanographene Hybrids*, *Chem. Commun.* **2012**, *48*, 8745-8747.

89. C. B. K. C, S. K. Das, K. Ohkubo, S. Fukuzumi, F. D'Souza, *Ultrafast Charge Separation in Supramolecular Tetrapyrrole-Graphene Hybrids*, *Chem. Commun.* **2012**, *48*, 11859-11861.

90. J. Geng, B.-S. Kong, S. B. Yang, H.-T. Jung, *Preparation of Graphene Relying on Porphyrin Exfoliation of Graphite*, *Chem. Commun.* **2010**, *46*, 5091-5093.

91. F. G. Brunetti, H. Isla, J. Aragó, E. Ortí, E. M. Pérez, N. Martín, *Exploiting Multivalent Nanoparticles for The Supramolecular Functionalization of Graphene with A Nonplanar Recognition Motif*, *Chem. Eur. J.* **2013**, *19*, 9843-9848.

92. J. Malig, N. Jux, D. Kiessling, J.-J. Cid, P. Vázquez, T. Torres, D. M. Guldi, *Towards Tunable Graphene/Phthalocyanine–PPV Hybrid Systems*, *Angew. Chem. Int. Ed.* **2011**, *50*, 3561-3565.

93. L. Brinkhaus, G. Katsukis, J. Malig, R. D. Costa, M. Garcia-Iglesias, P. Vázquez, T. Torres, D. M. Guldi, *Tuning The Stability of Graphene Layers by Phthalocyanine-Based oPPV Oligomers Towards Photo- and Redox Active Materials*, *Small* **2013**, *9*, 2348-2357.

94. M. Castelain, H. J. Salavagione, R. Gomez, J. L. Segura, *Supramolecular Assembly of Graphene with Functionalized Poly(fluorene-alt-phenylene): The Role of The Anthraquinone Pendant Groups*, *Chem. Commun.* **2011**, *47*, 7677-7679.

95. Z. Sun, J. Vivekananthan, D. A. Guschin, X. Huang, V. Kuznetsov, P. Ebbinghaus, A. Sarfraz, M. Muhler, W. Schuhmann, *High-Concentration Graphene Dispersions with Minimal Stabilizer: A Scaffold for Enzyme Immobilization for Glucose Oxidation*, *Chem. Eur. J.* **2014**, *20*, 5752-5761.

96. R. J. Fullerton, D. P. Cole, K. D. Behler, S. Das, F. Irin, D. Parviz, M. N. F. Hoque, Z. Fan, M. J. Green, *Graphene Non-Covalently Tethered with Magnetic Nanoparticles*, *Carbon* **2014**, *72*, 192-199.

97. R. Otero, J. M. Gallego, A. L. Vázquez de Parga, N. Martín, R. Miranda, *Molecular Self-Assembly at Solid Surfaces*, *Adv. Mater.* **2011**, *23*, 5148-5176.

98. K. S. Mali, J. Greenwood, J. Adisoejoso, R. Phillipson, S. De Feyter, *Nanostructuring Graphene for Controlled and Reproducible Functionalization*, *Nanoscale* **2015**, *7*, 1566-1585.

99. T.-C. Tseng, C. Urban, Y. Wang, R. Otero, S. L. Tait, M. Alcamí, D. Écija, M. Trelka, J. M. Gallego, N. Lin, M. Konuma, U. Starke, A. Nefedov, A. Langner, C. Wöll, M. Á. Herranz, F. Martín, N. Martín, K. Kern, R. Miranda, *Charge-Transfer-Induced Structural Rearrangements at Both Sides of Organic/Metal Interfaces*, *Nat. Chem.* **2010**, *2*, 374-379.

100. K. Yang, W. D. Xiao, Y. H. Jiang, H. G. Zhang, L. W. Liu, J. H. Mao, H. T. Zhou, S. X. Du, H. J. Gao, *Molecule–Substrate Coupling Between Metal Phthalocyanines and Epitaxial Graphene Grown on Ru(0001) and Pt(111)*, *J. Phys. Chem. C* **2012**, *116*, 14052-14056.

101. J. Mao, H. Zhang, Y. Jiang, Y. Pan, M. Gao, W. Xiao, H. J. Gao, *Tunability of Supramolecular Kagome Lattices of Magnetic Phthalocyanines Using Graphene-Based Moiré Patterns as Templates*, *J. Am. Chem. Soc.* **2009**, *131*, 14136-14137.

102. S. Barja, M. Garnica, J. J. Hinarejos, A. L. Vazquez de Parga, N. Martín, R. Miranda, *Self-Organization of Electron Acceptor Molecules on Graphene*, *Chem. Commun.* **2010**, *46*, 8198-8200.

103. M. Garnica, D. Stradi, S. Barja, F. Calleja, C. Diaz, M. Alcami, N. Martín, A. L. Vazquez de Parga, F. Martín, R. Miranda, *Long-Range Magnetic Order in A Purely Organic 2D Layer Adsorbed on Epitaxial Graphene*, *Nat. Phys.* **2013**, *9*, 368-374.

104. J. Lu, P. S. E. Yeo, Y. Zheng, Z. Yang, Q. Bao, C. K. Gan, K. P. Loh, *Using The Graphene Moiré Pattern for The Trapping of C_{60} and Homoepitaxy of Graphene*, *ACS Nano* **2012**, *6*, 944-950.

105. J. Cho, J. Smerdon, L. Gao, Ö. Süzer, J. R. Guest, N. P. Guisinger, *Structural and Electronic Decoupling of C_{60} from Epitaxial Graphene on SiC*, *Nano Lett.* **2012**, *12*, 3018-3024.

106. M. Roos, D. Künzel, B. Uhl, H.-H. Huang, O. Brandao Alves, H. E. Hoster, A. Gross, R. J. Behm, *Hierarchical Interactions and Their Influence upon The Adsorption of Organic Molecules on A Graphene Film*, *J. Am. Chem. Soc.* **2011**, *133*, 9208-9211.

107. X. Sun, J. Zhang, X. Wang, C. Zhang, P. Hu, Y. Mu, X. Wan, Z. Guo, S. Lei, *Oligothiophenes on CVD Graphene Grown on Multi-Crystalline Copper Foil: Supramolecular Assembly and Impact of Morphology*, *Chem. Commun.* **2013**, *49*, 10317-10319.

108. W. Chen, S. Chen, D. C. Qi, X. Y. Gao, A. T. S. Wee, *Surface Transfer p-Type Doping of Epitaxial Graphene*, *J. Am. Chem. Soc.* **2007**, *129*, 10418-10422.

109. Y.-L. Wang, J. Ren, C.-L. Song, Y.-P. Jiang, L.-L. Wang, K. He, X. Chen, J.-F. Jia, S. Meng, E. Kaxiras, Q.-K. Xue, X.-C. Ma, *Selective Adsorption and Electronic Interaction of F_{16}CuPc on Epitaxial Graphene*, *Phys. Rev. B* **2010**, *82*, 245420.

110. B. Li, A. V. Klekachev, M. Cantoro, C. Huyghebaert, A. Stesmans, I. Asselberghs, S. De Gendt, S. De Feyter, *Toward Tunable Doping in Graphene FETs by Molecular Self-Assembled Monolayers*, *Nanoscale* **2013**, *5*, 9640-9644.

111. W. Zhang, C.-T. Lin, K.-K. Liu, T. Tite, C.-Y. Su, C.-H. Chang, Y.-H. Lee, C.-W. Chu, K.-H. Wei, J.-L. Kuo, L.-J. Li, *Opening An Electrical Band Gap of Bilayer Graphene with Molecular Doping*, *ACS Nano* **2011**, *5*, 7517-7524.

112. J. M. P. Alaboson, Q. H. Wang, J. D. Emery, A. L. Lipson, M. J. Bedzyk, J. W. Elam, M. J. Pellin, M. C. Hersam, *Seeding Atomic Layer Deposition of High-k Dielectrics on Epitaxial Graphene with Organic Self-Assembled Monolayers*, *ACS Nano*, **2011**, *5*, 5223-5232.

113. C. Casiraghi, A. Hartschuh, H. Qian, S. Piscanec, C. Georgi, A. Fasoli, K. S. Novoselov, D. M. Basko, A. C. Ferrari, *Raman Spectroscopy of Graphene Edges*, *Nano Lett.* **2009**, *9*, 1433-1441.

114. J. M. Englert, P. Vecera, K. C. Knirsch, R. A. Schäfer, F. Hauke, A. Hirsch, *Scanning-Raman-Microscopy for The Statistical Analysis of Covalently Functionalized Graphene*, *ACS Nano* **2013**, *7*, 5472-5482.

115. X. Dong, D. Fu, W. Fang, Y. Shi, P. Chen, L.-J. Li, *Doping Single-Layer Graphene with Aromatic Molecules*, *Small* **2009**, *5*, 1422-1426.

116. Q. Su, S. Pang, V. Alijani, C. Li, X. Feng, K. Müllen, *Composites of Graphene with Large Aromatic Molecules*, *Adv. Mater.* **2009**, *21*, 3191-3195.

117. a) Z. Ni, Y. Wang, T. Yu, Z. Shen, *Raman Spectroscopy and Imaging of Graphene*, *Nano Res.* **2008**, *1*, 273-291. b) L. M. Malard, M. A. Pimenta, G. Dresselhaus, M. S. Dresselhaus, *Raman Spectroscopy in Graphene*, *Phys. Rep.* **2009**, *473*, 51-87.

118. J. N. Coleman, *Liquid Exfoliation of Defect-Free Graphene*, *Acc. Chem. Res.* **2013**, *46*, 14-22.

119. Y. Yamashita, Y. Kobayashi, T. Miyashi, *p-Quinodimethane Analogues of Tetrathiafulvalene*, *Angew. Chem. Int. Ed.* **1989**, *28*, 1052-1053.

120. F. G. Brunetti, J. L. Lopez, C. Atienza, N. Martín, *π-Extended TTF: A Versatile Molecule for Organic Electronics*, *J. Mater. Chem.* **2012**, *22*, 4188-4205.

121. Y. Takano, S. Obuchi, N. Mizorogi, R. García, M. Á. Herranz, M. Rudolf, S. Wolfrum, D. M. Guldi, N. Martín, S. Nagase, T. Akasaka, *Stabilizing Ion and Radical Ion Pair States in A Paramagnetic Endohedral Metallofullerene/π-Extended Tetrathiafulvalene Conjugate*, *J. Am. Chem. Soc.* **2012**, *134*, 16103-16106.

122. J. Mateos-Gil, L. Rodriguez-Perez, M. Moreno Oliva, G. Katsukis, C. Romero-Nieto, M. A. Herranz, D. M. Guldi, N. Martín, *Electroactive Carbon Nanoforms: A Comparative Study Via Sequential Arylation and Click Chemistry Reactions*, *Nanoscale* **2015**, *7*, 1193-1200.

123. E. M. Perez, B. M. Illescas, M. A. Herranz, N. Martín, *Supramolecular Chemistry of π-Extended Analogues of TTF and Carbon Nanostructures*, *New J. Chem.* **2009**, *33*, 228-234.

124. L. Moreira, J. Calbo, R. M. Krick Calderon, J. Santos, B. M. Illescas, J. Arago, J.-F. Nierengarten, D. M. Guldi, E. Orti, N. Martín, *Unveiling The Nature of Supramolecular Crown Ether-C_{60} Interactions*, *Chem. Sci.* **2015**, *6*, 4426-4432.

125. J. L. López, C. Atienza, A. Insuasty, J. López-Andarias, C. Romero-Nieto, D. M. Guldi, N. Martín, *Concave Versus Planar Geometries for The Hierarchical Organization of Mesoscopic 3D Helical Fibers*, *Angew. Chem. Int. Ed.* **2012**, *51*, 3857-3861.

126. J. López-Andarias, J. L. López, C. Atienza, F. G. Brunetti, C. Romero-Nieto, D. M. Guldi, N. Martín, *Controlling The Crystalline Three-dimensional Order in Bulk Materials by Single-Wall Carbon Nanotubes*, *Nat. Commun.* **2014**, *5*, 3763.

127. A. J. Moore, M. R. Bryce, *Generation and Trapping of Phosphorus Stabilized 4,5-Ethylenedithio-1,3-dithiol-2-ide Carbanions: Synthesis of Ethylenedithio-1,3-dithiafulvalenes*, *Synthesis* **1991**, 26-28.

128. M. Á. Herranz, C. Ehli, S. Campidelli, M. Gutiérrez, G. L. Hug, K. Ohkubo, S. Fukuzumi, M. Prato, N. Martín, D. M. Guldi, *Spectroscopic Characterization of Photolytically Generated Radical Ion Pairs in Single-Wall Carbon Nanotubes Bearing Surface-Immobilized Tetrathiafulvalenes*, *J. Am. Chem. Soc.* **2008**, *130*, 66-73.

129. P. D. Jones, T. E. Glass, *Exploring The Effects of Cooperative Interactions on Affinity Using A Pinwheel Sensor System, Tetrahedron* **2004**, *60*, 11057-11065.

130. M. C. Díaz, B. M. Illescas, C. Seoane, N. Martín, *Synthesis and Electron-Donor Ability of The First Conjugated π-Extended Tetrathiafulvalene Dimers*, *J. Org. Chem.* **2004**, *69*, 4492-4499.

131. W. Baik, W. Luan, H. J. Lee, C. H. Yoon, S. Koo, B. H. Kim, *Efficient One-Pot Transformation of Aminoarenes to Haloarenes Using Halodimethylsulfonium Halides Generated In Situ, Can. J. Chem.* **2005**, *83*, 213-219.

132. a) E. M. Pérez, L. Sánchez, G. Fernández, N. Martín, *exTTF as A Building Block for Fullerene Receptors. Unexpected Solvent-Dependent Positive Homotropic Cooperativity*, *J. Am. Chem. Soc.* **2006**, *128*, 7172-7173. b) E. M. Perez, N. Martín, *Curves Ahead: Molecular Receptors for*

Fullerenes Based on Concave-Convex Complementarity, *Chem. Soc. Rev.* **2008**, *37*, 1512-1519.

133. A. T. Haedler, H. Misslitz, C. Buehlmeyer, R. Q. Albuquerque, A. Köhler, H.-W. Schmidt, *Controlling The π-Stacking Behavior of Pyrene Derivatives: Influence of H-Bonding and Steric Effects in Different States of Aggregation*, *ChemPhysChem* **2013**, *14*, 1818-1829.

134. Das. A, Pisana. S, Chakraborty. B, Piscanec. S, S. K. Saha, U. V. Waghmare, K. S. Novoselov, H. R. Krishnamurthy, A. K. Geim, A. C. Ferrari, A. K. Sood, *Monitoring Dopants by Raman Scattering in An Electrochemically Top-Gated Graphene Transistor*, *Nat. Nanotechnol.* **2008**, *3*, 210-215.

135. M. E. Lipińska, S. L. H. Rebelo, M. F. R. Pereira, J. A. N. F. Gomes, C. Freire, J. L. Figueiredo, *New Insights into The Functionalization of Multi-walled Carbon Nanotubes with Aniline Derivatives*, *Carbon* **2012**, *50*, 3280-3294.

136. C. Urban, D. Écija, Y. Wang, M. Trelka, I. Preda, A. Vollmer, N. Lorente, A. Arnau, M. Alcamí, L. Soriano, N. Martín, F. Martín, R. Otero, J. M. Gallego, R. Miranda, *Growth and Structure of Self-Assembled Monolayers of A TTF Derivative on Au(111)*, *J. Phys. Chem. C* **2010**, *114*, 6503-6510.

137. E. Laviron, *General Expression of The Linear Potential Sweep Voltammogram in The Case of Diffusionless Electrochemical Systems*, *J. Electroanal. Chem.* **1979**, *101*, 19-28.

138. M. Gouterman, *The Porphyrins*, Academic Press, New York, **1978**.

139. a) H. Imahori, T. Umeyama, K. Kurotobi, Y. Takano, *Self-Assembling Porphyrins and Phthalocyanines for Photoinduced Charge Separation and Charge Transport*, *Chem. Commun.* **2012**, *48*, 4032-4045. b) T. Hasobe, *Porphyrin-Based Supramolecular Nanoarchitectures for Solar Energy Conversion*, *J. Phys. Chem. Lett* **2013**, *4*, 1771-1780. c) T. Umeyama, H. Imahori, *Photofunctional Hybrid Nanocarbon Materials*, *J. Phys. Chem. C* **2013**, *117*, 3195-3209.

140. S. Vela, S. Bauroth, C. Atienza, A. Molina-Ontoria, D. M. Guldi, N. Martín, *Determining The Attenuation Factor in Molecular Wires Featuring Covalent and Noncovalent Tectons*, *Angew. Chem. Int. Ed.* **2016**, *55*, 15076-15080.

141. Y. Hizume, K. Tashiro, R. Charvet, Y. Yamamoto, A. Saeki, S. Seki, T. Aida, *Chiroselective Assembly of A Chiral Porphyrin−Fullerene Dyad: Photoconductive Nanofiber with A Top-Class Ambipolar Charge-Carrier Mobility*, *J. Am. Chem. Soc.* **2010**, *132*, 6628-6629.

142. J. K. Sprafke, S. D. Stranks, J. H. Warner, R. J. Nicholas, H. L. Anderson, *Noncovalent Binding of Carbon Nanotubes by Porphyrin Oligomers*, *Angew. Chem. Int. Ed.* **2011**, *50*, 2313-2316.

143. H.-X. Wang, K.-G. Zhou, Y.-L. Xie, J. Zeng, N.-N. Chai, J. Li, H.-L. Zhang, *Photoactive Graphene Sheets Prepared by "Click" Chemistry*, *Chem. Commun.* **2011**, *47*, 5747-5749.

144. a) J. S. Lindsey, I. C. Schreiman, H. C. Hsu, P. C. Kearney, A. M. Marguerettaz, *Rothemund and Adler-Longo Reactions Revisited: Synthesis of Tetraphenylporphyrins Under Equilibrium Conditions*, *J. Org. Chem.* **1987**, *52*, 827-836. b) P. D. Rao, S. Dhanalekshmi, B. J. Littler, J. S. Lindsey, *Rational Syntheses of Porphyrins Bearing up to Four Different Meso Substituents*, *J. Org. Chem.* **2000**, *65*, 7323-7344.

145. M. J. Plater, S. Aiken, G. Bourhill, *A New Synthestic Route to Donor-acceptor Porphyrins*, *Tetrahedron* **2002**, *58*, 2405-2413.

146. N. M. Loim, E. S. Kelbyscheva, *Synthesis of Dendrimers with Terminal Formyl Groups*, *Russ. Chem. Bull.* **2004**, *53*, 2080-2085.

147. R. Kumar, M. Sankar, *Synthesis, Spectral, and Electrochemical Studies of Electronically Tunable β-Substituted Porphyrins with Mixed Substituent Pattern*, *Inorg. Chem.* **2014**, *53*, 12706-12719.

148. A. V. Safronov, N. I. Shlyakhtina, T. A. Everett, M. R. VanGordon, Y. V. Sevryugina, S. S. Jalisatgi, M. F. Hawthorne, *Direct Observation of Bis(dicarbollyl)nickel Conformers in Solution by Fluorescence Spectroscopy: An Approach to Redox-Controlled Metallacarborane Molecular Motors*, *Inorg. Chem.* **2014**, *53*, 10045-10053.

149. S. Yang, L. Dunsch, *A Large Family of Dysprosium-Based Trimetallic Nitride Endohedral Fullerenes: $Dy_3N@C_{2n}$ $(39 \leq n \leq 44)$*, *J. Phys. Chem. B* **2005**, *109*, 12320-12328.

150. J. J. Snellenburg, S. P. Laptenok, R. Seger, K. M. Mullen, I. H. M. van Stokkum, *Glotaran: A Java-Based Graphical User Interface for The R Package TIMP*, *J. Stat. Soft.* **2012**, *49*, 1-22.

151. G. Sforazzini, E. Orentas, A. Bolag, N. Sakai, S. Matile, *Toward Oriented Surface Architectures with Three Coaxial Charge-Transporting Pathways*, *J. Am. Chem. Soc.* **2013**, *135*, 12082-12090.

152. a) C. X. Guo, H. B. Yang, Z. M. Sheng, Z. S. Lu, Q. L. Song, C. M. Li, *Layered Graphene/Quantum Dots for Photovoltaic Devices*, *Angew. Chem. Int. Ed.* **2010**, *49*, 3014-3017. b) H. Xin, S. Subramaniyan, T.-W. Kwon, S. Shoaee, J. R. Durrant, S. A. Jenekhe, *Enhanced Open Circuit Voltage and Efficiency of Donor–Acceptor Copolymer Solar Cells by Using Indene-C_{60} Bisadduct*, *Chem. Mater.* **2012**, *24*, 1995-2001.

153. a) A. Le Goff, B. Reuillard, S. Cosnier, *A Pyrene-Substituted Tris(bipyridine)osmium(II) Complex as A Versatile Redox Probe for Characterizing and Functionalizing Carbon Nanotube- and Graphene-Based Electrodes*, *Langmuir* **2013**, *29*, 8736-8742. b) M. Kohmoto, H. Ozawa, L. Yang, T. Hagio, M. Matsunaga, M.-a. Haga, *Controlling The Adsorption of Ruthenium Complexes on Carbon Surfaces Through Noncovalent Bonding with Pyrene Anchors: An Electrochemical Study*, *Langmuir* **2016**, *32*, 4141-4152.

154. a) Q. Xie, E. Perez-Cordero, L. Echegoyen, *Electrochemical Detection of C_{60}^{6-} and C_{70}^{6-}: Enhanced Stability of Fullerides in Solution*, *J. Am. Chem. Soc.* **1992**, *114*, 3978-3980. b) L. Echegoyen, L. E. Echegoyen, *Electrochemistry of Fullerenes and Their Derivatives*, *Acc. Chem. Res.* **1998**, *31*, 593-601.

155. D. M. Guldi, M. Prato, *Excited-State Properties of C_{60} Fullerene Derivatives*, *Acc. Chem. Res.* **2000**, *33*, 695-703.

156. a) D. M. Guldi, N. Martín, *Fullerenes: From Synthesis to Optoelectronic Properties*, Springer, **2002**. b) G. Accorsi, N. Armaroli, *Taking Advantage of The Electronic Excited States of [60]-Fullerenes*, *J. Phys. Chem. C* **2010**, *114*, 1385-1403.

157. C. Villegas, E. Krokos, P.-A. Bouit, J. L. Delgado, D. M. Guldi, N. Martín, *Efficient Light Harvesting Anionic Heptamethine Cyanine-[60] and [70]Fullerene Hybrids*, *Energy Environ. Sci.* **2011**, *4*, 679-684.

158. H. Isla, E. M. Pérez, N. Martín, *High Degree of Polymerization in A Fullerene-Containing Supramolecular Polymer*, *Angew. Chem. Int. Ed.* **2014**, *53*, 5629-5633.

159. A. Insuasty, C. Atienza, J. L. Lopez, N. Martín, *Supramolecular Pentapeptide-Based Fullerene Nanofibers: Effect of Molecular Chirality*, *Chem. Commun.* **2015**, *51*, 10506-10509.

160. D. Garcia, L. Rodriguez-Perez, M. A. Herranz, D. Pena, E. Guitian, S. Bailey, Q. Al-Galiby, M. Noori, C. J. Lambert, D. Perez, N. Martín, *A C_{60}-Aryne Building Block: Synthesis of A Hybrid All-Carbon Nanostructure*, *Chem. Commun.* **2016**, *52*, 6677-6680.

161. a) M. Maggini, G. Scorrano, M. Prato, *Addition of Azomethine Ylides to C_{60}: Synthesis, Characterization, and Functionalization of Fullerene Pyrrolidines*, *J. Am. Chem. Soc.* **1993**, *115*, 9798-9799. b) M. Prato, M. Maggini, *Fulleropyrrolidines: A Family of Full-Fledged Fullerene Derivatives*, *Acc. Chem. Res.* **1998**, *31*, 519-526.

162. J. A. Mann, T. Alava, H. G. Craighead, W. R. Dichtel, *Preservation of Antibody Selectivity on Graphene by Conjugation to A Tripod Monolayer*, *Angew. Chem. Int. Ed.* **2013**, *52*, 3177-3180.

163. L. Moreira, B. M. Illescas, N. Martín, *Supramolecular Complexation of Carbon Nanostructures by Crown Ethers*, *J. Org. Chem.* **2017**, *82*, 3347-3358.

164. P. Thordarson, in *Supramolecular Chemistry: From Molecules to Nanomaterials*, John Wiley & Sons, Ltd, **2012**.

165. L. Moreira, J. Calbo, B. M. Illescas, J. Aragó, I. Nierengarten, B. Delavaux-Nicot, E. Ortí, N. Martín, J.-F. Nierengarten, *Metal-atom Impact on The Self-Assembly of Cup-and-Ball Metalloporphyrin–Fullerene Conjugates*, *Angew. Chem. Int. Ed.* **2015**, *54*, 1255-1260.

166. P. D. W. Boyd, M. C. Hodgson, C. E. F. Rickard, A. G. Oliver, L. Chaker, P. J. Brothers, R. D. Bolskar, F. S. Tham, C. A. Reed, *Selective Supramolecular Porphyrin/Fullerene Interactions 1*, *J. Am. Chem. Soc.* **1999**, *121*, 10487-10495.

167. D. Sun, F. S. Tham, C. A. Reed, L. Chaker, P. D. W. Boyd, *Supramolecular Fullerene-Porphyrin Chemistry. Fullerene Complexation by Metalated "Jaws Porphyrin" Hosts*, *J. Am. Chem. Soc.* **2002**, *124*, 6604-6612.

168. M. Nappa, J. S. Valentine, *The Influence of Axial Ligands on Metalloporphyrin Visible Absorption Spectra. Complexes of Tetraphenylporphinatozinc*, *J. Am. Chem. Soc.* **1978**, *100*, 5075-5080.

169. H.-H. Tsai, M. C. Simpson, *Isolated Impact of Ruffling on The Vibrational Spectrum of Ni Porphyrins. Diagnosing Out-of-Plane Distortions*, *J. Phys. Chem. A* **2004**, *108*, 1224-1232.

170. a) G. Fernández, E. M. Pérez, L. Sánchez, N. Martín, *Self-Organization of Electroactive Materials: A Head-to-Tail Donor–Acceptor Supramolecular Polymer*, *Angew. Chem. Int. Ed.* **2008**, *47*, 1094-1097. b) E. M. Pérez, N. Martín, *π-π Interactions in Carbon Nanostructures, Chem. Soc. Rev.* **2015**, *44*, 6425-6433.

171. Y. Liu, Z. Fan, H.-Y. Zhang, C.-H. Diao, *Binding Ability and Self-Assembly Behavior of Linear Polymeric Supramolecules Formed by Modified β-Cyclodextrin*, *Org. Lett.* **2003**, *5*, 251-254.

172. S. Qu, M. Li, L. Xie, X. Huang, J. Yang, N. Wang, S. Yang, *Noncovalent Functionalization of Graphene Attaching [6,6]-Phenyl-C_{61}-butyric Acid Methyl Ester (PCBM) and Application as Electron Extraction Layer of Polymer Solar Cells*, *ACS Nano* **2013**, *7*, 4070-4081.

173. N. L. Allinger, Y. H. Yuh, J. H. Lii, *Molecular Mechanics. The MM3 Force Field for Hydrocarbons. 1*, *J. Am. Chem. Soc.* **1989**, *111*, 8551-8566.

174. J. W. Ponder, *TINKER Version 7.1* **2015**, http://dasher.wustl.edu/tinker.

175. E. F. Pettersen, T. D. Goddard, C. C. Huang, G. S. Couch, D. M. Greenblatt, E. C. Meng, T. E. Ferrin, *UCSF Chimera—A Visualization System for Exploratory Research and Analysis*, *J. Comput. Chem.* **2004**, *25*, 1605-1612.

176. W. L. F. Armarego, C. L. L. Chai, *Purification of Laboratory Chemicals*, Elsevier, **2003**.

177. a) W. S. Hummers, R. E. Offeman, *Preparation of Graphitic Oxide*, *J. Am. Chem. Soc.* **1958**, *80*, 1339. b) E. Casero, A. M. Parra-Alfambra, M. D. Petit-Domínguez, F. Pariente, E. Lorenzo, C. Alonso, *Differentiation Between Graphene Oxide and Reduced Graphene by Electrochemical Impedance Spectroscopy (EIS)*, *Electrochem. Commun.* **2012**, *20*, 63-66. c) E. Casero, C. Alonso, L. Vázquez, M. D. Petit-Domínguez, A. M. Parra-Alfambra, M. de la Fuente, P. Merino, S. Álvarez-García, A. de Andrés, F. Pariente, E. Lorenzo, *Comparative Response of Biosensing Platforms Based on Synthesized Graphene Oxide and Electrochemically Reduced Graphene*, *Electroanalysis* **2013**, *25*, 154-165.

178. H.-L. Guo, X.-F. Wang, Q.-Y. Qian, F.-B. Wang, X.-H. Xia, *A Green Approach to The Synthesis of Graphene Nanosheets*, *ACS Nano* **2009**, *3*, 2653-2659.

179. G. J. Marshallsay, M. R. Bryce, *Synthesis and Multistage Redox Properties of 9,10-Bis(1,3-dithiol-2-ylidene)-9,10-dihydroanthracene Derivatives Functionalized with Ferrocenyl and Tetrathiafulvalenyl Units*, *J. Org. Chem.* **1994**, *59*, 6847-6849.

180. S. González, N. Martín, D. M. Guldi, *Synthesis and Properties of Bingel-Type Methanofullerene-π-Extended-TTF Diads and Triads*, *J. Org. Chem.* **2003**, *68*, 779-791.